

GRANT 15R/34
2600 054 523

454250
pgs 98

CONTROL OF CAVITY RESONANCE USING OSCILLATORY BLOWING

by

Alison Lamp Scarfe and Ndaona Chokani

Funded by the Cooperative Agreement NCC-1-335



Table of Contents

LIST OF TABLES	VI
LIST OF FIGURES	VII
NOMENCLATURE	XIV
1 INTRODUCTION	1
1.1 Cavity Flow Physics	2
1.2 Flow Control	6
1.2.1 Cavity Flow Control	6
1.2.2 Oscillatory Blowing and Pulsed Jet Blowing	8
1.3 Objectives of Research	10
2 EXPERIMENTAL METHODS	12
2.1 Experimental Set-up	12
2.1.1 Test Facility	12
2.1.2 Test Model	13
2.1.3 Actuator	16
2.1.4 Instrumentation	20
2.1.4.1 Wall pressure system	20
2.1.4.2 Hot-wire anemometer system	22
2.1.4.3 Traverse system	22
2.1.5 Data Acquisition System	23
2.2 Experimental Procedures	25
2.2.1 Hot-wire Calibration	25
2.2.1.1 Wind tunnel hot-wire calibration.....	26
2.2.1.2 Bench-top hot-wire calibration	26
2.2.2 Surface Measurements.....	27

2.2.2.1	Mean surface pressure measurements.....	27
2.2.2.2	Unsteady surface pressure measurements.....	27
2.2.3	Off-Surface Hot-Wire Measurements.....	28
2.2.4	Experimental Conditions	29
2.3	Data Processing	29
2.3.1	Spectrum.....	29
2.3.2	Auto and Cross Correlation	30
2.3.3	Bicoherence Estimation	32
2.3.4	Wavelet Analysis	33
2.4	Actuator Calibration	35
2.4.1	Calibration Set-up.....	35
2.4.2	Calibration Procedures.....	36
2.4.3	Oscillatory Blowing Calibration.....	37
3	RESULTS	44
3.1	Characteristics of Baseline Cavity Flow.....	44
3.2	Effectiveness of Control.....	49
3.2.1	Steady Blowing.....	49
3.2.2	Zero-Net Mass Oscillatory Blowing.....	58
3.2.2.1	Effect of forcing frequency.....	58
3.2.2.2	Effect of hole geometry	63
3.3	Auto Correlation Analysis.....	72
3.3.1	Baseline.....	72
3.3.2	Steady Blowing.....	73
3.3.3	Zero Net Mass Oscillatory Blowing	78
3.4	Cross Correlation Analysis	82
3.4.1	Baseline.....	82
3.4.2	Steady Blowing.....	85
3.4.3	Zero Net Mass Oscillatory Blowing	90

3.5	Bispectral Analysis.....	95
3.5.1	Baseline.....	96
3.5.2	Steady Blowing.....	100
3.5.3	Zero Net Mass Oscillatory Blowing.....	109
3.6	Wavelet Analysis.....	118
3.6.1	Baseline.....	118
3.6.2	Steady Blowing.....	123
3.6.3	Near-Zero Net Mass Oscillatory Blowing.....	129
3.7	Shear Layer Measurements.....	134
3.7.1	Baseline.....	134
3.7.2	Steady Blowing.....	138
3.7.3	Near-Zero Net Mass Oscillatory Blowing.....	144
3.7.3.1	Effect of forcing frequency and blowing amplitude.....	144
3.7.3.2	Effect of blowing angle.....	151
4	CONCLUDING REMARKS	157
4.1	Summary of Results.....	157
4.1.1	Steady blowing.....	157
4.1.2	Near-zero Net mass oscillatory blowing.....	158
4.2	Dynamics and mechanisms of control.....	159
4.3	Recommendations.....	160
5	REFERENCES	161
A	APPENDICES	165
A.1	Actuator Design.....	165
A.2	Experimental Uncertainty.....	178

List of Tables

Table 2.1: Summary of hole plate characteristics.	20
Table 3.1: Predicted and actual modal frequencies of the baseline cavity flow. $L/D = 4$, $M_\infty = 0.2$	48
Table A.1: Description of the actuator components.....	166
Table A.1: Uncertainty of tunnel properties and calculated values.	178
Table A.2: Repeatability of tunnel properties between runs.....	178

List of Figures

Figure 1.1: Noise sources on a commercial aircraft.....	1
Figure 1.1: Open cavity flow features. a) Schlieren image b) schematic.....	3
Figure 1.1: Active control system.....	8
Figure 2.1: Probe Calibration Tunnel with instrument rack.....	13
Figure 2.1: Cavity model inside the tunnel plenum, showing the hot-wire set-up.	14
Figure 2.2: Cavity-tunnel modal interaction, $L/D=2$. a) without acoustic liner b) with acoustic liner.....	15
Figure 2.1: Actuator set-up on the bench-top.....	16
Figure 2.2: Diagram of rotary pulse valve actuator.	17
Figure 2.3: Flow diagram of actuator system.....	19
Figure 2.1: Wall pressure tap locations of the cavity model.....	22
Figure 2.1: Computer network used in the PCT experiments.....	23
Figure 2.2: Overview of PCT-5 instrument controls.....	25
Figure 2.1: Hot-wire calibration set-up, with sidewall removed.....	26
Figure 2.1: Cavity coordinate system for the hot-wire traverse.....	28
Figure 2.1: Morlet mother wavelet.....	34
Figure 2.2: The effect of scale on the Morlet wavelets in the frequency domain.....	35
Figure 2.1: Velocity and pressure calibration data, $f_t = 140Hz$, configuration SSA: a) time trace b) spectra.	41
Figure 2.2: Blowing velocity vs. actuator delivery chamber pressure, configuration SSA.	41
Figure 2.3: Resonant characteristics of the actuator at different input/output conditions, configuration SSA.	42

Figure 2.4: Calibration of unsteady velocity vs. actuator delivery chamber pressure, $f_f = 140\text{Hz}$, configuration SSA.....	43
Figure 2.5: Actuator output during cavity test, $M = 0.2$, configuration SSA: a) measured p'/ρ b) calculated $\langle c_\mu \rangle$	44
Figure 3.1: Mach number distribution along the tunnel ceiling. Baseline cavity flow...	45
Figure 3.2: Time-mean pressures. Baseline cavity flow. $M_\infty = 0.2$	46
Figure 3.3: Spectra for baseline cavity flow. $M_\infty = 0.2$	48
Figure 3.1: Effectiveness of steady blowing control at rear wall location. a) momentum coefficient, b) velocity ratio, c) Reynolds number.	53
Figure 3.2: Effectiveness of steady blowing control at front floor location. a) momentum coefficient, b) velocity ratio, c) Reynolds number.	54
Figure 3.3: Spectra showing effect of hole size, $c_\mu = 0.01$: a) rear wall b) front floor locations.	55
Figure 3.4: Spectra showing effect of hole shape, $c_\mu = 0.01$: a) rear wall b) front floor locations.	56
Figure 3.5: Spectra showing effect of blowing angle, $c_\mu = 0.01$: a) rear wall b) front floor locations.....	57
Figure 3.1: Effect of forcing frequency at rear location, $M_\infty = 0.2$, Configuration SSA. a) $\langle c_\mu \rangle = 2 \times 10^{-6}$; b) $\langle c_\mu \rangle = 2 \times 10^{-5}$; c) $\langle c_\mu \rangle = 2 \times 10^{-4}$; d) $\langle c_\mu \rangle = 2 \times 10^{-3}$	60
Figure 3.2: Effect of forcing frequency at floor location, $M_\infty = 0.2$, Configuration SSA. a) $\langle c_\mu \rangle = 2 \times 10^{-6}$; b) $\langle c_\mu \rangle = 2 \times 10^{-5}$; c) $\langle c_\mu \rangle = 2 \times 10^{-4}$; d) $\langle c_\mu \rangle = 2 \times 10^{-3}$	62
Figure 3.1: Effectiveness of zero net-mass oscillatory blowing on second cavity mode, rear location. a) $f_f = 200\text{ Hz}$; b) $f_f = 400\text{ Hz}$; c) $f_f = 550\text{ Hz}$	66
Figure 3.2: Effectiveness of zero net-mass oscillatory blowing on second cavity mode, floor location. a) $f_f = 200\text{ Hz}$; b) $f_f = 400\text{ Hz}$; c) $f_f = 550\text{ Hz}$	68
Figure 3.3: Spectra showing effect of hole size, $\langle c_\mu \rangle = 1 \times 10^{-5}$, $f_f = 550\text{Hz}$: a) rear wall b) floor locations.	69
Figure 3.4: Spectra showing effect of hole shape; $\langle c_\mu \rangle = 1 \times 10^{-5}$, $f_f = 550\text{Hz}$: a) rear wall b) floor locations.....	70

Figure 3.5: Spectra showing the effect of blowing angle; $\langle c_{\mu} = 1 \times 10^{-5} \rangle$, $f_f = 550Hz$: a) rear wall b) floor locations.	71
Figure 3.1: Baseline auto-correlations of rear and floor locations.	73
Figure 3.1: Auto-correlations showing the effect of hole size using steady blowing, $c_{\mu} = 0.01$: a) rear b) floor locations.	75
Figure 3.2: Auto-correlations showing the effect of hole shape using steady blowing, $c_{\mu} = 0.01$: a) rear b) floor locations.	76
Figure 3.3: Auto-correlations showing the effect of blowing angle using steady blowing, $c_{\mu} = 0.01$: a) rear b) floor locations.	77
Figure 3.1: Auto-correlations showing the effect of hole size using oscillatory blowing, $f_f = 550Hz$, $\langle c_{\mu} \rangle = 1 \times 10^{-5}$: a) rear b) floor locations.	79
Figure 3.2: Auto-correlations showing the effect of hole shape using oscillatory blowing, $f_f = 550Hz$, $\langle c_{\mu} \rangle = 1 \times 10^{-5}$: a) rear b) floor locations.	80
Figure 3.3: Auto-correlations showing the effect of blowing angle using oscillatory blowing, $f_f = 550Hz$, $\langle c_{\mu} \rangle = 1 \times 10^{-5}$: a) rear b) floor locations.	81
Figure 3.1: Baseline relationship between the rear and floor transducers. a) cross-correlation b) coherence c) phase angle.	84
Figure 3.1: Effect of hole size on the relationship between the rear and floor transducers using steady blowing; $c_{\mu} = 0.01$. a) cross-correlation b) coherence c) phase angle.	87
Figure 3.2: Effect of hole shape on the relationship between the rear and floor transducers using steady blowing; $c_{\mu} = 0.01$. a) cross-correlation b) coherence c) phase angle.	88
Figure 3.3: Effect of blowing angle on the relationship between the rear and floor transducers using steady blowing; $c_{\mu} = 0.01$. a) cross-correlation b) coherence c) phase angle.	89
Figure 3.1: Effect of hole size on the relationship between the rear and floor transducers using oscillatory blowing; $f_f = 550Hz$, $\langle c_{\mu} \rangle = 1 \times 10^{-5}$. a) cross-correlation b) coherence c) phase angle.	92
Figure 3.2: Effect of hole shape on the relationship between the rear and floor transducers using oscillatory blowing; $f_f = 550Hz$, $\langle c_{\mu} \rangle = 1 \times 10^{-5}$. a) cross-correlation b) coherence c) phase angle.	93

Figure 3.3: Effect of blowing angle on the relationship between the rear and floor transducers using oscillatory blowing; $f_f = 550\text{Hz}$, $\langle c_{\mu} \rangle = 1 \times 10^{-5}$. a) cross-correlation b) coherence c) phase angle.	95
Figure 3.1: Symmetry properties of auto and cross bicoherence.	96
Figure 3.1: Bicoherence of the baseline data. a) Rear b) floor locations.	99
Figure 3.2: Baseline Cross bicoherence. Rear and floor locations.....	100
Figure 3.1: Auto bicoherence for steady blowing: rear wall location. a) configuration R1, b) configuration R2, c) configuration R3, d) configuration RA, e) configuration SS, f) configuration SSA, g) configuration LS.	103
Figure 3.2: Auto bicoherence for steady blowing: front floor location. a) configuration R1, b) configuration R2, c) configuration R3, d) configuration RA, e) configuration SS, f) configuration SSA, g) configuration LS.	106
Figure 3.3: Cross-bicoherence using steady blowing: Rear and floor locations. a) configuration R1, b) configuration R2, c) configuration R3, d) configuration RA, e) configuration SS, f) configuration SSA, g) configuration LS.....	108
Figure 3.1: Auto-bicoherence using oscillatory blowing: Rear location. a) configuration R1, b) configuration R2, c) configuration R3, d) configuration RA, e) configuration SS, f) configuration SSA, g) configuration LS.	112
Figure 3.2: Auto-bicoherence using oscillatory blowing: Floor location. a) configuration R1, b) configuration R2, c) configuration R3, d) configuration RA, e) configuration SS, f) configuration SSA, g) configuration LS.....	115
Figure 3.3: Cross-bicoherence using oscillatory blowing: Rear and floor locations. a) configuration R1, b) configuration R2, c) configuration R3, d) configuration RA, e) configuration SS, f) configuration SSA, g) configuration LS.....	118
Figure 3.1: Baseline time series of wavelet coefficients at the rear wall: a) frequency map, b) modal frequencies.	120
Figure 3.2: Baseline time series of wavelet at the front floor: a) frequency map, b) modal frequencies.....	121
Figure 3.3: Spectra of the baseline wavelet coefficients of the modal frequencies: a) rear wall, b) front floor.....	123
Figure 3.1: Wavelet coefficients at rear wall location with steady blowing: $c_{\mu} = 0.01$, configuration SSA.....	123

Figure 3.2: Fourier spectra of wavelet coefficients at the rear wall location with steady blowing control: $c_\mu = 0.01$, configuration R1.....	125
Figure 3.3: Fourier spectra of wavelet coefficients at the rear wall location with steady blowing control: $c_\mu = 0.01$, configuration R2.....	126
Figure 3.4: Fourier spectra of wavelet coefficients at the rear wall location with steady blowing control: $c_\mu = 0.01$, configuration R3.....	126
Figure 3.5: Fourier spectra of wavelet coefficients at the rear wall location with steady blowing control: $c_\mu = 0.01$, configuration RA.....	127
Figure 3.6: Fourier spectra of wavelet coefficients at the rear wall location with steady blowing control: $c_\mu = 0.01$, configuration SS.....	127
Figure 3.7: Fourier spectra of wavelet coefficients at the rear wall location with steady blowing control: $c_\mu = 0.01$, configuration SSA.....	128
Figure 3.8: Fourier spectra of wavelet coefficients at the rear wall location with steady blowing control: $c_\mu = 0.01$, configuration LS.....	128
Figure 3.1: Wavelet coefficients at the rear wall location using oscillatory blowing; $\langle c_\mu \rangle = 1 \times 10^{-5}$, $f_f = 550Hz$, configuration SSA.....	129
Figure 3.2: Fourier spectra of wavelet coefficients at the rear wall location using oscillatory blowing control: $\langle c_\mu \rangle = 1 \times 10^{-5}$, $f_f = 550Hz$, configuration R1.....	130
Figure 3.3: Fourier spectra of wavelet coefficients at the rear wall location using oscillatory blowing control: $\langle c_\mu \rangle = 1 \times 10^{-5}$, $f_f = 550Hz$, configuration R2.....	131
Figure 3.4: Fourier spectra of wavelet coefficients at the rear wall location using oscillatory blowing control: $\langle c_\mu \rangle = 1 \times 10^{-5}$, $f_f = 550Hz$, configuration R3.....	131
Figure 3.5: Fourier spectra of wavelet coefficients at the rear wall location using oscillatory blowing control: $\langle c_\mu \rangle = 1 \times 10^{-5}$, $f_f = 550Hz$, configuration RA.....	132
Figure 3.6: Fourier spectra of wavelet coefficients at the rear wall location using oscillatory blowing control: $\langle c_\mu \rangle = 1 \times 10^{-5}$, $f_f = 550Hz$, configuration SS.....	132
Figure 3.7: Fourier spectra of wavelet coefficients at the rear wall location using oscillatory blowing control: $\langle c_\mu \rangle = 1 \times 10^{-5}$, $f_f = 550Hz$, configuration SSA.....	133
Figure 3.8: Fourier spectra of wavelet coefficients at the rear wall location using oscillatory blowing control: $\langle c_\mu \rangle = 1 \times 10^{-5}$, $f_f = 550Hz$, configuration LS.....	133

Figure 3.1: Baseline mean and rms velocity profiles.....	136
Figure 3.2: Streamwise evolution of spectra in the baseline cavity flow.....	137
Figure 3.3: Streamwise evolution of velocity fluctuations for the baseline case.....	137
Figure 3.1: Mean velocity profiles with steady blowing control.....	140
Figure 3.2: Rms velocity profiles with steady blowing control.....	140
Figure 3.3: Streamwise evolution of spectra with steady blowing control; configuration SS, $c_{\mu} = 0.02$	141
Figure 3.4: Streamwise evolution of spectra with steady blowing control; configuration SSA, $c_{\mu} = 0.02$	141
Figure 3.5: Streamwise evolution of spectra with steady blowing control; configuration LS, $c_{\mu} = 0.03$	142
Figure 3.6: Streamwise evolution of velocity fluctuations using steady blowing control. a) rms b) second cavity mode, c) third cavity mode.....	143
Figure 3.1: Mean velocity profiles with oscillatory blowing control, configuration SS.	146
Figure 3.2: Rms velocity profiles with oscillatory blowing control, configuration SS.	146
Figure 3.3: Streamwise evolution of spectra with oscillatory blowing control; configuration SS, $f_f = 580 \text{ Hz}$, $\langle c_{\mu} \rangle = 2 \times 10^{-4}$	147
Figure 3.4: Streamwise evolution of spectra with oscillatory blowing control; configuration SS, $f_f = 580 \text{ Hz}$, $\langle c_{\mu} \rangle = 7 \times 10^{-4}$	147
Figure 3.5: Streamwise evolution of spectra with oscillatory blowing control; configuration SS, $f_f = 300 \text{ Hz}$, $\langle c_{\mu} \rangle = 2 \times 10^{-4}$	148
Figure 3.6: Streamwise evolution of velocity fluctuations using oscillatory blowing control for Plate SS: a) rms b) second cavity mode, c) third cavity mode, d) 300 Hz , e) 580 Hz	151
Figure 3.1: Mean velocity profiles with oscillatory blowing control.....	153
Figure 3.2: Rms velocity profiles with oscillatory blowing control.....	153
Figure 3.3: Streamwise evolution of spectra with oscillatory blowing control; configuration SSA, $f_f = 580 \text{ Hz}$, $\langle c_{\mu} \rangle = 6 \times 10^{-4}$	154

Figure 3.4: Streamwise evolution of velocity fluctuations using oscillatory blowing control at $f_1=580Hz$: a) rms, b) second cavity mode, c) third cavity mode. d) $580Hz$	156
Figure A.1: Actuator delivery chamber.....	167
Figure A.2: Side wall of the delivery chamber.	168
Figure A.3: Hole insert plate.	169
Figure A.4: Actuator housing which contains the rotor assembly.	170
Figure A.5: Motor mount, which attaches the motor to the housing assembly.....	171
Figure A.6: Rotor.	172
Figure A.7: Rotor axle. Links the motor to the rotor via a coupling.....	173
Figure A.8: Rotor cap.....	174
Figure A.9: Housing end plate.	175
Figure A.10: Assembly drawing of the actuator.	176
Figure A.11: Exploded assembly view of the actuator with coupling and bearings.....	177

Nomenclature

a	Wavelet scale
A	Area
A/D	Analog to Digital converter
B	Bispectrum
b^2	Bicoherence
c_μ	Steady momentum coefficient
$\langle c_\mu \rangle$	Fluctuating momentum coefficient
D	Cavity depth
f	Frequency
\hat{G}_{xx}	Auto-spectrum estimate
k_v	Disturbance convection speed
L	Cavity length
m	Mode number
M_∞	Freestream Mach number
p, P	Pressure
PCT	Probe Calibration Tunnel
q	Dynamic pressure
r	Time lag
\hat{R}_{xy}	Cross-correlation function

u	Jet velocity
U	Velocity
VR	Velocity Ratio, $(\rho_j U_j^2 / \rho_\infty U_\infty^2)^{1/2}$
W	Wavelet coefficients
x_{te}	Extent of separated flow
X	Streamwise direction
X, Y	Fourier Transform of time series x, y
Z	Cross-streamwise direction
γ	Ratio of specific heats
$\hat{\gamma}_{xy}^2$	Coherence estimate
θ	Phase angle
ρ	Density
$\hat{\rho}_{xy}$	Cross-correlation coefficient
τ	Time lag
ω_ψ	Morlet wavelet constant = 5.5
ψ	Mother wavelet function

Superscript:

'	Unsteady, fluctuating
*	Conjugate

Subscript:

∞	Freestream value
f	Forcing
i, j	Components
j	Jet quantity
m	m th mode
N	Nyquist
r, ref	Reference quantity
rms	Root mean square value
t	Total value
x, y	Time series x, y

1 Introduction

A primary concern of today's commercial aircraft designer is the reduction of the aircraft's noise levels during flight. The tighter noise regulations mandated by new Federal Air Regulations and the increased traffic to/from airports are the major factors that motivate a reduction in aircraft noise levels. The primary noise sources of an aircraft that include the body, engines, the flaps and slats, landing gear and wheel wells are illustrated in Figure 1.1. Due to the advent of quieter engines, airframe noise is now the major noise source of an aircraft during descent¹ when the engines are at a low setting and the aircraft is in the high lift, high drag configuration with its flaps, slats, and landing gear deployed. Experimental studies² conducted on full-scale aircraft have identified the wheel bays as one of the main sources of airframe noise producing 5-10dB increases in the spectrum.

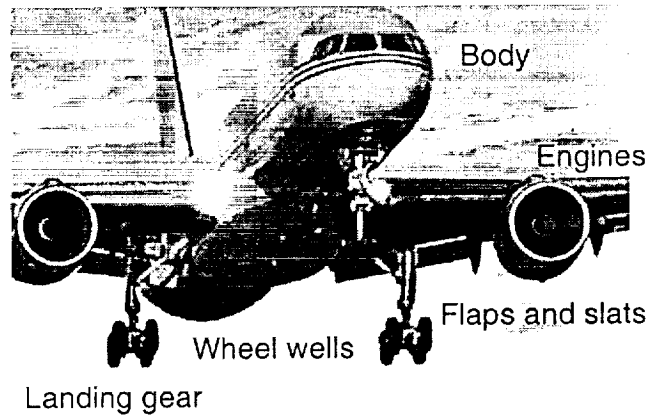


Figure 1.1: Noise sources on a commercial aircraft.

The wheel wells may be modeled as a rectangular cut-out in a surface, or cavity. The oscillatory character of the cavity flow is the source of the intensive noise signature. There is thus interest to understand the physics of cavity flows and to develop methods to suppress the cavity oscillations.

1.1 Cavity Flow Physics

Cavity flows may be classified into three oscillation types:³ fluid dynamic, fluid-resonant, and fluid-elastic. In the fluid dynamic cavity flows, the oscillations are primarily controlled by the vortical structures in the shear layer and their interaction with the rear wall. For fluid resonant cavity flows, the acoustics of the cavity exhibit standing waves in the cavity, which controls the oscillations. In fluid elastic cavity flows, the oscillations are coupled to the motion of a solid boundary. In wheel wells, the cavity flows exhibit the characteristics of both fluid dynamic and fluid resonant oscillations.

The cavity flows of interest to this work are also termed “open type” cavity flows, and generally occur for a cavity with length-to-depth (L/D) ratio less than 7-10. For larger L/D ratios, “closed” cavity flows in which the shear layer impinges onto the cavity floor occur, and the cavity does not resonate. Some of the features of open cavity flow are shown in Figure 1.2. The Schlieren image in Figure 1.2a shows the shear layer that spans the cavity opening. A large vortical structure is seen in the shear layer near the cavity rear wall. In Figure 1.2b, the key elements of the cavity flow are illustrated. The incoming boundary layer separates at the leading edge of the cavity to form the shear layer that bridges the cavity opening. Instabilities, or vortices, are formed at the

separation point. These instabilities grow in size as they are convected downstream in the shear layer. The instabilities impinge on the surface as the shear layer reattaches at the rear wall. Due to this impingement, acoustic disturbances are formed and propagate upstream. At the front wall, the disturbances interact with the shear layer at its separation point. At this location of maximum receptivity, additional vortices are generated; the feedback loop between the vortices and acoustic disturbances is then closed, and distinct cavity tones (or modes) are produced.

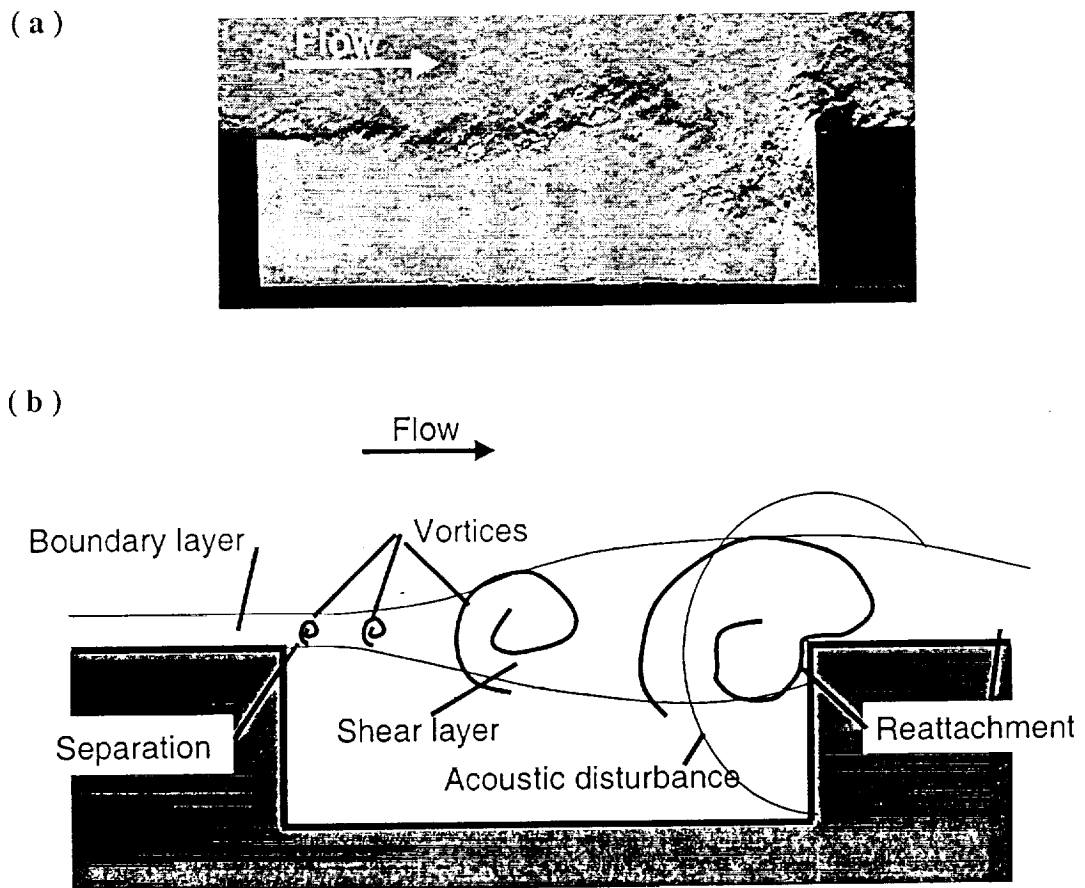


Figure 1.2: Open cavity flow features. a) Schlieren image b) schematic.

Several methods have been developed to predict the frequencies of the resonant modes. These methods predict well the modal frequencies, however, they do poorly in determining the amplitudes of the modes. Rossiter⁴ developed the first method to predict the cavity resonant modes in an incompressible fluid. This semi-empirical formula was modified by Heller and Bliss⁵ to account for compressibility effects. This modified equation is:

$$f_m = \frac{U_\infty}{L} \frac{m - \alpha}{\sqrt{1 + \frac{\gamma - 1}{2} M_\infty^2}} + \frac{1}{k_v} \quad (1.1)$$

where γ is the ratio of specific heats, M_∞ and U_∞ are the freestream Mach number and flow speed respectively, L is the cavity length, and f_m are the resonant frequencies corresponding to the m^{th} mode. There are two empirical constants in the equation: α which is related to the phase lag between the vortices in the shear layer and the upstream traveling acoustic disturbances; and k_v , which is the ratio of the convection speed of the vortices to the freestream speed. The values of the constants depend on the L/D ratio and M_∞ . For a cavity with $L/D=4$, typical values at low Mach number are $\alpha=0.25$ and $k_v=0.66$.

Tam and Block developed a mathematical model of the cavity tones.⁶ This model couples the shear layer instabilities with the acoustic feedback and more accurately predicts the cavity modes. A periodic acoustic line source at the rear lip of the cavity is used in this model and the propagation and reflections of the acoustic waves from the bottom and front wall of the cavity are modeled. The finite thickness of the shear layer, which is found to be an important element in the resonance process, is accounted for.

Computational Fluid Dynamics (CFD) methods have more recently been used to predict the amplitudes and frequencies of the resonant modes. The primary challenges of the CFD approaches are to model the large-scale turbulent structures without having excessive dissipation and to adequately resolve the time-scales of interest. Extensive CFD work has been done for cavity flows using the Reynolds Averaged Navier-Stokes (RANS) equations and is summarized by Chokani.⁷ Hankey and Shang conducted one of the first viscous cavity simulations.⁸ They used the explicit predictor-corrector method of MacCormack with the Cebeci-Smith eddy viscosity turbulence model. More recently, Zhang and Edwards⁹ have modeled the supersonic cavity flow using an explicit method with a $k-\omega$ turbulence model. Rizzeta used a modified Baldwin-Lomax turbulence model in an explicit method to compute both two-dimensional and three-dimensional cavity flows. In comparison to the explicit methods, implicit schemes do not suffer from the excessively restrictive time-step limitations; however implicit methods require large amounts of memory. Baysal et. al.¹⁰ used an implicit upwind scheme with a Baldwin-Lomax turbulence model, and obtained good agreement with measured steady and fluctuating surface pressures. An implicit central difference scheme using a modified Baldwin-Lomax model was developed by Morgenstern and Chokani,¹¹ and applied to hypersonic cavity flows. Sinha et. al.¹² have compared the results from RANS, with several turbulence models, to the prediction of a large eddy simulation (LES) method. They found that the RANS predictions are sensitive to the turbulence model, and the more accurate modeling of the large-scale vortical structures using the LES method produced better agreement with experiments than RANS.

The basic cavity flows have been studied in several experiments. Plentovich¹³ has reported the mean surface pressures in open and closed cavity flows over a range of subsonic and transonic speeds. Mean wall pressures were also presented for supersonic cavity flows with varying cavity length to depth ratios by Stallings and Wilcox.¹⁴ They also found that the width of the cavity influenced the amplitude of the cavity pressures. Spectra of the fluctuating wall pressures were examined by Tracy and Plentovich.¹⁵ The cavity L/D , W/D , and Mach numbers were examined and the spectra used to describe the open and closed cavity flows.

1.2 Flow Control

1.2.1 Cavity Flow Control

Since the 1960's, much research has been conducted to control cavity resonance. The early techniques of attenuating the self-oscillatory behavior of cavity flows were passive methods, whereby fixed changes/modifications are made to modify the cavity and thus disrupt the feedback process. Some examples of these are spoilers^{4,5} and trailing edge slants⁵, to modify the impingement of the shear layer at the downstream wall, and cowls⁵, to interrupt the mass transfer above the cavity downstream wall. More recently, leading edge ramps¹⁶ and rear wall modifications using passive venting and swept back, inclined geometry¹⁷ have been examined. Passive pneumatic control, which uses the pressure difference in the cavity to transport fluid along the cavity floor, has also been investigated.¹⁸ Passive control methods are inexpensive and simple. At certain flow conditions, these methods are very effective in suppressing the cavity oscillations.

However, since passive methods use permanent devices, the cavity resonance at an off-design condition or in time-varying conditions may actually be worse than the cavity resonance without passive control.

Active control methods on the other hand, have the potential to be continuously changed to adapt to different flow conditions. An active control system is required to implement active flow control. This system consists of three components: the sensor, a controller, and an actuator Figure 1.3. In an open loop control system, the actuator is operated independently of the sensor; in a closed loop control system the actuator and sensor are continuously and automatically adjusted through the controller. Although active control systems are more complex, active control has the potential to reduce cavity resonance over a wide range of conditions. Several actuation approaches for active control in cavity flows have been studied. Vakili et al.¹⁹ used distributed air injection upstream of the cavity to obtain up to $27dB$ decrease in the peak sound pressure level. Cattafesta et al.²⁰ used a flapping plate at the front wall of the cavity to demonstrate both open and closed loop control of the cavity oscillations; the closed loop control, using mode cancellation was more effective. Shaw²¹ found that pulsed blowing through a slot located at the front edge of the cavity was more effective than steady blowing. Sarno and Franke²² found that both steady and pulsed blowing through a slot located just within the cavity on the front wall were equally effective.

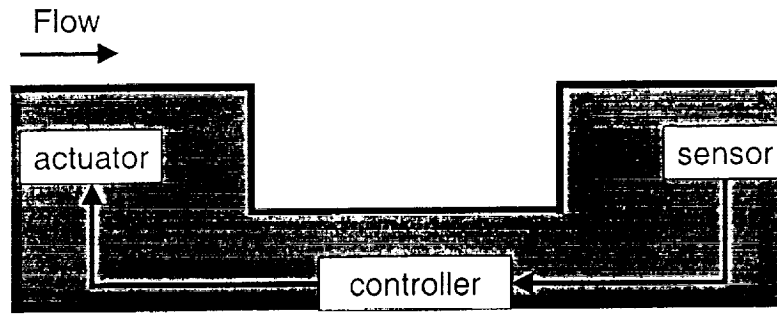


Figure 1.3: Active control system.

In a recent computational study, Lamp and Chokani²³ demonstrated the suppression of resonance in a supersonic cavity flow using jet blowing. Time-accurate, two-dimensional, Reynolds-Averaged Navier-Stokes (RANS) simulations of the cavity flow were conducted. A small jet, placed at the front lip of the cavity, was found to be effective in reducing the amplitude of the pressure fluctuations in the cavity. The effectiveness of the control was found to strongly depend upon the amplitude and frequency of the blowing jet. Cross-correlations of unsteady pressures sampled in the cavity showed that the timing of the events were unaffected by the blowing. Auto-correlation analysis however, showed that structures in the cavity shear layer were significantly smaller with jet blowing. The potential of the small jet to form the basis of an adaptive active control scheme, motivated the present wind tunnel experiments using oscillatory blowing.

1.2.2 Oscillatory Blowing and Pulsed Jet Blowing

Oscillatory and pulsed jet blowing have recently received a lot of attention in the control of boundary layer flow separation. Oscillatory blowing, a cyclic action of

blowing and suction applied through a streamwise directed slot, has been found to be successful in delaying flow separation over an airfoil.^{24, 25, 26, 27} The attendant benefits of the oscillatory blowing control on an airfoil are an increase in the lift and a reduction in the drag. Oscillatory blowing can be considered to consist of two components: a time-mean component, and a fluctuating component. The mean, c_{μ} , and the fluctuating, $\langle c_{\mu} \rangle$ momentum coefficients are used to characterize the respective amplitudes. Oscillatory blowing, with zero or non-zero net mass flux, has been observed to be more effective than steady blowing. In particular with oscillatory blowing a fluctuating momentum coefficient, $\langle c_{\mu} \rangle$, that is an order of magnitude smaller than the mean momentum coefficient, c_{μ} , of steady blowing yields the same degree of flow separation control. This effectiveness can be accomplished with zero net-mass oscillatory blowing; that is the mean momentum coefficient, c_{μ} , is zero. The oscillatory blowing is also described in terms of a forcing frequency. A dimensionless frequency, $F^+ = f x_c / U_{\infty}$, of the order of unity, is found to be most effective. The observations from the experiment indicate that the mechanism of control using oscillatory blowing is the addition of high momentum fluid into the separated flow on the airfoil.

Similar to oscillatory blowing, vortex generator jets (VGJ), re-energize the separated boundary layer flow by transferring high momentum fluid from the outer region of the boundary layer towards the wall. This is accomplished by introducing the high momentum fluid through small diameter holes in the surface. Lin²⁸ used vortex generator jets to control the separation of the flow over a backward-facing ramp. Lin found that hole size, blowing angle, velocity ratio between the jet and freestream, and the

hole spacing determined the effectiveness of VGJ. Compared with steady blowing from a slot, the VGJ were much more effective in reducing the flow separation.

Pulsed vortex generator jets (PVGJ) have more recently been used to control the separation on airfoils.^{29, 30, 31} The effect of forcing frequency, momentum coefficient, duty cycle, hole diameter, and hole spacing of the jets have been examined. PVGJ is found to be more effective than steady VGJ.

1.3 Objectives of Research

The previous work shows that oscillatory blowing and pulsed VGJ are effective for the control of flow separation. Although steady and pulsed blowing have been used in previous studies to suppress cavity resonance, only blowing through a slot or porous surface have been examined. In our new approach to the control of cavity resonance, a combination of both zero net-mass oscillatory blowing and pulsed VGJ is employed. There are several advantages to this new approach. First, compared to blowing through slots, blowing through discrete holes use an order of magnitude less mass flow to gain the same control effectiveness. Secondly, VGJ generate vortices, which can persist over long distances, and therefore, have the potential to modify the cavity shear in even large L/D open cavity flows. Thirdly, compared to pulsed blowing with non-zero-net mass, zero-net mass oscillatory blowing is more practicable since on an aircraft, the required air must be bled from the engine.

There are three main objectives of this research:

- to suppress cavity resonance using zero net-mass oscillatory blowing;

- to determine the mechanism of control; and
- to identify key parameters that influence the effectiveness of the control.

The overview of this dissertation is as follows. The experimental procedures and measurement techniques are discussed in chapter 2. In chapter 3, the results of the experiment are presented. The chapter begins with a detailed discussion of the characteristics of the cavity flow without flow control. The effectiveness of steady and near-zero net mass oscillatory blowing are then described. The effects of the hole size, hole shape, blowing angle, momentum coefficient, and forcing frequency are all examined. The analysis includes spectra, to describe the distribution of energy; auto-correlations, to examine the large-scale structures; cross-correlation analysis, to examine the timing of events; bicoherence analysis, to examine the phase coupling of the resonant modes; and wavelet analysis, to examine the mode switching behavior. The effect of blowing on the amplitude of velocity fluctuations and mixing in the cavity shear layer is then finally examined. The conclusions and recommendations for future work are presented in chapter 4.

2 Experimental Methods

2.1 Experimental Set-up

2.1.1 Test Facility

The experiment was conducted in the Probe Calibration Tunnel (PCT) at the NASA Langley Research Center. The PCT is a blow-down, pressure tunnel with a capability for the independent control of Mach number, Reynolds number, and total temperature. A high-pressure bottle field and a steam heater system are used to provide dried, pressurized air to the PCT. The tunnel stagnation temperature can be varied from $255K$ to $367K$ ($\pm 0.5K$), and the tunnel stagnation pressure from $0.2atm$ to $10atm$ ($\pm 1.4 \times 10^{-4}atm$). Anti-turbulence screens and a sintered plate located in the settling chamber are used to condition the flow. The nozzle contracts from a circular inlet of $30.5cm$ ($12in$) diameter to a $5.1cm$ ($2in$) \times $15.2cm$ ($6in$) rectangular nozzle exit. The test section is located downstream of the nozzle exit, within a plenum, which is equipped with rectangular Schlieren windows for optical access, Figure 2.1. The flow exits through a diffuser and is exhausted to atmosphere.

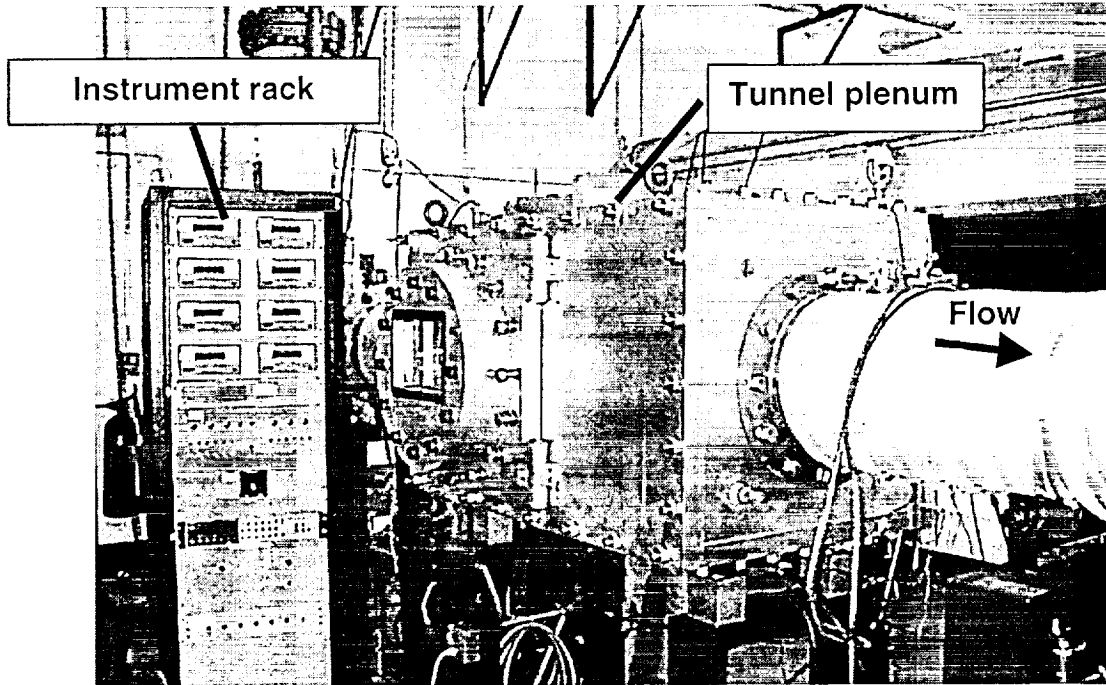


Figure 2.1: Probe Calibration Tunnel with instrument rack.

2.1.2 Test Model

Within the tunnel plenum, the cavity model is mounted 30cm (11in) downstream of the nozzle exit in the ceiling, as shown in Figure 2.2. The cavity has a fixed length of 15.2cm (6in), and spans the width of the test section, 5.1cm (2in). The cavity floor plate can be adjusted to produce cavity depths from 0.0cm (0.0in) to 76.2cm (3.0in). For the present experiment, the depth was set at 3.8cm (1.5in) to produce a $L/D = 4$. A small angle diffuser is attached downstream of the cavity to recover the pressure.

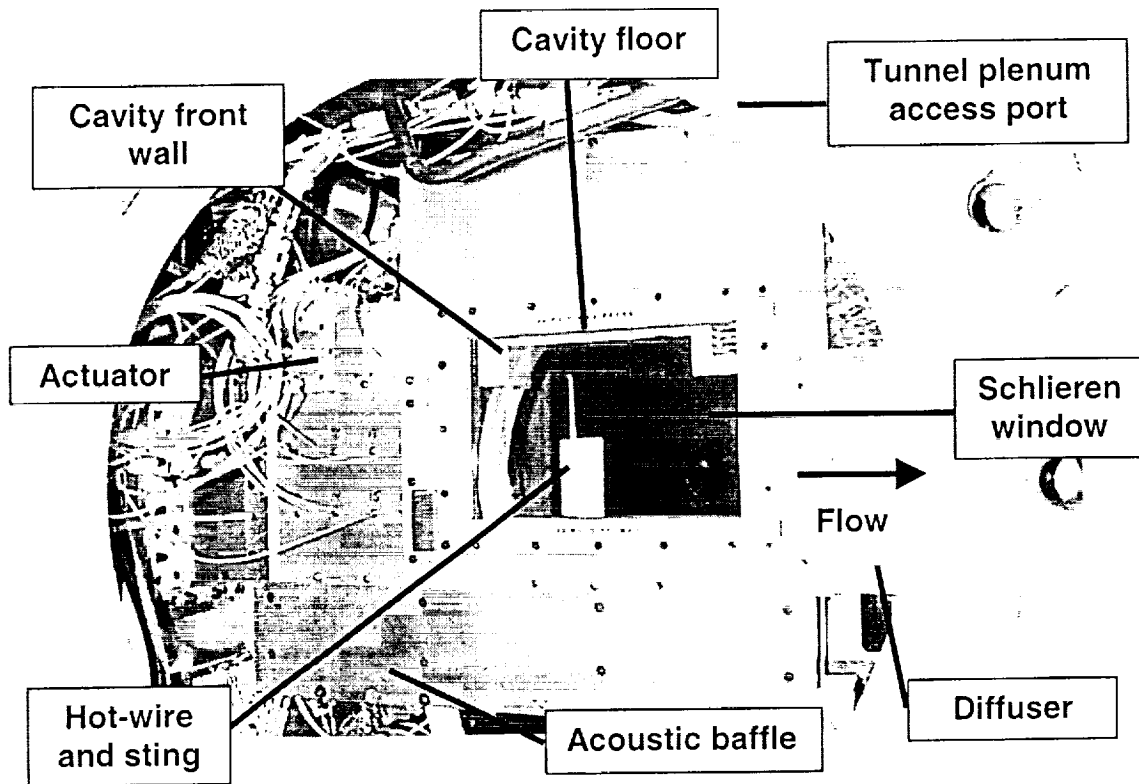


Figure 2.2: Cavity model inside the tunnel plenum, showing the hot-wire set-up.

An acoustic baffle is used in the cavity ceiling to reduce coupling between the cavity and tunnel acoustic modes. The baffle consisted of acoustic foam wedges, which absorb the sound waves, thus eliminating the cavity-tunnel acoustic interaction. Figure 2.3 shows the calculated tunnel modal frequencies and predicted cavity resonant modes. The curved lines show the calculated tunnel modal frequencies, the straight lines indicate the predicted cavity resonant modes, and the symbols the experimentally measured cavity modes. In the absence of the acoustic baffle, the tunnel modal frequencies, Figure 2.3a, are seen to drive the cavity resonant modes to their maximum amplitude. When the acoustic baffle is used, the cavity-tunnel acoustic interaction is eliminated and the maximum amplitude follows the predicted cavity resonant frequencies. For the hot-wire

shear layer surveys, a streamwise slot in the baffle enabled the hot-wire probe to be traversed in the streamwise direction. No slot was present in the baffle used for the other measurements.

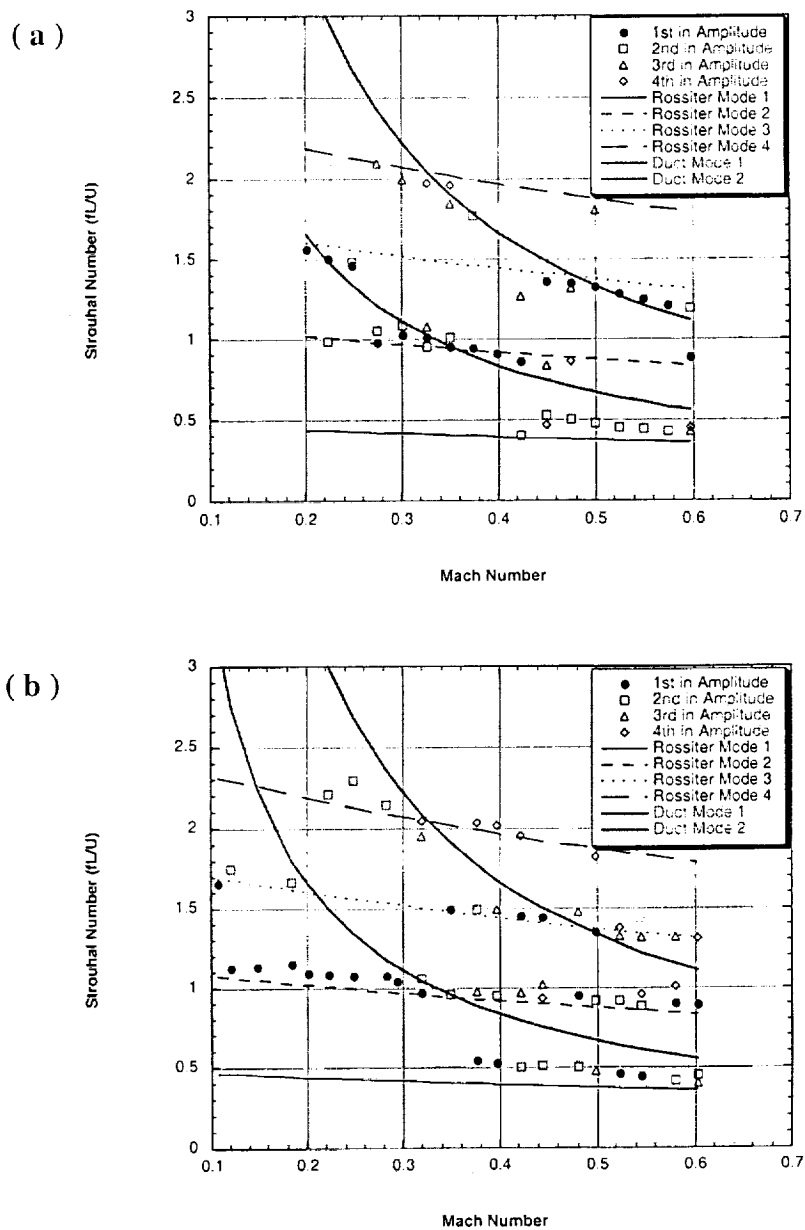


Figure 2.3: Cavity-tunnel modal interaction, $L/D=2$. a) without acoustic liner
b) with acoustic liner³².

2.1.3 Actuator

An actuator was designed and fabricated at North Carolina State University to provide the steady and oscillatory blowing, Figure 2.4. Details of the actuator's design are presented in Appendix A.1. Two flow control valves regulate the air entering into and exiting from the actuator, Figure 2.5. A hollow rotor with slots around its circumference is housed in a stator that has a slot opening to the delivery chamber. Air is allowed to enter the delivery chamber when a rotor slot is aligned with the slot of the stator. As the rotor rotates, pulses of air are generated as the air gets "chopped" as it enters the delivery chamber. Zero net-mass oscillatory blowing is achieved by regulating the flow control valves to allow equal amounts of mass to enter and evacuate the delivery chamber. The combined effect of the rotary pulse valve and flow control valves is to

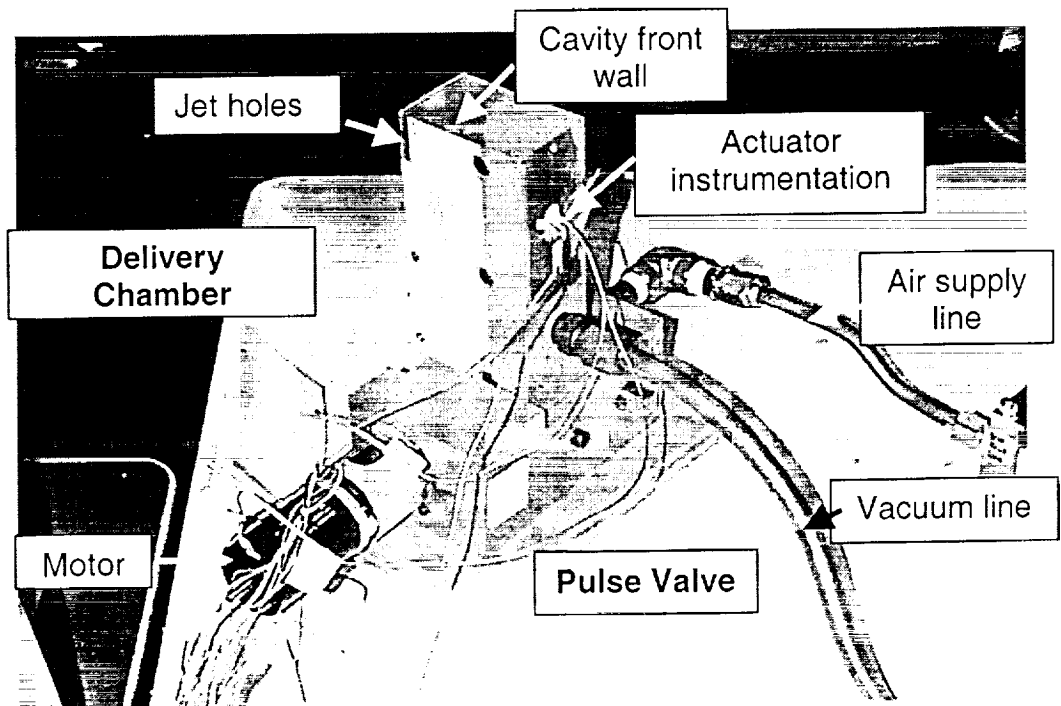


Figure 2.4: Actuator set-up on the bench-top.

produce suction and blowing at the jet exit. Steady blowing is achieved by fixing the rotor in an “open” position, which allows air to flow into the delivery chamber. Within the delivery chamber, the wall temperature, time-mean wall static pressure, and unsteady wall pressure, are measured as shown in Figure 2.5. The wall temperature is measured by a K-type thermocouple. A 1000torr Barocel Pressure Sensor (Datametrics model 570 with an electronic manometer, model 1174) is used to measure the time-mean static pressure referenced to the tunnel static pressure. A Kulite XCS-062-15D differential pressure transducer is used to measure the unsteady wall pressure.

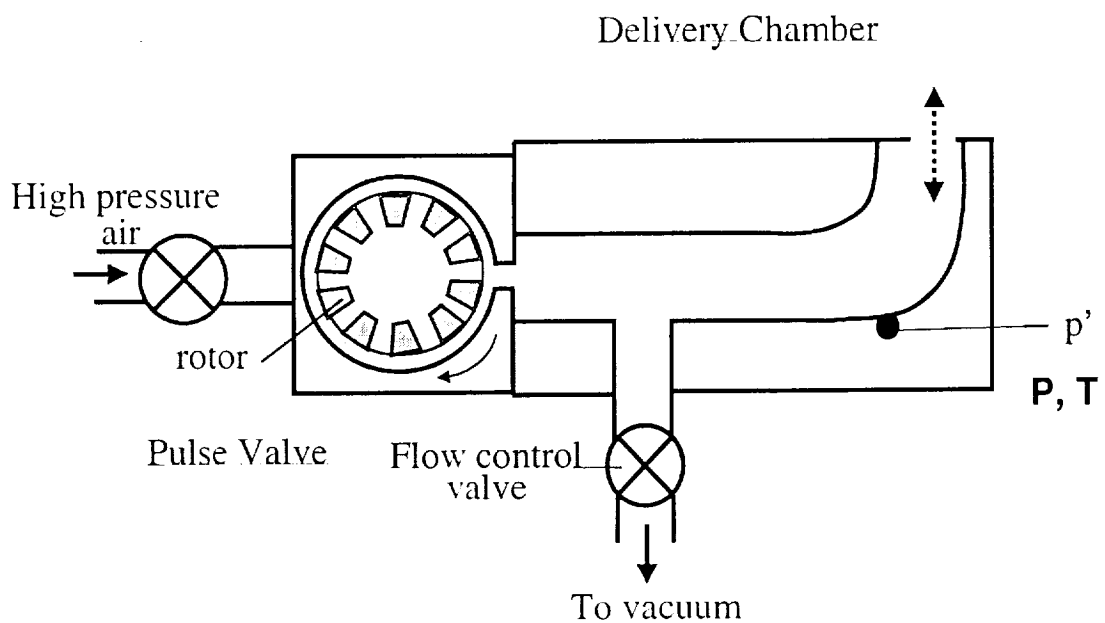


Figure 2.5: Diagram of rotary pulse valve actuator.

A 100 Watt DC brushless motor (Maxon Motor model EC040-070-38) is used to turn the rotor. A brushless motor was chosen for: its low electrical noise; its low maintenance and durability; and for its excellent speed control. The motor is operated by

electrical commutations that are produced by the controller (Maxon model MMC-EC040036-05P300C). An external voltage source of 0-5Volts, applied to the controller, is used to control the motor speed and hence the pulsing frequency. The pulsing frequency is determined from the rotor's rotational speed, which is measured using a Hall effect sensor located in the motor. A frequency to DC converter (Pioneer Magnetics, Inc. model PM1870) is used to convert the sensor output to a voltage. A buffer isolated the DC converter from the Hall effect sensor.

A schematic diagram of the installation of the pulse actuator in the wind tunnel is shown in Figure 2.6. Two Hastings Mass Flow Controllers, model HFC-203D, which can control flow rates up to either 300SLPM or 500SLPM, are installed outside of the tunnel plenum and regulate the flow entering and exiting the actuator. These flow controllers both meter and control the mass flow rates. Two Hastings Power Supplies (model 200) are used with the flow controllers. Filtered air at $690kN/m^2$ (100psi) is supplied to the actuator. The tunnel total pressure is held above $207kN/m^2$ (30psia). The pressure difference between the tunnel and the room allows the room to be used as the vacuum environment to which the mean air component from the actuator delivery chamber can be exhausted. A check valve is installed to prevent damage in case the tunnel is over pressurized.

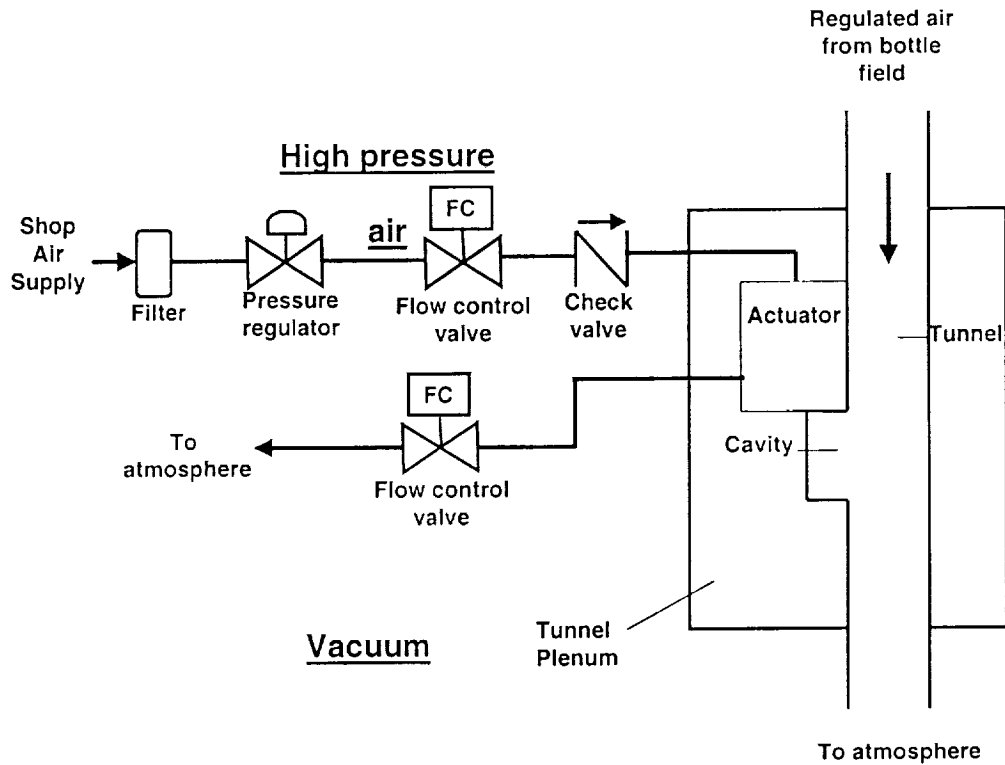


Figure 2.6: Flow diagram of actuator system.

The actuator is mounted in the tunnel plenum, just upstream of the cavity. The walls of the actuator delivery chamber form the tunnel floor and cavity front wall, Figure 2.2. The air exiting from the actuator delivery chamber is introduced into the tunnel through a slot or pair of holes located 0.25cm (0.1in) upstream of the leading edge of the cavity. In the experiment, interchangeable plates (configurations R1-LS), that give a range of hole sizes, shapes, and blowing directions, and a blank plate are examined. The details of the plates are given in Table 2.1. Each plate has two holes that are spaced 1.52cm (0.6in) apart, and are equidistant from the tunnel sidewalls with the exception of a Spanwise Long slot configuration, configuration LS. The holes have a pitch angle of 90°

with respect to the free stream direction and a skew angle, with respect to the direction of the span of the cavity of either 45° or 90°.

Table 2.1: Summary of hole plate characteristics.

Plate #	Description	Width / diameter	Length	Hole Area	Blowing angle (skew)
Blank	No holes	-	-	-	-
R1	Round holes	0.16cm (0.063in)		0.039cm ² (0.006in ²)	90°
R2	Round holes	0.289cm (0.113in)		0.130cm ² (0.020in ²)	90°
R3	Round holes	0.32cm (0.125in)		0.158cm ² (0.025in ²)	90°
RA	Round	0.16cm (0.063in)		0.039cm ² (0.006in ²)	45°
SS	Streamwise Slots	0.16cm (0.063in)	0.41cm (0.16in)	0.120cm ² (0.186in ²)	90°
SSA	Streamwise Angled Slots	0.16cm (0.063in)	0.41cm (0.16in)	0.120cm ² (0.186in ²)	45°
LS	Long Slot	3.81cm (1.5in)	0.16cm (0.063in)	0.605cm ² (0.938in ²)	90°

2.1.4 Instrumentation

2.1.4.1 Wall pressure system

Interchangeable tunnel wall sections form the sidewalls of the cavity model. The cavity sidewalls are formed by the Schlieren window wall sections, Figure 2.2, during the hot-wire measurements. The tunnel sidewalls, instrumented with pressure taps, are used during the measurement of the cavity pressures. The locations of the pressure taps in the sidewall are shown in Figure 2.7. There are two rows of taps that span the tunnel nozzle and cavity sections, and a row that spans the cavity opening. Taps are clustered vertically

near the cavity opening at locations 3.0cm (1.2in) from the rear and front walls of the cavity. The other tunnel sidewall is a mirror image of the taps shown in Figure 2.7.

Along the centerline of the cavity floor, 11 pressure taps are evenly spaced at intervals of 1.5cm (0.6in). Four pressure taps, offset 1.3cm (0.5in) from the centerline, are located along the cavity floor 3.0cm (1.2in) from the front and rear walls. Six taps are located along the centerline of the rear wall at 0.6cm (0.25in) intervals; no pressure taps are located on the front wall. Pressure taps are located along the centerline of the ceiling and floor of the diffuser, and spaced at intervals of 5.1cm (2in).

Two pressure transducers are used in this experiment. A differential pressure transducer (Endevco model 8507C-2) is located on the floor, 0.13cm (0.05in) downstream from the front wall along the centerline, and a second differential pressure transducer (Endevco model 8507C-5) is located on the rear wall, 4.4mm below the cavity edge along the centerline. The transducers are 2.42mm (0.095in) in diameter. The model 8507C-2 transducer has a frequency response of 70kHz , and differential pressure range of 0.14atm (2psi); the model 8507C-5 transducer has a frequency response of 85kHz , and differential pressure range of 0.34atm (5psi).

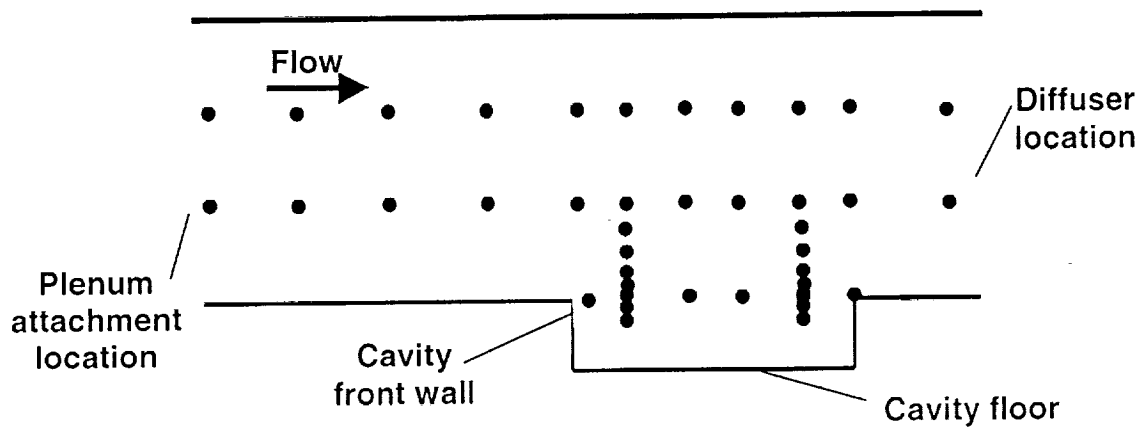


Figure 2.7: Wall pressure tap locations of the cavity model.

2.1.4.2 Hot-wire anemometer system

Velocity measurements of the cavity shear layer were made with a hot-wire anemometer system. This system is comprised of a hot-wire probe, sting, and anemometer. A Dantec, right angle probe with a single, $5.0 \times 10^{-3} \text{mm}$ (0.0002in) platinum plated tungsten wire is used. The probe is sting-mounted on a traverse system that is contained within the tunnel plenum. The aerodynamically shaped sting is placed through the acoustic baffle in the ceiling of the cavity-model; see Figure 2.2. The traverse moves the probe along the centerline in the streamwise (X) and cross-streamwise (Z) directions. A constant temperature anemometer (DISA model 55M101) with a standard bridge is used to control the wire voltage.

2.1.4.3 Traverse system

A two-axis traverse system was used to move the hot-wire probe. The traverse system consists of two linear stages, and a controller. The linear stages used are Klinger

Scientific Corp translation stage models MT160.100 and MT160.200. The model MT160.200 has a 20cm traverse range with a resolution of 10 μ m and is used to move the hot-wire in the streamwise direction. Model MT160.100 has a 10cm traverse range with a resolution of 10 μ m and is used to move the hot-wire in the direction normal to the freestream. A controller (Klinger CCI.2) is used to control both stages.

2.1.5 Data Acquisition System

A network of computers, Figure 2.8, is used to control the instruments and data acquisition, using programs written in LabVIEW[®]. The data acquisition and control tasks are divided amongst the computers due to the size and memory requirements of the computer programs. The first computer, "PCT 2", is used to acquire the tunnel parameters. A second computer, "PCT 1", is used to control the mean-pressure measurement system (ESP), while the third computer, "PCT 5", is dedicated to the A/D system (VXI). Both "PCT 1" and "PCT 5" control the pulsed rotary valve actuator through the data acquisition system (HP 3852A). All data are stored on either the computer's local hard drive or a Jazz disk, and then transferred to recordable CDs.

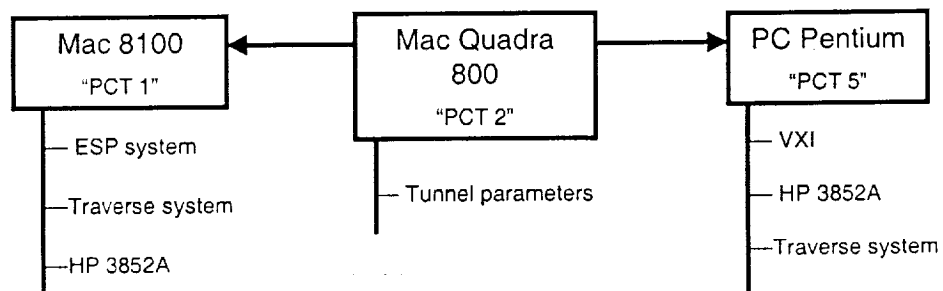


Figure 2.8: Computer network used in the PCT experiments.

The Electrically Scanned Pressures (ESP) model 8600 system is used to measure the mean pressures from the 152 wall pressure taps. This system electronically multiplexes the pressure port channels at speeds of up to 50,000 channels/second. The modules (pressure scanners) have 32 ports and contain one piezoelectric pressure transducer per port. Four $17.2 \pm 0.017 \text{ kN/m}^2$ ($2.5 \pm 0.0025 \text{ psi}$) modules are used for the tunnel wall ports; two $68.95 \pm 0.034 \text{ kN/m}^2$ ($10 \pm 0.005 \text{ psi}$) modules are used for the rear cavity wall and diffuser ports. The ESP system is self-sufficient in that it can calibrate the transducers internally; this minimizes the effects of temperature and pressure on the transducer's calibration. To calibrate the modules, a $206.9 \pm 0.041 \text{ kN/m}^2$ ($30 \pm 0.006 \text{ psi}$) Pressure Calibrate Unit (PCU) is used for the 68.95 kN/m^2 modules, and a 34.5 kN/m^2 ($5 \pm 0.001 \text{ psi}$) PCU is used for the 17.2 kN/m^2 modules.

Figure 2.9 shows the details of the data acquisition and control through "PCT 5". The VXI system, using the Hewlett Packard E1433A digitizer card, is used to acquire the fluctuating data from the transducers and the hot-wire. Each card can simultaneously filter and sample 8 channels of data. The VXI system has 16-bit resolution and has phase matching between channels, within $\pm 0.05^\circ$ at 1 kHz ; this is well suited for cross-correlation analysis.

The Data Acquisition/Control Unit (HP 3852A) is equipped with interchangeable cards. For this experiment, the digital voltmeter (HP 44701A) is used in conjunction with two cards: HP 44705F, and HP 44727. The HP 44705F card, a 20 channel solid-state relay multiplexer, is used to acquire the actuator's pressure and temperature from the Barocel manometer and thermocouple respectively, the flow rates from the flow control

valves, and the motor speed from the frequency to DC converter. The HP 44727 card, a 4-channel voltage/current controller, which can output voltages from 0-10volts is used to set the voltages to control the flow rates for the flow control valves, and to control the motor speed.

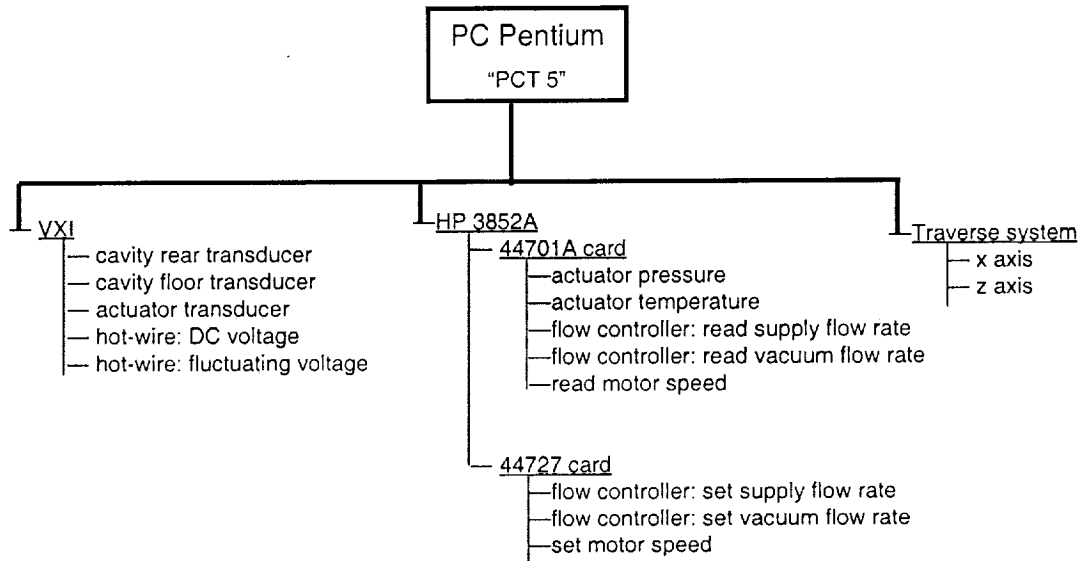


Figure 2.9: Overview of PCT-5 instrument controls.

2.2 Experimental Procedures

2.2.1 Hot-wire Calibration

Two different calibrations of the hot-wires were conducted. For the bench-top the calibrations were conducted at elevated pressures.

2.2.1.1 Wind tunnel hot-wire calibration

The hot-wire used for the cavity shear layer measurements was calibrated in the PCT. The cavity floor was lowered to be aligned with the surrounding walls and therefore, no cavity was present. The blank insert plate was also installed on the actuator; that is no control flow is introduced. The hot-wire was positioned just upstream of the cavity location, see Figure 2.10. For the calibration, the Mach number was varied from $M_\infty = 0.05$ to $M_\infty = 0.4$ using a step size of $\Delta M_\infty = 0.025$ at a constant total temperature and total pressure.

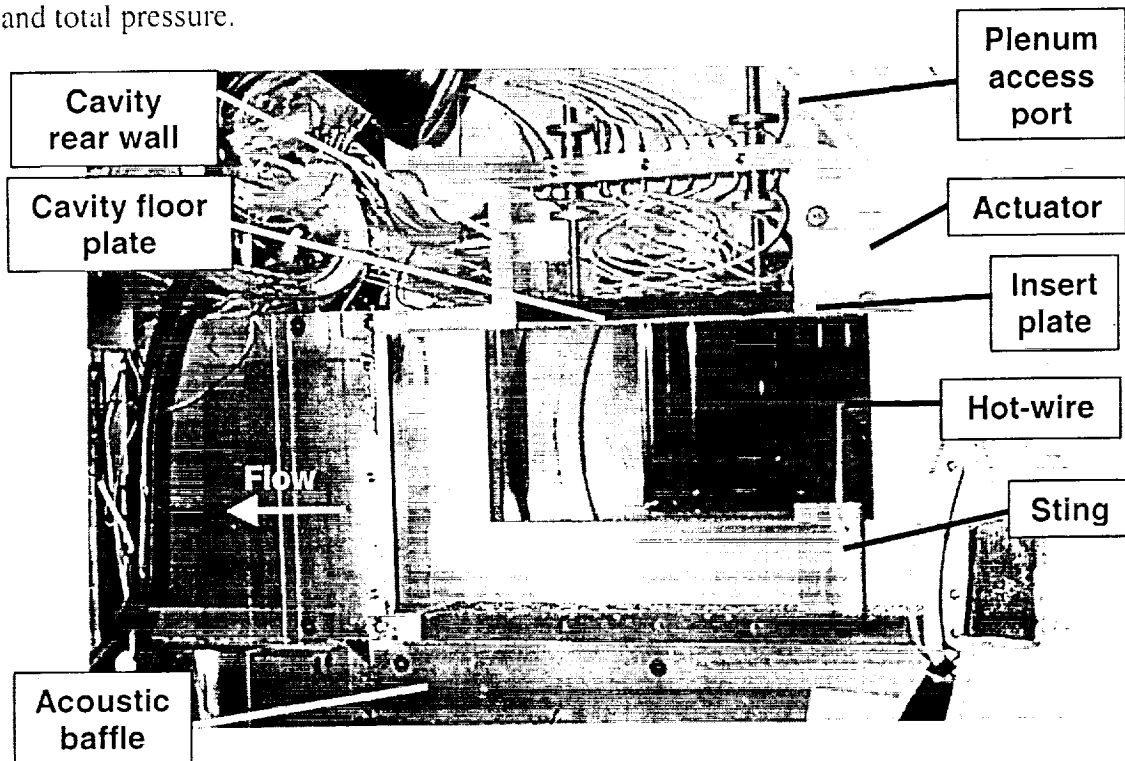


Figure 2.10: Hot-wire calibration set-up, with sidewall removed.

2.2.1.2 Bench-top hot-wire calibration

The bench-top hot-wire calibration was conducted using the jet flow exiting from a circular cross-section tube. The exiting jet mean velocity profiles are flat, that is a “top-

hat" shape. The static pressure at the jet exit was measured using an absolute pressure transducer (Druck DPI model 140). A 690kN/m^2 (100psi) Barocel transducer (Datametrics model 570 with an electronic manometer, model 1174) was used to measure the stagnation pressure of the air entering the calibration tube. The measurements from a pitot-static probe, obtained separately from the hot-wire measurements, were used to correlate the hot-wire voltage with the jet exit velocity.

2.2.2 Surface Measurements

2.2.2.1 Mean surface pressure measurements

The time-mean wall pressures were measured using the ESP system. After the tunnel had been brought to condition, the ESP system was calibrated using a standard five-point calibration. The calibration pressures spanned the expected range of wall pressures. For each port, 3810 data points were measured, and the average of the data recorded. A fourth-order curve fit was applied to the data for each port. The ESP system was calibrated after each new tunnel condition. After the ESP system was calibrated, the wall pressure data were then measured. For each wall port, 6380 data points were measured and averaged.

2.2.2.2 Unsteady surface pressure measurements

The VXI system was used to obtain the fluctuating pressures from the cavity rear wall, front floor, and the actuator transducers. The data were band-pass filtered at

0.01Hz, and 4000Hz. The sampling rate was 10240Hz. For each test condition, 51200 samples per transducer were taken.

2.2.3 Off-Surface Hot-Wire Measurements

The origin of the coordinate system for the cavity hot-wire measurements is at the front cavity lip, Figure 2.11. The positive streamwise (X) direction is downstream of the front lip, and the positive cross-streamwise (Z) direction is directed away from the cavity into the freestream. A cathetometer was used to position the hot-wire close to the origin at the beginning of each shear layer profile run. The probe was located 0.66mm (0.026in) downstream of the front wall in the X-direction to assure that the wire clears the front wall of the cavity when the wire was traversed into the cavity.

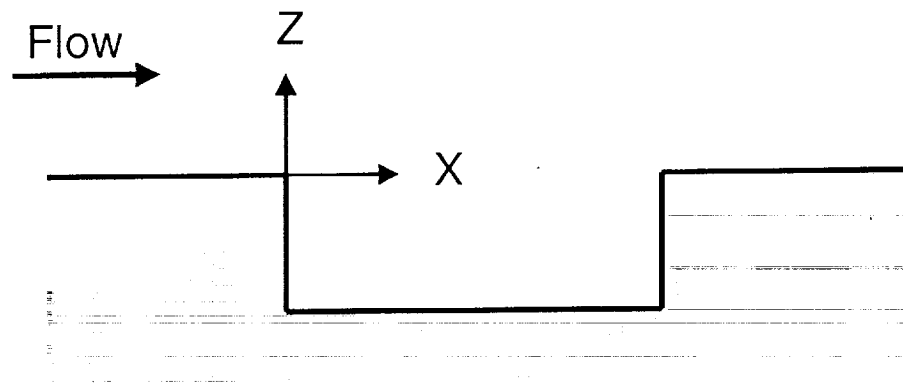


Figure 2.11: Cavity coordinate system for the hot-wire traverse.

A coarse, even spaced X-Z grid was used to initially characterize the shear layer. A finer grid with measurements clustered in the vicinity of the shear layer was then used to detail the shear layer flow. At each X station, 35 points in the Z-direction, clustered around the inflection and peak rms locations within the shear layer, were measured.

2.2.4 Experimental Conditions

The freestream Mach number is 0.2; this is a speed representative of an aircraft's landing speed. The total pressure of $207kN/m^2$ ($30psia$) was selected to provide: an adequate actuator vacuum source which is created by the tunnel-room pressure differential; an adequate air supply pressure range to the actuator; and at least a $60kN/m^2$ ($10psi$) pressure differential for the flow control valves to operate. This total pressure was the lower pressure limit, which provides an adequate vacuum with minimal range reduction for large amplitude blowing. The total temperature is $300^{\circ}K$ ($80^{\circ}F$). The total pressure and temperature are held within $\pm 1\%$ and the Mach number $\pm 2\%$

2.3 Data Processing

2.3.1 Spectrum

The spectra in terms of a Sound Pressure Level (SPL) are computed as follows. The data are divided into segments 1024 points long, with an overlap of 25%. The mean is subtracted from each segment. A Hanning window is applied to the segment before using the Fast Fourier Transform (FFT). This pressure data is then converted to SPL by using

$$SPL = 20 \log_{10} \frac{P'}{P_{ref}} \quad (2.5)$$

$P_{ref} = 20\mu N/m^2$. These ensembles are then averaged together. The frequency resolution is $10Hz$. The overall SPL is given when P' is replaced by the P_{rms} .

2.3.2 Auto and Cross Correlation

Auto-correlation analysis is used to determine the size of the structures, and cross-correlation analysis to calculate the time delay of events between two stations. The cross-correlation function for digitized time series, $x(m\Delta t)$, $y(m\Delta t)$, is given by³³:

$$\hat{R}_{xy}(r\Delta t) = \frac{1}{N-r} \sum_{n=1}^{N-r} x(n\Delta t)y[(n+r)\Delta t] \quad (2.6)$$

for time lags of $r = 0, 1, 2, \dots, m$ with $m < N$ where N is the number of points in the time series. For the auto-correlation, the same time series is used for both $x(m\Delta t)$ and $y(m\Delta t)$ in the above equation. Equation 2.6 can be normalized by the square root of each auto-correlation to give the cross-correlation coefficient:

$$\hat{\rho}_{xy}(r\Delta t) = \frac{\hat{R}_{xy}(r\Delta t)}{\sqrt{\hat{R}_{xy}(0)}\sqrt{\hat{R}_{xy}(0)}} \quad r = 0, 1, 2, \dots, m \quad (2.7)$$

The normalized values range between $-1.0 \leq \hat{\rho}_{xy}(r\Delta t) \leq 1.0$. The mean is removed from the time series before the correlation is calculated. The calculations are computed using MATLAB[®].

The coherence between two time series is a measure of how well the input corresponds to the output at each frequency. The values range from 0 to 1; a value of

zero indicates no relationship between the signals, and a value of one indicates a constant parameter, single input/output linear system. The coherence, $\hat{\gamma}_{xy}^2(f_k)$, is calculated by:

$$\hat{\gamma}_{xy}^2(f_k) = \frac{|\hat{G}_{xy}(f_k)|^2}{\hat{G}_{xx}(f_k)\hat{G}_{yy}(f_k)} \quad k = 0, 1, 2, \dots, N/2 \quad (1.8)$$

where

$$\hat{G}_{xx}(f_k) = \frac{2}{n_d N \Delta t} \sum_{i=1}^{n_d} |X_i(f_k)|^2 \quad (1.9)$$

is the autospectrum estimate, X is the Fourier transform of $x(m\Delta t)$, and n_d is the number of ensembles. For this analysis, the series was divided into ensembles of 1024 samples with no overlap. The mean was removed from each ensemble before a Hanning window was applied. The calculations were computed using MATLAB[®]. For the baseline measurement, the coherence values from 40 time samples were averaged together.

The phase angle between two time samples can also be used to compute the time lag between the signals. This time lag, τ , can be computed by the following relationship:

$$\tau = \frac{\theta_{xy}(f)}{2\pi f} \quad (2.10)$$

where f is the frequency and θ_{xy} is the phase angle. The phase angle is computed by

$$\theta_{xy} = \tan^{-1} \left[\frac{\text{real}(G_{xy})}{\text{imaginary}(G_{xy})} \right] \quad (2.11)$$

For the baseline measurement, the phase angles determined from 40 time samples were averaged together.

2.3.3 Bicoherence Estimation

Bispectral analysis was conducted to examine the nonlinear phase coupling between pairs of frequencies. If there is a nonlinear interaction between waves with frequencies of f_i , f_j , and $f_i + f_j$, the frequencies are phase coupled. This coupling is measured as a large value in the bispectrum. The auto-bispectrum is defined by^{34, 35}

$$B_{xxx}(f_i, f_j) = \lim_{T \rightarrow \infty} \frac{1}{T} E \left[X(f_i)X(f_j)X^*(f_i + f_j) \right] \quad (2.12)$$

where $E[]$ is the expected value, and the asterisk denotes the complex conjugate.

Normalizing Equation 2.12 by the power spectrum produces the auto-bicoherence, b_{xxx}^2 , as shown in the equation below. The bicoherence is bound by 0 and 1. A bicoherence value greater than zero indicates that the frequencies are nonlinearly coupled, while a zero value indicates that there is no coupling between the frequencies f_i , f_j , and $f_i + f_j$.

$$b_{xxx}^2(f_i, f_j) = \frac{|B_{xxx}(f_i, f_j)|^2}{E[|X(f_i)X(f_j)|^2]E[|X(f_i + f_j)|^2]} \quad (2.13)$$

Similarly, the cross bispectrum and cross bicoherence values are calculated using the equations below.

$$B_{xy}(f_i, f_j) = \lim_{T \rightarrow \infty} \frac{1}{T} E \left[X(f_i)X(f_j)Y^*(f_i + f_j) \right] \quad (2.14)$$

$$b_{xy}^2(f_i, f_j) = \frac{|B_{xy}(f_i, f_j)|^2}{E[|X(f_i)X(f_j)|^2]E[|Y(f_i + f_j)|^2]} \quad (2.15)$$

The bicoherence calculation uses a 512 point FFT, which produces a frequency resolution of $20Hz$. An overlap of 50% is used to obtain more averages. Each calculation contains 200 ensemble averages. A Hanning window is used in the analysis to reduce spectral leakage.

2.3.4 Wavelet Analysis

Wavelet analysis is used to examine transients in the cavity frequencies. Fourier based spectra and bispectra produce details of the frequency content averaged over the time series that is analyzed; on the other hand, wavelet analysis preserves the time-dependent details of the frequency content. Wavelets are transformable functions, which are localized in both time and Fourier space, and have a zero mean. The mother wavelet is translated and dilated to allow both time and frequency information of the time series to be examined. Although there are many types of wavelet functions, the complex-valued, continuous, Morlet wavelet is used here. The Morlet wavelet has been used in other fluid dynamic applications^{36,37} and is chosen due to its good time and frequency resolution. The mother Morlet wavelet transform in the time domain is:

$$\psi(t) = e^{i\omega_{\psi}t} e^{-|t|^2/2} \quad (2.16)$$

where ω_{ψ} is a constant that forces the function to be admissible. In this work, a value of 5.5 is used. The Morlet transform function in the time domain is shown in Figure 2.12.

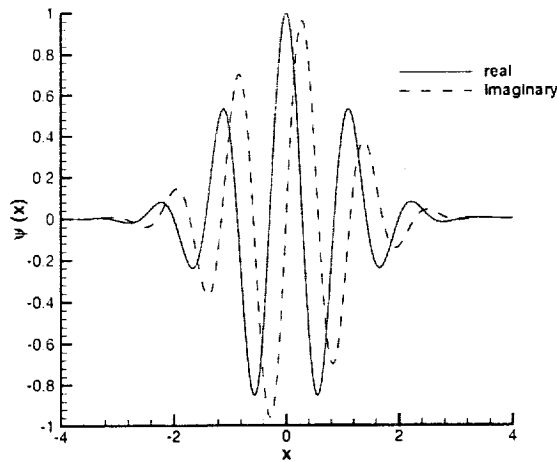


Figure 2.12: Morlet mother wavelet.

The dilated wavelet is given as:

$$\psi_{a,\tau}(t) = a^{-1/2} \psi\left(\frac{t-\tau}{a}\right) \quad (2.17)$$

where a is the wavelet scale parameter. Equations 2.16 and 2.17 are combined into the continuous wavelet transform, Equation 2.18, to calculate the wavelet coefficients.

$$W(a, \tau) = \int_{-\infty}^{\infty} x(t) \psi_{a,\tau}^*(t) dt \quad (2.18)$$

The asterisk denotes the complex conjugate. The wavelet coefficients correspond to the energy density beneath the wavelet function in Fourier space. The dilated Morlet wavelet is a constant “Q” function, which conserves the total energy density. The drawback of this feature is that the bandwidth increases with the frequency, which produces a poorer resolution at high frequencies. This effect can be seen in Figure 2.13 where the scale $a=1$ indicates the larger frequency.

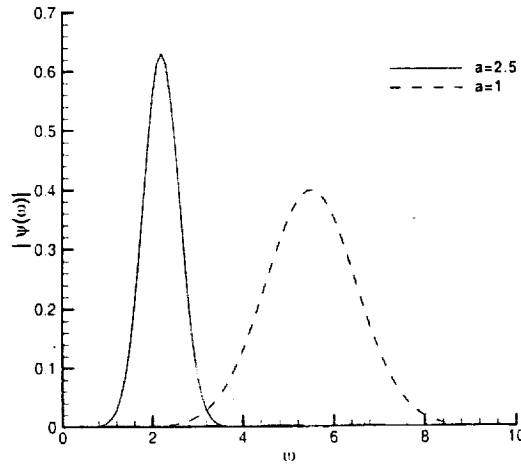


Figure 2.13: The effect of scale on the Morlet wavelets in the frequency domain.

The wavelet scale and frequency, f , are related by the following equation:

$$f = \frac{T\omega_\psi}{\pi\Delta t N a} \quad (2.19)$$

where T is the length of the mother wavelet, and N is the number of samples of the mother wavelet. This equation shows that the frequency is inversely proportional to the wavelet scale. The method outlined in Jordan et al.³⁸ is used to calculate the wavelet coefficients.

2.4 Actuator Calibration

2.4.1 Calibration Set-up

Since the flow exiting from the actuator into the freestream cannot be measured during the wind tunnel tests, a bench-top calibration of the actuator was conducted. The calibration correlated the measured properties in the delivery chamber with the velocities

of the jet exiting from the interchangeable hole plates. The bench-top set-up was similar to the tunnel set-up. Filtered, regulated 6.8atm (100psi) air was used for the high-pressure air source, while a 12.5m (41ft) vacuum sphere, at pressures $0.04\text{-}0.13\text{atm}$ ($30\text{-}100\text{torr}$), was used as the vacuum source. The hot wire anemometer system described in section 2.1.4.2 was used to measure the jet velocities. The hot-wire was positioned within 0.13cm (0.05in) of the exit and was perpendicular to the exiting flow. An absolute pressure transducer was used to measure the pressure inside the delivery chamber. An 8 channel A/D converter (Iotech model ADC488/8SA) was used to obtain the fluctuating data from the pressure transducer and the hot-wire. The data were filtered using a dual channel low-pass filter (Stanford Research Systems model SR640). A Data Acquisition/Control Unit (HP 3852A) was used to measure the actuator parameters.

2.4.2 Calibration Procedures

The actuator was calibrated for both steady blowing and near-zero net mass oscillatory blowing. During the calibration, unsteady measurements of the pressure in the delivery chamber and from the hot-wire were taken simultaneously. Average values of the pressure and temperature within the delivery chamber were also measured and recorded in conjunction to the unsteady measurements. The actuator was calibrated over its full range of blowing amplitudes and pulsing frequencies.

The calibration of the actuator was found to be sensitive to its temperature. Therefore the temperature of the actuator was regulated at $300 \pm 2^\circ\text{K}$ ($80 \pm 4^\circ\text{F}$), which corresponded to the tunnel total temperature used during the cavity measurements. The

fluctuating hot-wire voltage and the fluctuating pressure data were both AC coupled and low pass filtered at $4kHz$ before being sampled at $10kHz$. The mean hot-wire voltage was measured by the HP 3852A.

The dimensionless mean and fluctuating momentum coefficients, c_μ and $\langle c_\mu \rangle$, respectively, were used to quantify the performance of the blowing. These coefficients are given as:

$$c_\mu = \frac{\rho u^2 A_j}{q A_r} \quad (2.1)$$

$$\langle c_\mu \rangle = \frac{\rho u'^2 A_j}{q A_r} \quad (2.2)$$

The area of the front cavity wall was used as the reference area, A_r .

The measured jet velocity, for the steady blowing mode of operation, agreed well with the jet exit velocity determined from the isentropic relations and the ratio of the delivery chamber pressure to the ambient pressure. Therefore, the isentropic relations were used to calculate the blowing momentum used in the steady blowing cavity control experiments.

2.4.3 Oscillatory Blowing Calibration

For oscillatory blowing, the approach developed by Seifert and Pack²⁵ was followed to estimate $\langle c_\mu \rangle$. Specifically, the relationships:

$$u' \propto \frac{p'}{\rho} \quad (2.3)$$

$$u'^2 \propto \frac{p'}{\rho} \quad (2.4)$$

are used to correlate u' , p' , and ρ measured in the bench-top tests with the p'/ρ measured in the wind tunnel experiments; $\langle c_{\mu} \rangle$ could then be estimated. Since the hot-wire cannot sense flow direction, the hot-wire data were de-rectified using the delivery chamber pressure signal as a reference. For each forcing frequency, both curve fit relationships, Equations 2.3 and 2.4, were applied to the unsteady velocity data. Equation 2.3 is used for the data over the lower pressure range; Equation 2.4 is used for the data over the higher pressure range. The intersection of the two curves determined the appropriate range of the two relations.

Calibration data for near-zero net mass oscillatory blowing was obtained for all hole configurations. The calibration results for the SSA configuration are examined in this section; these results are similar to the calibration results obtained for the other hole plates. A sample time trace of the near-zero net mass oscillatory blowing data is shown in Figure 2.14a with its corresponding spectra in Figure 2.14b. The measured hot-wire and de-rectified data, which accounted for the reversed flow, are shown compared with the pressure data. The forcing frequency of $140Hz$ appears as the dominant peak in the spectra. The harmonics of this frequency are also observed and are present due to the on-off action of the rotor-stator design in the actuator. The relative amplitudes of the fundamental-to-harmonics are similar for the de-rectified hot-wire and pressure data. Figure 2.15 shows the relationship between the normalized pressure and unsteady

velocity. The data covers a range of forcing frequencies and blowing amplitudes of near-zero net mass oscillatory blowing. The blowing amplitude is a function of both the forcing frequency and input/output volumetric flow rates. The blowing amplitudes in terms of the momentum flux are presented in Figure 2.16. The large amplitude peak around 140Hz is due to the resonant characteristic of the delivery chamber. It is seen that an increase in the input/output volumetric flow rates produces an increase in the blowing amplitude.

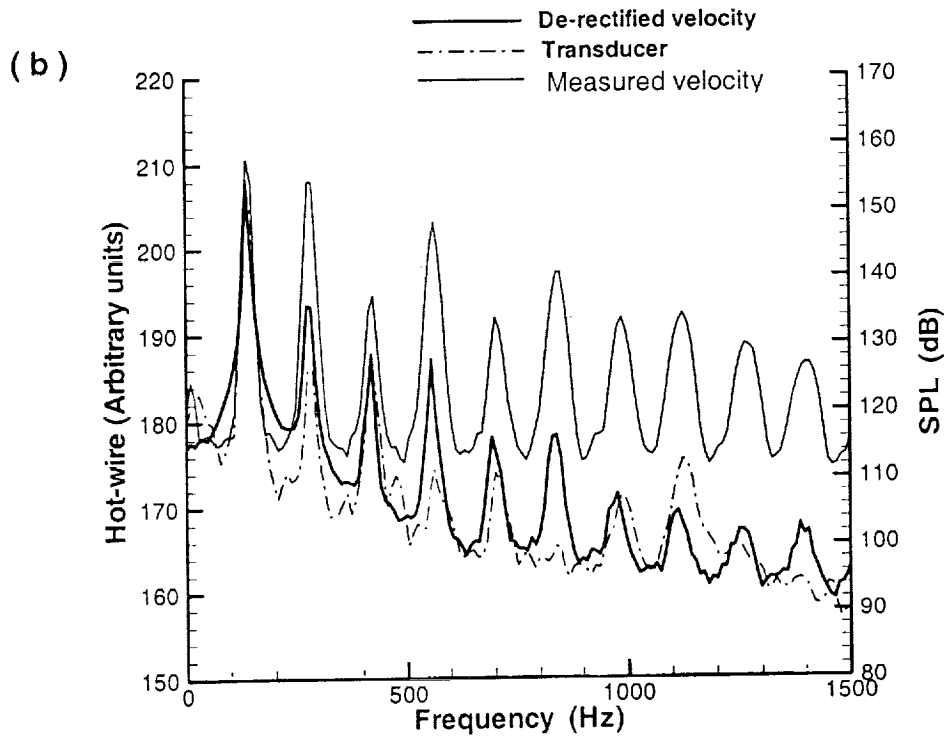
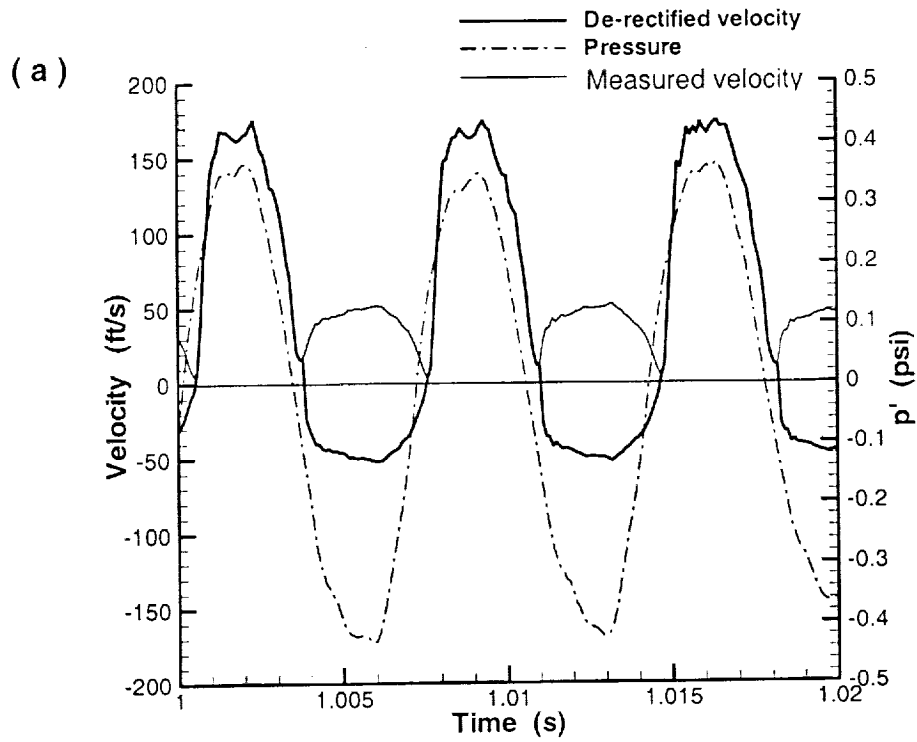


Figure 2.14: Velocity and pressure calibration data, $f_f = 140\text{Hz}$, configuration SSA:
a) time trace b) spectra.

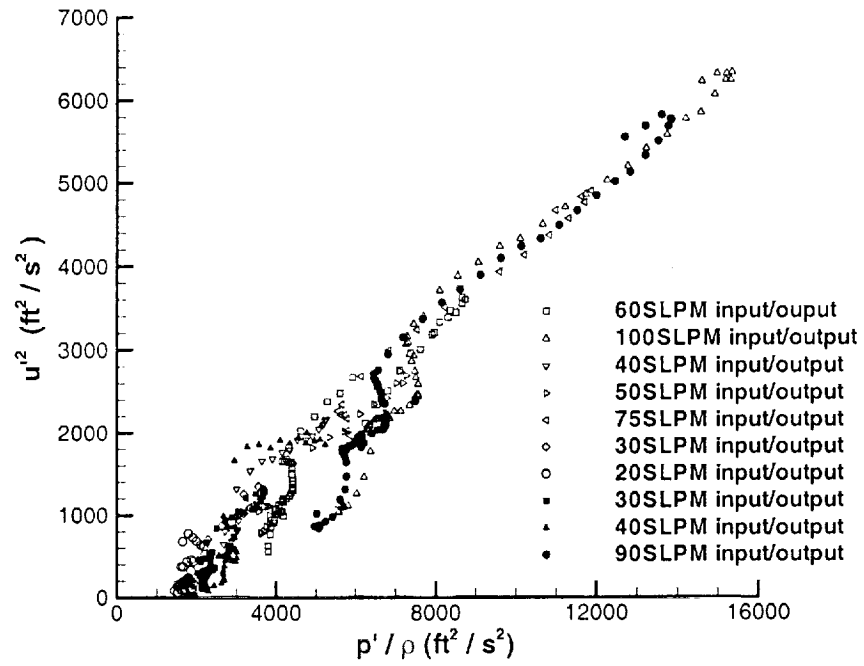


Figure 2.15: Blowing velocity vs. actuator delivery chamber pressure, configuration SSA.

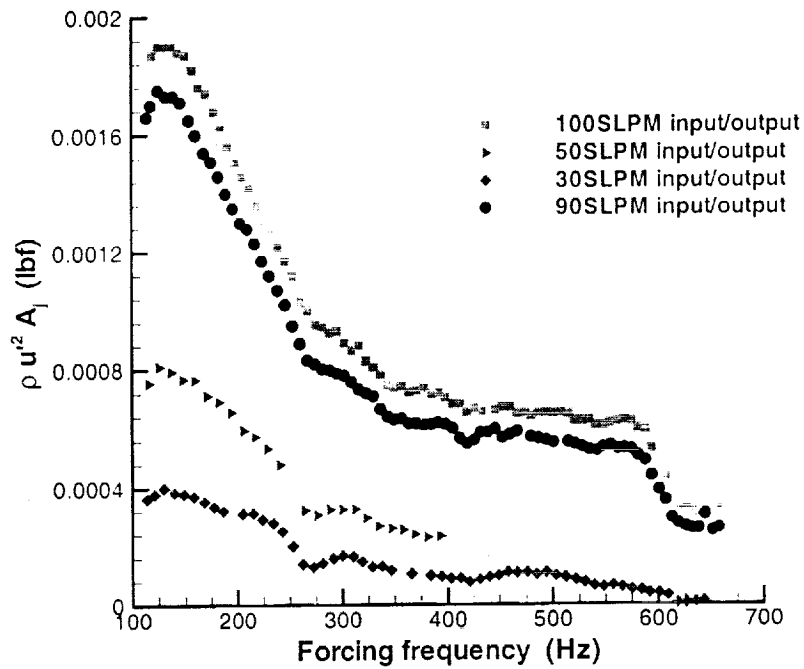


Figure 2.16: Resonant characteristics of the actuator at different input/output conditions, configuration SSA.

Figure 2.17 shows a representative calibration using Equations 2.3 and 2.4 for the two calibration curve fits with a forcing frequency of 140Hz. For large values of p'/ρ , p' and u'^2 are linearly related, while for small values of p'/ρ , p' and u' are linearly related. Similar curve fits were applied to the calibration data for all other hole configurations and forcing frequencies. Figure 2.18 shows a representative sample of data acquired during a cavity control run. Figure 2.18a shows the measured pressure in the actuator's delivery chamber while Figure 2.18b shows the unsteady momentum coefficient, determined using the actuator calibration results. The largest unsteady momentum coefficient for this hole configuration is 0.002.

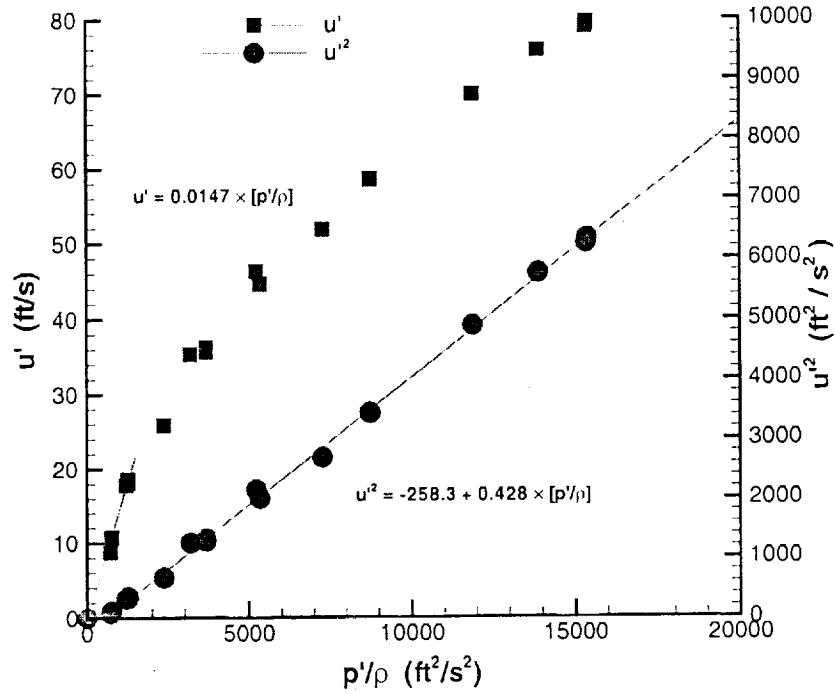
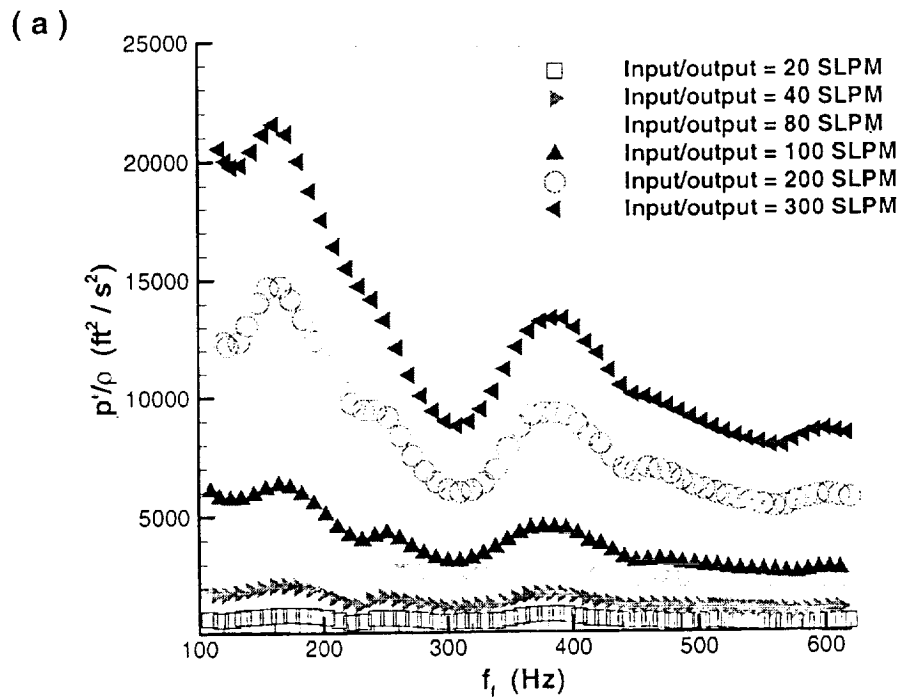


Figure 2.17: Calibration of unsteady velocity vs. actuator delivery chamber pressure, $f_r = 140\text{Hz}$, configuration SSA.



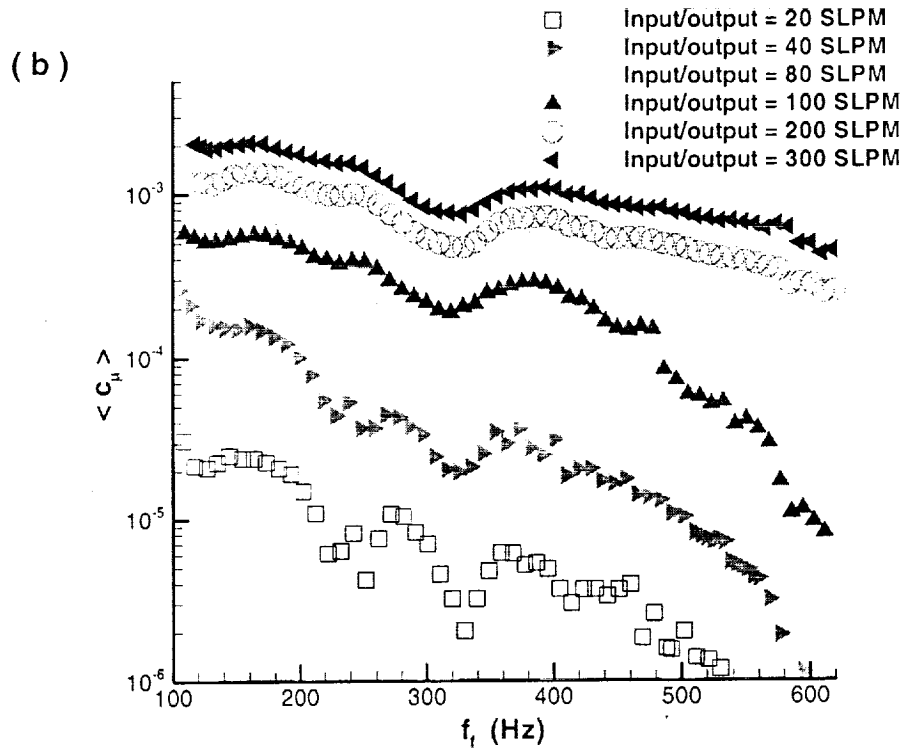


Figure 2.18: Actuator output during cavity test, $M = 0.2$, configuration SSA:
 a) measured p'/ρ b) calculated $\langle c_{\mu} \rangle$.

3 Results

3.1 Characteristics of Baseline Cavity Flow

The Mach number profiles along the tunnel ceiling for a range of conditions are shown in Figure 3.1. The cavity front wall is located at $X/L = 0.0$ and the rear wall is at $X/L = 1.0$. For the higher Mach numbers, the flow accelerates due to a large separation bubble that is located just downstream of the cavity and which obstructs the flow. For Mach numbers 0.4 and lower, the speed over the cavity section remains essentially constant.

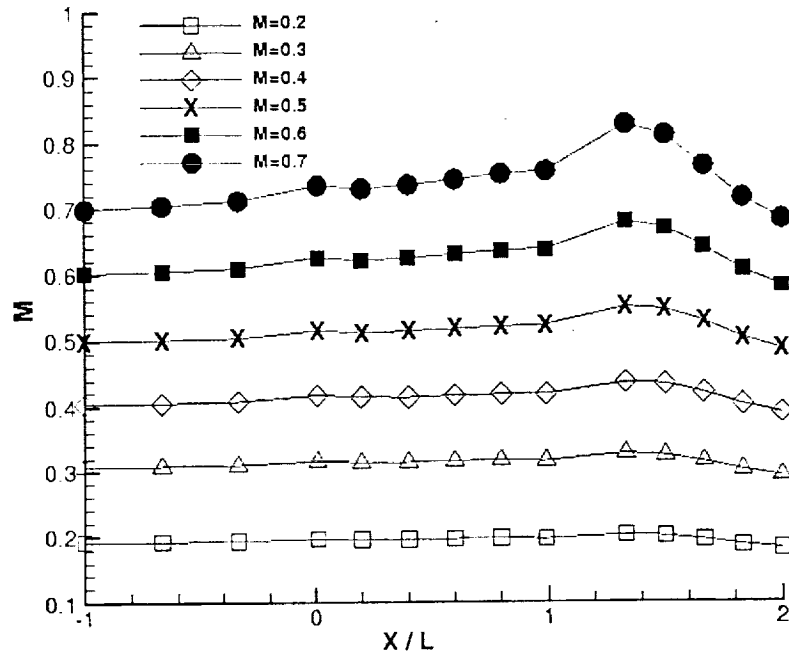


Figure 3.1: Mach number distribution along the tunnel ceiling. Baseline cavity flow.

The time-mean pressures for the baseline cavity at $M_\infty = 0.2$, $Re=6.2 \times 10^6/m$ are shown in Figure 3.2. The uniform pressure distribution along the tunnel ceiling in the vicinity of the cavity indicates that the cavity flow occurs in a near-zero pressure gradient environment. Along the tunnel floor, the pressure distribution is characteristic of an open cavity flow. At the middle of the cavity, the flow accelerates due to the large vortex located at the rear of the cavity. The flow then decelerates upon reaching the rear wall due to the impinging shear layer as seen by the large pressure rise. The pressure distribution along the cavity opening (shear layer) closely follows the floor. However at the rear of the cavity, the flow does not decelerate as much compared to the floor

distribution. All of the cavity flow experiments are conducted at a Mach number of $M_\infty = 0.2$ and Reynolds number of $9.2 \times 10^6/m$.

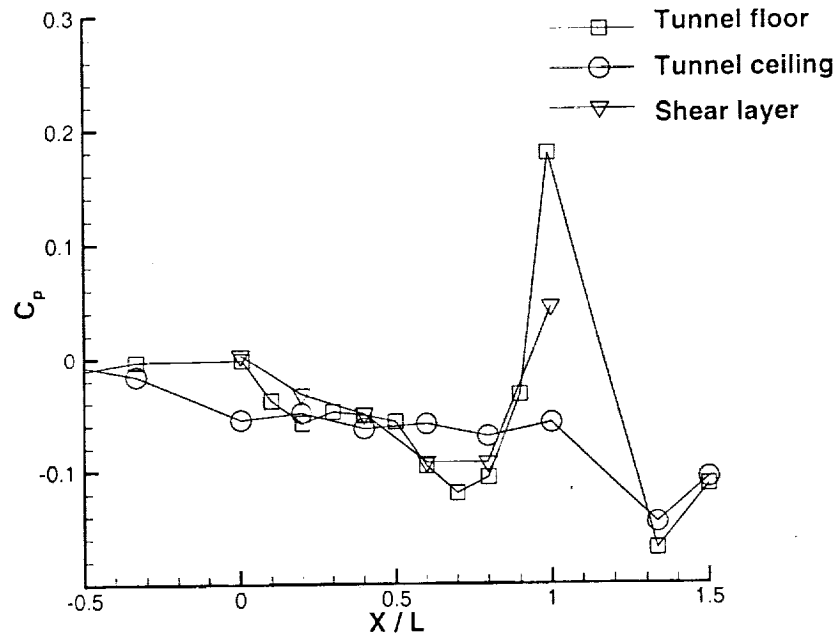


Figure 3.2: Time-mean pressures. Baseline cavity flow. $M_\infty = 0.2$.

The spectra obtained at the front floor and rear wall transducer locations with no cavity control (baseline) are shown in Figure 3.3. 2201600 points are used to obtain the spectra, and the spectral resolution is $2Hz$. The measured modal frequencies are compared to the predictions from the Rossiter semi-empirical equation in Table 3.1. Small differences between the experiment and the semi-empirical equation are observed and occur primarily for two reasons. First, in the semi-empirical equation a representative value of 0.66 is used for the convection speed constant, k_c . However, there is weak dependence of k_c on the magnitude of the resonant frequency, and its value may

lie in the range 0.59-0.73³⁹. Secondly, the semi-empirical equation assumes a two-dimensional flow whereas in the experiment, the flow field is three-dimensional due to the presence of the tunnel sidewalls.

It can also be seen in Figure 3.3 that the overall pressures at the rear wall are larger than at the floor location. This is due to the larger levels of turbulence intensities in the shear layer. At the rear wall location, the resonant modes also have larger amplitude due to the oscillatory motion of the shear layer as it impinges on the rear wall. The higher broadband levels at the rear wall compared to the front floor, reduce the amplitude of the cavity modes relative to the broadband levels.

The second mode has the largest amplitude at both the rear and floor locations. The focus of the present work is thus to assess the effectiveness of blowing in reducing the amplitude of this cavity mode.

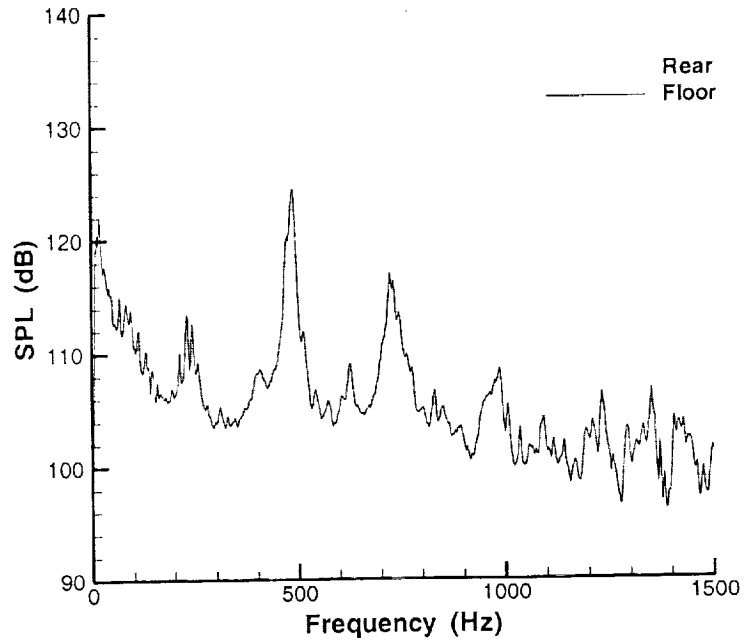


Figure 3.3: Spectra for baseline cavity flow. $M_\infty = 0.2$.

Table 3.1: Predicted and actual modal frequencies of the baseline cavity flow. $L/D = 4$, $M_\infty = 0.2$.

Mode	f (Hz) (experiment)	f (Hz) (theory)	Difference
1 st	246	198	24 %
2 nd	488	463	5 %
3 rd	724	727	0.4 %
4 th	986	992	0.6 %

3.2 Effectiveness of Control

3.2.1 Steady Blowing

The effect of steady blowing on the dominant second cavity mode is shown in Figure 3.4 and Figure 3.5 for the rear wall and the floor transducer locations, respectively. Figure 3.4a and Figure 3.5a show the effect of the momentum coefficient, c_{μ} , on the SPL for all hole configurations; Figure 3.4b and Figure 3.5b show the effect of the velocity ratio, VR on the SPL; and Figure 3.4c and Figure 3.5c show the effect of the jet's Reynolds number on the SPL. Along the y-ordinate, the SPL reduction, ΔdB , is defined as the difference between the SPL with and without blowing, is shown. A positive ΔdB indicates an increase in SPL compared to the baseline case while a negative ΔdB indicates a decrease in SPL. The uncertainty in the ΔdB measurements is $\pm 1\text{dB}$. It is seen that steady blowing is effective in reducing the amplitude of the second cavity mode for all hole configurations. Overall, steady blowing is more effective at higher blowing momentums, c_{μ} , velocity ratios, VR, and Reynolds numbers. It is noteworthy that the reductions are achieved using relatively small velocity ratios (~ 1) in contrast to the flow separation control on a backwards facing ramp using steady vortex generator jets (VR ~ 6.8)²⁸ and flow separation control on an airfoil using pulsed vortex generator jets (VR $\sim 2-10$).⁴⁰

The effect of hole size is seen at both the rear and floor locations by comparing the results of the R1, R2, and R3 configurations. The reduction for a given momentum coefficient scales with the hole size; that is the larger hole diameter achieves the largest

overall SPL reduction. For the three round hole configurations, the reduction is fairly insensitive to the VR as seen in Figure 3.4b and Figure 3.5b. The greater reductions produced by the large diameter holes, R3, may be attributed to the jet's deeper penetration into the freestream⁴¹. In Figure 3.4c and Figure 3.5c, the data generally collapse onto one curve when normalized by the Reynolds number. The exceptions are the small round hole configurations, R1 and RA, and the SSA configuration. The shift towards higher Reynolds number for the R1 configuration indicates that a larger velocity is needed to produce the same reduction in amplitude when compared to the other hole configurations. The spectra showing the effect of hole size are shown in Figure 3.6. The blowing momentum is 0.01. All of the cavity modes show a decrease in amplitude; the SPL reduction again scales with the hole size. For the R3 configuration, at the rear location, steady blowing reduces the broadband levels and reduces the amplitudes of the resonant modes close to these reduced broadband levels.

The effect of hole geometry can be seen from the different levels of reduction for hole configurations R2, SS, and LS (round, streamwise slot, and long slot) in Figure 3.4 and Figure 3.5. Configuration R2 is the most efficient in reducing the SPL at both the rear and floor wall locations. The LS configuration is not as effective and requires an order of magnitude larger momentum coefficient to reach the same reduction levels at the rear and front locations as the configuration R2. However, the LS configuration has the largest overall reduction at the rear location for these three configurations. Similar VR are needed by these configurations to produce the same SPL reductions. A smaller VR compared to the R2 and SS configurations is needed for the LS configuration to produce

the larger reductions in SPL. For the jet Reynolds number, the LS configuration has a larger Reynolds number when the slot width (spanwise diameter) is used in contrast to the slot length (streamwise direction)*. Figure 3.7 shows the spectra comparing hole geometry, using a blowing momentum of 0.01 for each configuration. At the rear location, the LS configuration amplifies the third mode. The SS configuration has the greatest reductions of the SPL amplitudes at the first, third, and fourth modes. At the floor location, the LS configuration amplifies the first cavity mode and has minimal reductions on the other modes. The R2 configuration reduces the amplitude more at the second mode, and is slightly more effective than the SS configuration for the higher modes.

The effect of blowing angle is seen in Figure 3.4a and Figure 3.5a by comparing the R1, RA, SS, and SSA configurations. Blowing at 45° (configurations RA and SSA) is more effective compared to blowing at 90° (configurations R1 and SS). For the same momentum coefficient, blowing at 45° produces a larger reduction in the SPL and a greater overall reduction in the SPL. Figure 3.4b and Figure 3.5b show that a lower VR is needed for blowing at an angle to produce the same reduction in SPL. Examining Figure 3.4c and Figure 3.5c, a lower Re is needed for blowing at 45° to produce the same amount of SPL reduction. This decrease is due to the lower velocities required by blowing at an angle. Figure 3.8 shows the effect of the blowing angle on the spectra. Blowing both at an angle and at 90° is successful in reducing the SPL at all four modes;

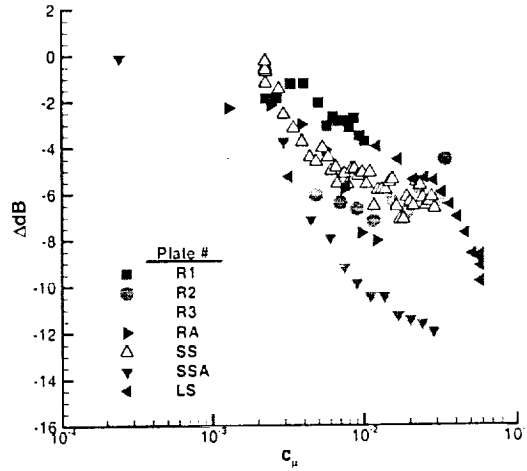
* Even with the latter dimension, the data of the LS configuration do not collapse onto the

however, blowing at 45° is more effective. At the rear location, the SSA configuration reduces the overall broadband levels and suppresses completely the resonant modes. For the RA configuration, the modal amplitudes have been reduced, however, the modes are still apparent. The greater reduction in SPL for blowing at 45° is due to the additional vorticity that the skewed jets produce compared to 90° blowing.

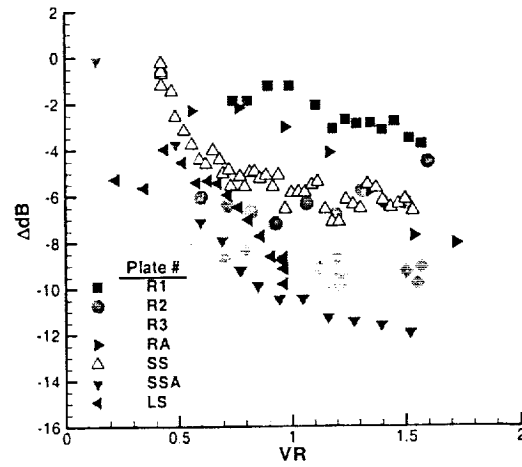
Overall, configuration SSA is the most effective hole configuration for steady blowing. This configuration has the greatest overall reduction in SPL at both the rear and floor locations. The peaks of the resonant modes are reduced to the broadband levels at the rear location and are substantially reduced at the floor location. Furthermore, skewed blowing requires a lower velocity to achieve these reductions compared to perpendicular blowing. Blowing momentum coefficients of the order 1×10^{-2} are required to accomplish these effects.

data of the other configurations.

(a)



(b)



(c)

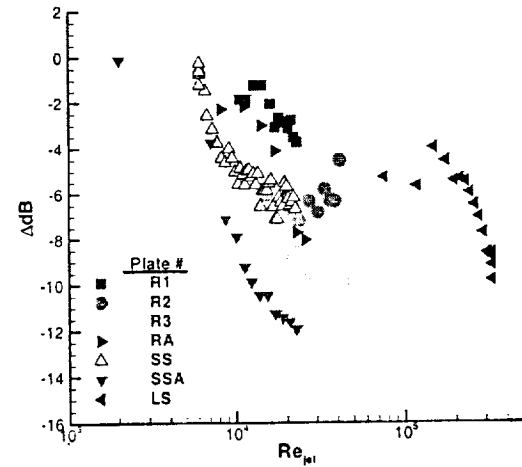
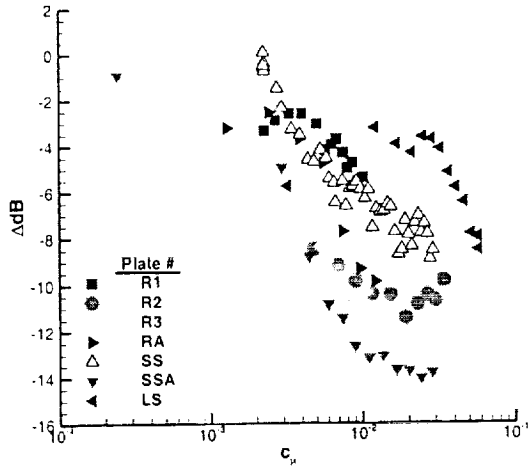
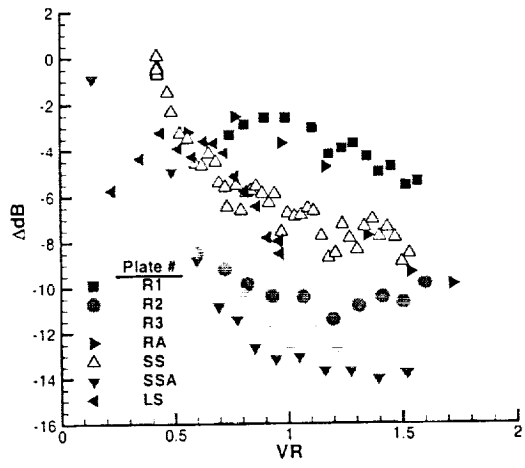


Figure 3.4: Effectiveness of steady blowing control at rear wall location. a) momentum coefficient, b) velocity ratio, c) Reynolds number.

(a)



(b)



(c)

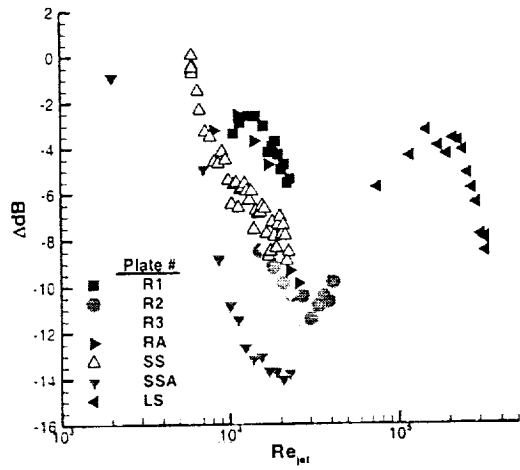


Figure 3.5: Effectiveness of steady blowing control at front floor location.
a) momentum coefficient, b) velocity ratio, c) Reynolds number.

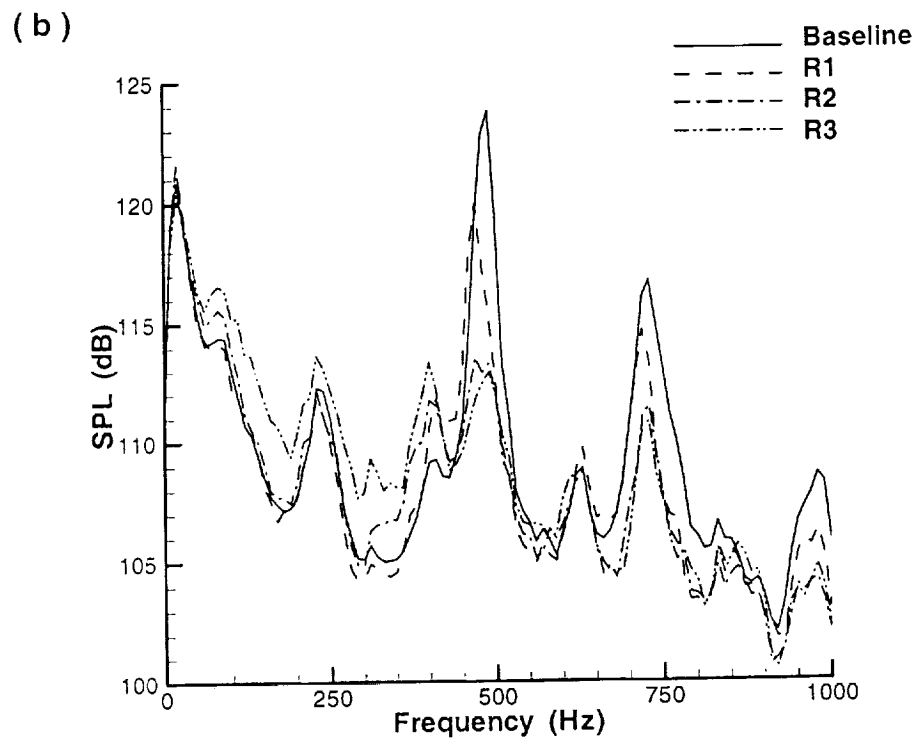
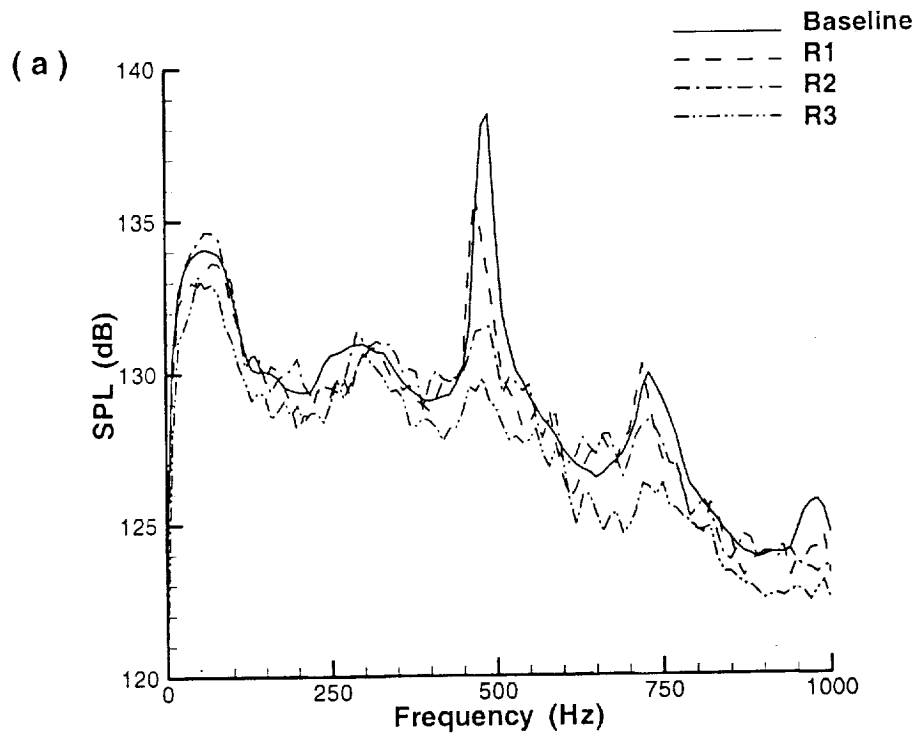


Figure 3.6: Spectra showing effect of hole size, $c_{\mu} = 0.01$:
 a) rear wall b) front floor locations.

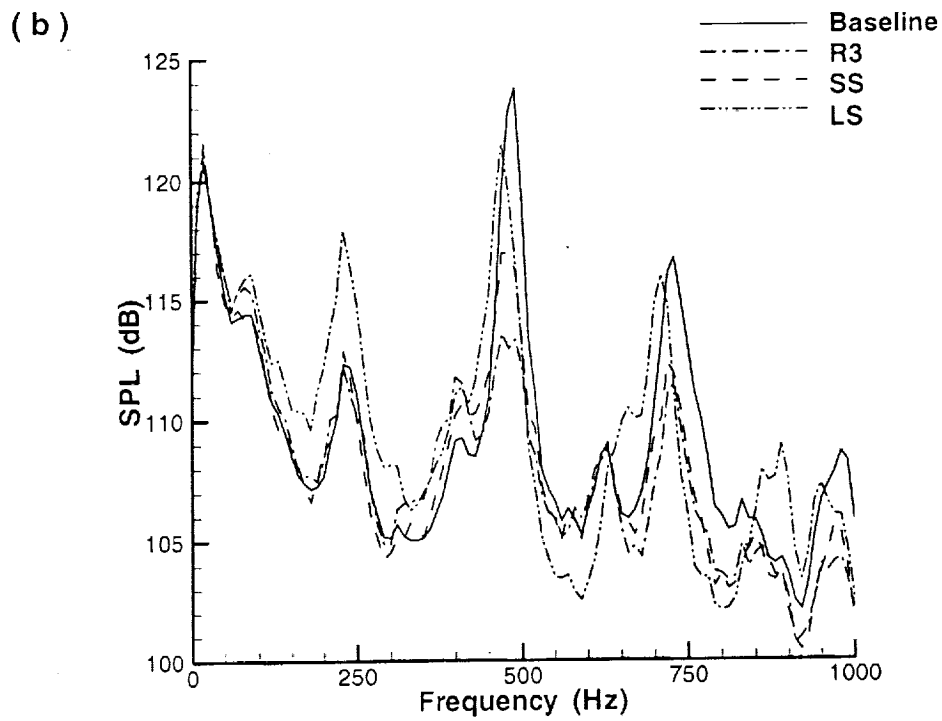
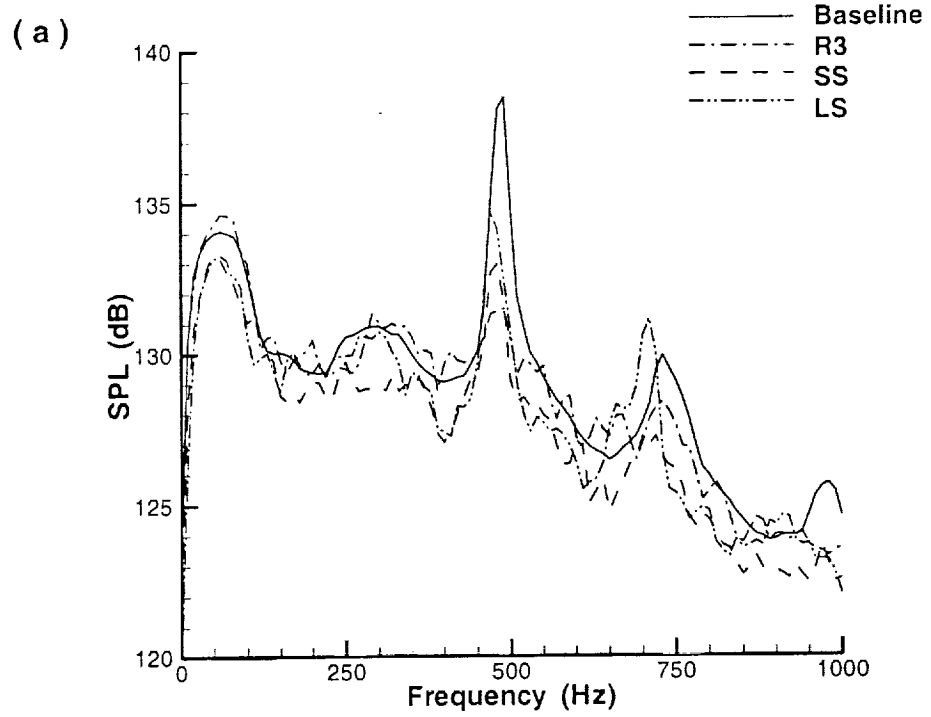


Figure 3.7: Spectra showing effect of hole shape, $c_\mu = 0.01$:
 a) rear wall b) front floor locations.

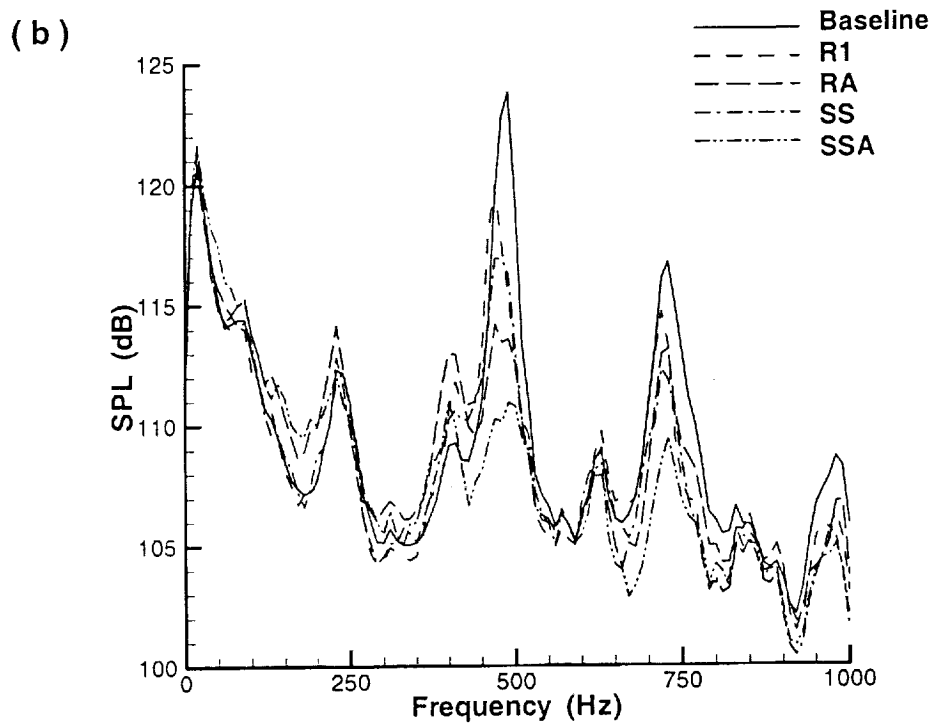
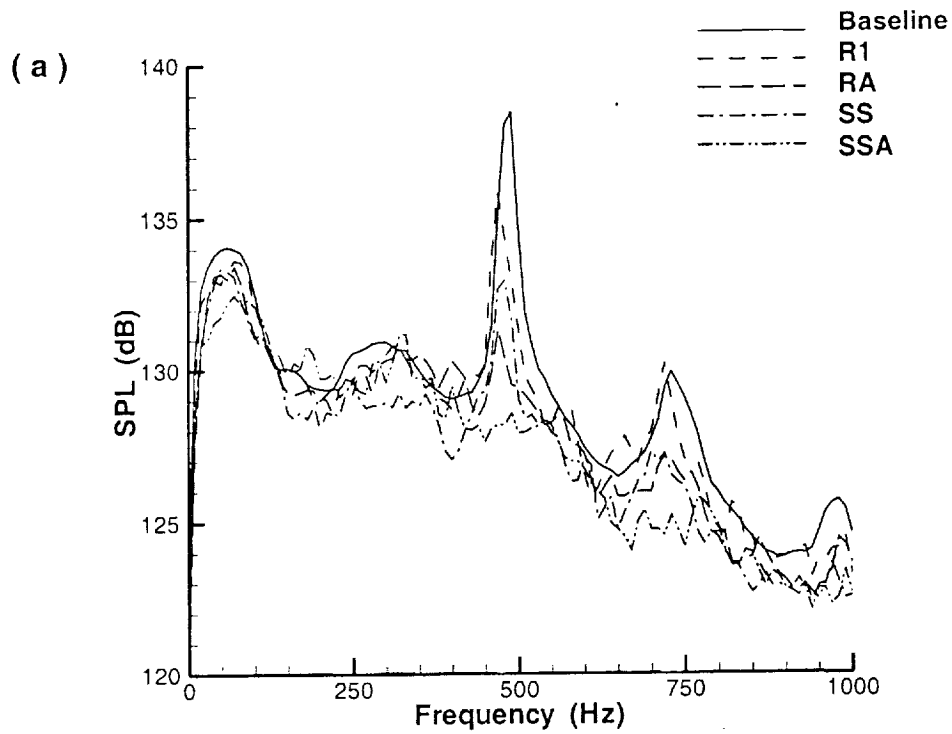


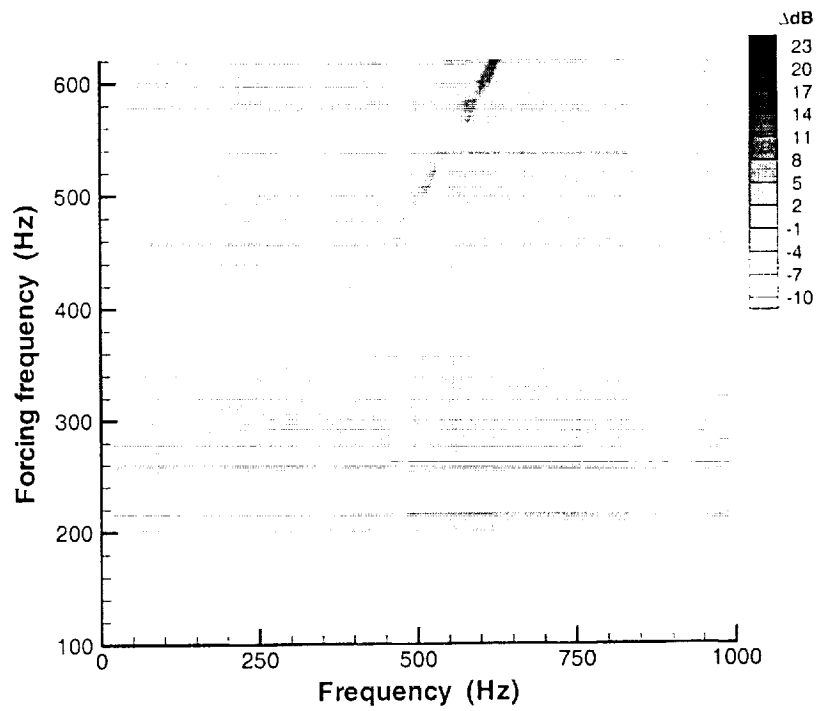
Figure 3.8: Spectra showing effect of blowing angle, $c_\mu = 0.01$:
 a) rear wall b) front floor locations.

3.2.2 Zero-Net Mass Oscillatory Blowing

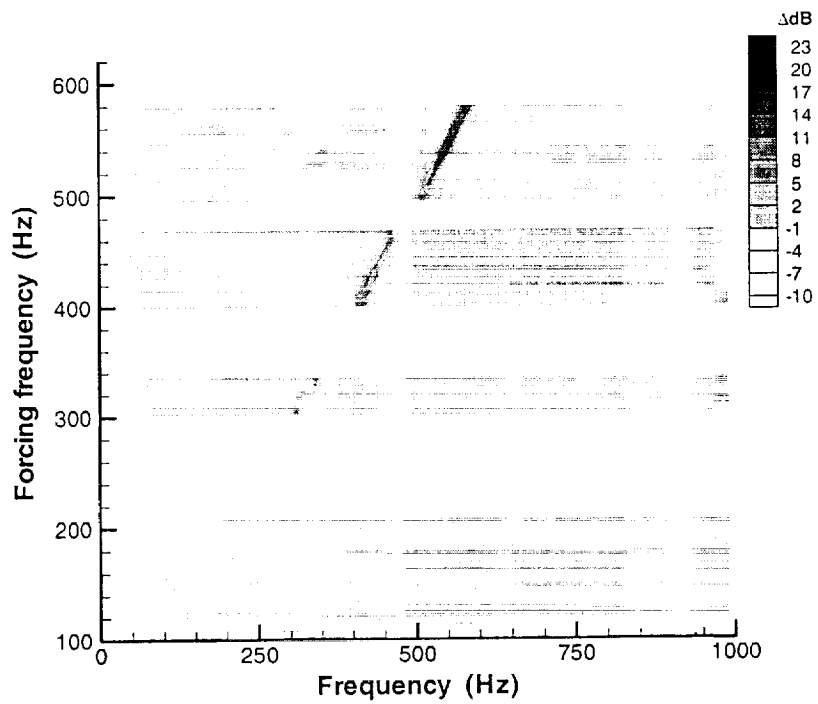
3.2.2.1 Effect of forcing frequency

The contour plots of the spectra in Figure 3.9 and Figure 3.10 show the effect of forcing frequency. The forcing frequency covers a range of 100Hz to 620Hz . No data are available over the range of forcing frequencies that show no contour values. The data presented are from the configuration SSA. The sequence of plots show different amplitudes of blowing at the rear wall and floor locations: Figure 3.9 and Figure 3.10a for $\langle c_\mu \rangle = 2 \times 10^{-6}$; Figure 3.9b and Figure 3.10b for $\langle c_\mu \rangle = 2 \times 10^{-5}$; Figure 3.9c and Figure 3.10c for $\langle c_\mu \rangle = 2 \times 10^{-4}$; Figure 3.9d and Figure 3.10d for $\langle c_\mu \rangle = 2 \times 10^{-3}$. The signature of the forcing frequency is seen by the high amplitude line along *forcing frequency = frequency*. The additional high amplitude diagonal lines seen in Figure 3.9c-d and Figure 3.10c-d indicate the harmonics of the forcing frequency. The amplitude of the forcing frequencies and their harmonics increase with increasing momentum coefficient. It is seen that the resonant cavity modes are more effectively suppressed with increasing momentum coefficient. Forcing at frequencies higher than 500Hz is the most effective in reducing the SPL of the second mode.

(a)



(b)



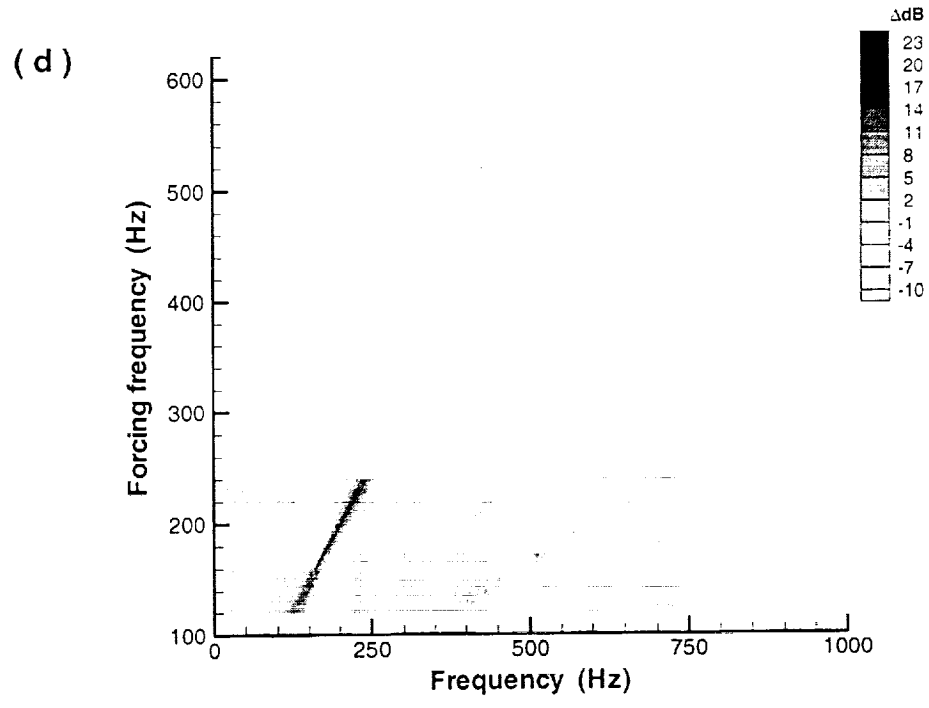
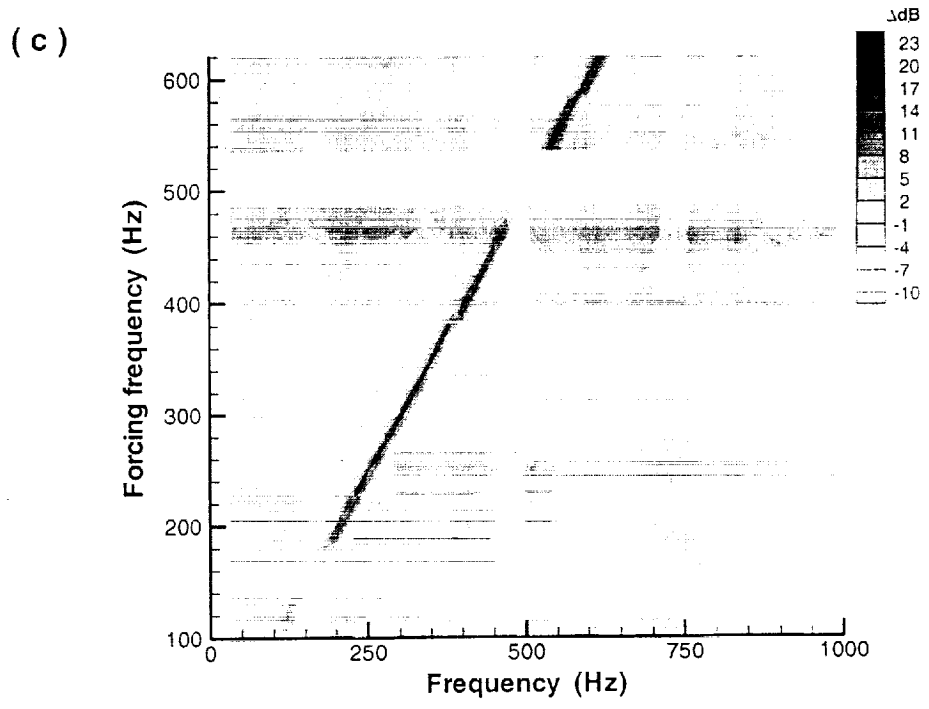
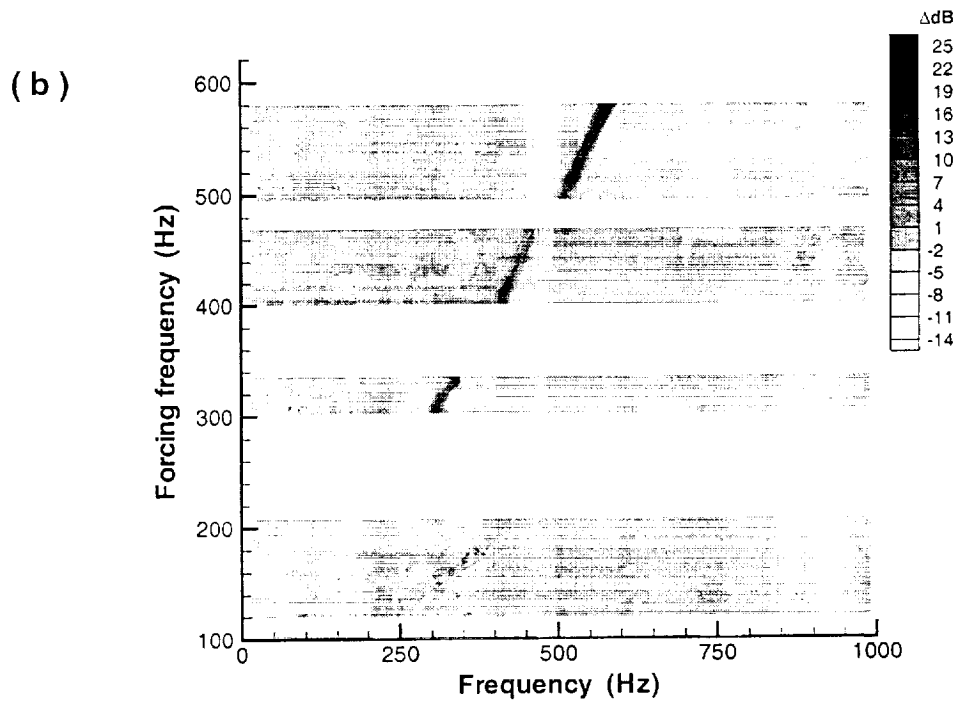
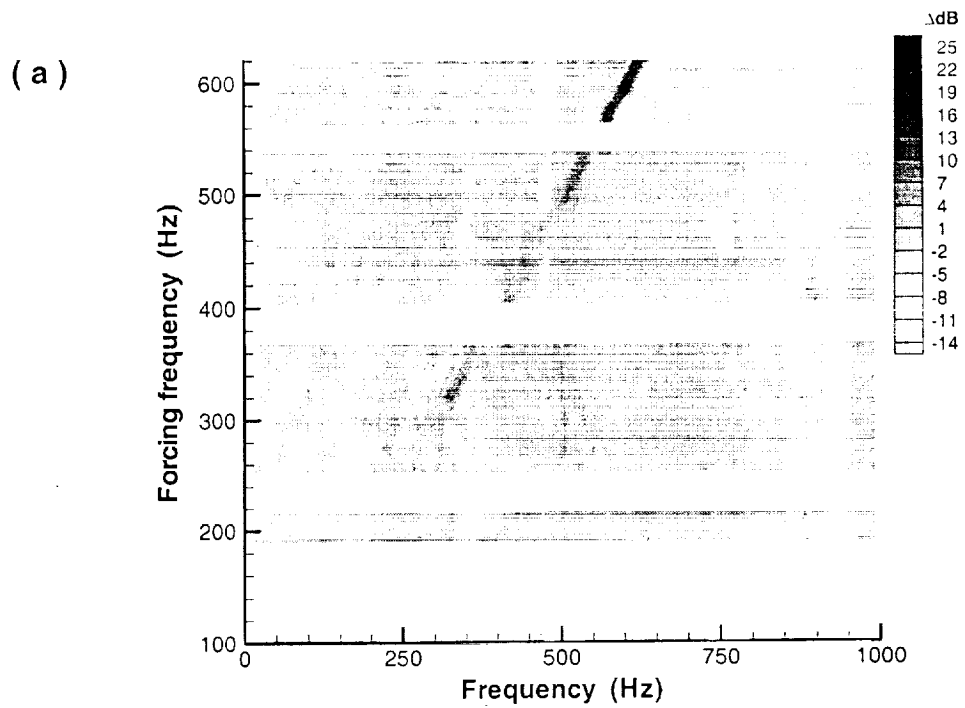


Figure 3.9: Effect of forcing frequency at rear location, $M_\infty = 0.2$, Configuration SSA. a) $\langle c_\mu \rangle = 2 \times 10^{-6}$; b) $\langle c_\mu \rangle = 2 \times 10^{-5}$; c) $\langle c_\mu \rangle = 2 \times 10^{-4}$; d) $\langle c_\mu \rangle = 2 \times 10^{-3}$.



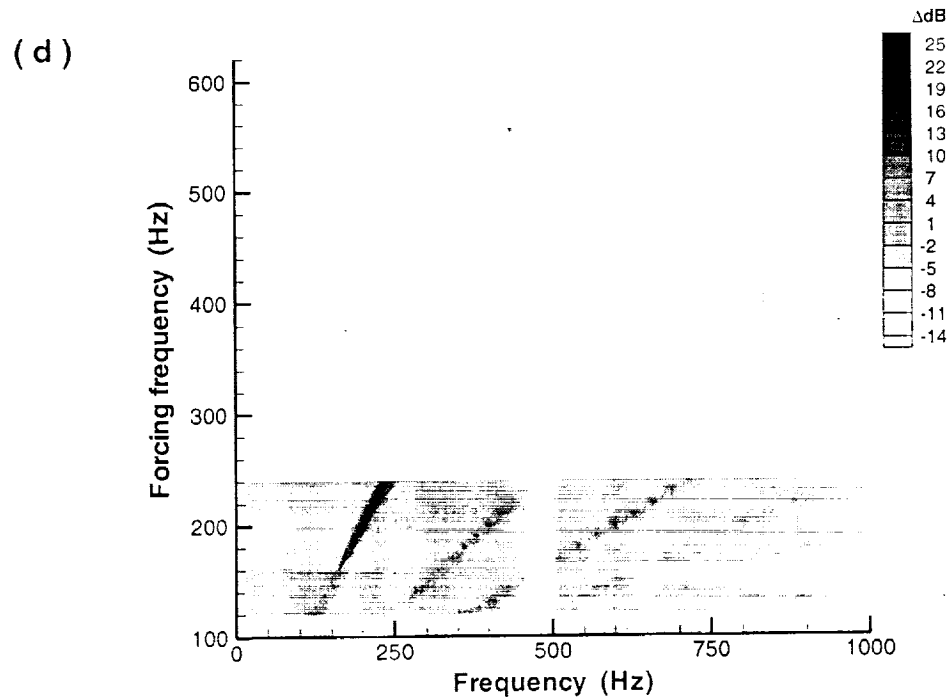
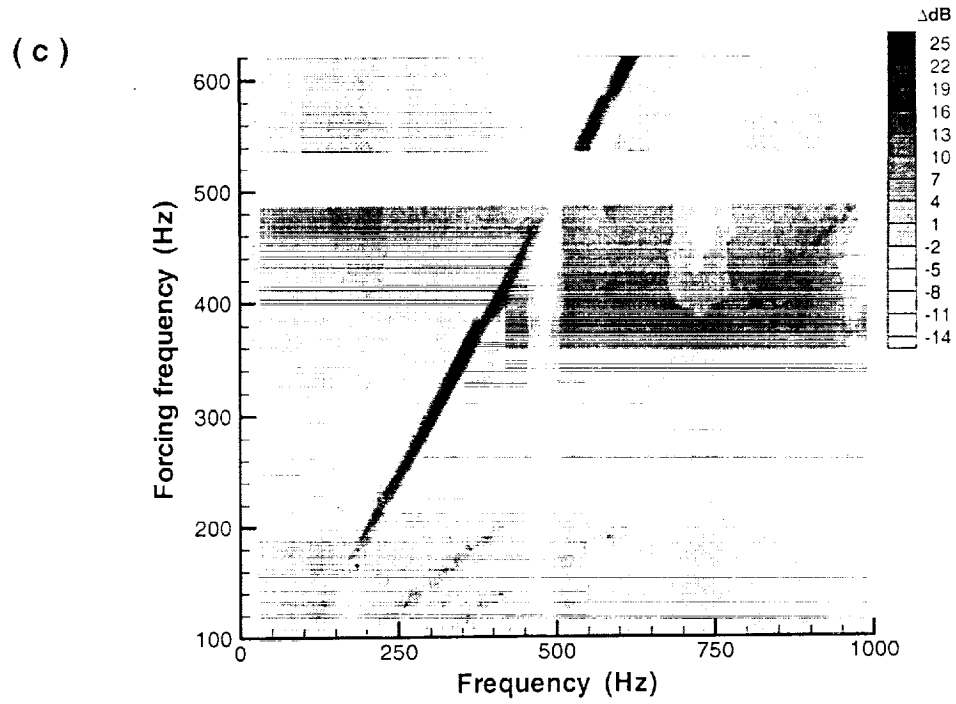


Figure 3.10: Effect of forcing frequency at floor location, $M_\infty = 0.2$, Configuration SSA. a) $\langle c_\mu \rangle = 2 \times 10^{-6}$; b) $\langle c_\mu \rangle = 2 \times 10^{-5}$; c) $\langle c_\mu \rangle = 2 \times 10^{-4}$; d) $\langle c_\mu \rangle = 2 \times 10^{-3}$.

Figure 3.11 and Figure 3.12 summarize the effectiveness of near-zero net mass oscillatory blowing. The reduction of the SPL amplitude of the second cavity mode is examined and the results for three forcing frequencies, 200Hz , 400Hz , and 550Hz , are shown. With a forcing frequency of 200Hz , Figure 3.11a and Figure 3.12a, all configurations show a similar effectiveness and significant SPL reductions are achieved with an unsteady momentum coefficient of 1×10^{-3} or higher. Configurations SS, SSA, LS, and R3 have the largest reductions, 8dB , at the rear location; configuration LS has the largest reduction, 12dB , at the floor location. The oscillatory blowing is more effective when the forcing is at 400Hz , Figure 3.11b and Figure 3.12b. Significant reductions in SPL at both locations occur with an unsteady momentum coefficient of 1×10^{-4} , which is an order of magnitude smaller than the previous case. Configurations SS, SSA, LS, and R3 have reductions of 13dB and 9dB at the rear and floor locations respectively. The most effective oscillatory blowing is obtained using a forcing frequency of 550Hz , Figure 3.11c and Figure 3.12c. Significant reductions in SPL are obtained with an unsteady momentum coefficients, as small as 1×10^{-5} .

3.2.2.2 Effect of hole geometry

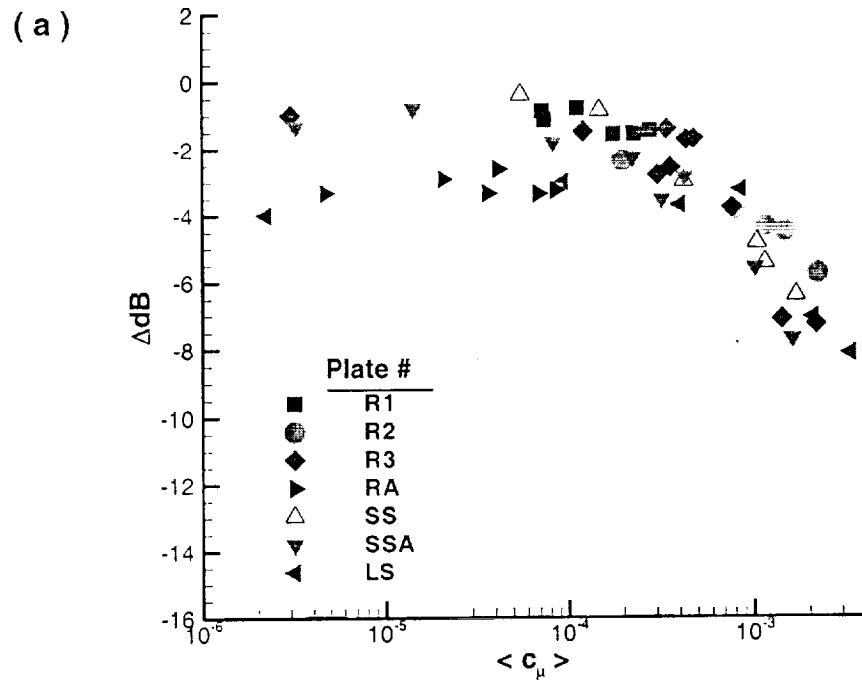
The effect of hole size can be seen by comparing the results of configurations R1, R2, and R3 in Figure 3.11c and Figure 3.12c. The SPL reductions scales with the hole size. Blowing with the small round holes, configuration R1, is the least effective and yields reductions only of 1dB and 3dB at the rear and floor locations. Configuration R3, large round holes configuration, is more effective and reductions of 8dB and 12dB at the

rear and floor locations, respectively, are measured. Figure 3.13 shows the spectra for these three hole configurations with $\langle c_{\mu} \rangle = 1 \times 10^{-5}$ and $f_f = 550\text{Hz}$. The signature of the 550Hz forcing frequency is clearly seen and becomes more pronounced with increasing hole size. The SPL reduction of the second cavity mode increases with increasing hole size.

The effect of hole shape can be seen by comparing the results for configurations R2, SS, and LS, in Figure 3.11c and Figure 3.12c. At the rear location, the LS and SS configurations are the most effective and reduce the second mode by 8dB with $\langle c_{\mu} \rangle = 1 \times 10^{-6}$. The LS configuration is more effective in reducing the second cavity mode at the floor location and yields the maximum SPL reduction of 13dB at $\langle c_{\mu} \rangle = 1 \times 10^{-6}$. The R2 configuration is not as effective, and achieves a SPL reduction of 6dB at the rear, and 11dB at the floor locations. Figure 3.14a and b shows the spectra for the three configurations R2, SS, and LS at $\langle c_{\mu} \rangle = 1 \times 10^{-5}$. Similar to the previous case, the forcing frequency of 550Hz is seen and the SPL reduction of the second mode increases with the increase in amplitude at the forcing frequency. The LS configuration shows the only significant decrease at the third mode at both locations. For the first mode and the broadband levels at the lower frequencies, both SS and LS configurations increase the amplitude; the LS produce the largest increase of 4dB at both locations.

The effect of the blowing angle is examined by comparing the results of configurations R1, RA, SS, and SSA, Figure 3.11c and Figure 3.12c. The measured SPL reductions of the small round holes configurations (R1 and RA) show that blowing at 45° is more effective. The streamwise slots however show that blowing at 45° is not as

effective and with blowing levels greater than $\langle c_{\mu} \rangle = 1 \times 10^{-4}$, the two slot configurations achieve similar SPL reductions of $8dB$ and $14dB$ at the rear and floor locations respectively. The corresponding spectra are shown in Figure 3.15a and b.



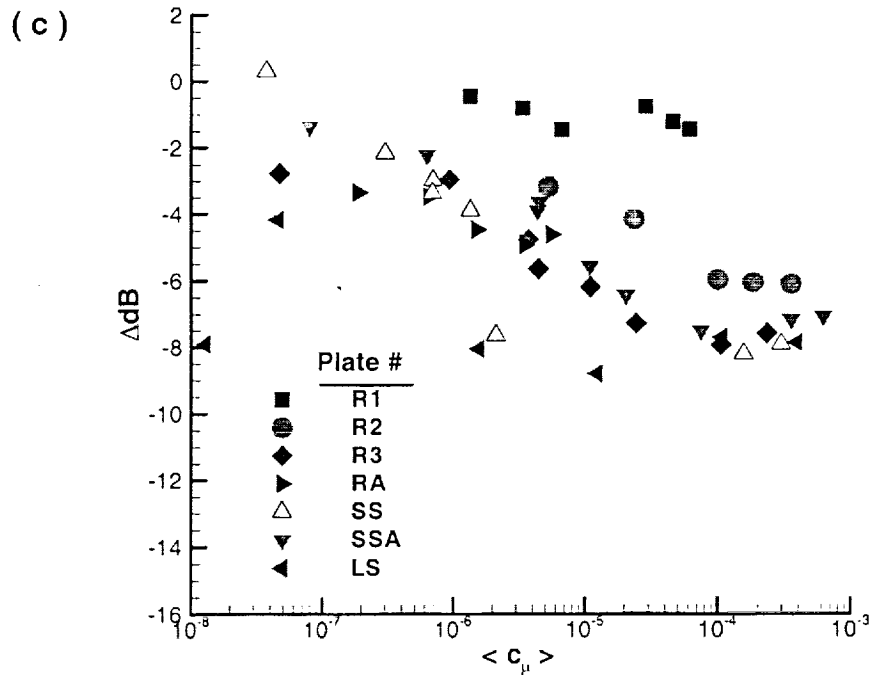
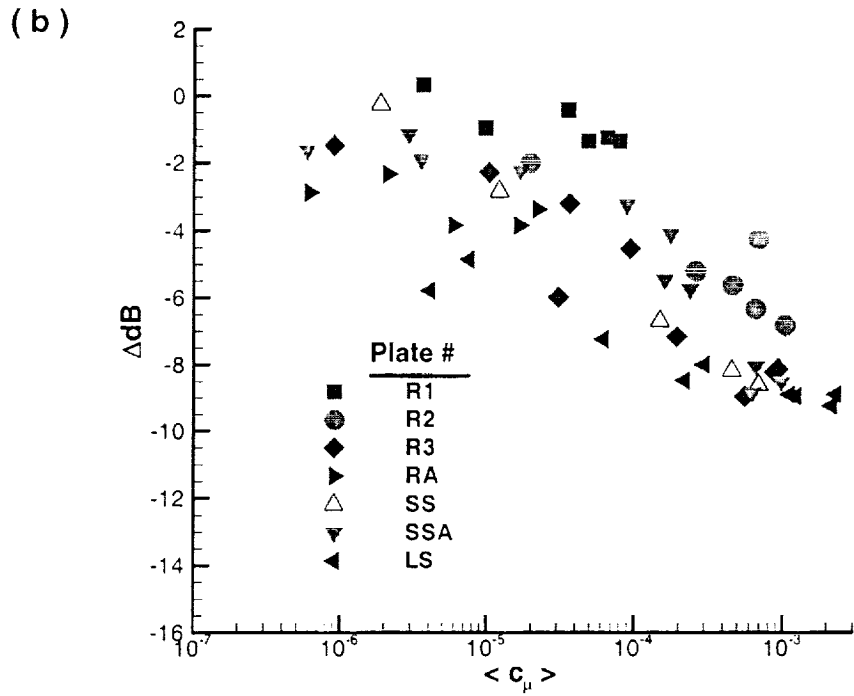
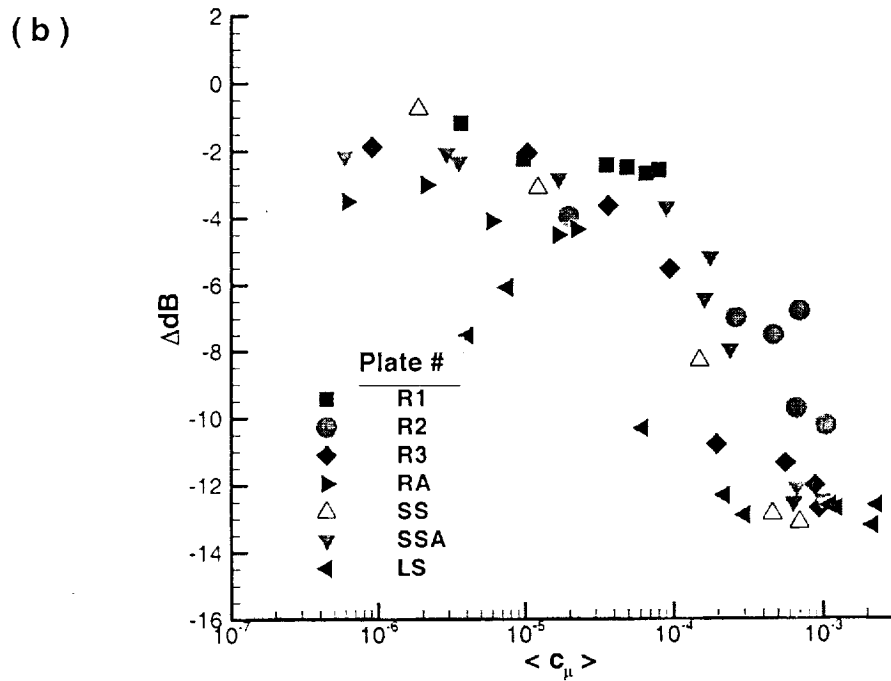
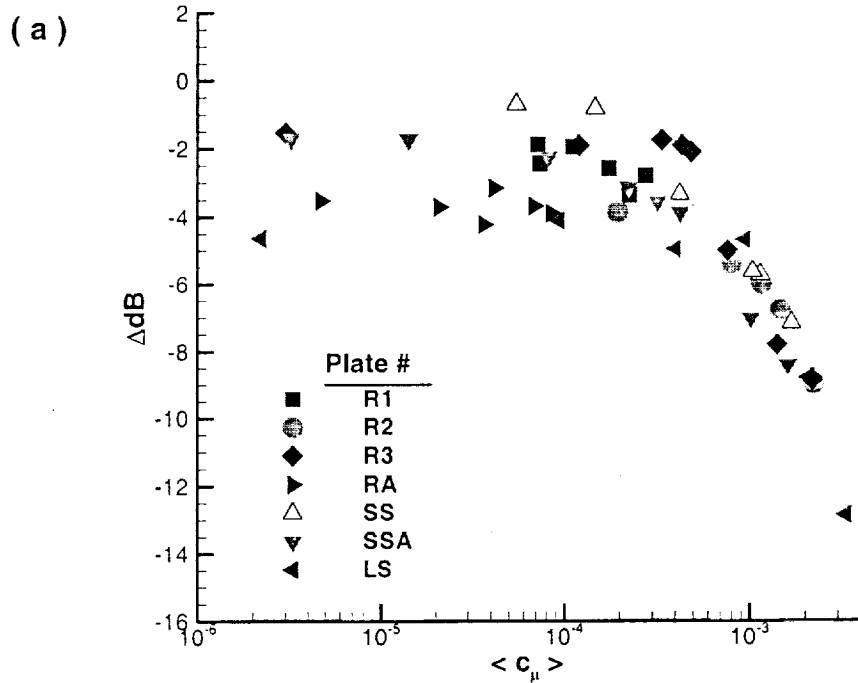


Figure 3.11: Effectiveness of zero net-mass oscillatory blowing on second cavity mode, rear location. a) $f_f = 200$ Hz; b) $f_f = 400$ Hz; c) $f_f = 550$ Hz.



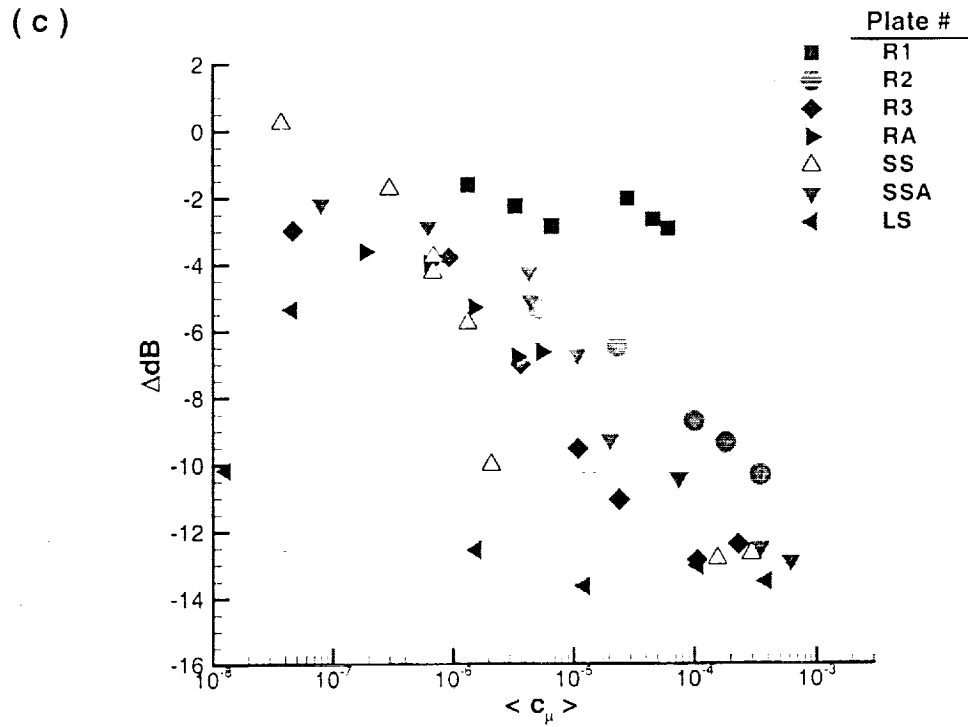
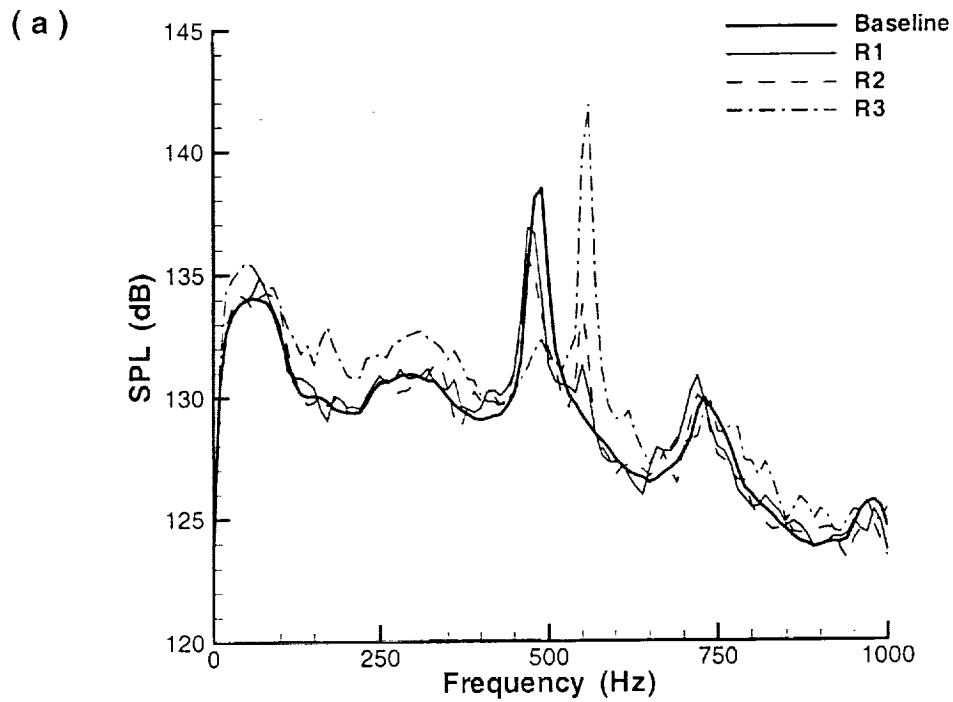


Figure 3.12: Effectiveness of zero net-mass oscillatory blowing on second cavity mode, floor location. a) $f_f = 200$ Hz; b) $f_f = 400$ Hz; c) $f_f = 550$ Hz.



(b)

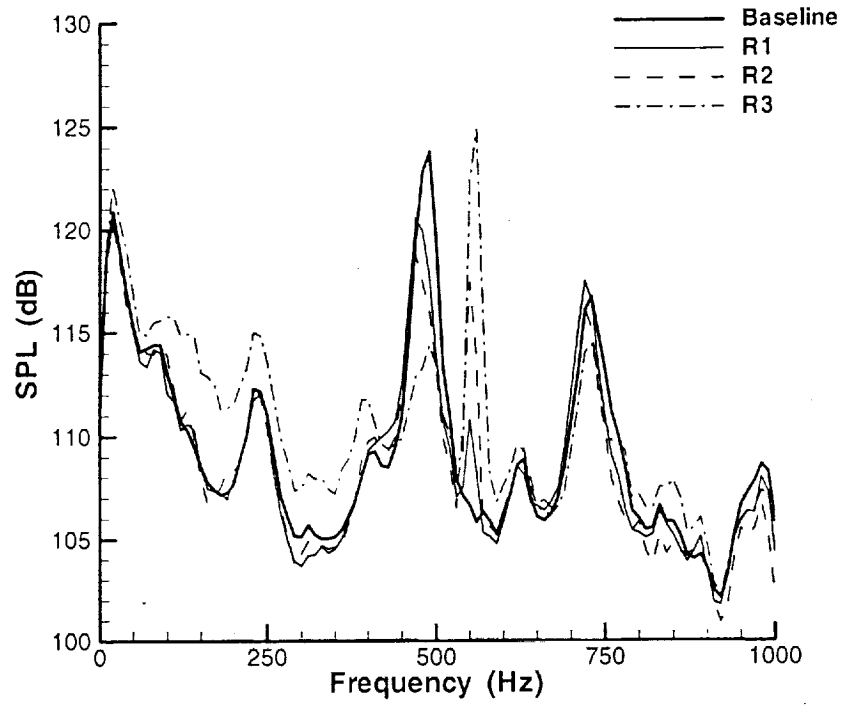


Figure 3.13: Spectra showing effect of hole size, $\langle c_{\mu} = 1 \times 10^{-5} \rangle$, $f_r = 550 Hz$:
a) rear wall b) floor locations.

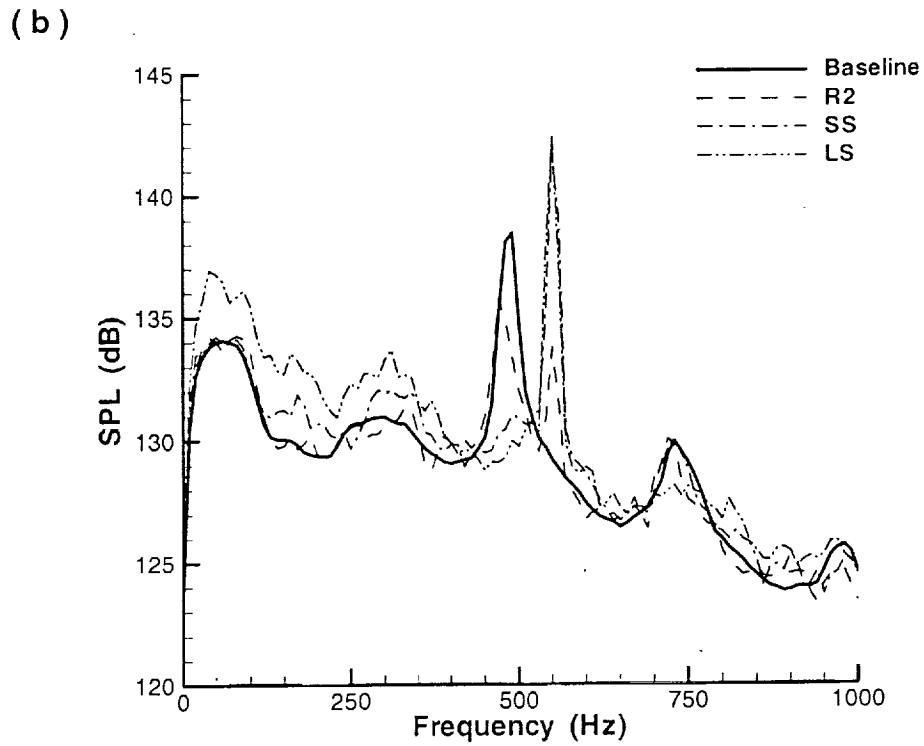
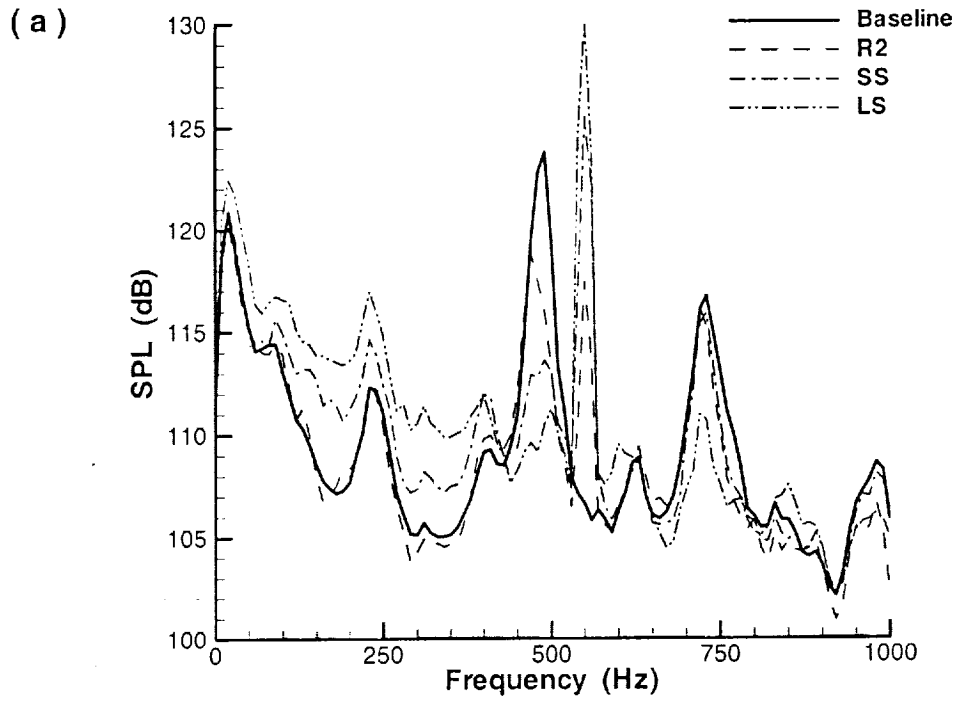


Figure 3.14: Spectra showing effect of hole shape; $\langle c_{\mu} = 1 \times 10^{-5} \rangle$, $f_t = 550\text{Hz}$:
 a) rear wall b) floor locations.

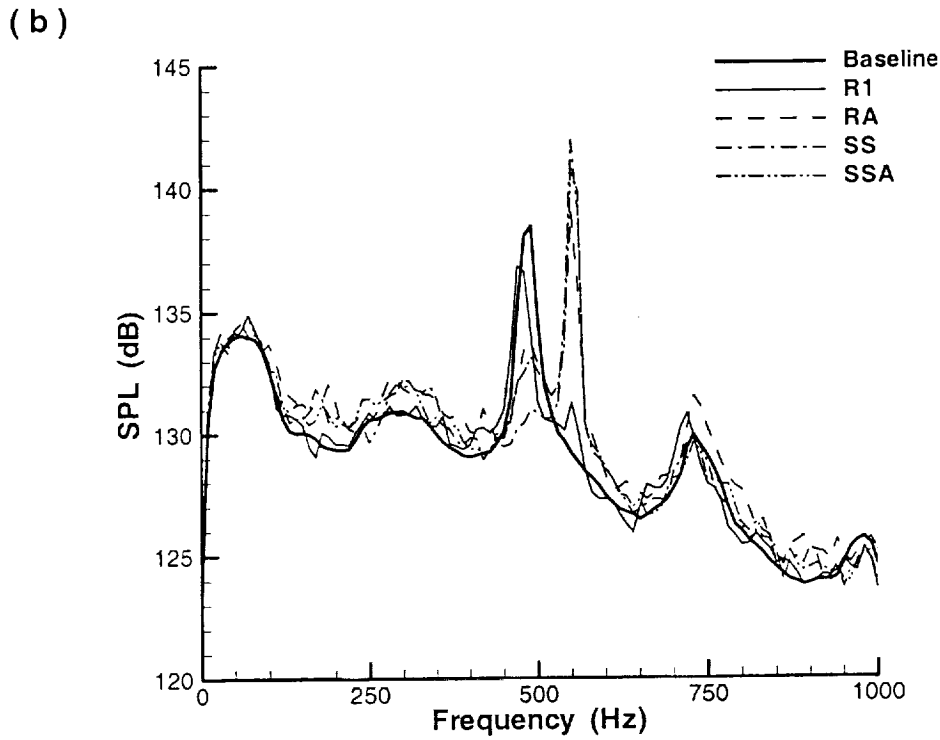
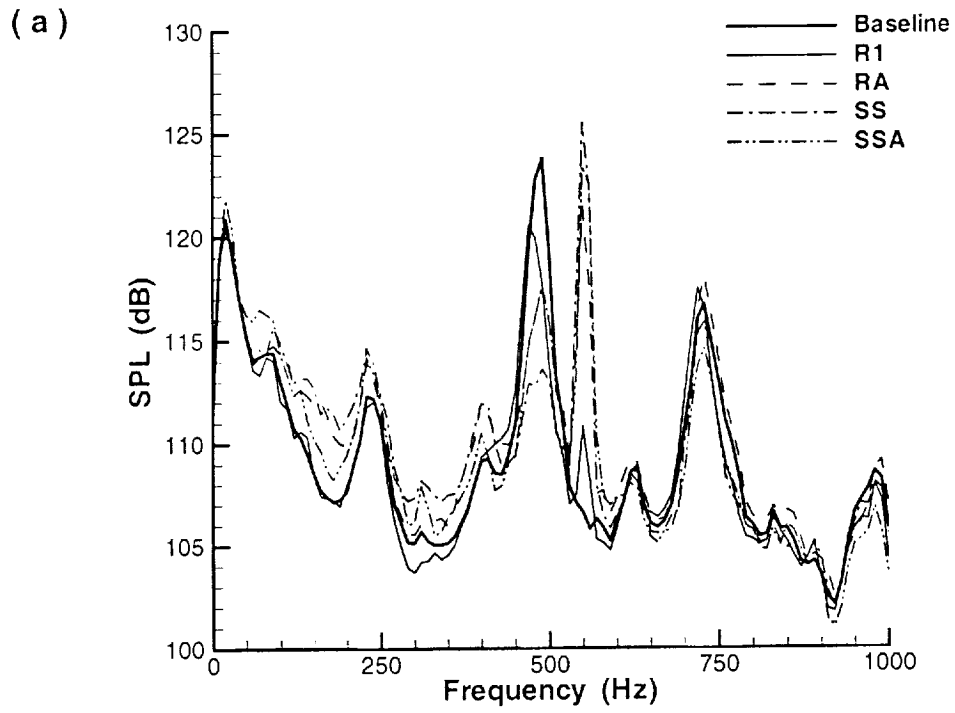


Figure 3.15: Spectra showing the effect of blowing angle; $\langle c_\mu = 1 \times 10^{-5} \rangle$, $f_f = 550\text{Hz}$:
 a) rear wall b) floor locations.

3.3 Auto Correlation Analysis

3.3.1 Baseline

Auto-correlation analysis and the spectra both describe the periodic nature of the cavity flow. However, the results of auto-correlation analysis are presented in the time domain. This presentation allows the effect of blowing on the relative size of the large-scale structures to be assessed.

Figure 3.16 shows the auto-correlations for the baseline case. The sinusoidal character with near constant amplitude peaks indicates the strongly periodic nature of the cavity flow. The time lag ($\tau = 2.05msec$) at the first peak indicates that the second mode ($490Hz \approx 1/\tau$) dominates the periodicity of the flow. The relatively low amplitude of the peaks is indicative of the relatively large broadband background on which the periodic flow is superimposed. At the rear location, the amplitudes are lower due to the higher levels of the turbulence intensity in the impinging shear layer. The first zero crossing of the auto-correlation occurs at a larger time lag for the rear wall compared to the floor. This difference indicates that the size of the large-scale shear layer structures at the rear wall is larger than those at the front of the cavity.

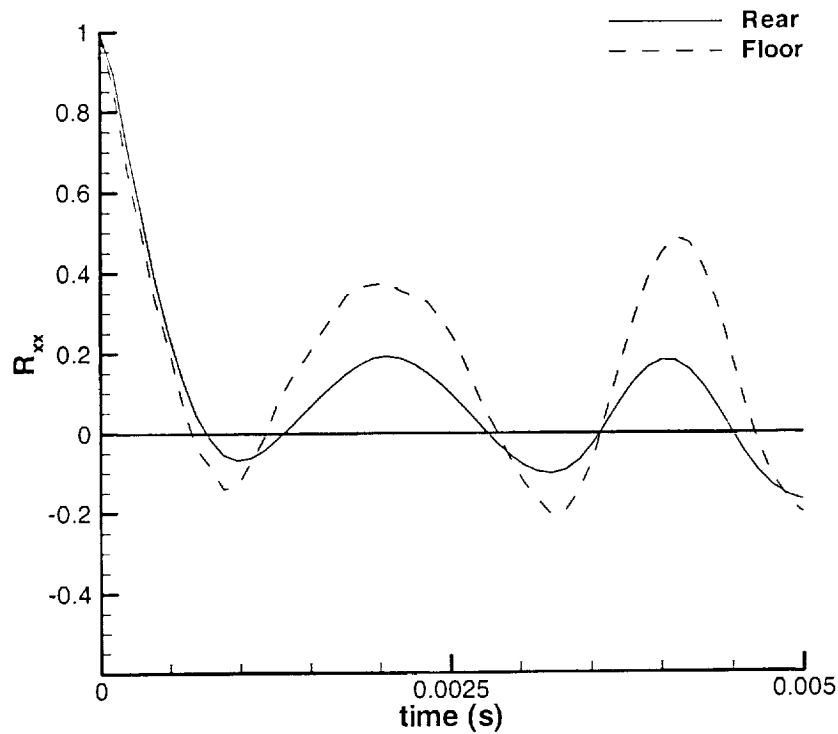


Figure 3.16: Baseline auto-correlations of rear and floor locations.

3.3.2 Steady Blowing

The effect of hole size is examined in Figure 3.17. The momentum coefficient is $c_{\mu} = 0.01$. With increasing hole size, the periodicity of the auto-correlation and the amplitudes in the peaks of the auto-correlation decrease. The reduced periodicity is indicative of a modification to the feedback loop in the cavity flow and the lessened influence of the second cavity mode. At a given time delay, for example $\tau \approx 0.8ms$, the higher correlation coefficients suggest that the large-scale structures are larger. The small holes, configuration R1, show a modest increase compared to the baseline, whereas the larger hole configurations show the larger increases in size. The reduced variation in

the amplitudes suggests higher broadband levels relative to the resonant peaks as previously seen in the spectra.

The effect of hole shape is examined in Figure 3.18. The momentum coefficient is $c_{\mu} = 0.01$. The periodicity and the amplitude in the auto-correlation are reduced for all three hole configurations. The results suggest that the round hole, configuration R3, and streamwise slot, configuration SS, are more effective than the LS configuration in changing the character of the cavity flow.

Figure 3.19 shows the effect of blowing angle. The blowing at 45° using the streamwise slots is seen to have the most pronounced effect on the dynamics of the cavity. At the rear location, the effect of blowing angle shows results similar to those observed in the spectra. Blowing at an angle, configurations RA and SSA, produces the largest change.

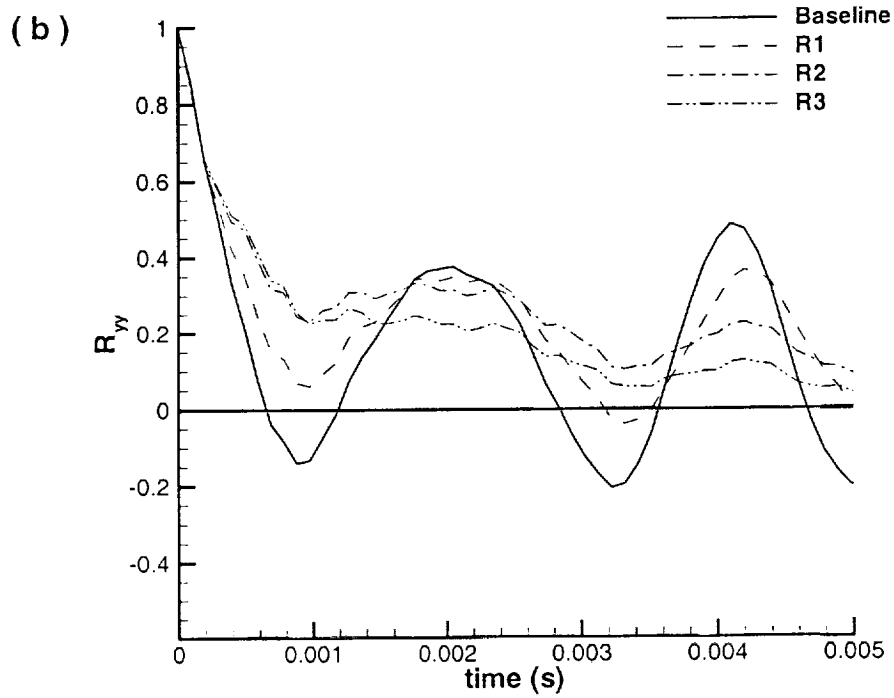
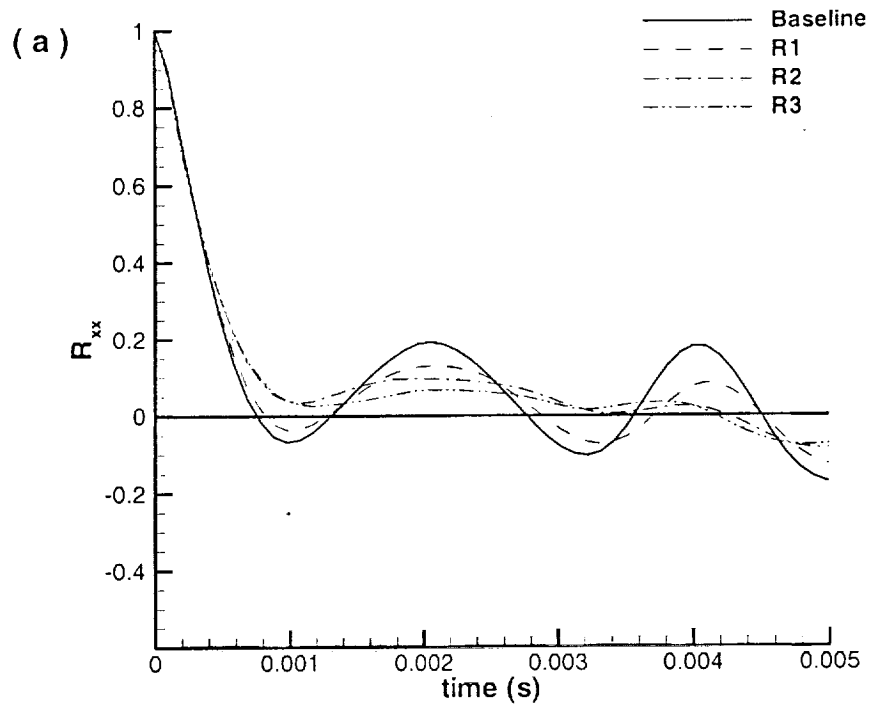


Figure 3.17: Auto-correlations showing the effect of hole size using steady blowing, $c_{\mu} = 0.01$: a) rear b) floor locations.

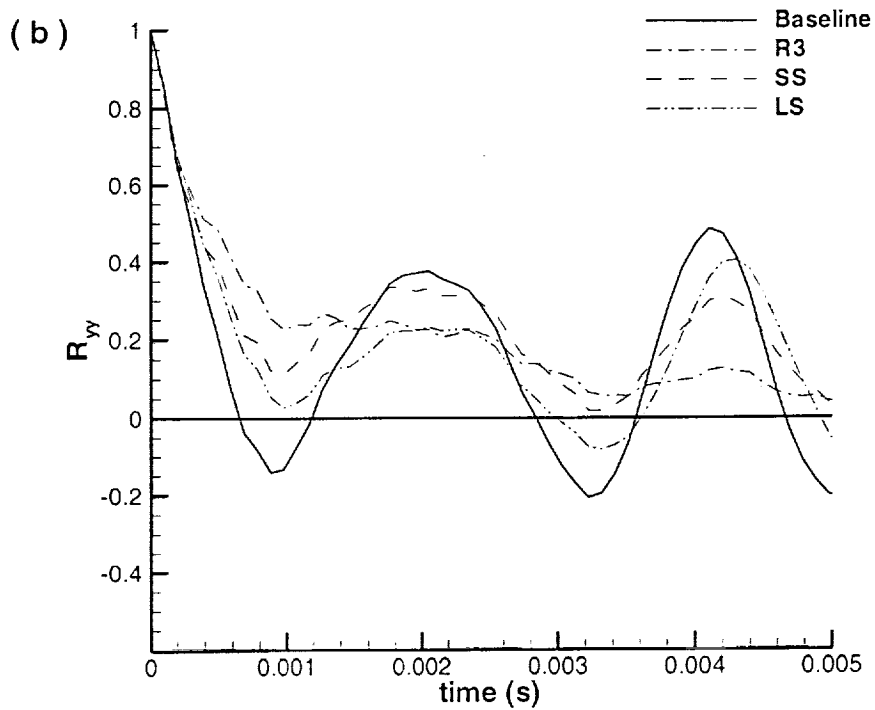
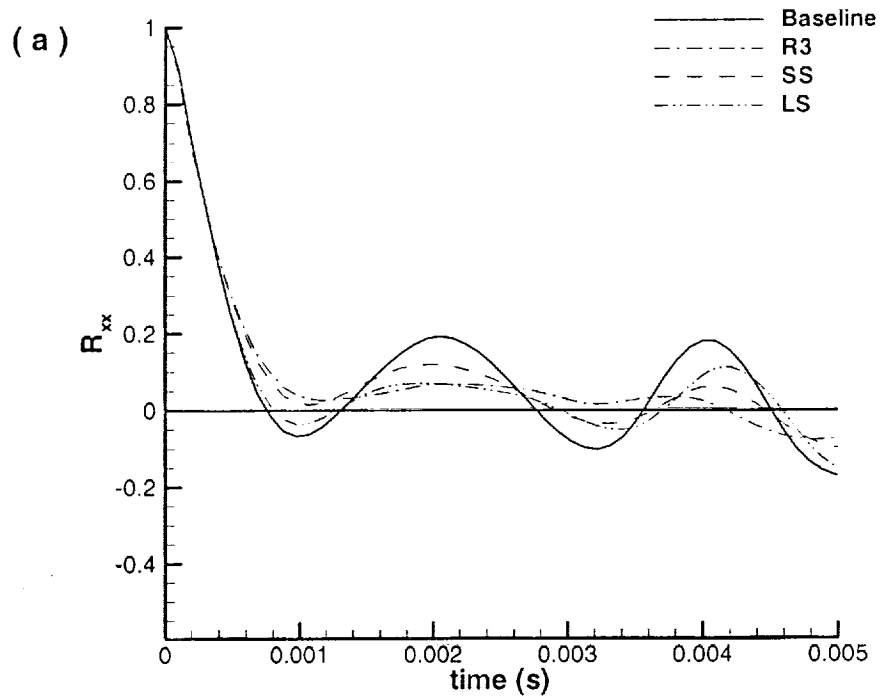


Figure 3.18: Auto-correlations showing the effect of hole shape using steady blowing, $c_{\mu} = 0.01$: a) rear b) floor locations.

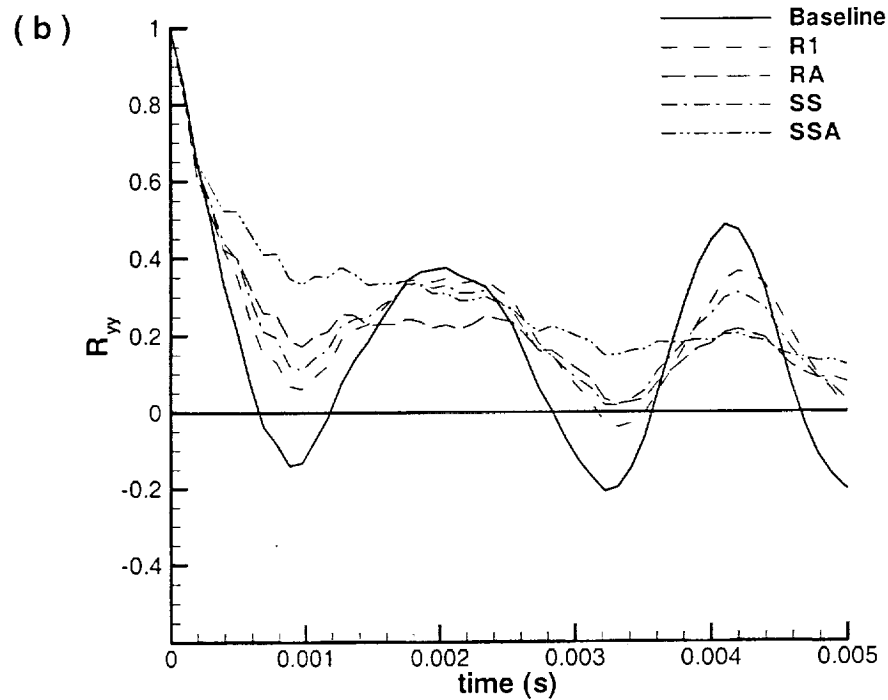
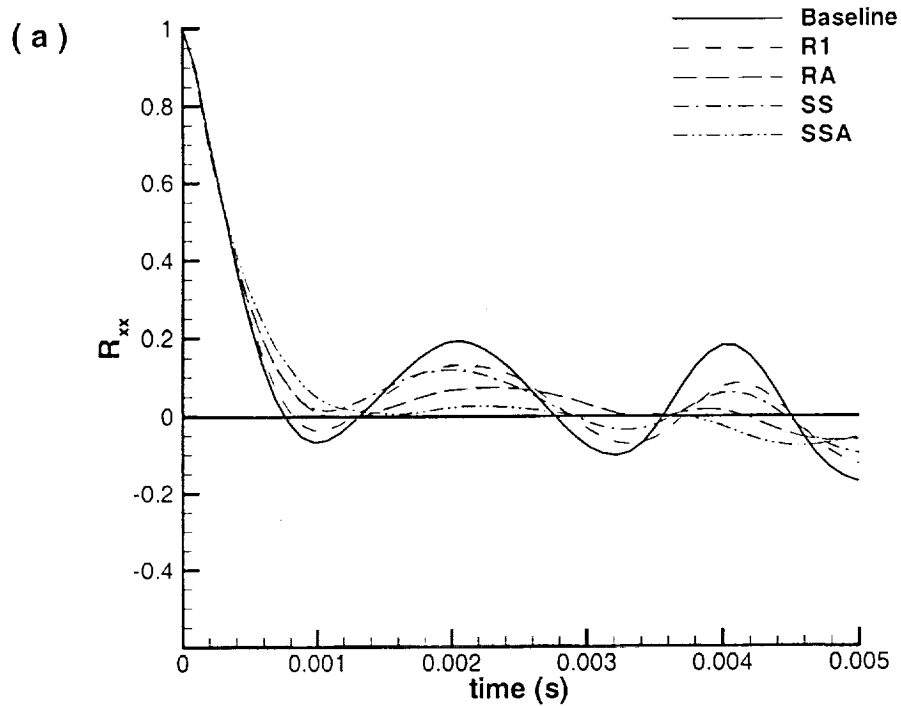


Figure 3.19: Auto-correlations showing the effect of blowing angle using steady blowing, $c_{\mu} = 0.01$: a) rear b) floor locations.

3.3.3 Zero Net Mass Oscillatory Blowing

Figure 3.20 shows the effect of hole size using near-zero net mass oscillatory blowing. The momentum coefficient is $\langle c_{\mu} \rangle = 1 \times 10^{-5}$ and forcing frequency is $550 Hz$. At the rear location, the amplitudes of the peaks with blowing are similar to the baseline case. This confirms the observation in the spectra that the broadband levels do not increase with oscillatory blowing. For the large hole configuration R3, the location of the first peak in the auto-correlation is shifted to $\tau = 1.8 msec$ indicating that the dominant frequency is the forcing frequency.

Figure 3.21 shows the effect of hole shape. The forcing frequency modifies the periodicity of the cavity flow with control, as is seen by the shift in the location of the first peak at both the floor and rear wall locations. The periodicity is more pronounced at the floor location for the long slot, configuration LS.

Figure 3.22 shows the effect of blowing angle. For the round hole configurations, blowing at 45° , configuration RA, improves the effectiveness of the oscillatory blowing in comparison to the normal configuration R1. For the streamwise slots configurations SS and SSA, blowing is effective, however, blowing at 45° produces the largest change in the dynamics of the cavity flow.

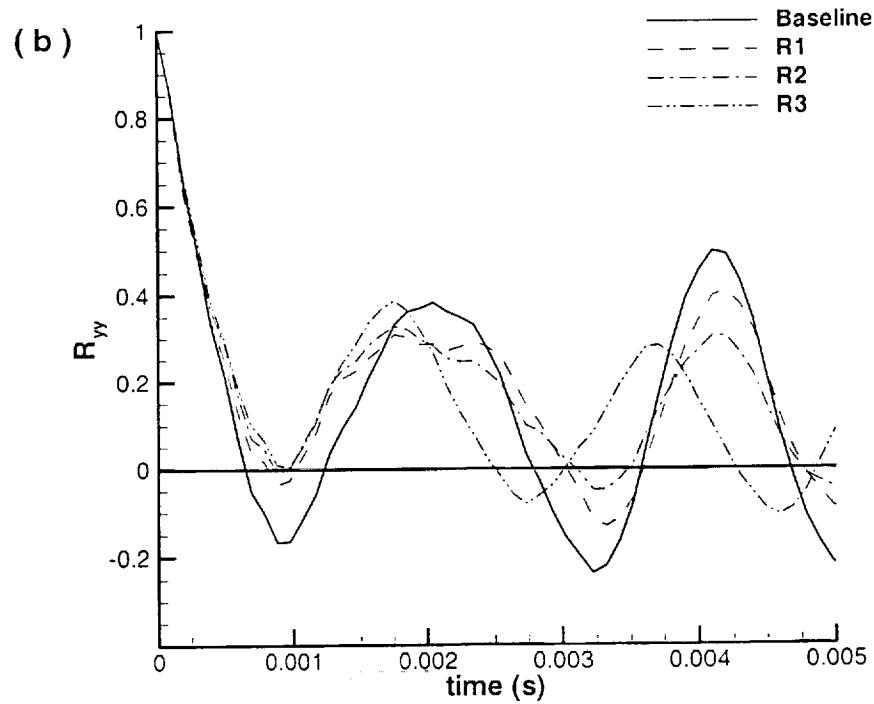
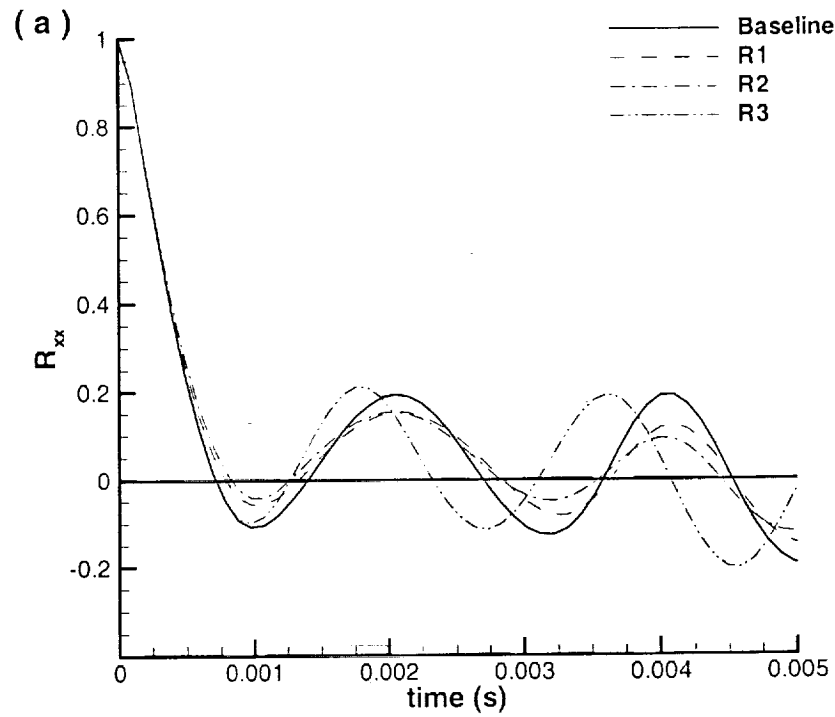


Figure 3.20: Auto-correlations showing the effect of hole size using oscillatory blowing, $f_f = 550\text{Hz}$, $\langle c_\mu \rangle = 1 \times 10^{-5}$: a) rear b) floor locations.

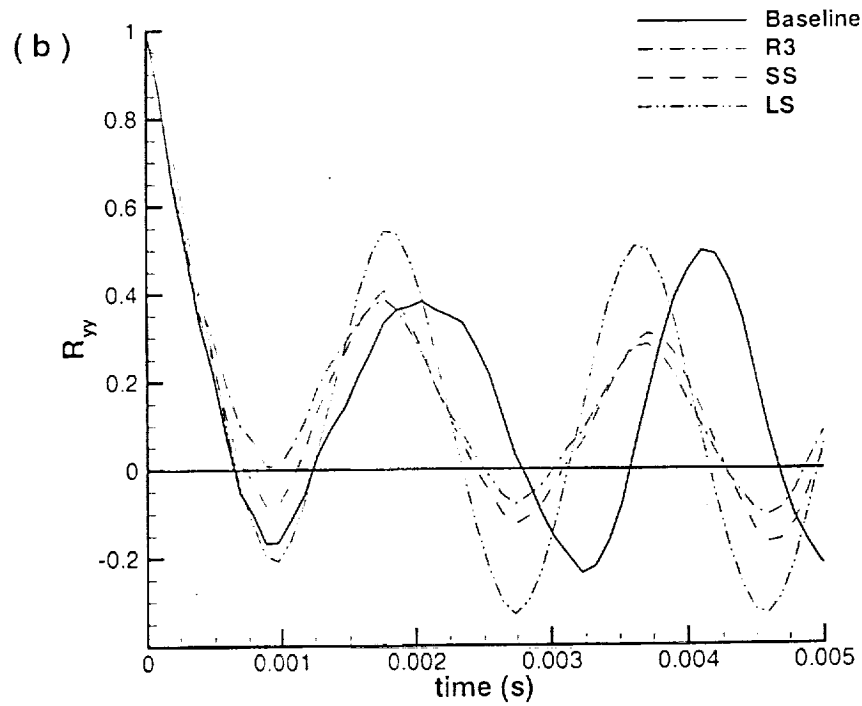
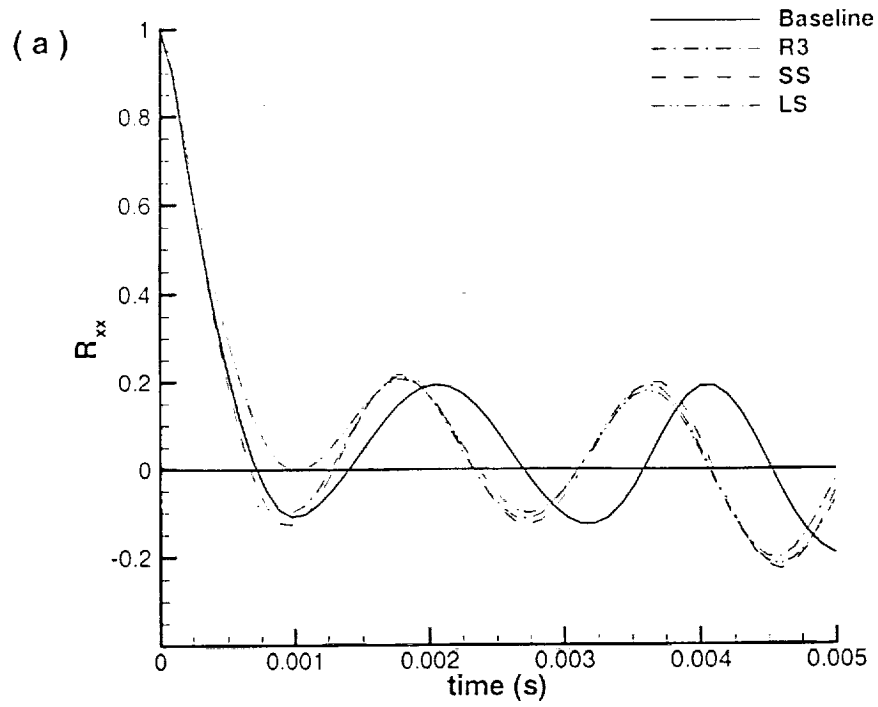


Figure 3.21: Auto-correlations showing the effect of hole shape using oscillatory blowing, $f_t = 550\text{Hz}$, $\langle c_\mu \rangle = 1 \times 10^{-5}$: a) rear b) floor locations.

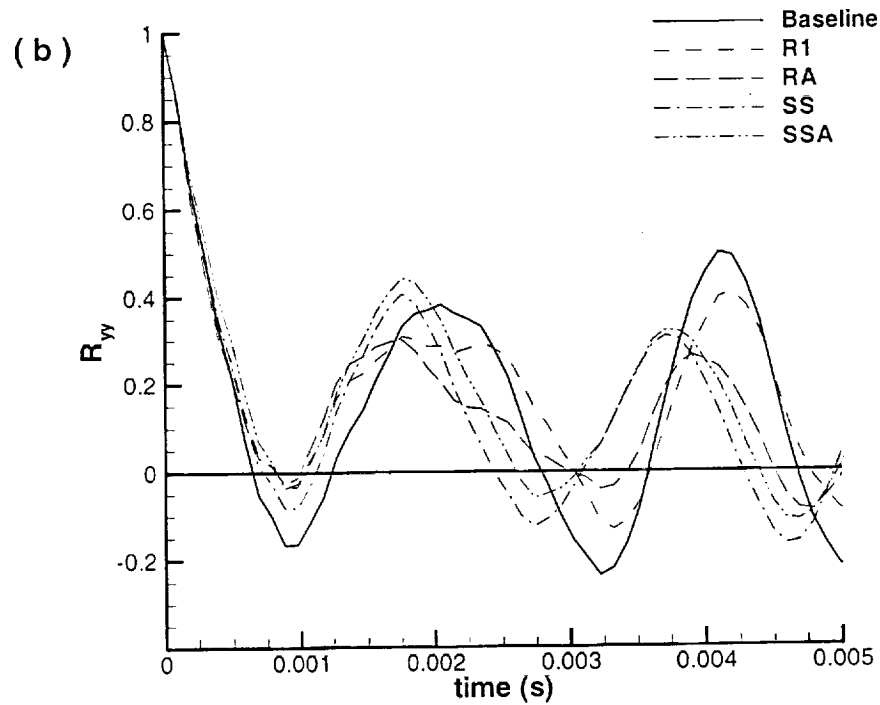
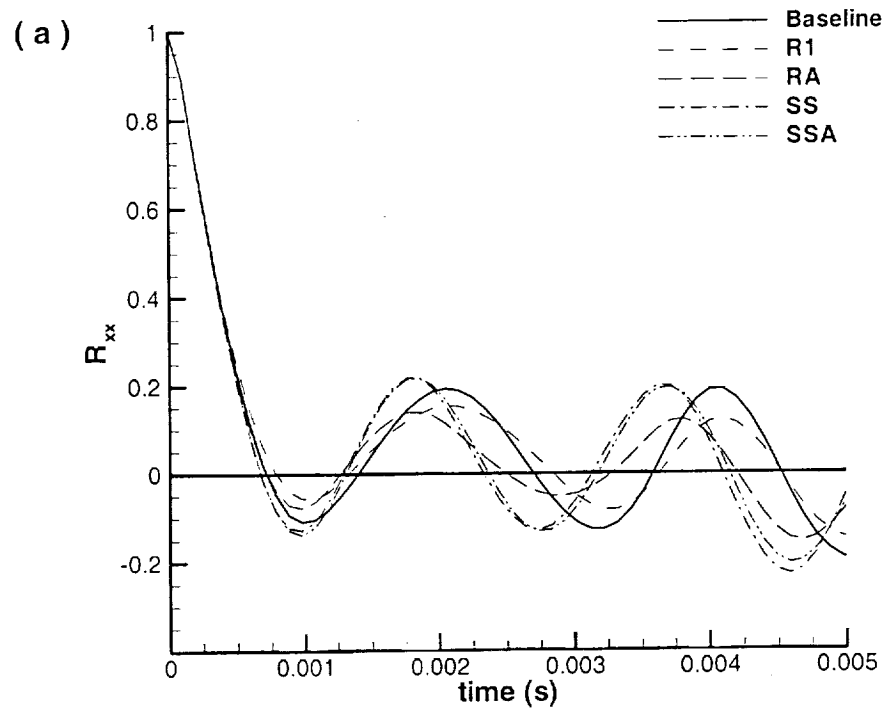


Figure 3.22: Auto-correlations showing the effect of blowing angle using oscillatory blowing, $f_r = 550\text{Hz}$, $\langle c_\mu \rangle = 1 \times 10^{-5}$: a) rear b) floor locations.

3.4 Cross Correlation Analysis

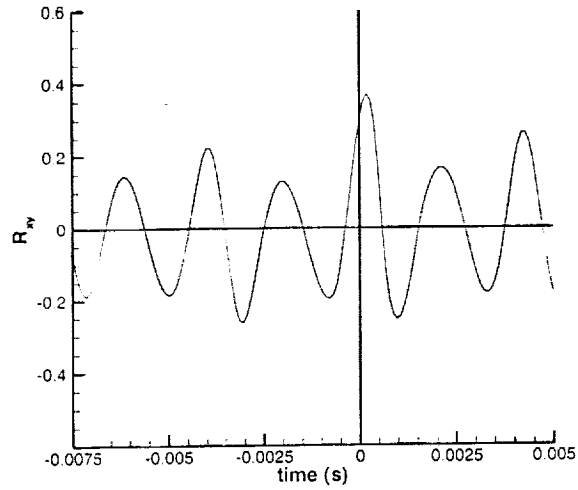
Cross-correlation analysis, using the fluctuating pressure data at the floor and rear wall, was used to assess the effects of the jet blowing on the timing of events within the cavity. The coherence and the phase lag were also examined to further quantify the changes in the character of the cavity flow.

3.4.1 Baseline

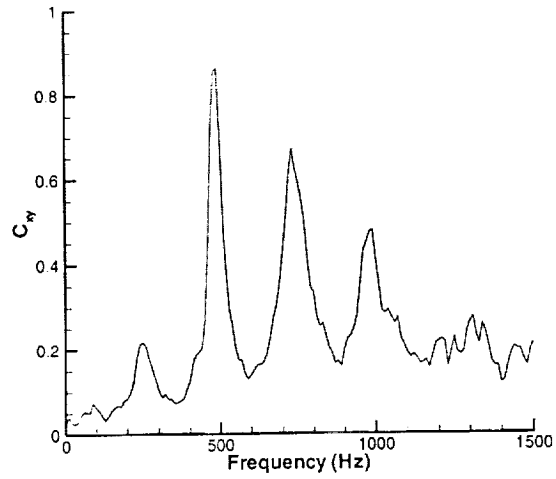
Figure 3.23 shows the cross-correlation coefficient, the coherence, and the phase angle. In the plot of the cross-correlation coefficient, the peaks with a positive time lag indicate a wave traveling from the rear wall location to the front floor location. These peaks are said to be in quadrant I and the waves are referred to as forward traveling waves. The peaks with negative time lags occur in quadrant II and denote rearward traveling waves, which are waves traveling from the front towards the rear. The convection velocity of the wave is calculated as the ratio of the distance between the two measurement locations and the time lag at the peak amplitude. The time lag of the first peak location ($\tau \approx 0.2msec$) in quadrant I corresponds to a forward wave traveling at the speed of sound. The time lag of the first peak location ($\tau = 1.9msec$) in quadrant II does not have a physical meaning, as the corresponding convection speed is faster than the freestream velocity. The next peak at $\tau=3.9msec$, which has the largest amplitude in quadrant II, corresponds to a convection velocity of $39m/s$, 55% of the freestream speed. This speed is less than the value of $k_v=0.66$ that is used in the Rossiter equation. The amplitudes of the cross-correlation coefficients are relatively low due to the large

broadband levels. In Figure 3.23b, the first four cavity modes, 246Hz , 488Hz , 722Hz , and 990Hz , can clearly be identified as they have large values of coherence. The coherence is most pronounced at the second cavity mode, and least pronounced at the first mode. The phase lag is shown in Figure 3.23c. Although the two transducers are not phase matched, we can infer details of the wave propagation. The phase shows a positive slope for frequencies less than 300Hz , and negative slopes for frequencies above 300Hz . The positive slope suggests that dominant flow is from the rear wall location to the front floor location and a negative slope the converse. Thus we can infer that the first cavity mode (246Hz) is a forward traveling acoustic wave and the higher cavity modes are rearward traveling vortical disturbances. The phase data above 1300Hz are not suited for analysis. These data contain errors due to the wrapping of values close to π and $-\pi$. As the data are ensemble averaged resulting in phase angles less than $|\pi|$, the wrapping effect is accentuated.

(a)



(b)



(c)

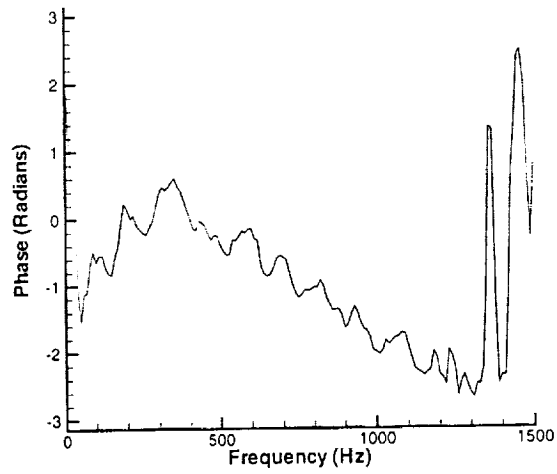


Figure 3.23: Baseline relationship between the rear and floor transducers.
a) cross-correlation b) coherence c) phase angle.

3.4.2 Steady Blowing

The effect of steady blowing is examined in Figure 3.24 through Figure 3.26. The blowing momentum coefficient is 0.001. The effect of hole size is examined in Figure 3.24. In Figure 3.24a, the location of the peaks in the cross-correlations are unchanged indicating that steady blowing has no effect on the timing of the wave propagation. The coherence shown in Figure 3.24b indicates that the coherence of the cavity modes is reduced; the effect is most pronounced with the largest hole, configuration R3. The phase angle presented in Figure 3.24c, indicate that the basic wave propagation characteristics are unaffected by steady blowing.

The effect of hole shape is shown in Figure 3.25. The timing of the forward traveling wave, quadrant I, and rearward traveling wave, in quadrant II, as inferred from the physical significant peaks are not altered. The round hole, configuration R3, is the least coherent for all cavity modes. For the long slot, configuration LS, the first and third modes have a larger coherence between the rear and floor locations. The coherence is slightly reduced at the cavity modes for the streamwise slot, configuration SS. The third mode for both slot configurations (SS and LS) has shifted from 730Hz to 710Hz. The phase angle shown in Figure 3.25c, indicates that there are no significant changes in the wave structure.

The effect of the blowing angle is shown in Figure 3.26. In Figure 3.26a for quadrant I, the time lag location of the first peak of the cross-correlation is not altered for the different blowing cases; therefore, the rearward traveling wave is propagating at the sound speed. For the forward traveling waves, quadrant II, the time lag location for the

second peak also has not been altered, hence the propagation speed is unchanged. In Figure 3.26b, blowing at 45° (RA and SSA configurations) produces a much lower coherence at the cavity resonant frequencies. For the second cavity mode, the SSA configuration has no significant coherence between the rear and floor locations. In Figure 3.26c, there is no change in the phase angle for the different blowing cases, suggesting that steady blowing does not alter the wave structure.

Steady blowing does not alter the timing of cavity events for either the forward or rearward traveling waves. The coherence amplitudes at the cavity resonant frequencies are dependent upon the hole plate configuration. The streamwise angled slot, configuration SSA, has the largest reduction for the second resonant mode. The long slot increases the coherence for the first and third modes. For all other configurations, the coherence has decreased at all cavity modes. The least reduction is produced by the small round holes, configuration R1. For all steady blowing cases, the phase angles are unaltered, which suggests that blowing does not alter the wave structure.

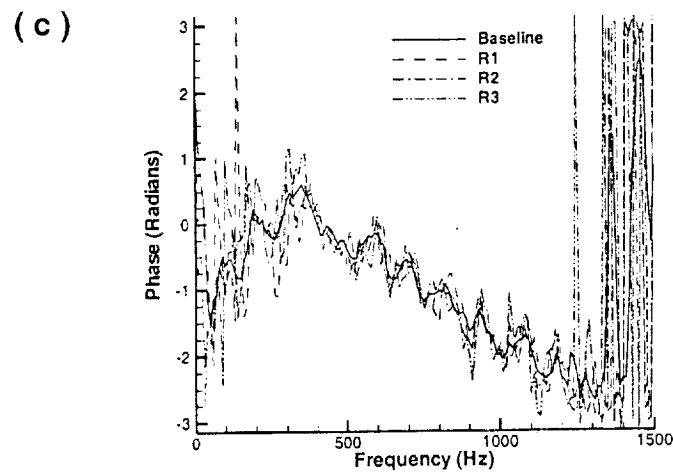
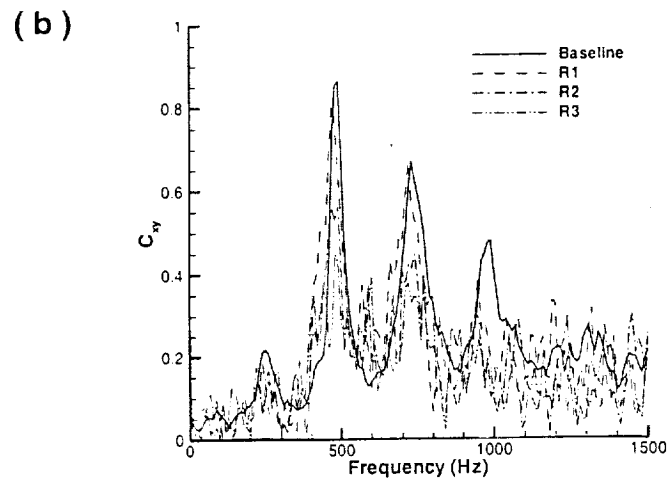
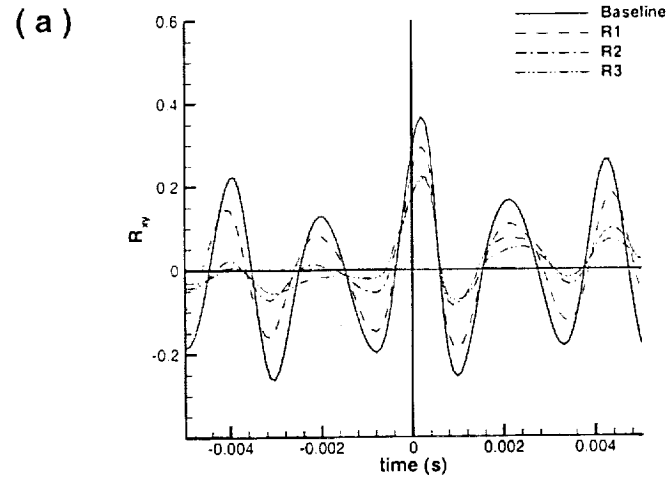


Figure 3.24: Effect of hole size on the relationship between the rear and floor transducers using steady blowing; $c_{\mu} = 0.01$.
 a) cross-correlation b) coherence c) phase angle.

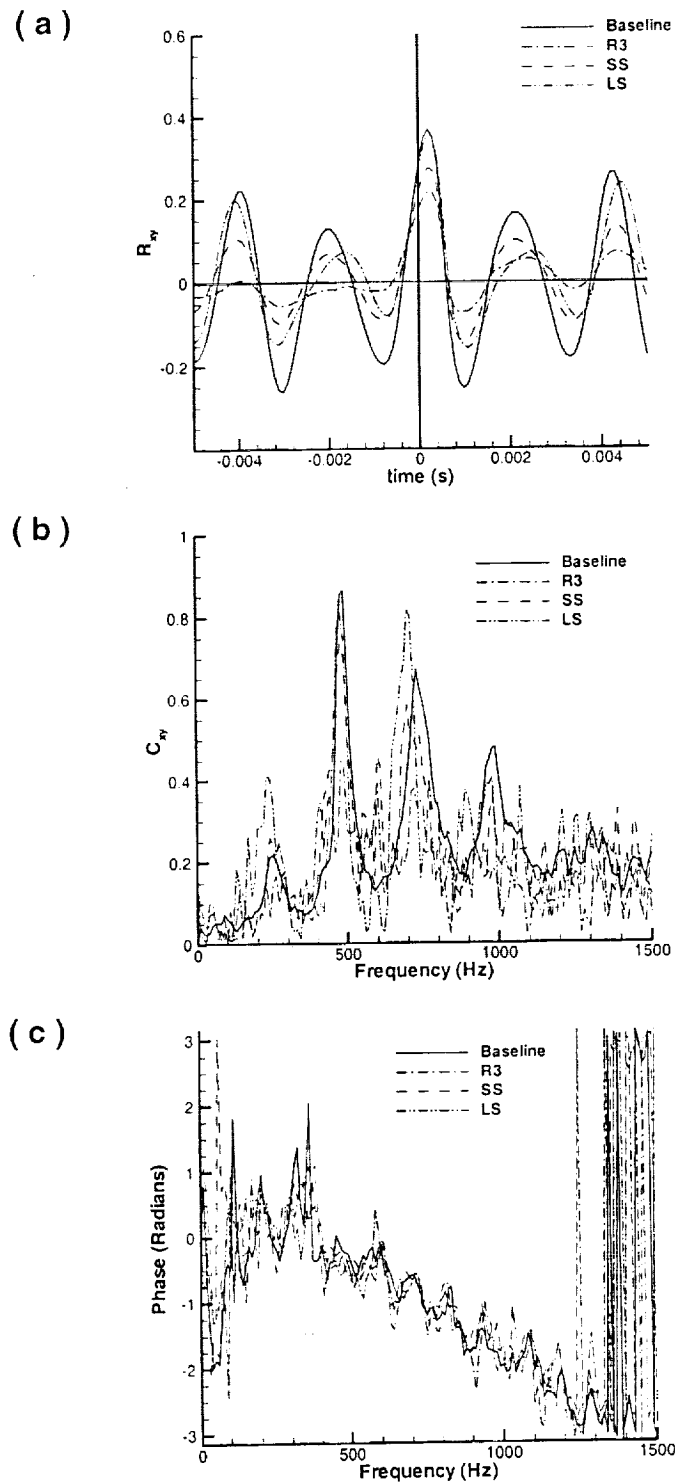


Figure 3.25: Effect of hole shape on the relationship between the rear and floor transducers using steady blowing; $c_{\mu} = 0.01$.
 a) cross-correlation b) coherence c) phase angle.

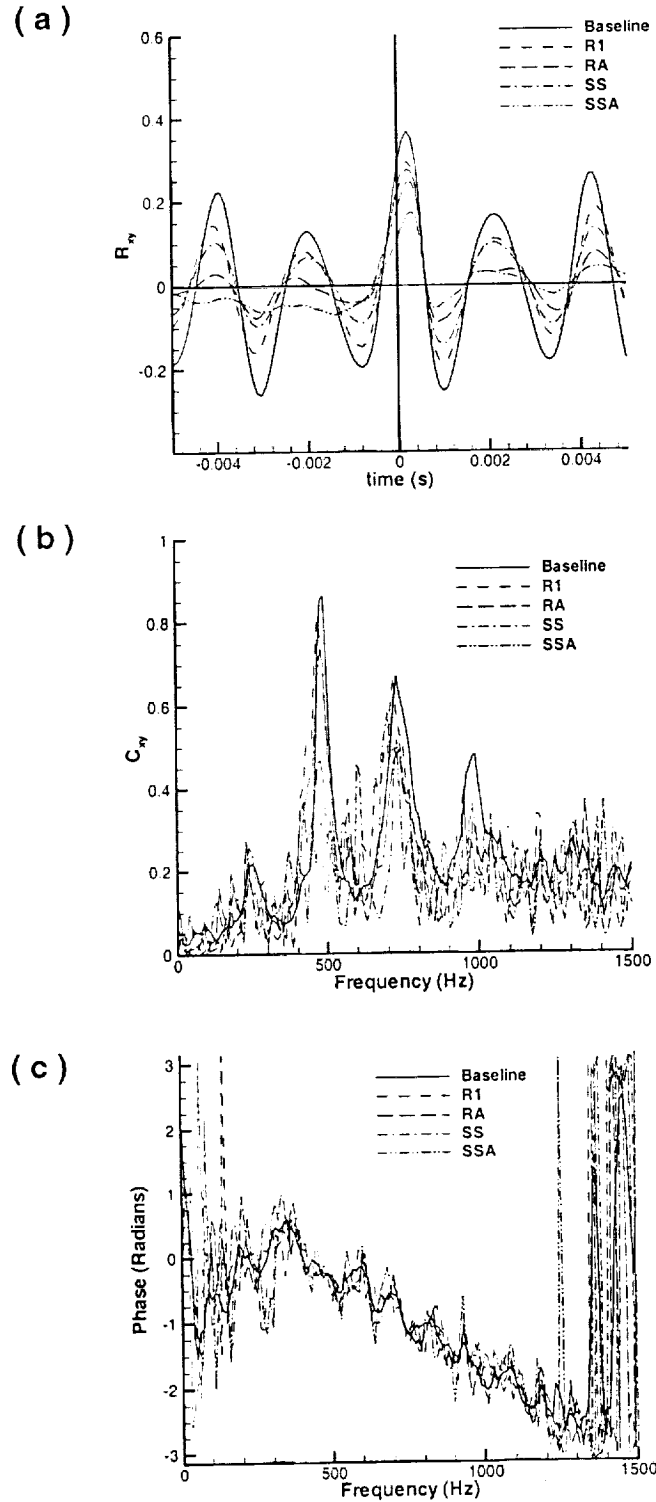


Figure 3.26: Effect of blowing angle on the relationship between the rear and floor transducers using steady blowing; $c_{\mu} = 0.01$.
 a) cross-correlation b) coherence c) phase angle.

3.4.3 Zero Net Mass Oscillatory Blowing

The effect of near-zero oscillatory blowing is shown in Figure 3.27 through Figure 3.29. For all cases, the unsteady momentum coefficient is $\langle c_{\mu} \rangle = 1 \times 10^{-5}$ and forcing frequency is $f_f = 550 \text{ Hz}$. The effect of hole size is examined in Figure 3.27. In Figure 3.27a, the cross-correlation for the three round hole configurations are compared to the baseline. In quadrant I, the location of the first peak is unchanged compared to the baseline, indicating that the rearward traveling acoustic wave is moving at the speed of sound. The forward traveling wave, denoted by the peak in quadrant II, however, changes with blowing. With configuration R3, the time lag at the second peak location is $\tau = 3.3 \text{ msec}$ which corresponds to a propagation speed at 66% of the freestream velocity. In Figure 3.27b, the forcing frequency and its higher harmonics have a high coherence value with the configurations R2 and R3, but for the small sized hole, configuration R1, there is little change in the coherence. The larger hole configuration R3, significantly reduces the coherence at the second, third, and fourth modes indicating that the oscillatory blowing control is effective in disrupting the feedback loop. In Figure 3.27c, the distribution of phase shows no significant changes compared to the baseline for the three blowing cases. This result suggests that the wave structure is unaltered.

The effect of hole shape is shown in Figure 3.28. The results show no change in the propagation of the acoustic wave, and that the vortical disturbances are now convected at 66% of the freestream speed. In Figure 3.28b, the level of the coherence at the second cavity mode, 490 Hz , is significantly reduced for all three hole configurations.

The long slot, configuration LS, also has the lowest coherence level at the third mode, 730Hz . In Figure 3.28c, it is seen that blowing does not modify the wave structure.

The effect of blowing angle is shown in Figure 3.29. The blowing at 45° has an effect on the propagation of the forward traveling waves, Figure 3.29a. The coherence for the second mode is reduced slightly, and the angled round hole, configuration RA, has a lower coherence than the normal blowing round hole, configuration R1. The opposite is true for the slot configuration in which the blowing at 45° yields a lower coherence Figure 3.29b. The phase angle, Figure 3.29c, shows no significant changes compared to the baseline case.

When effective, we observe that near-zero, net-mass oscillatory blowing changes the propagation of the vortical waves. The blowing control has no effect on the propagation of the acoustic waves and the basic wave structure in the cavity flow is not modified.

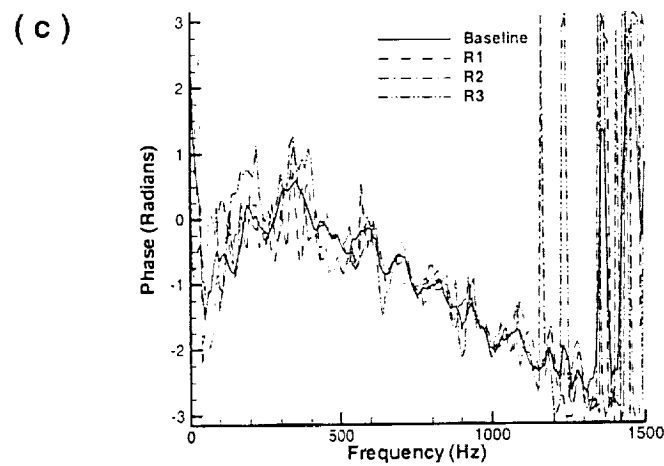
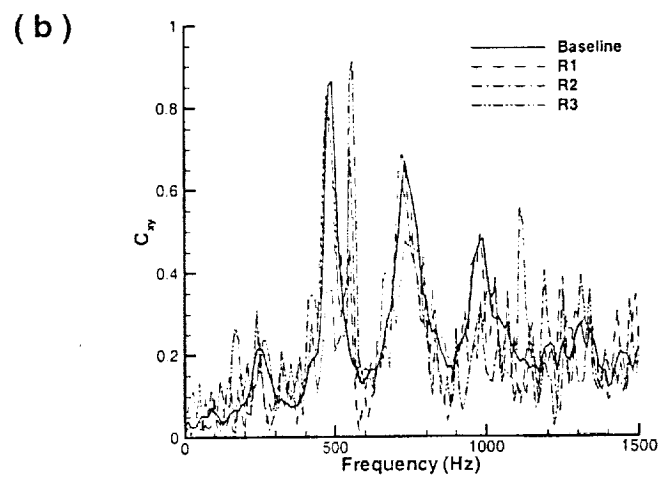
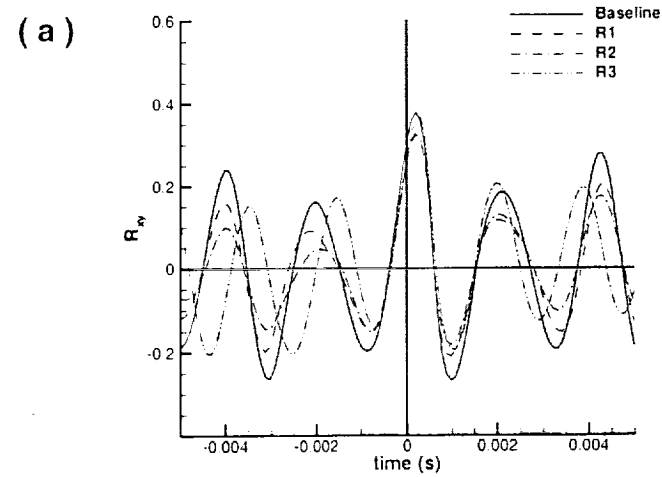


Figure 3.27: Effect of hole size on the relationship between the rear and floor transducers using oscillatory blowing; $f_f = 550\text{Hz}$, $\langle c_\mu \rangle = 1 \times 10^{-5}$.
 a) cross-correlation b) coherence c) phase angle.

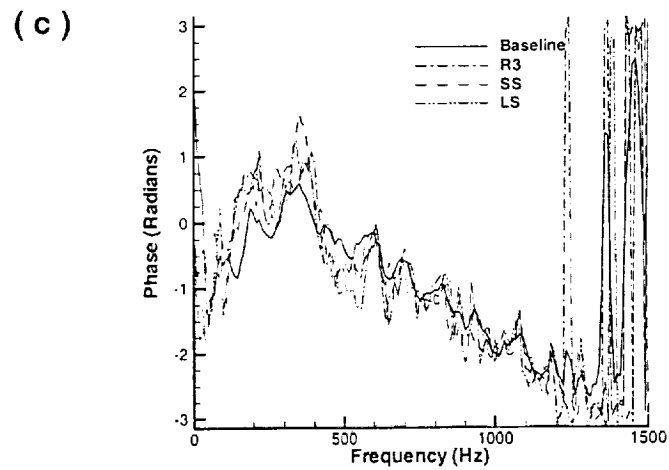
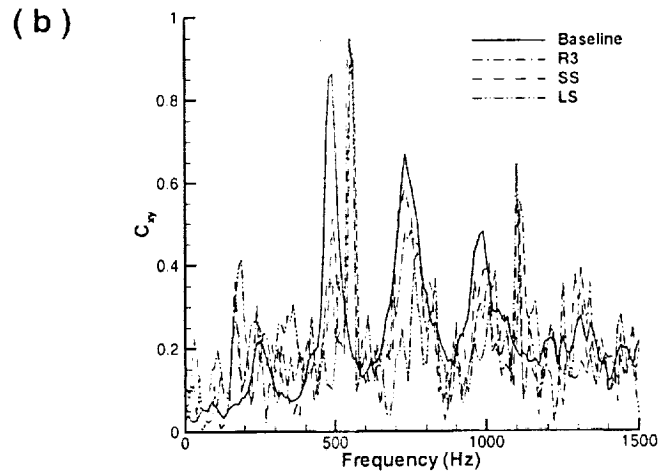
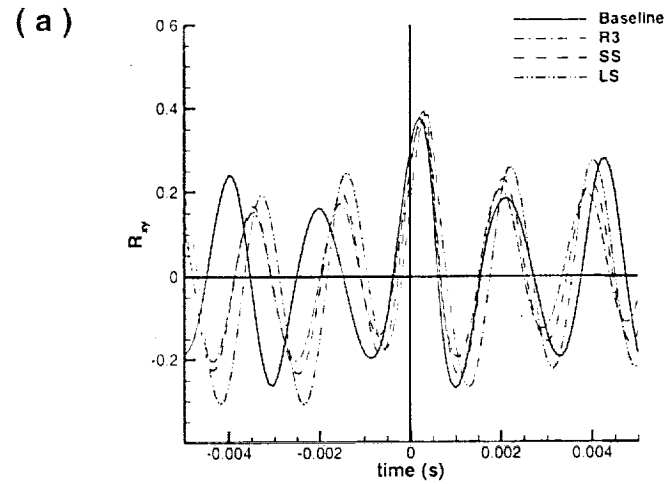
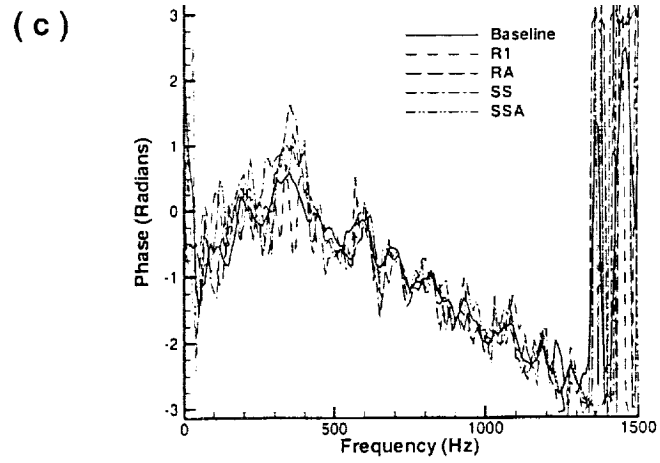
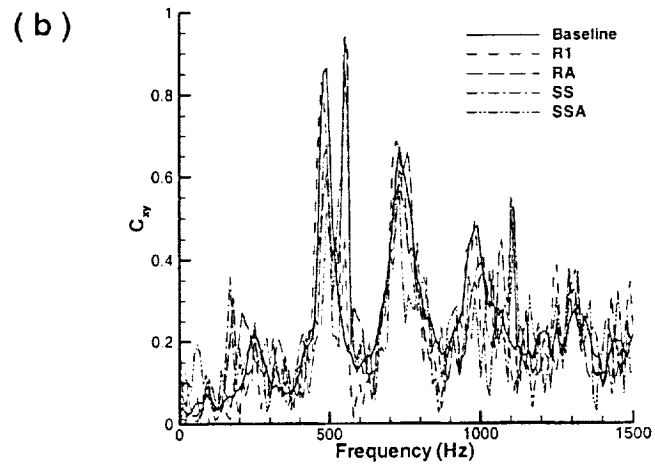
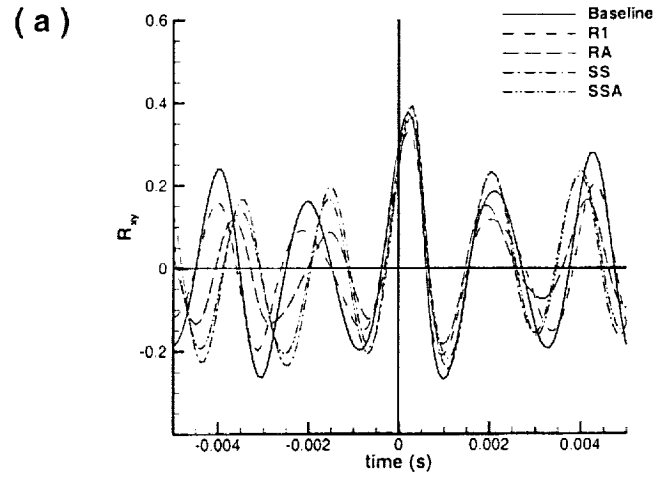


Figure 3.28: Effect of hole shape on the relationship between the rear and floor transducers using oscillatory blowing; $f_f = 550\text{Hz}$, $\langle c_\mu \rangle = 1 \times 10^{-5}$.
 a) cross-correlation b) coherence c) phase angle.



**Figure 3.29: Effect of blowing angle on the relationship between the rear and floor transducers using oscillatory blowing; $f_f = 550Hz$, $\langle c_\mu \rangle = 1 \times 10^{-5}$.
a) cross-correlation b) coherence c) phase angle.**

3.5 Bispectral Analysis

Bispectral analysis quantifies the quadratic phase coupling between frequency pairs. The quadratic phase coupling is important in fluid dynamics due to the quadratic $\bar{u} \cdot \nabla \bar{u}$ terms in the Navier-Stokes equation. Furthermore, nonlinear phase interactions are a mechanism by which energy can transfer between waves or modes. In turbulent shear layers and wakes, the energy transfer is usually accomplished through sum and difference components of the most unstable modes^{35, 42}.

Due to the symmetry properties of the auto and the cross bicoherence, the data plotted in the shaded region of Figure 3.30 is unique. Bicoherence values equal to one indicate that the frequency pairs are perfectly phase coupled, values less than one indicate that the pairs are weakly coupled, and values equal to zero indicate that they are not coupled. In the subsequent analysis, f_1 , f_2 , f_3 , and f_4 refer to the first (240Hz), second (480Hz), third (720Hz), and fourth (980Hz) cavity modes, respectively.

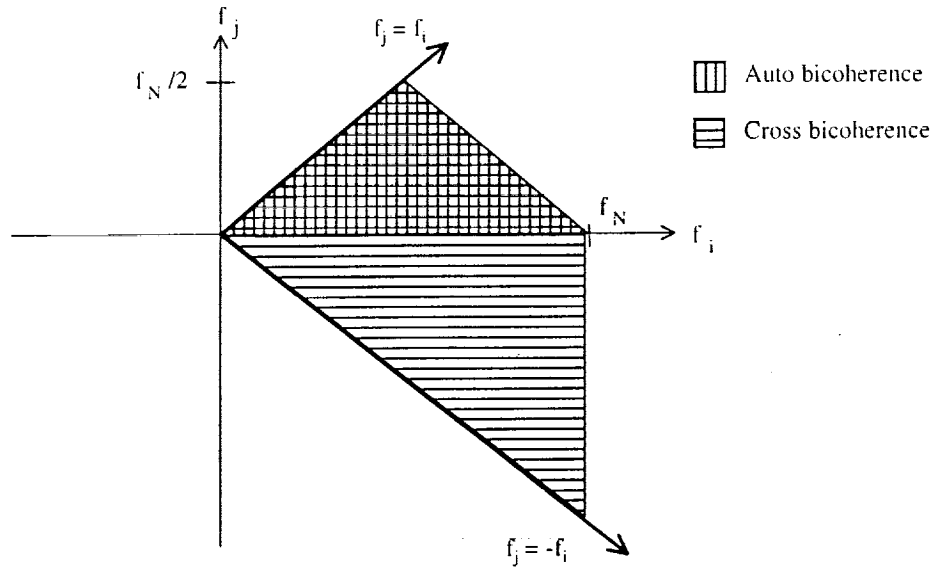


Figure 3.30: Symmetry properties of auto and cross bicoherence.

3.5.1 Baseline

The auto-bicoherence of the baseline cavity flow is shown in Figure 3.31. The range of frequencies for which the bicoherence values are plotted is 0Hz to 1500Hz . For frequencies above 1500Hz , the bicoherence levels are negligible. Overall, the bicoherence levels at the floor location are much higher than at the rear; this may be attributed to the larger amplitudes of the cavity modes relative to the broadband levels. At the rear wall location, the most elevated bicoherence levels at (f_2, f_2) indicate that the second cavity mode is phase coupled to its harmonic ($f_i + f_j = 960\text{Hz}$). Additional nonlinear interactions are observed that lie along horizontal and vertical lines, as well as along the diagonal lines $f_i + f_j = \text{constant}$. Along the vertical line (f_2, f_j) the significant nonlinear interaction is of the second cavity mode with a low frequency ($f_j = 40\text{Hz}$); this low frequency interaction suggests that nonlinear interactions occur across the broad

sidebands of the second cavity mode. Another nonlinear interaction is observed along the vertical line (f_2, f_j) , and this interaction is also located on the diagonal line $f_2 + f_j = 620Hz$. The peaks at $f = 140Hz$ and $f = 620Hz$ are observed in the spectra. Along the diagonal line a nonlinear interaction is observed at $(f_i = 400Hz, f_j = 220Hz)$. Additional nonlinear interactions are observed at $(f_i = 780Hz, f_j = 270Hz)$ and $(f_i = 920Hz, f_j = 130Hz)$ and lie along the diagonal line $f_i + f_j = 1050Hz$.

At the floor location, the spectra show multiple peaks that are associated with several nonlinear interactions observed in the plot of bicoherence, Figure 3.31b. The (f_2, f_2) nonlinear interaction is the most pronounced. The second significant bicoherence peak at (f_1, f_1) suggests that the first cavity mode is phase coupled with the second cavity mode $(f_i + f_j = 480Hz)$. Another significant peak of elevated bicoherence is observed along the vertical line (f_2, f_j) and, suggests that the second cavity mode is weakly phase coupled with the first cavity mode to generate the third cavity mode $(f_i + f_j = 720Hz)$. The spectra in Figure 3.3, shows additional peaks near the first and third modes at $244Hz$ and $732Hz$. Due to the limited resolution of the bicoherence, and since true cavity modes are independent of one another, these peaks instead of the cavity modes are produced by the aforementioned interactions with the second mode. The low bicoherence level along the horizontal line (f_i, f_2) indicates that the second cavity mode is interacting with a non-resonant frequency $(f_j = 620Hz)$ to produce an additional nonlinear interaction mode. These nonlinear interactions are identifiable in the spectra, Figure 3.3.

The cross-bicoherence of the baseline cavity flow is shown in Figure 3.32. The most elevated level the cross-bicoherence occurs at $(2f_2, -f_2)$ and a significant peak is also

seen at (f_2, f_2) . Additional peaks are observed along the diagonal line, $f_j = f_i - f_2$. It is thus evident that the second cavity mode drives the nonlinear interactions in the baseline cavity flow.

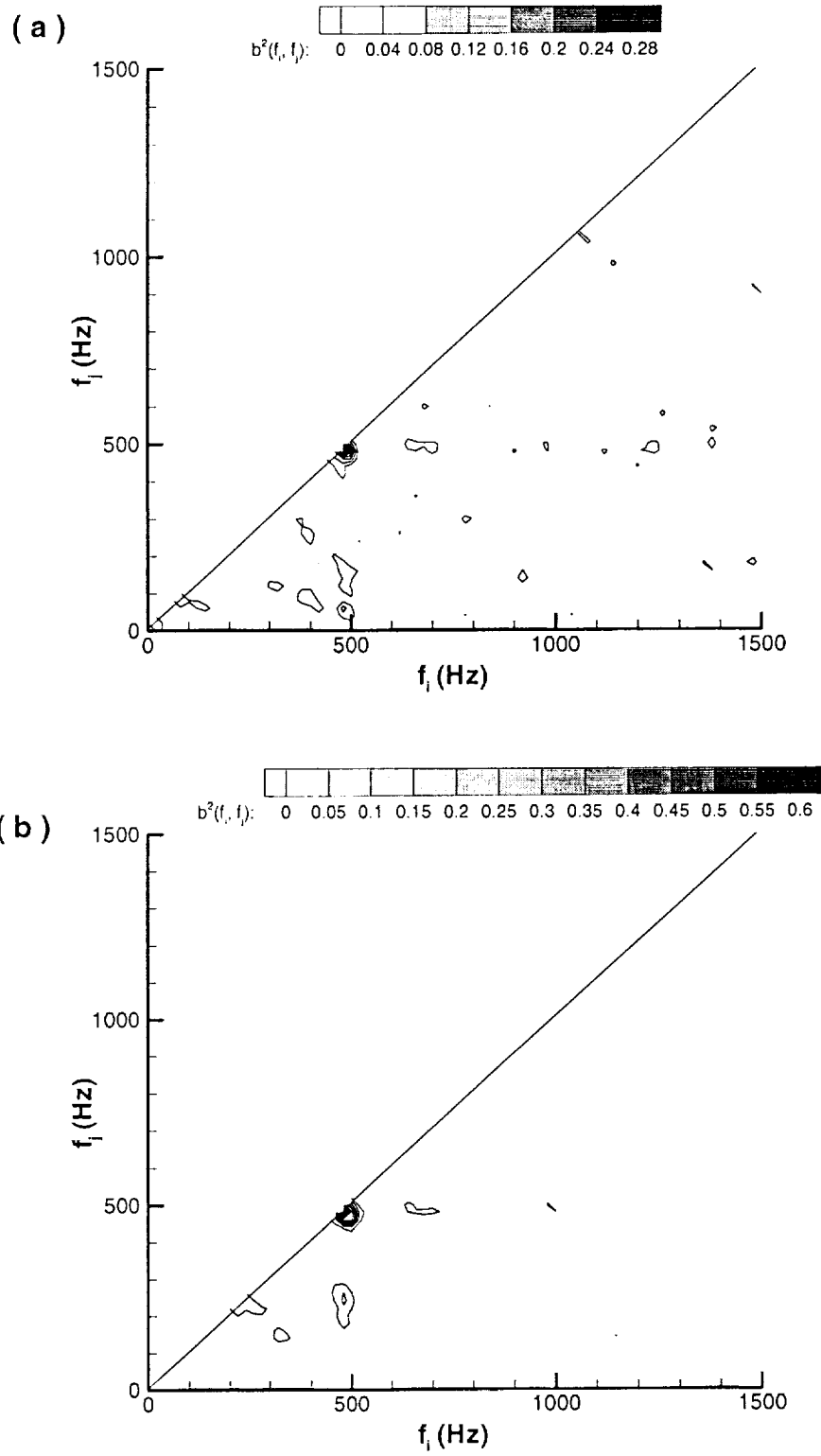


Figure 3.31: Bicoherence of the baseline data. a) Rear b) floor locations.

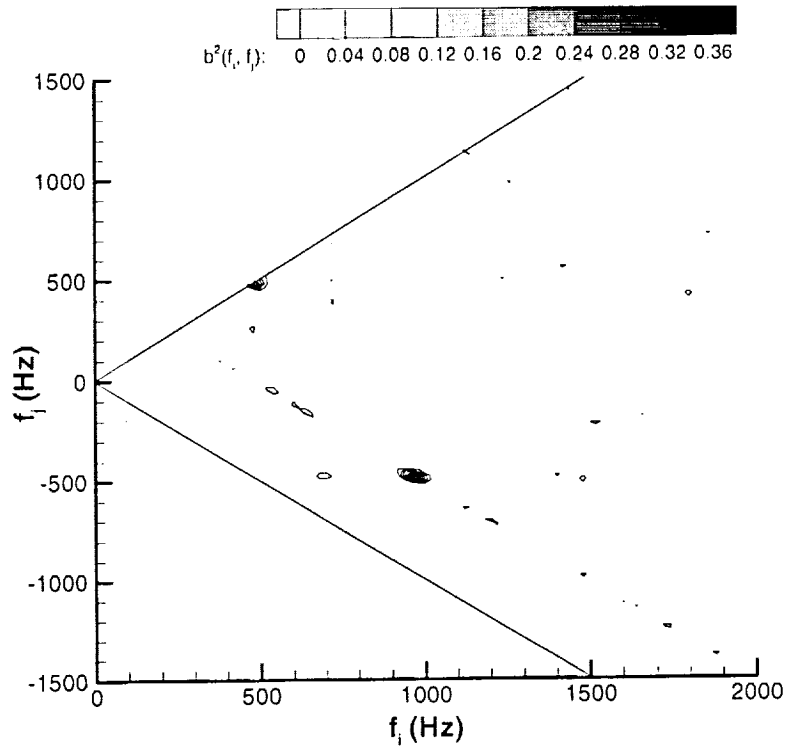


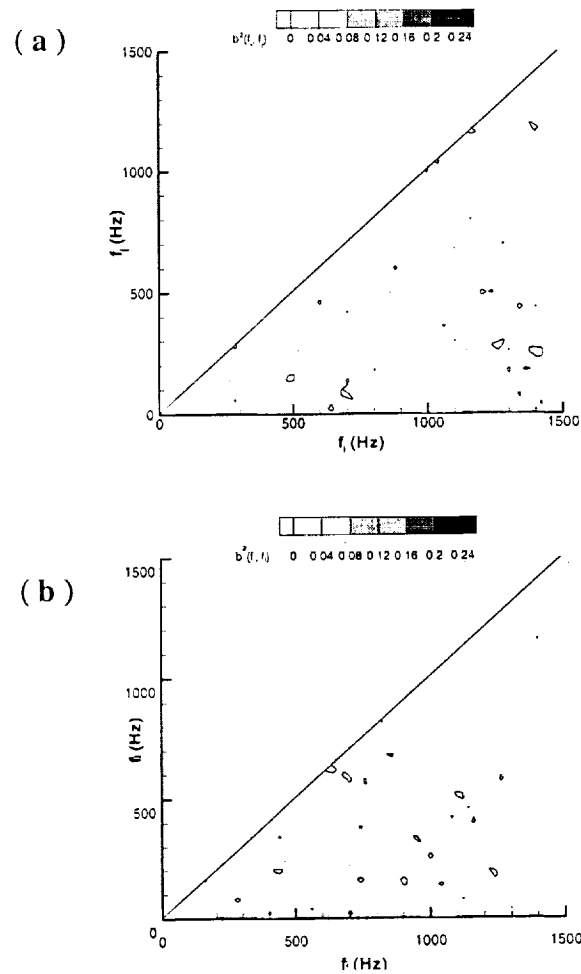
Figure 3.32: Baseline Cross bicoherence. Rear and floor locations.

3.5.2 Steady Blowing

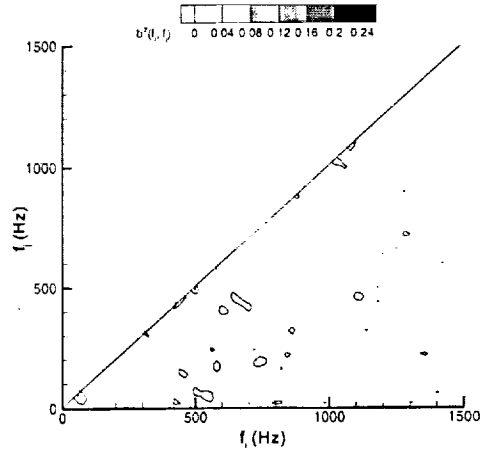
The effect of steady blowing is examined in the auto-bicoherence presented in Figure 3.33 and Figure 3.34 and the cross bicoherence presented in Figure 3.35. The momentum coefficient is $c_\mu = 0.01$. At the rear and floor locations it is seen that the steady blowing disrupts the nonlinear interactions arising from the second mode for all plate configurations with the exception of the small round hole configuration, configuration R1 at the floor location, and the long slot, configuration LS. The strength of the interaction is weaker in the configuration R1 compared with the baseline case; for

the configuration LS the nonlinear interactions observed in the baseline cavity flow are not weakened.

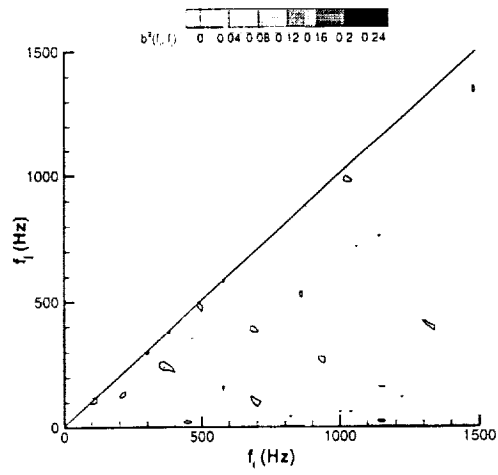
The spectra presented in Figure 3.7 confirm that the configuration LS is the least effective in suppressing the second cavity mode. A comparison of the bicoherence with the results for the baseline cavity flow also shows that the LS configuration is the least effective in modifying the cavity flow. The cross-bicoherence is presented in Figure 3.35. The data show that the nonlinear interactions driven by the second cavity mode remain significant with the configuration LS, whereas the configurations with blowing at 45° are the most effective in suppressing the nonlinear interactions.



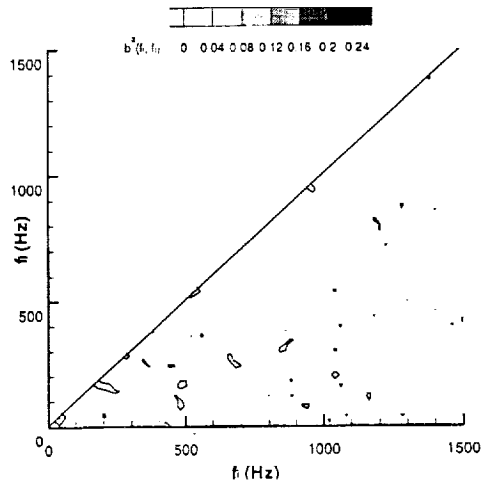
(c)



(d)



(e)



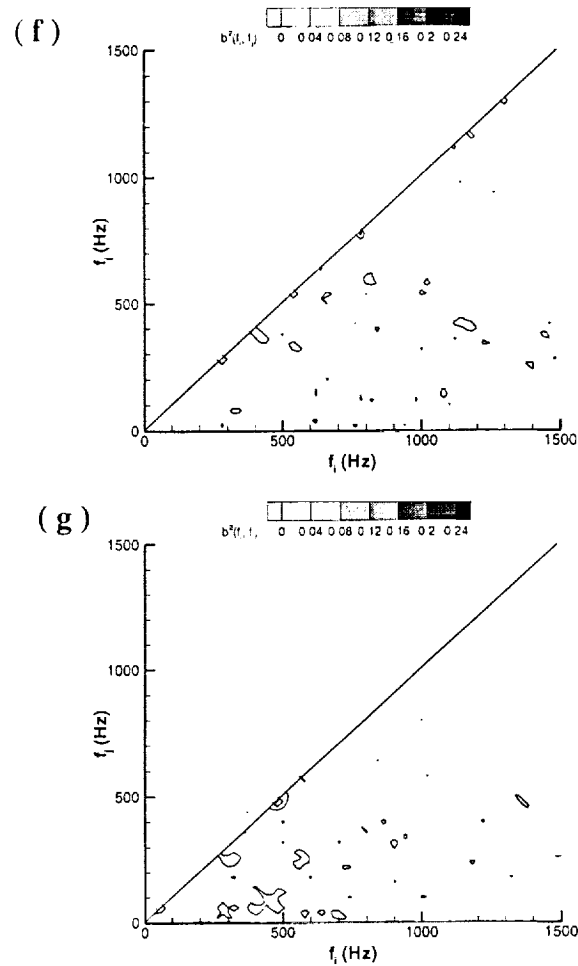
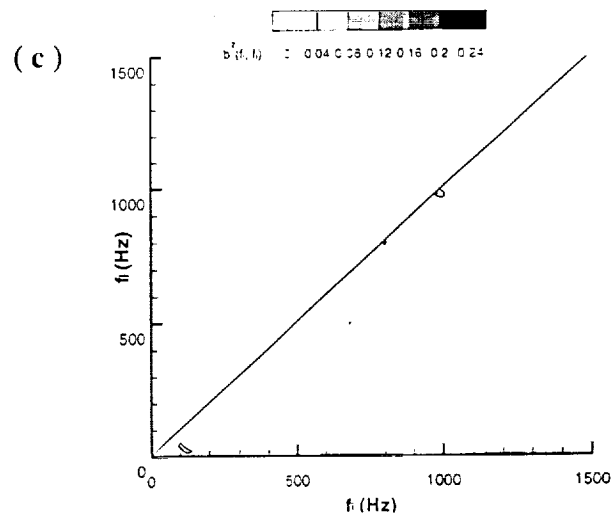
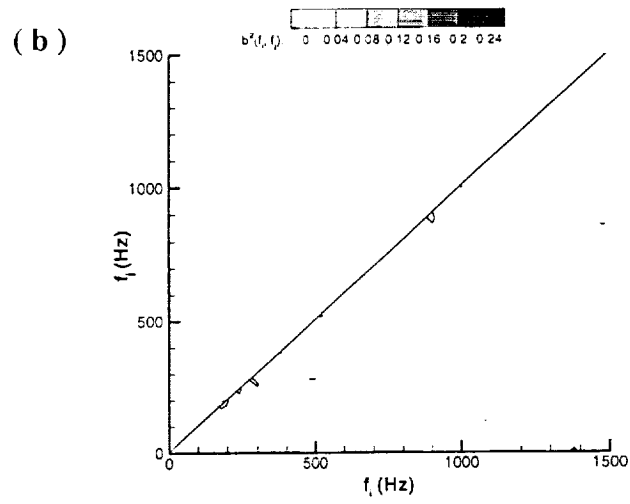
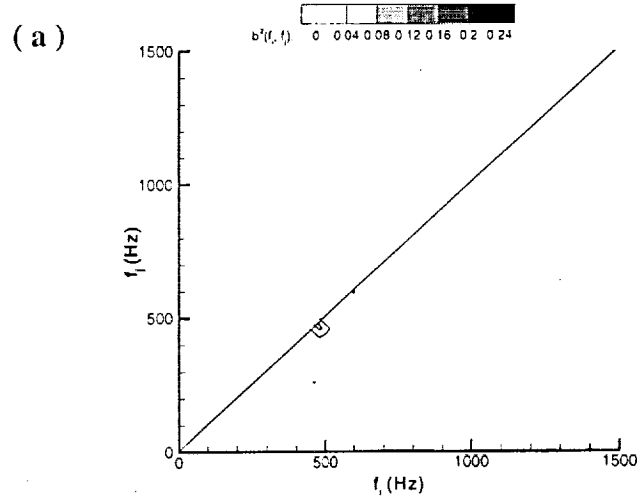
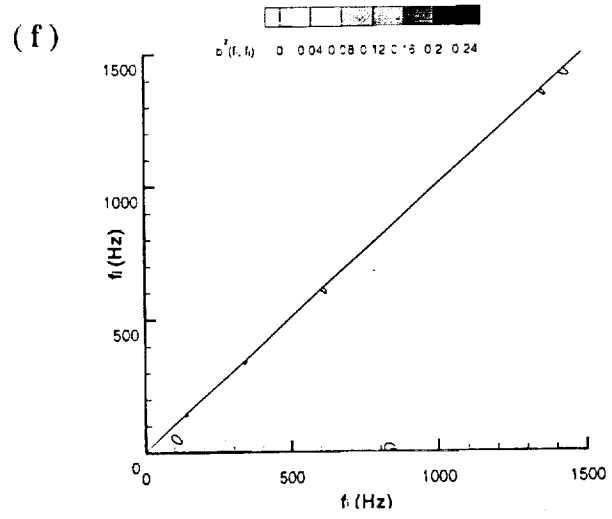
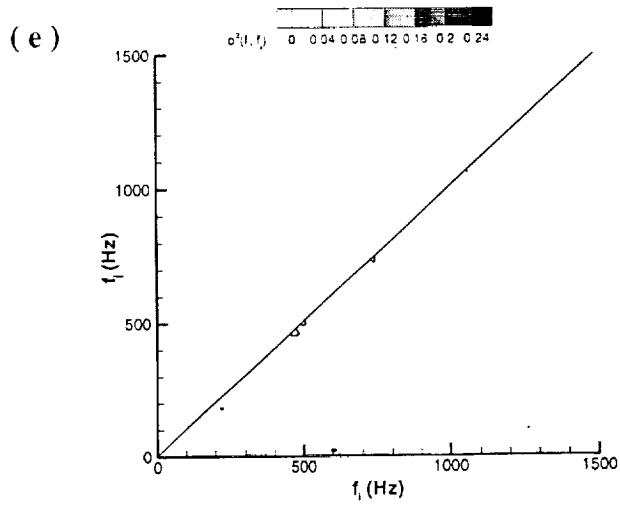
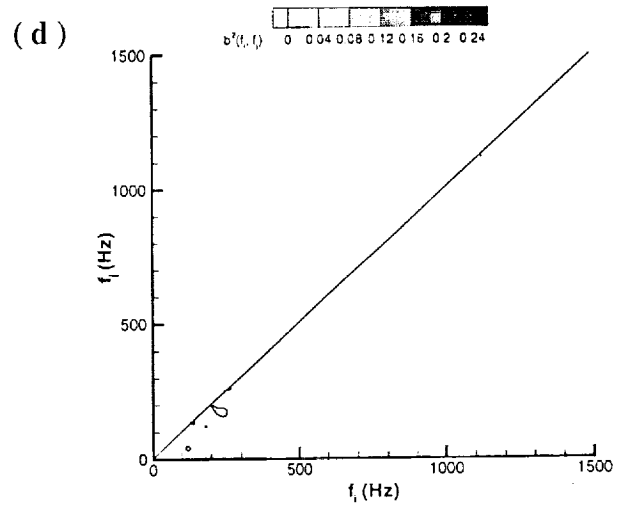


Figure 3.33: Auto bicoherence for steady blowing: rear wall location.
 a) configuration R1, b) configuration R2, c) configuration R3, d) configuration RA,
 e) configuration SS, f) configuration SSA, g) configuration LS.





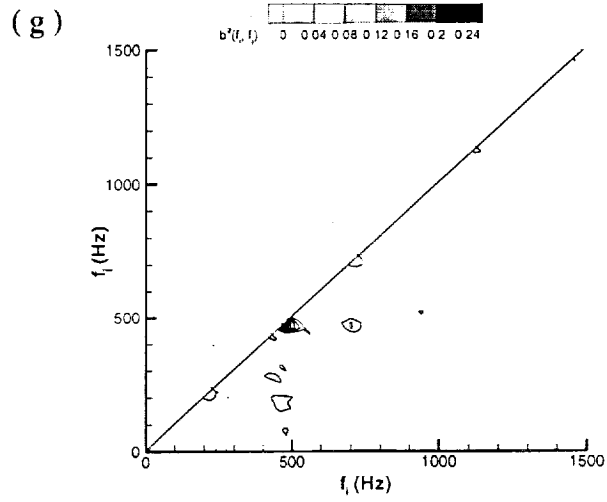
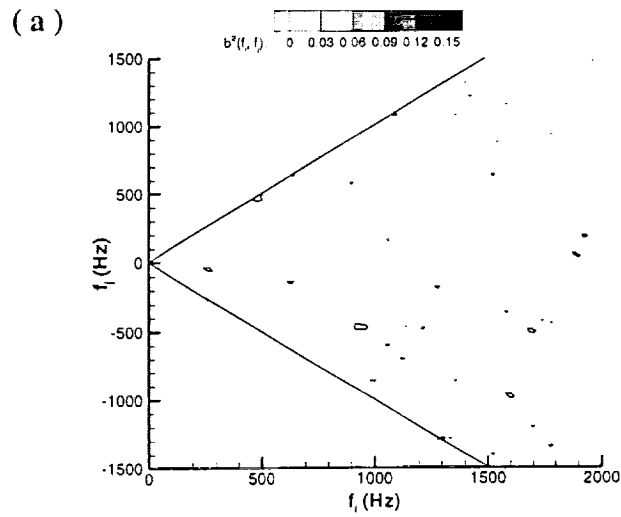
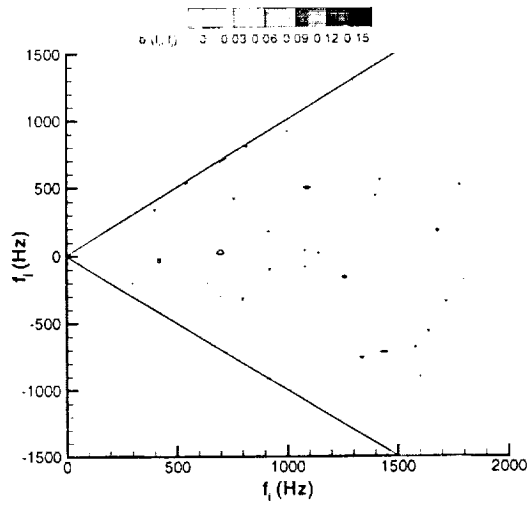


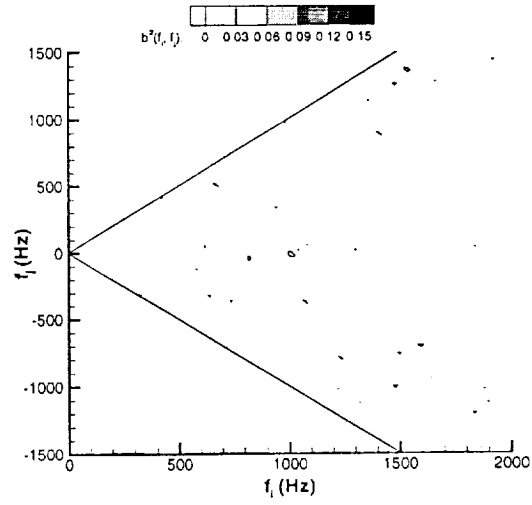
Figure 3.34: Auto bicoherence for steady blowing: front floor location.
 a) configuration R1, b) configuration R2, c) configuration R3, d) configuration RA,
 e) configuration SS, f) configuration SSA, g) configuration LS.



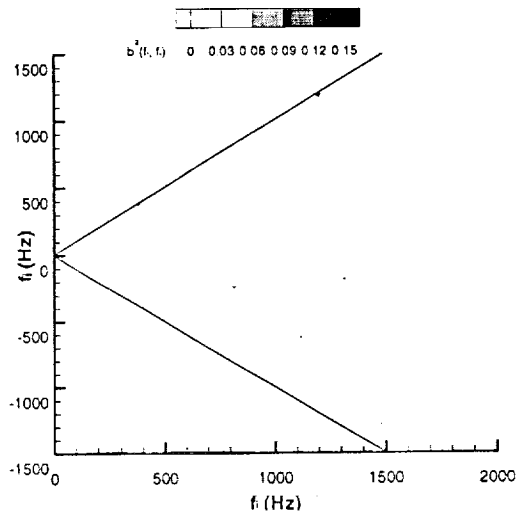
(b)



(c)



(d)



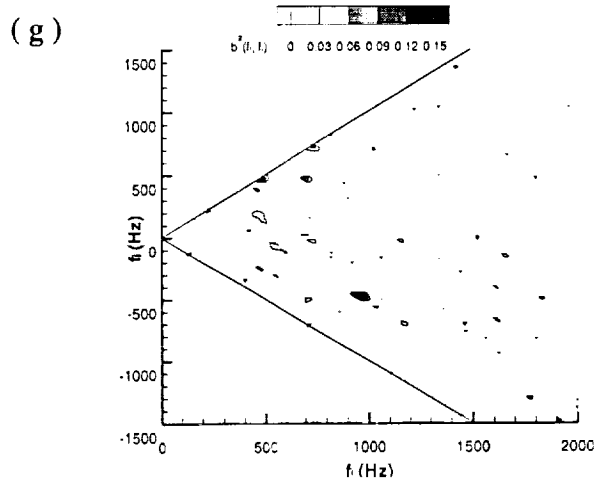
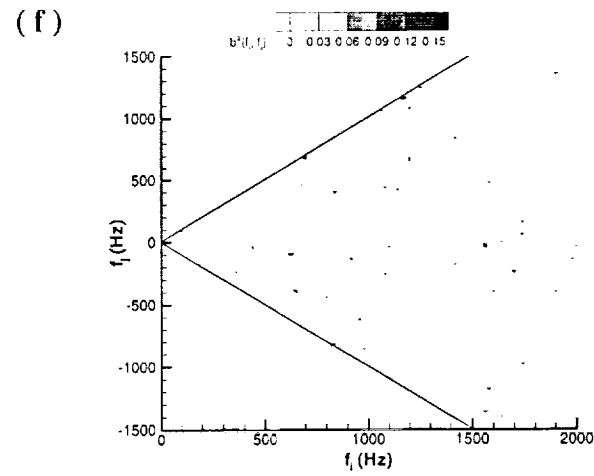
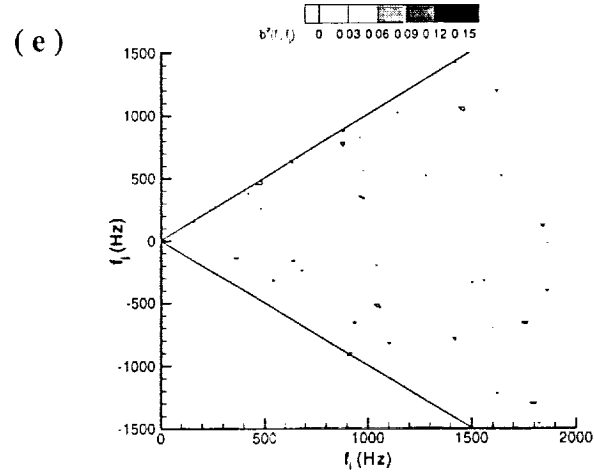
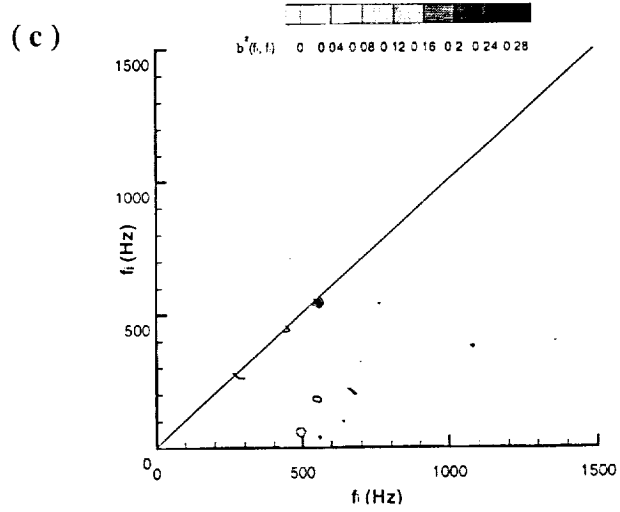
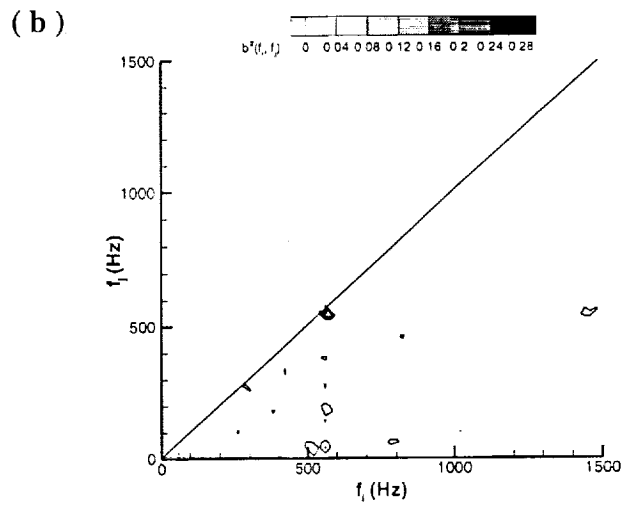
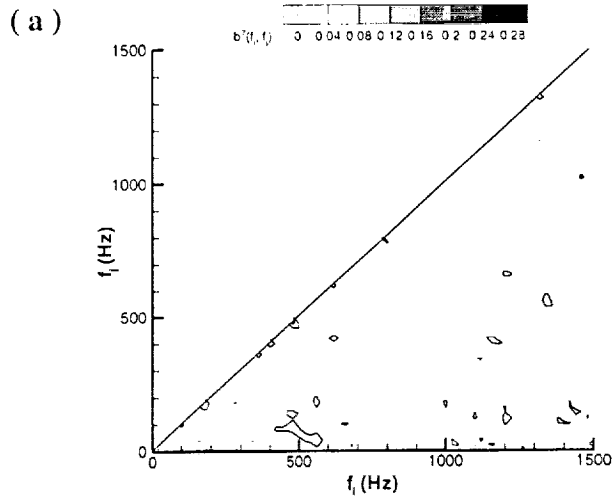


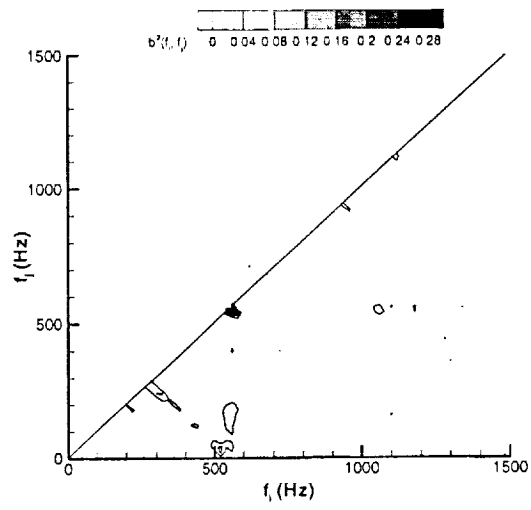
Figure 3.35: Cross-bicoherence using steady blowing: Rear and floor locations.
 a) configuration R1, b) configuration R2, c) configuration R3, d) configuration RA,
 e) configuration SS, f) configuration SSA, g) configuration LS.

3.5.3 Zero Net Mass Oscillatory Blowing

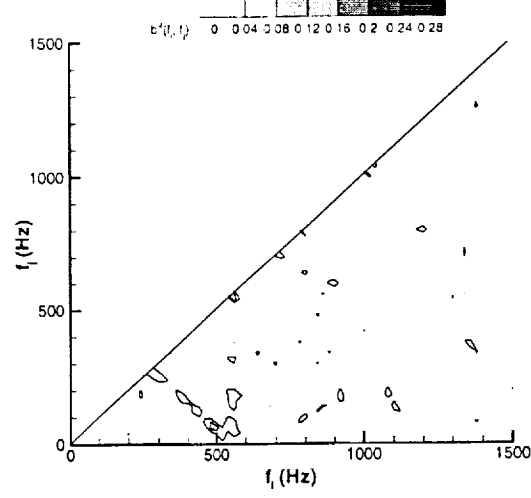
The auto-bicoherence and cross-bicoherence is shown in Figure 3.36, Figure 3.37, and Figure 3.38. The unsteady momentum coefficient is $\langle c_{\mu} \rangle = 1 \times 10^{-5}$ and the forcing frequency is 550Hz . The bicoherence results at the rear wall, Figure 3.36, show that the forcing of the oscillatory blowing generates nonlinear interactions that are now the dominant feature of the cavity flow. The most elevated bicoherence levels occur at $(550\text{Hz}, 550\text{Hz})$, and additional nonlinear interactions are observed along the vertical line $(550\text{Hz}, f_j)$, the horizontal line $(f_i, 550\text{Hz})$, and the diagonal line $f_i + f_j = 550\text{Hz}$. These nonlinear interactions are most pronounced in the cases where the oscillatory blowing is most effective, namely the configurations R3, RA, SS and LS. At the floor, Figure 3.37, the bicoherence results also show that the nonlinear interactions generated by the forcing are the dominant feature of the cavity flow, and that the oscillatory blowing is effective in suppressing the second cavity mode. The cross-bicoherence results are presented in Figure 3.38, and they show that the configurations R3, RA, SS, SSA and LS are dominated by nonlinear interactions of the forcing frequency; in particular elevated levels of bicoherence are observed at $(550\text{Hz}, 550\text{Hz})$, and along the diagonal line $f_j + f_i = -f_2$. In the cases of the configurations R1 and R2, where the oscillatory blowing the second cavity mode nonlinear interactions remain dominant.



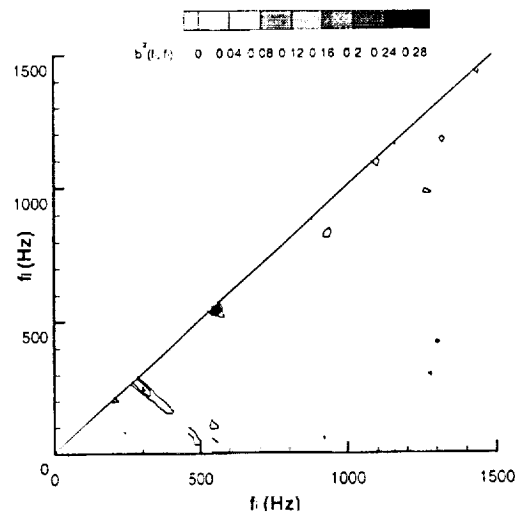
(d)



(e)



(f)



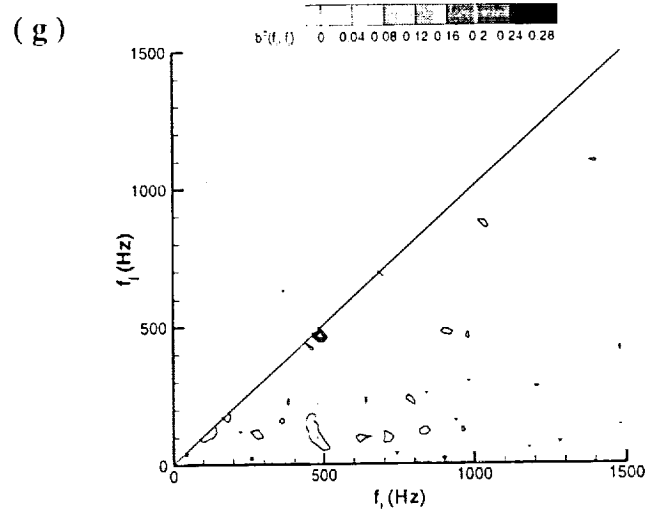
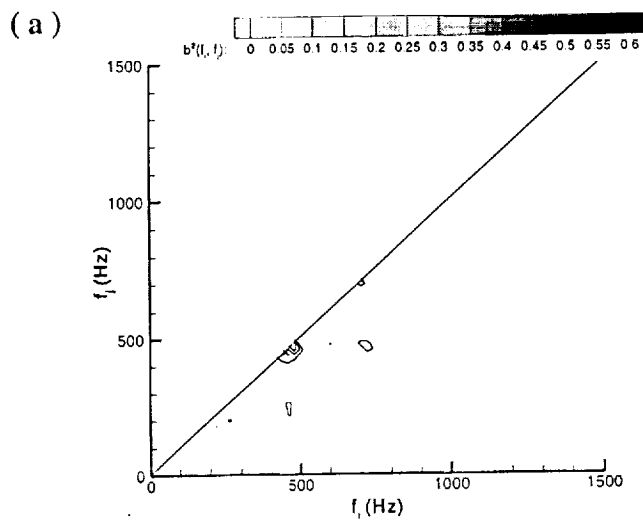
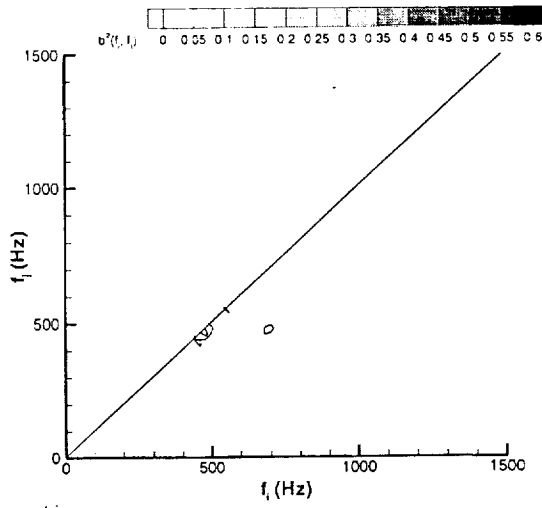


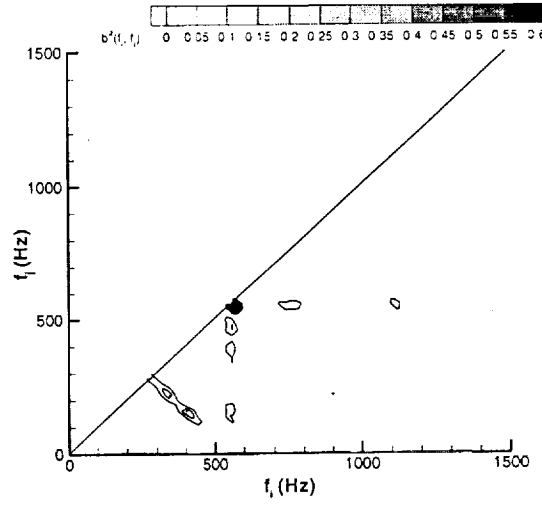
Figure 3.36: Auto-bicoherence using oscillatory blowing: Rear location.
 a) configuration R1, b) configuration R2, c) configuration R3, d) configuration RA,
 e) configuration SS, f) configuration SSA, g) configuration LS.



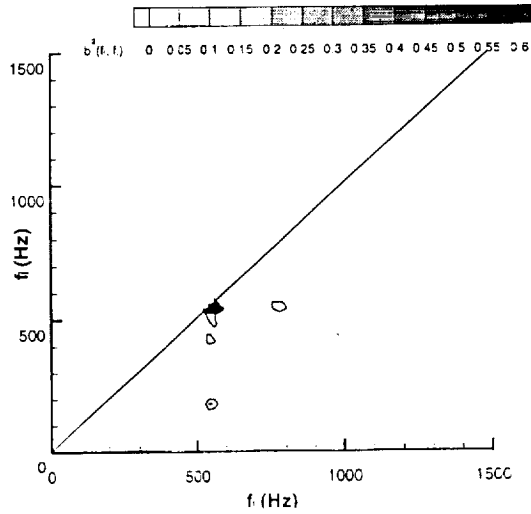
(b)



(c)



(d)



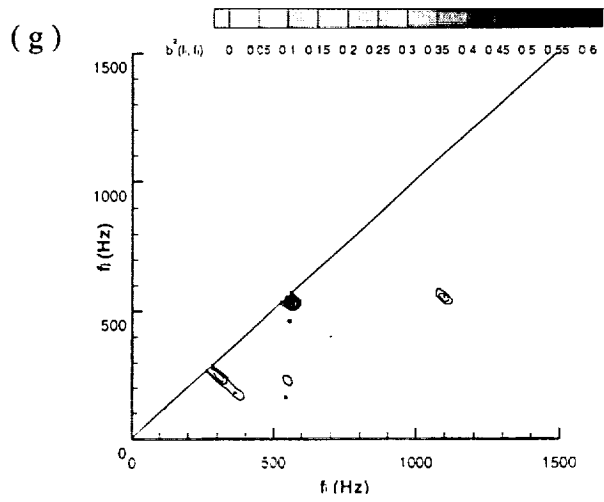
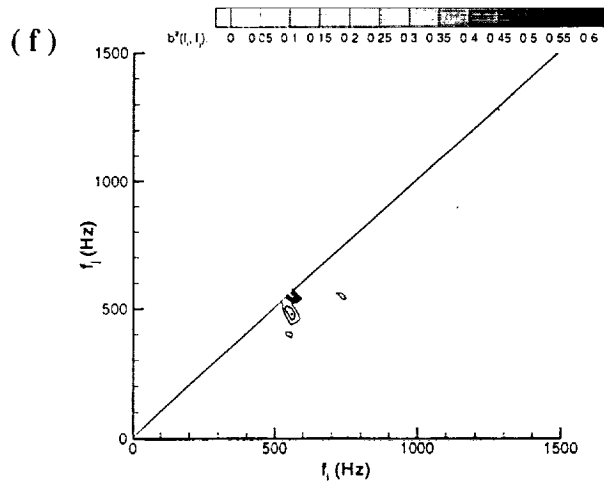
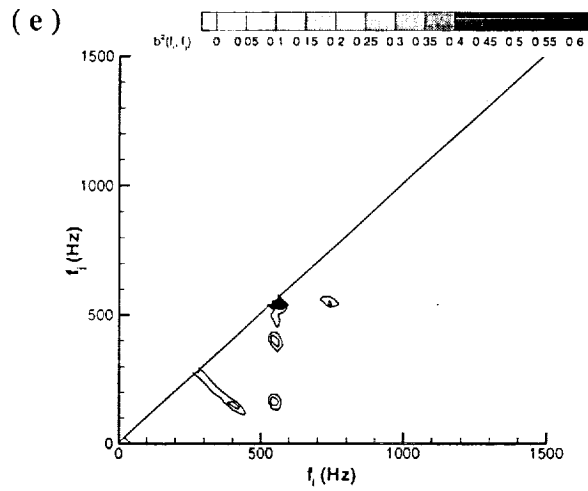
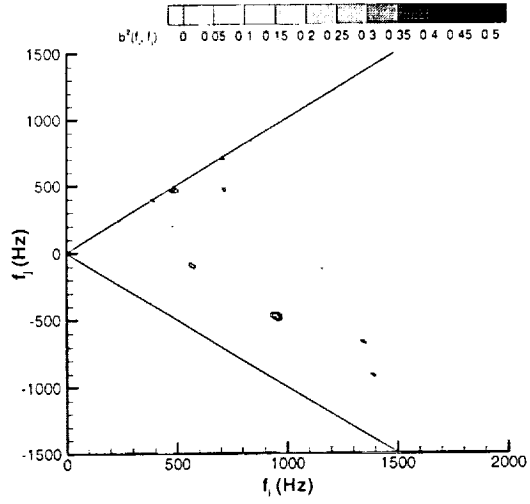
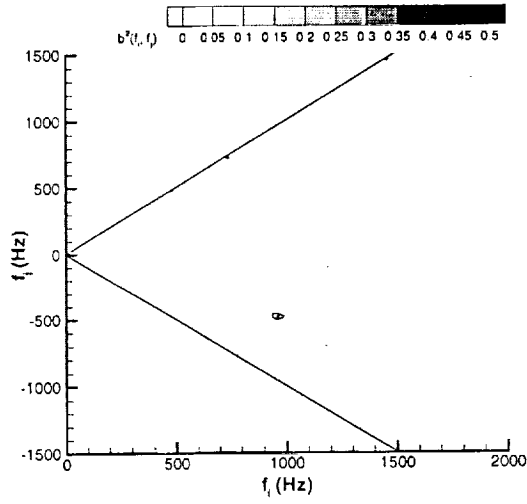


Figure 3.37: Auto-bicoherence using oscillatory blowing: Floor location.
a) configuration R1, b) configuration R2, c) configuration R3, d) configuration RA,
e) configuration SS, f) configuration SSA, g) configuration LS.

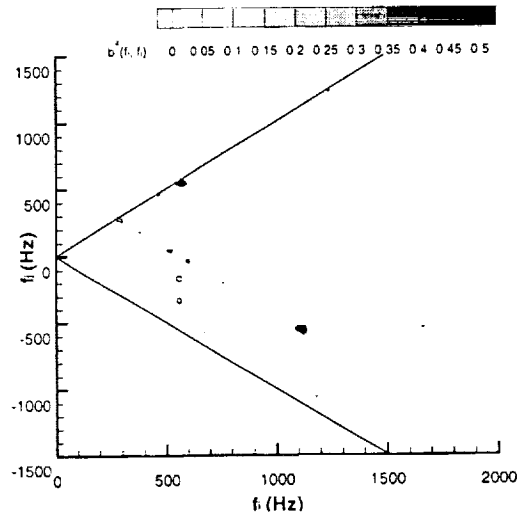
(a)



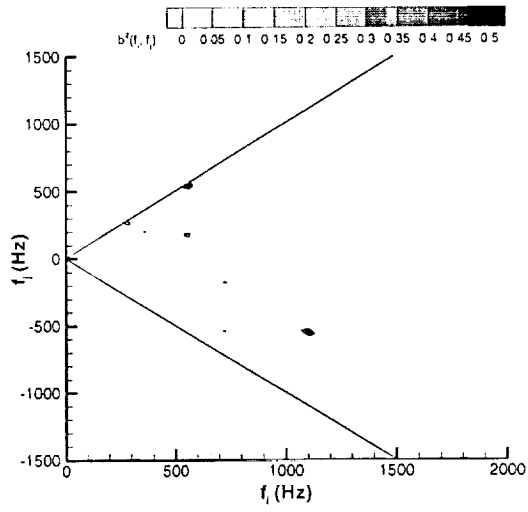
(b)



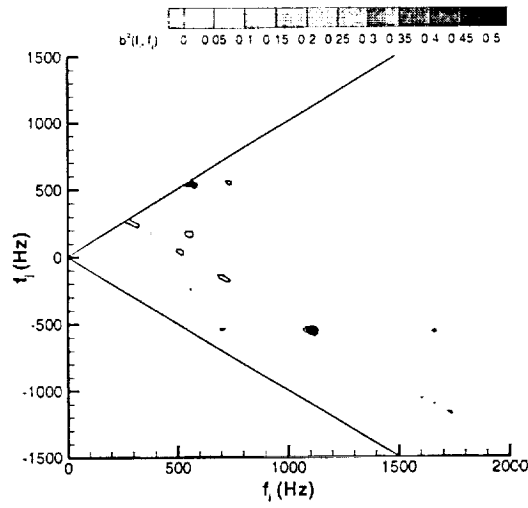
(c)



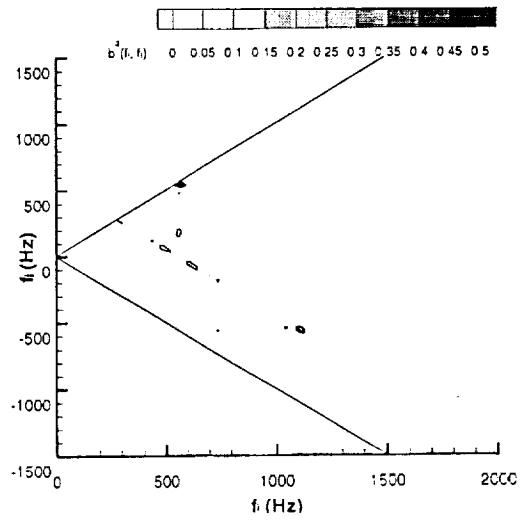
(d)



(e)



(f)



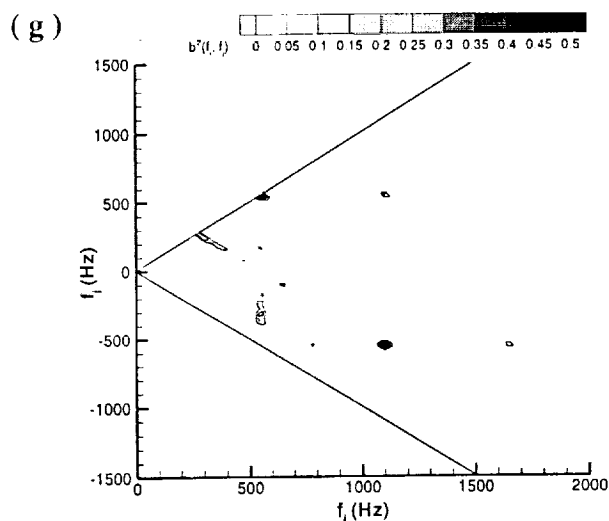


Figure 3.38: Cross-bicoherence using oscillatory blowing: Rear and floor locations. a) configuration R1, b) configuration R2, c) configuration R3, d) configuration RA, e) configuration SS, f) configuration SSA, g) configuration LS.

3.6 Wavelet Analysis

Previous work⁴³ has shown that mode switching amongst the first three cavity modes is a feature of the cavity resonance. Thus, the wavelet technique was used to examine the effect of steady and oscillatory blowing on the mode-switching behavior.

3.6.1 Baseline

The contours of the wavelet coefficients are shown in Figure 3.39. The magnitude of the wavelet coefficients corresponds to the energy density in the frequency band. In Figure 3.39a, the first two cavity modes, centered on frequencies of 250Hz and 490Hz, are seen to undergo relatively large variations in amplitude. The third cavity mode, 730Hz, is also modulated but with smaller variations. The time series traces of wavelet coefficients at the three cavity modes are plotted in Figure 3.39b. For each time

trace, the mean of the coefficients are subtracted and only the fluctuation of the coefficients about the mean are shown. The amplitude modulation of all the cavity modes is seen and the mode-switching behavior is also evident.

The corresponding data for the floor location are shown in Figure 3.40. The magnitudes of the wavelet coefficient at the floor location are much lower than at the rear wall location. All three cavity modes are amplitude modulated, that is mode switching is observed.

The Fourier spectra of the wavelet coefficients of each cavity mode are shown in Figure 3.41. The time series of wavelet coefficients consisted of 51200 data points and the spectral resolution is $5Hz$. At the rear wall location, Figure 3.41a, the spectra show a peak at $10Hz$ for the second cavity mode and $15Hz$ for the first and third cavity modes. The spectra at the floor location show similar results Figure 3.41b. These data indicate that the frequency of the amplitude modulation in the baseline cavity flow is $15Hz$.

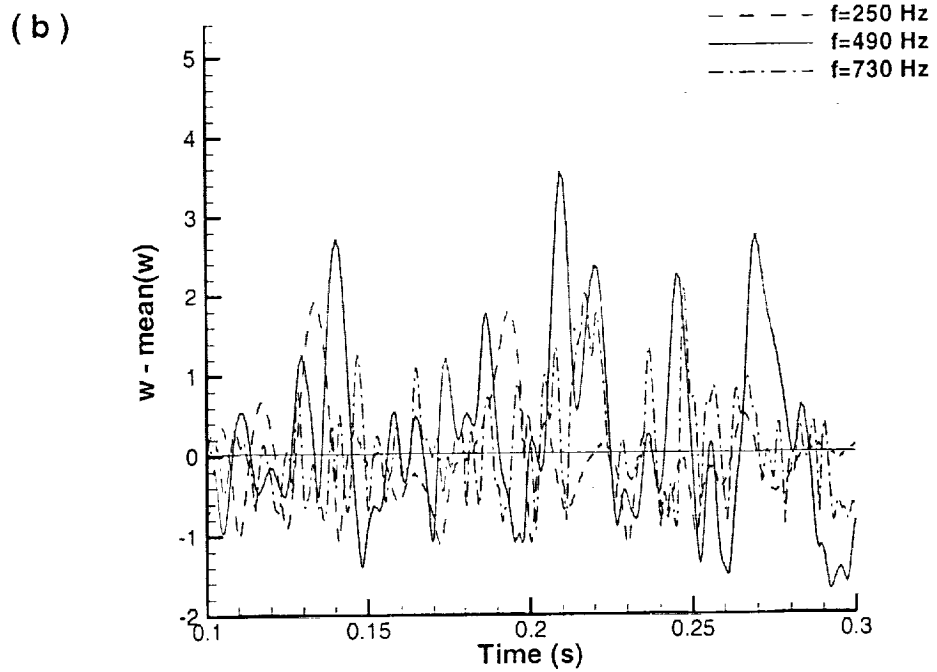
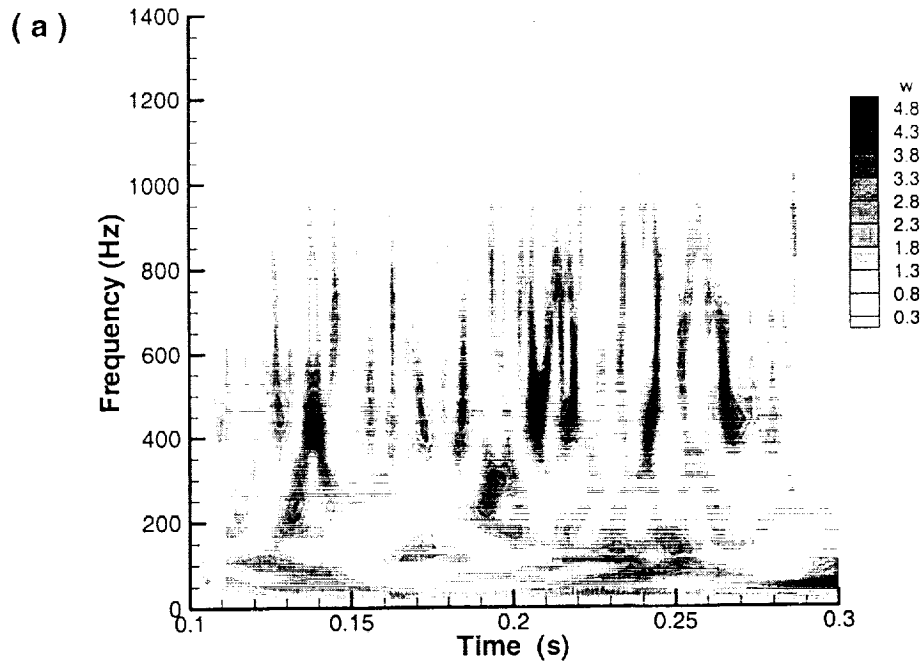


Figure 3.39: Baseline time series of wavelet coefficients at the rear wall:
a) frequency map, b) modal frequencies.

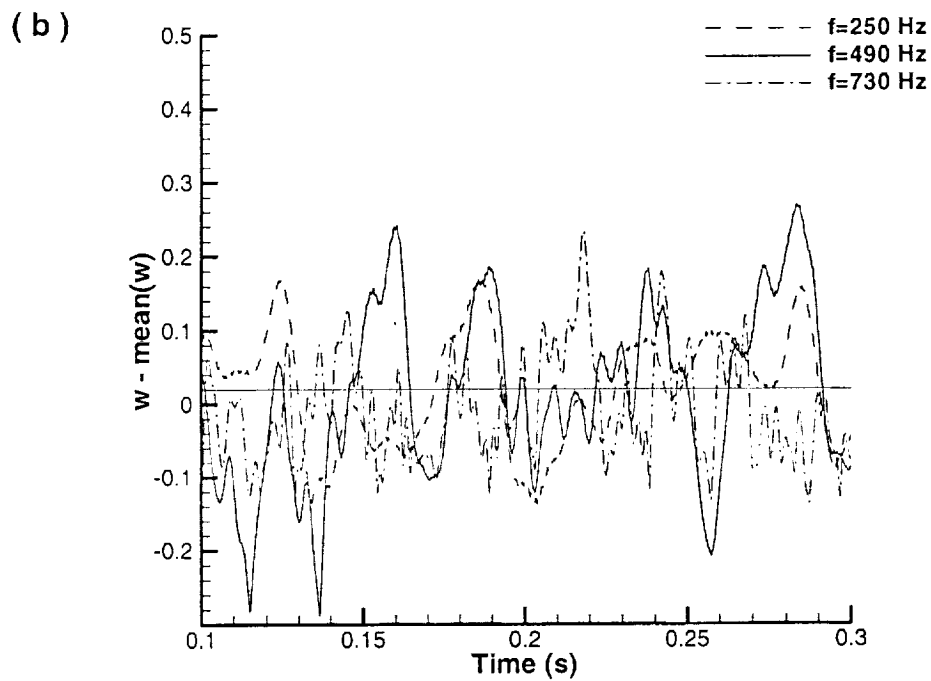
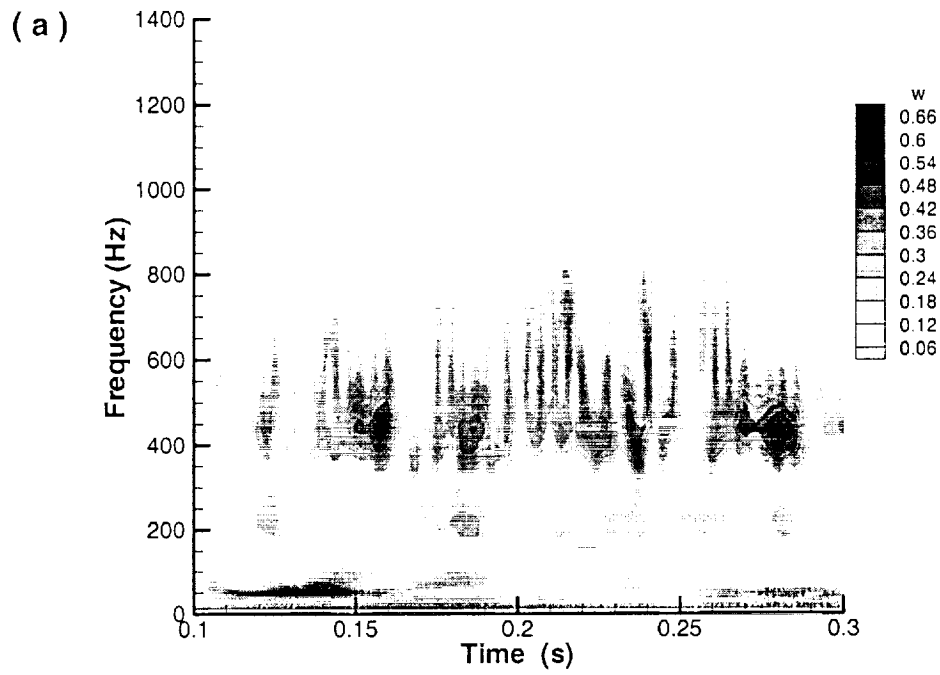


Figure 3.40: Baseline time series of wavelet at the front floor:
 a) frequency map, b) modal frequencies.

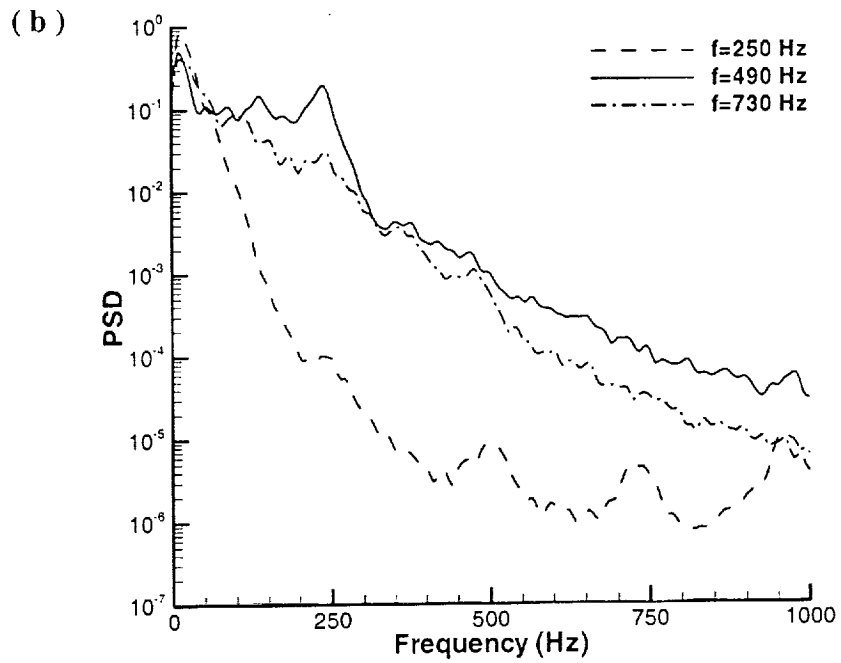
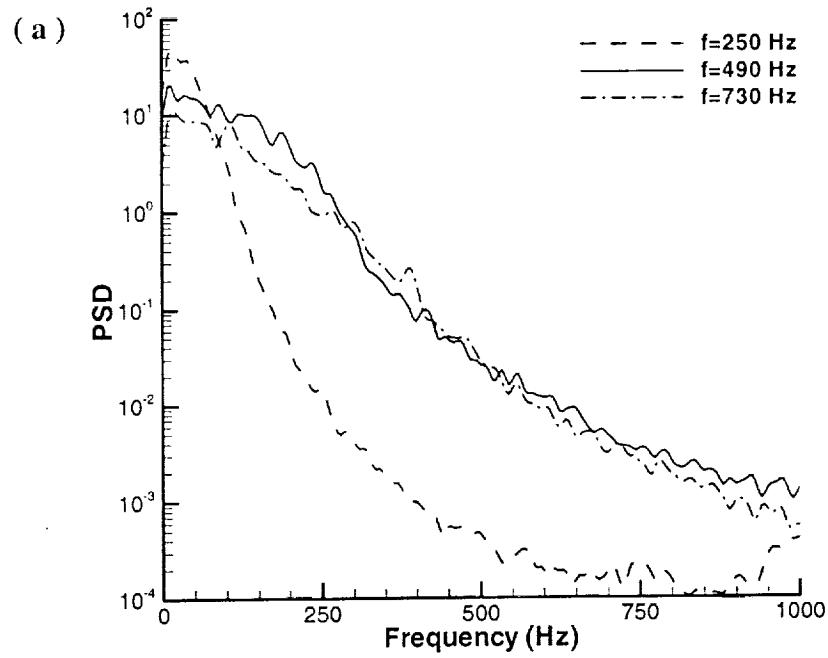


Figure 3.41: Spectra of the baseline wavelet coefficients of the modal frequencies:
a) rear wall, b) front floor.

3.6.2 Steady Blowing

The contours of the wavelet coefficients for the SSA configuration with a blowing momentum coefficient of $c_{\mu} = 0.01$ are shown in Figure 3.42. These data are representative of the steady blowing cases. The overall character of the contours is similar to the baseline cavity flow. The mode switching behavior of the three cavity modes is observed in the presence of steady blowing.

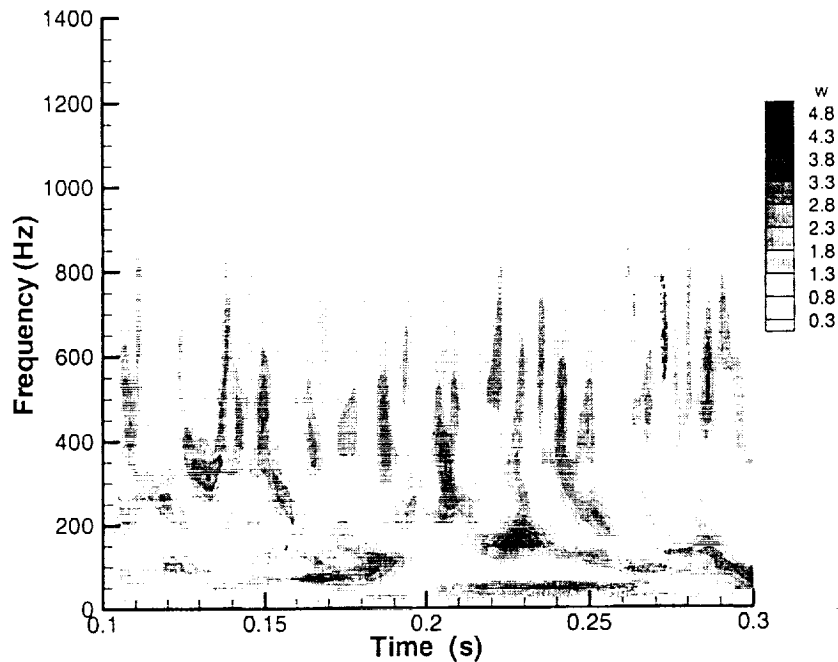


Figure 3.42: Wavelet coefficients at rear wall location with steady blowing:
 $c_{\mu} = 0.01$, configuration SSA.

The Fourier spectra of the wavelet coefficients for the seven hole configurations are presented in Figure 3.43 through Figure 3.49. The blowing momentum coefficient is $c_{\mu} = 0.01$.

The steady blowing reduces the peak-to-peak variations in the amplitude of the second cavity mode for the smaller round holes, configurations R1 and R2, Figure 3.43 and Figure 3.44. However, the steady blowing does not change the frequency of the amplitude modulation of all three cavity modes. The steady blowing through the large round holes, configuration R3, has a marked effect on the mode switching behavior as seen in Figure 3.45. In comparison to the smaller round hole configurations, the spectral amplitudes of the second and third modes are greatly reduced. Furthermore the frequency of the modulation of the second cavity mode is shifted to $35Hz$. The effect of steady blowing at angle through a round hole, configuration RA, is seen in Figure 3.46. The spectra show no distinct peaks indicating that the steady blowing is more effective in suppressing the cavity resonance.

The effect of steady blowing through the streamwise holes, configurations SS and SSA, is examined in Figure 3.47 and Figure 3.48. The amplitude modulation of the second cavity mode is clearly seen to be reduced, and the blowing at an angle is observed to be more effective than the blowing at a normal. For the configuration SS, the frequency of modulation occurs at $20Hz$, and for the configuration SSA, a small amplitude peak is observed at $55Hz$. The distribution of energy across the spectra for the third mode is reduced for both blowing configurations, but substantially more for the

configuration SSA. On the other hand, there is little change in the spectra for the first mode.

The effect of steady blowing on the mode switching behavior for the configuration LS is shown in Figure 3.49. The amplitude modulation of the second cavity mode is decreased, and there is little effect on the first and third cavity modes.

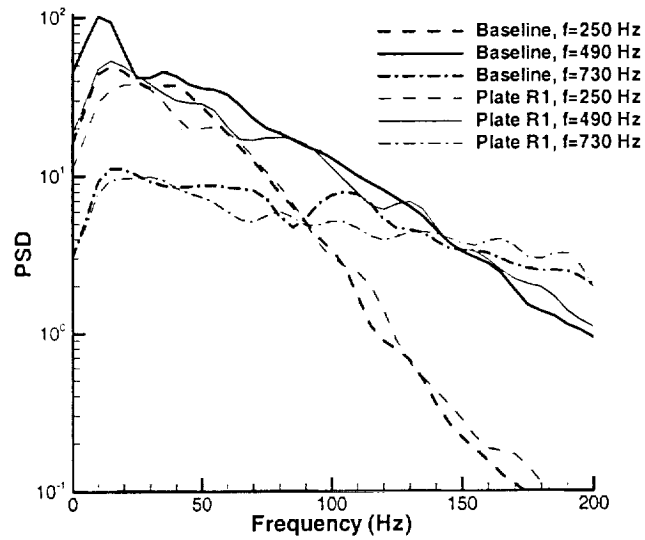


Figure 3.43: Fourier spectra of wavelet coefficients at the rear wall location with steady blowing control: $c_{\mu} = 0.01$, configuration R1.

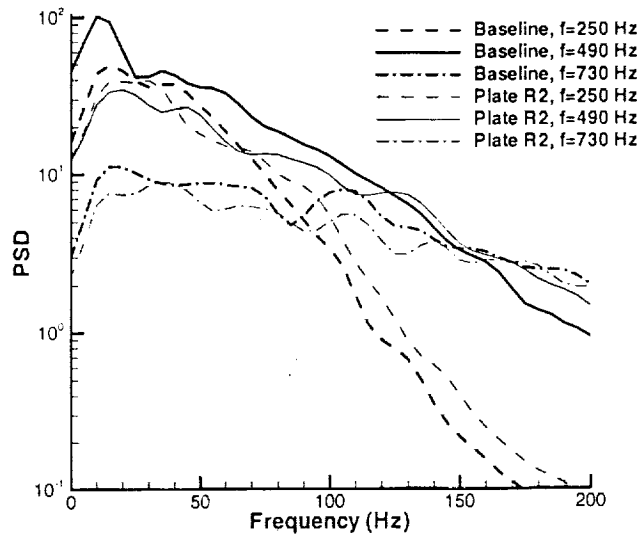


Figure 3.44: Fourier spectra of wavelet coefficients at the rear wall location with steady blowing control: $c_{\mu} = 0.01$, configuration R2.

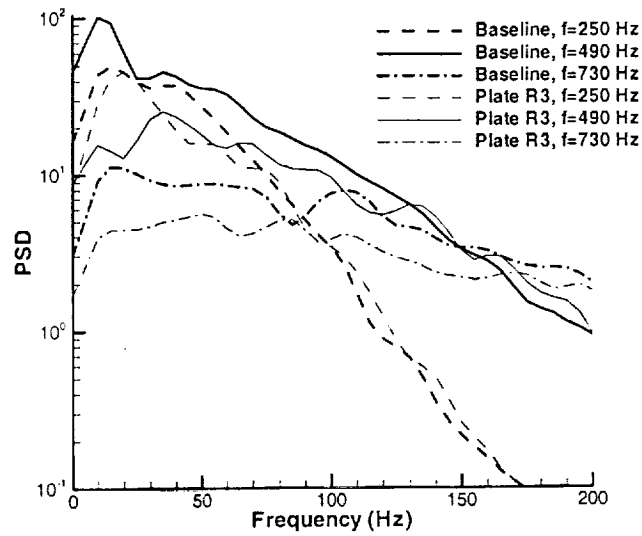


Figure 3.45: Fourier spectra of wavelet coefficients at the rear wall location with steady blowing control: $c_{\mu} = 0.01$, configuration R3.

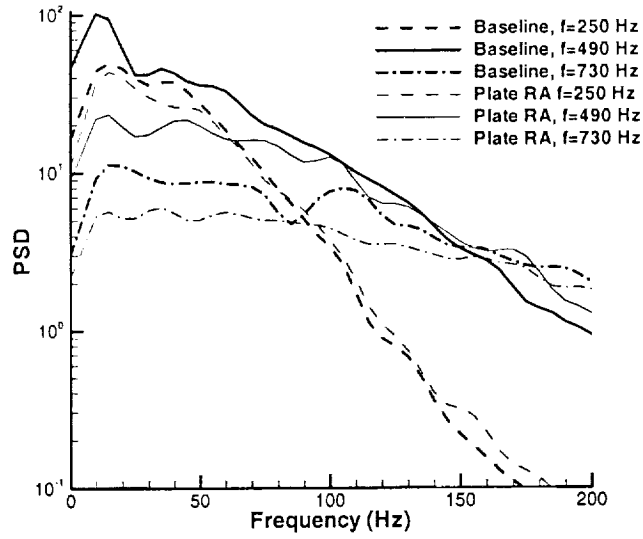


Figure 3.46: Fourier spectra of wavelet coefficients at the rear wall location with steady blowing control: $c_{\mu} = 0.01$, configuration RA.

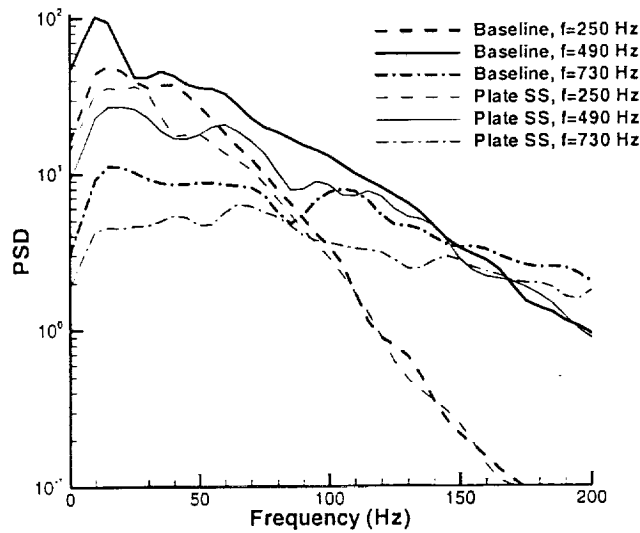


Figure 3.47: Fourier spectra of wavelet coefficients at the rear wall location with steady blowing control: $c_{\mu} = 0.01$, configuration SS.

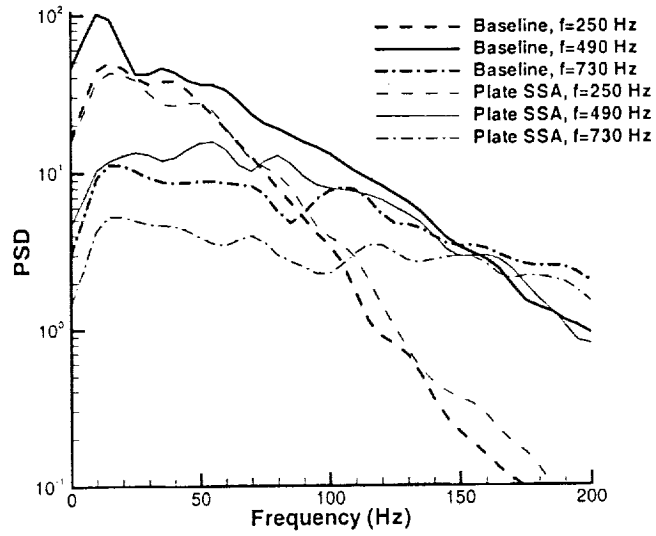


Figure 3.48: Fourier spectra of wavelet coefficients at the rear wall location with steady blowing control: $c_{\mu} = 0.01$, configuration SSA.

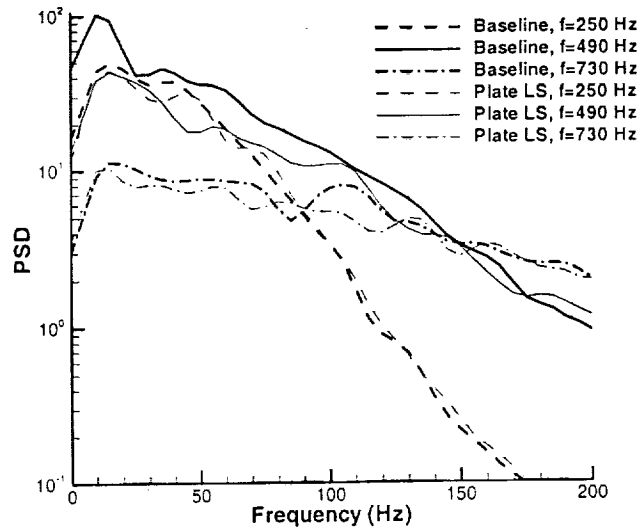


Figure 3.49: Fourier spectra of wavelet coefficients at the rear wall location with steady blowing control: $c_{\mu} = 0.01$, configuration LS.

3.6.3 Near-Zero Net Mass Oscillatory Blowing

The contours of the wavelet coefficients for the SSA configuration with near-zero net mass oscillatory blowing control are shown in Figure 3.50. The unsteady blowing momentum coefficient and forcing frequency are 1×10^{-5} and 550Hz , respectively. These data are representative of the near-zero net mass oscillatory blowing cases. The mode switching behavior of the cavity flow is still observed, as well as an additional modulation at the forcing frequency.

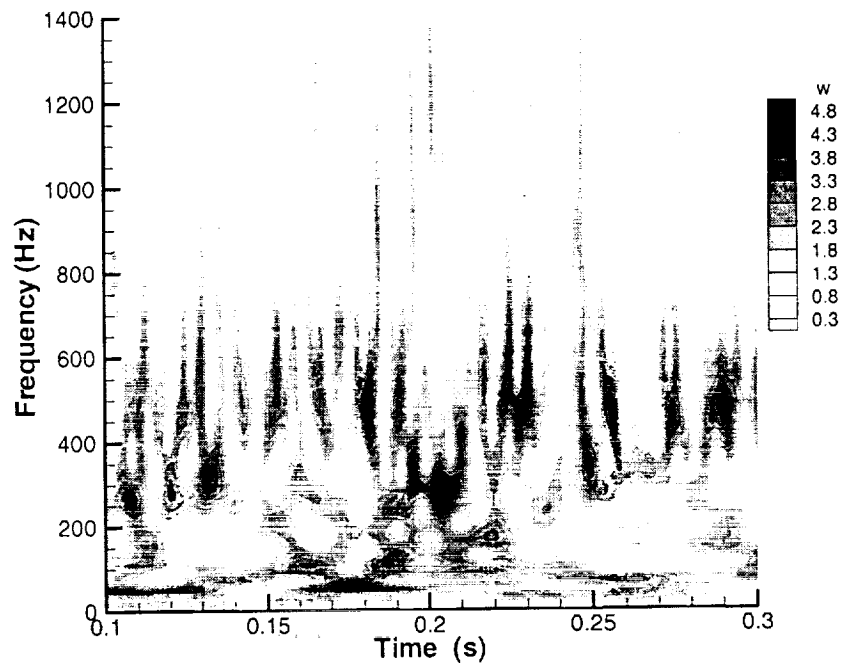


Figure 3.50: Wavelet coefficients at the rear wall location using oscillatory blowing; $\langle c_{\mu} \rangle = 1 \times 10^{-5}$, $f_f = 550\text{Hz}$, configuration SSA.

The Fourier spectra of the wavelet coefficients of the three cavity modes and forcing frequency for the seven hole configurations are presented in Figure 3.51 through

Figure 3.57. The data are from the rear wall location, the unsteady blowing momentum coefficient is $\langle c_{\mu} \rangle = 1 \times 10^{-5}$ and the forcing frequency is 550Hz .

For all hole configurations the oscillatory blowing is effective in reducing the modulation of the second cavity mode, and the modulation of the other two cavity modes. An exception is the configuration LS, where a significant increase in the amplitude modulation of the first cavity mode is observed. For all configurations, the wavelet coefficients at the forcing frequency are increased with the blowing.

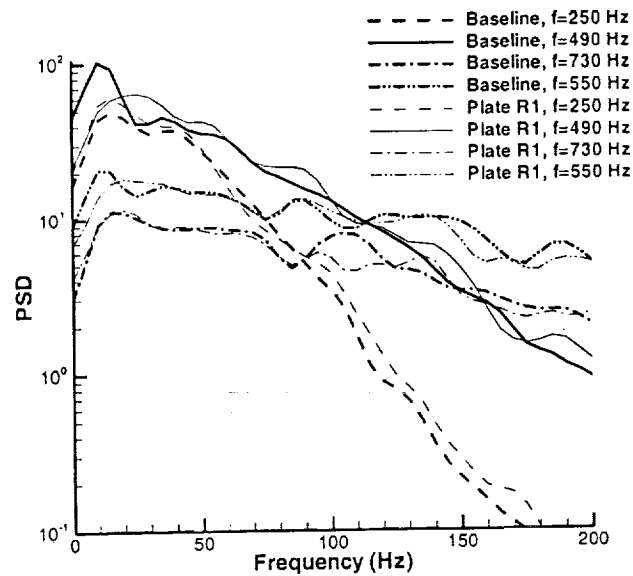


Figure 3.51: Fourier spectra of wavelet coefficients at the rear wall location using oscillatory blowing control: $\langle c_{\mu} \rangle = 1 \times 10^{-5}$, $f_f = 550\text{Hz}$, configuration R1.

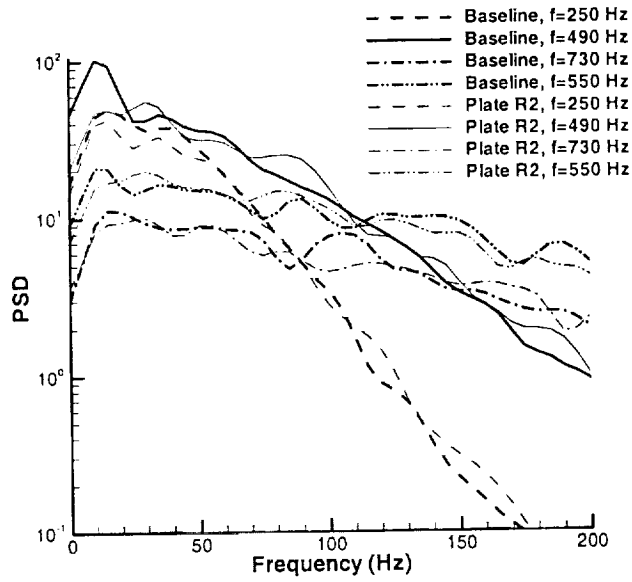


Figure 3.52: Fourier spectra of wavelet coefficients at the rear wall location using oscillatory blowing control: $\langle c_\mu \rangle = 1 \times 10^{-5}$, $f_f = 550 \text{ Hz}$, configuration R2.

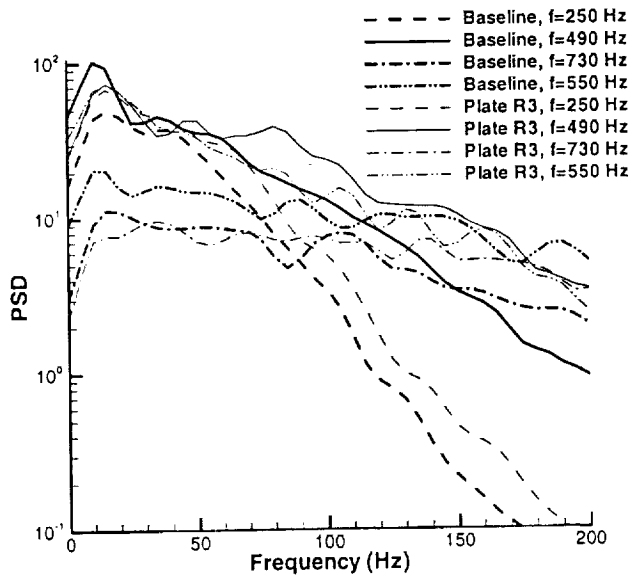


Figure 3.53: Fourier spectra of wavelet coefficients at the rear wall location using oscillatory blowing control: $\langle c_\mu \rangle = 1 \times 10^{-5}$, $f_f = 550 \text{ Hz}$, configuration R3.

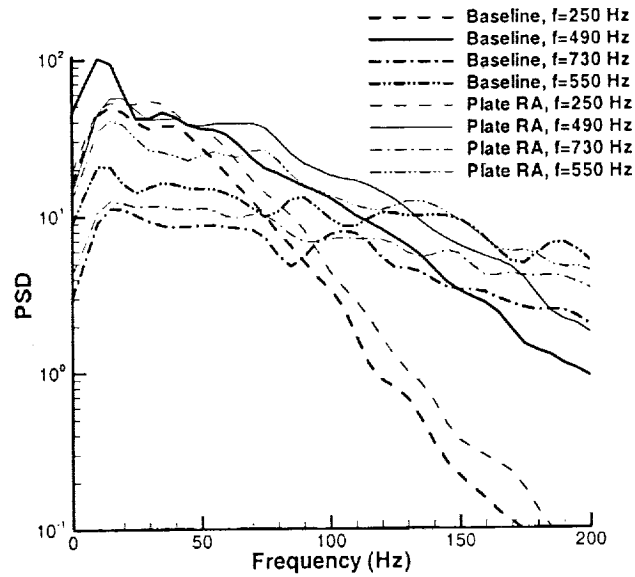


Figure 3.54: Fourier spectra of wavelet coefficients at the rear wall location using oscillatory blowing control: $\langle c_\mu \rangle = 1 \times 10^{-5}$, $f_f = 550 \text{ Hz}$, configuration RA.

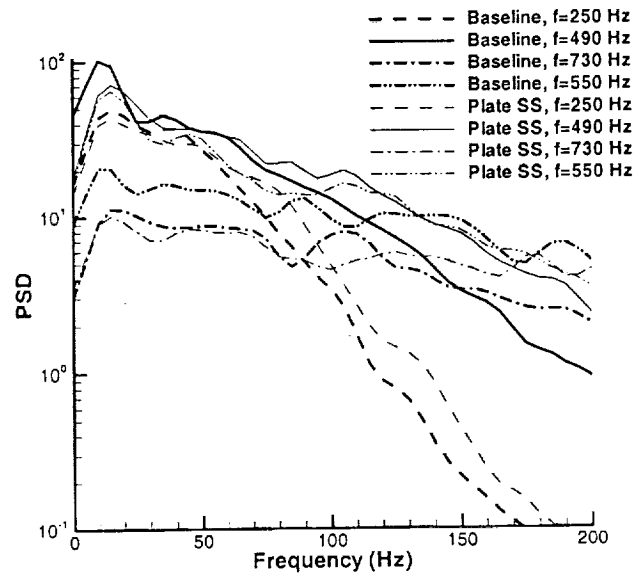


Figure 3.55: Fourier spectra of wavelet coefficients at the rear wall location using oscillatory blowing control: $\langle c_\mu \rangle = 1 \times 10^{-5}$, $f_f = 550 \text{ Hz}$, configuration SS.

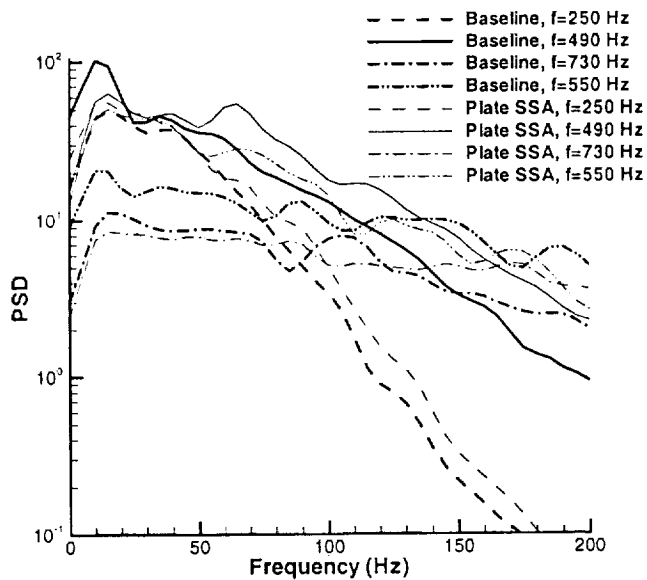


Figure 3.56: Fourier spectra of wavelet coefficients at the rear wall location using oscillatory blowing control: $\langle c_{\mu} \rangle = 1 \times 10^{-5}$, $f_f = 550 \text{ Hz}$, configuration SSA.

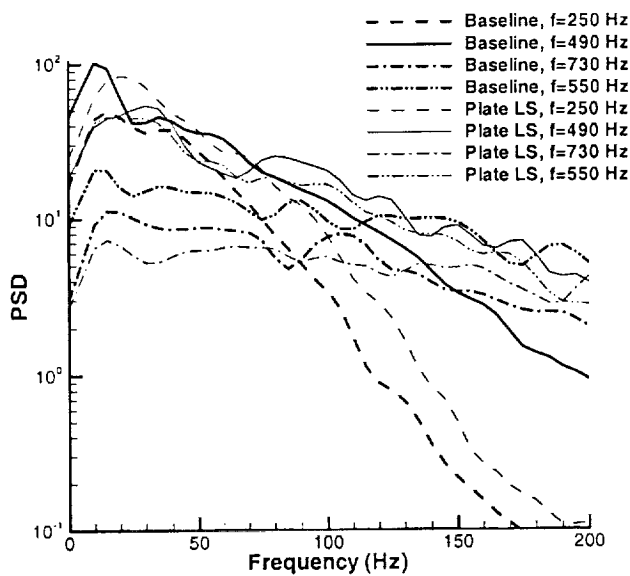


Figure 3.57: Fourier spectra of wavelet coefficients at the rear wall location using oscillatory blowing control: $\langle c_{\mu} \rangle = 1 \times 10^{-5}$, $f_f = 550 \text{ Hz}$, configuration LS.

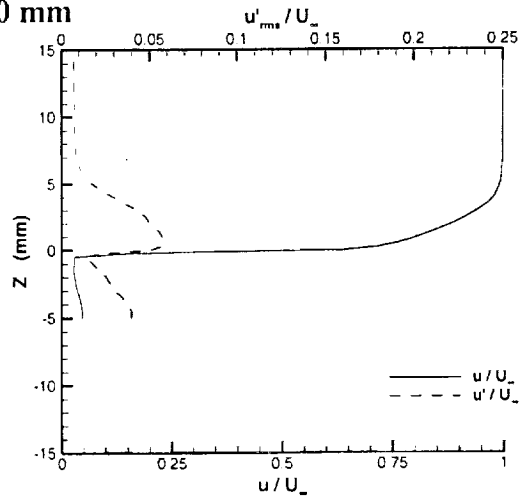
3.7 Shear Layer Measurements

Hot-wire measurements of the cavity shear layer were conducted for the baseline, and selected control cases. These selected steady and near-zero net mass oscillatory blowing control cases examined the effect of the momentum coefficient and blowing angle on the shear layer profiles.

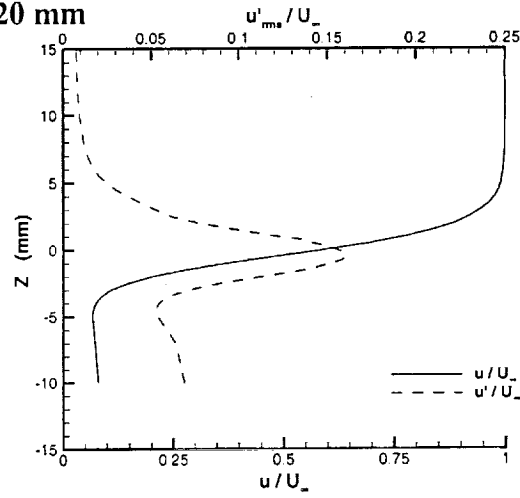
3.7.1 Baseline

The mean and rms velocity and profiles at three stations, $X=0$, 20 , and 50mm are shown in Figure 3.58. Positive Z values indicate locations outside of the cavity; and negative Z values indicate locations within the cavity. The velocities are normalized by the freestream velocity. The mean velocity profiles at $X=0\text{mm}$, exhibits the fullness typical of a turbulent boundary layer. The boundary layer thickness at this location is approximately 6mm and the turbulence intensity of the freestream is 0.6% . The peak rms velocity is located at $Z=0.05\text{mm}$ and is 6% of the freestream velocity. At $X=20\text{mm}$, the mean velocity profile more closely resembles that of a shear layer. The peak rms velocity is 16% of the freestream, and is located at $Z=-0.05\text{mm}$. The shear layer spans a height from $Z=-4\text{mm}$ to $Z=4\text{mm}$. At $X=50\text{mm}$, the shear layer is broader and spans from $Z=-10\text{mm}$ to $Z=8\text{mm}$; the peak rms is 20% of the freestream and is located at $Z=-1.25\text{mm}$.

X = 0 mm



X = 20 mm



X = 50 mm

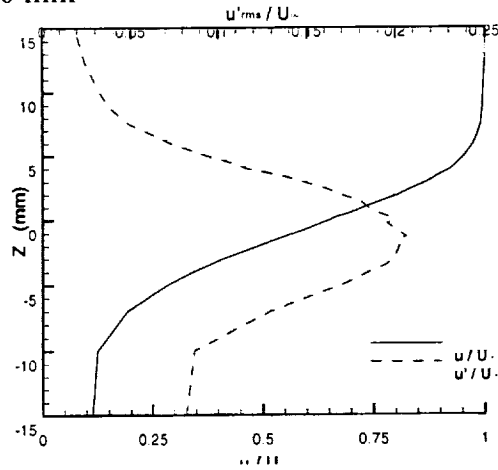


Figure 3.58: Baseline mean and rms velocity profiles.

Figure 3.59 shows the streamwise evolution of the spectra measured at the maximum rms location. The frequency resolution is 10Hz . The second and third cavity modes are clearly seen at 490Hz and at approximately 740Hz , respectively. The peak values as well as the amplitudes of the broadband increase in the downstream direction. The spatial evolution of rms velocity and the velocity fluctuations at the first three cavity modes are shown in Figure 3.60. Over the range $X=0\text{mm}$ to $X=20\text{mm}$ for the first mode and $X=0\text{mm}$ to $X\approx 25\text{mm}$ for the second and third modes, the exponential growth in the amplitude is linear. Over this region of linear growth, the growth rates are similar for the three cavity modes. From $X\approx 20\text{mm}$ for the first mode and from $X\approx 25\text{mm}$ for the second and third modes, the growth rates are nonlinear. The amplitudes of the three cavity modes saturates at $X\approx 50\text{mm}$. The growth of the rms velocity is linear from $X=0\text{mm}$ to 12mm and its amplitude also saturates at approximately $X\approx 50\text{mm}$.

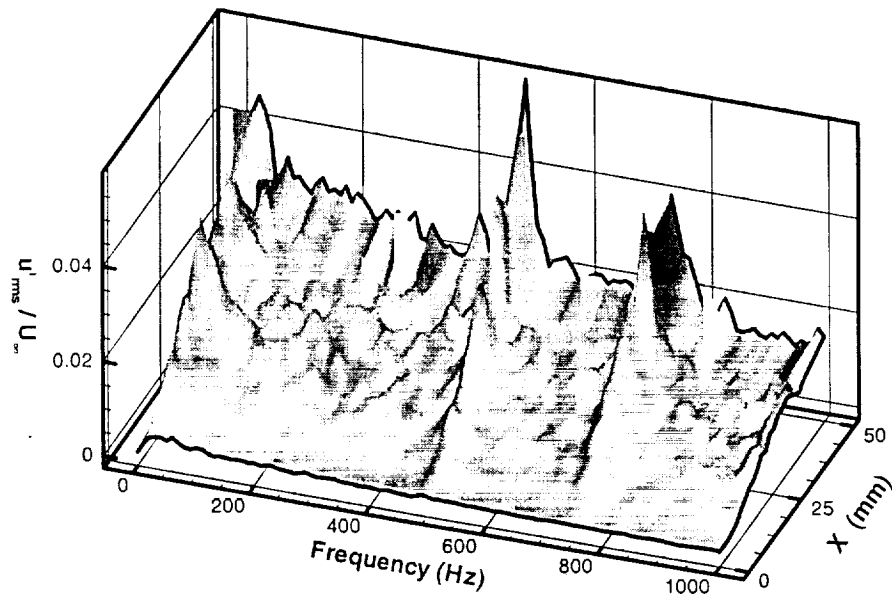


Figure 3.59: Streamwise evolution of spectra in the baseline cavity flow.

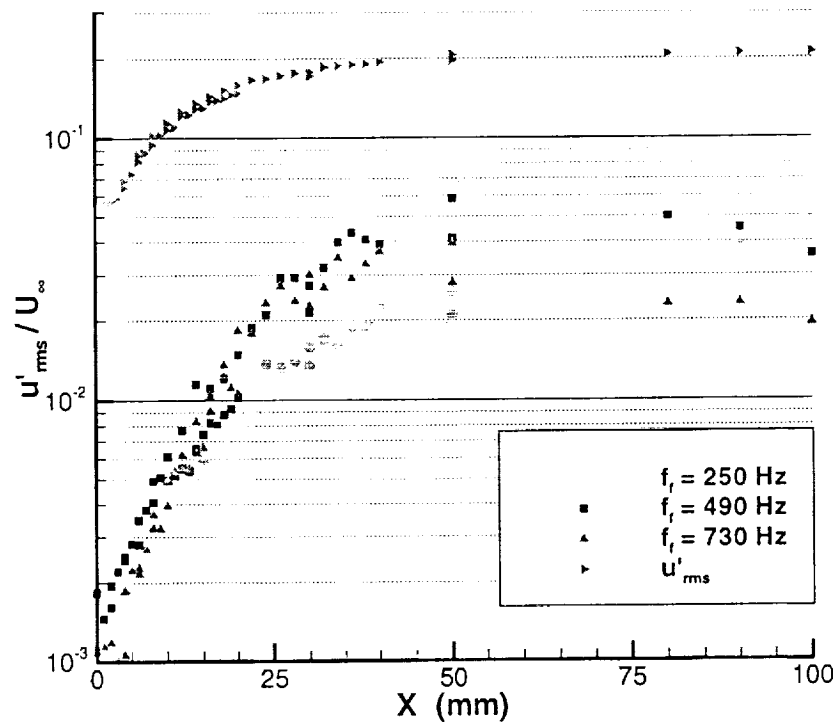


Figure 3.60: Streamwise evolution of velocity fluctuations for the baseline case.

3.7.2 Steady Blowing

The mean and rms velocity profiles with steady blowing for the three hole configurations SS, SSA, and LS are shown in Figure 3.61 and Figure 3.62, respectively. The momentum coefficients are $c_{\mu} = 0.02$ for the SS and SSA configurations and 0.03 for the LS configuration. At the front cavity lip, $X=0mm$, the velocity profiles are unchanged compared to the baseline, for the SS and SSA configurations. The mean velocity profile is less full for the LS configuration and the peak rms velocity is increased to 11%. At $X=20mm$, the mean velocity profile for the SSA configuration is fuller and the rms velocity profile shows a corresponding increase in the peak value; in addition, the shear layer is observed to be broader. For the SS configuration, the mean and rms velocity profiles are little changed compared to the baseline. For the LS configuration, the mean and rms velocity are displaced upward 2mm. At $X=60mm$ for the SS configuration, the mean velocity profile is less full. The SSA configuration has a slightly more developed velocity profile and a fuller rms velocity profile within the cavity region.

Figure 3.63 through Figure 3.65 show the streamwise evolution of the spectra. The steady blowing with the SS configuration, Figure 3.63, is seen to reduce the amplitudes of the second and third modes. The steady blowing however, also results in an increase in the spectral amplitudes over the low frequency range, $f < 50Hz$. For the SSA configuration, Figure 3.64, the amplitude of the cavity modes are suppressed. In contrast, for the LS configuration, Figure 3.65, the second and third modes are not suppressed nor are the amplitudes over the low frequency range amplified.

The streamwise evolution of the rms velocity and the velocity fluctuations at the second and third cavity modes are shown in Figure 3.66. In Figure 3.66a, the initial amplitude growth of the SS and SSA configurations are similar to the baseline case. The amplitude growth for the SS configuration closely follows the baseline over the region of measurement. For the SSA configuration, the range of linear growth extends further downstream, and the rms velocity saturates at a larger amplitude than the baseline. The amplitude growth for the LS configuration occurs at higher amplitudes than the SS and SSA configurations. The streamwise evolutions of the rms velocities centered on the second cavity mode ($f = 490\text{Hz}$) are presented in Figure 3.66b. The SS and SSA configurations have a similar streamwise evolution, suggesting that the blowing angle has little effect on the amplitude growth of the second mode with steady blowing. Steady blowing control with the LS configuration results in velocity fluctuations that are over an order of magnitude larger than the SS and SSA configurations. The evolution of the rms velocities centered on the third cavity mode, Figure 3.66c, are similar to the second mode; however for the LS configuration, the rms velocity fluctuations of the third cavity mode is comparable to those of the SS and SSA configurations.

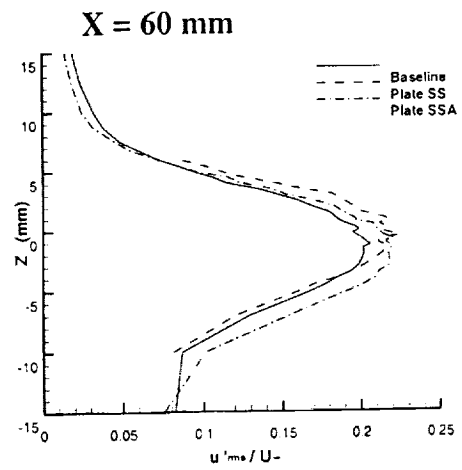
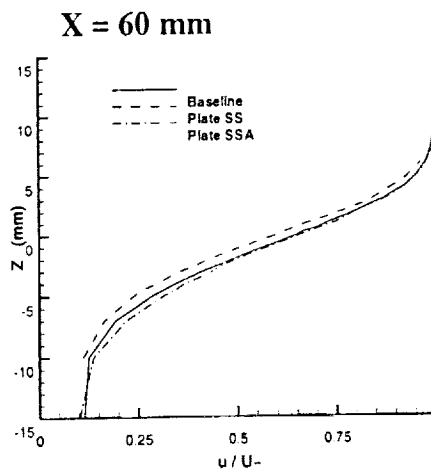
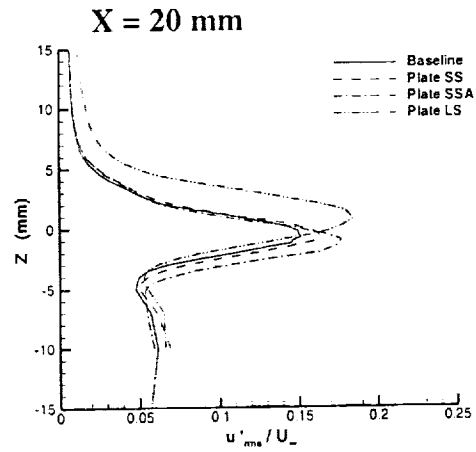
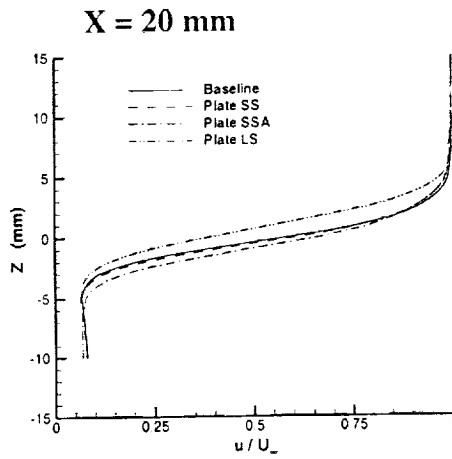
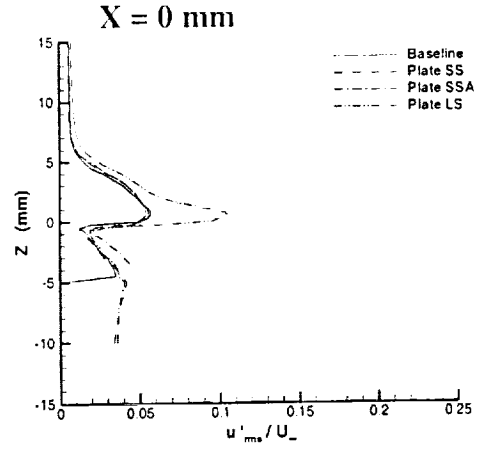
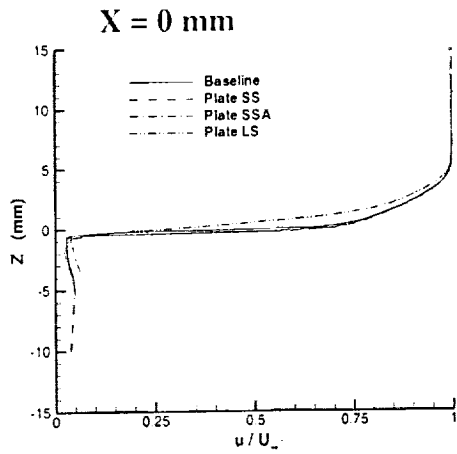


Figure 3.61: Mean velocity profiles with steady blowing control.

Figure 3.62: Rms velocity profiles with steady blowing control.

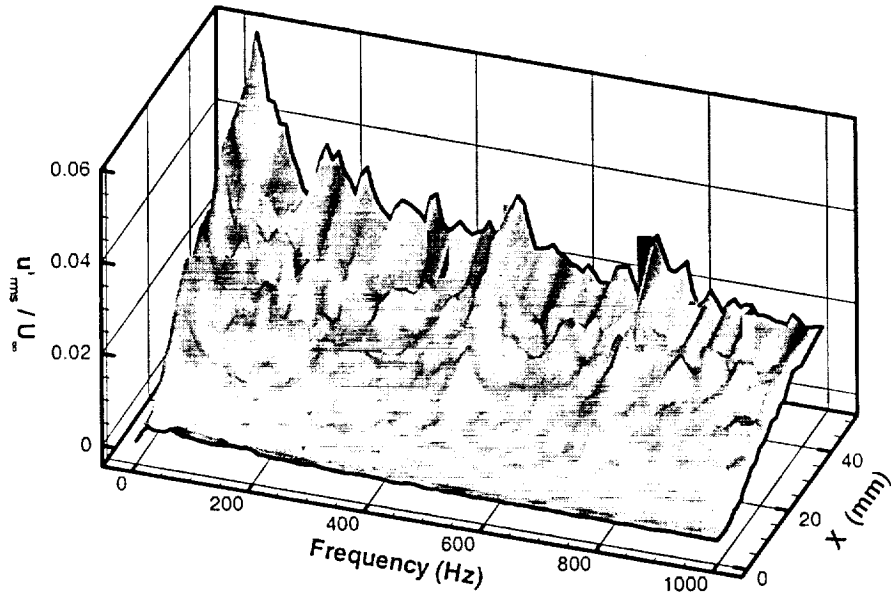


Figure 3.63: Streamwise evolution of spectra with steady blowing control; configuration SS, $c_{\mu} = 0.02$.

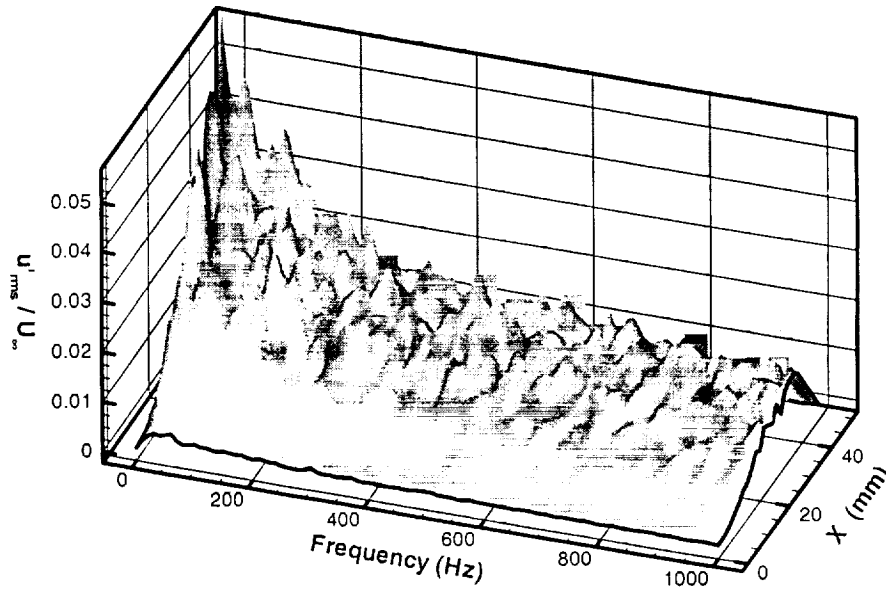


Figure 3.64: Streamwise evolution of spectra with steady blowing control; configuration SSA, $c_{\mu} = 0.02$.

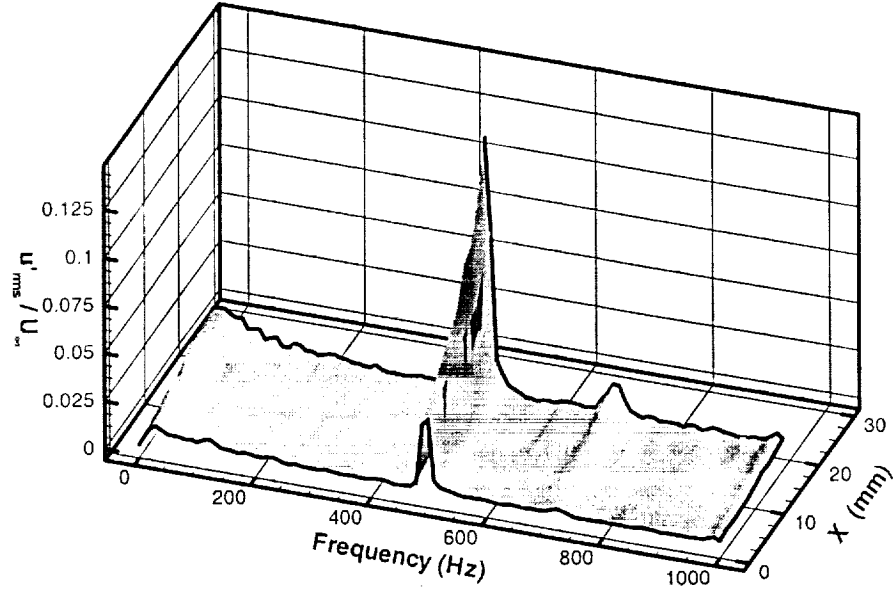
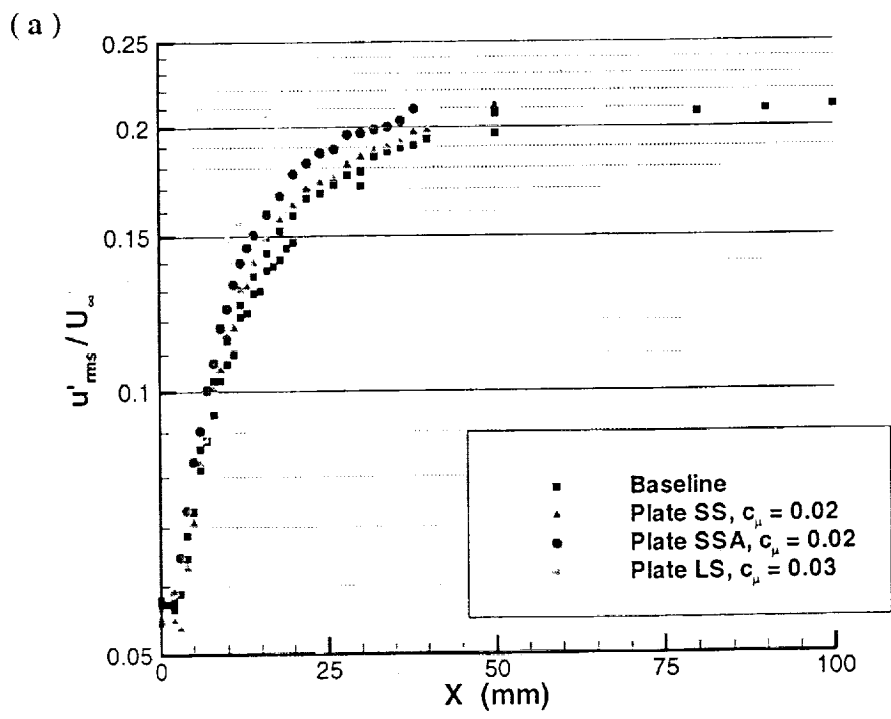


Figure 3.65: Streamwise evolution of spectra with steady blowing control; configuration LS, $c_{\mu} = 0.03$.



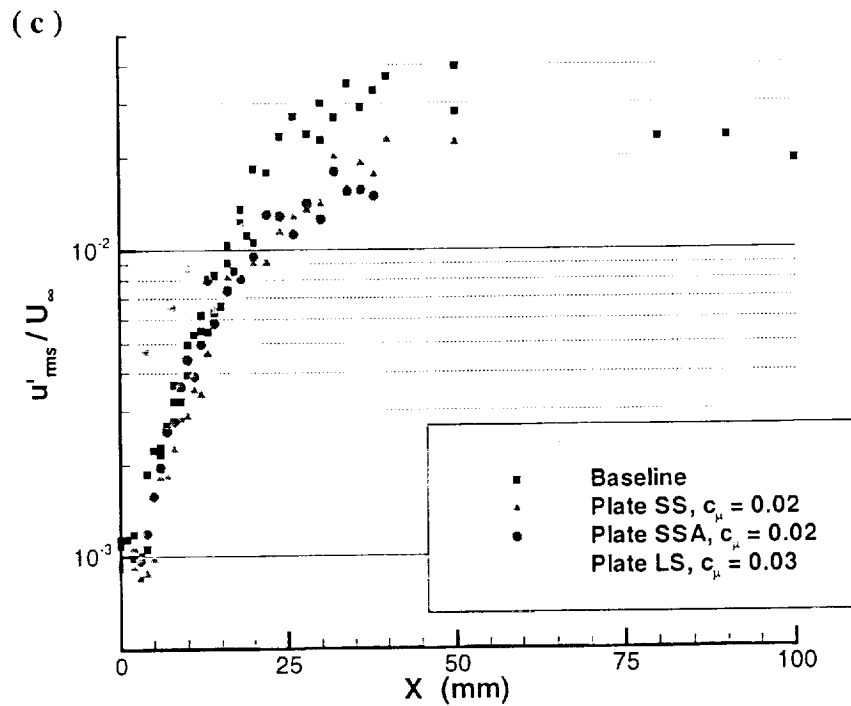
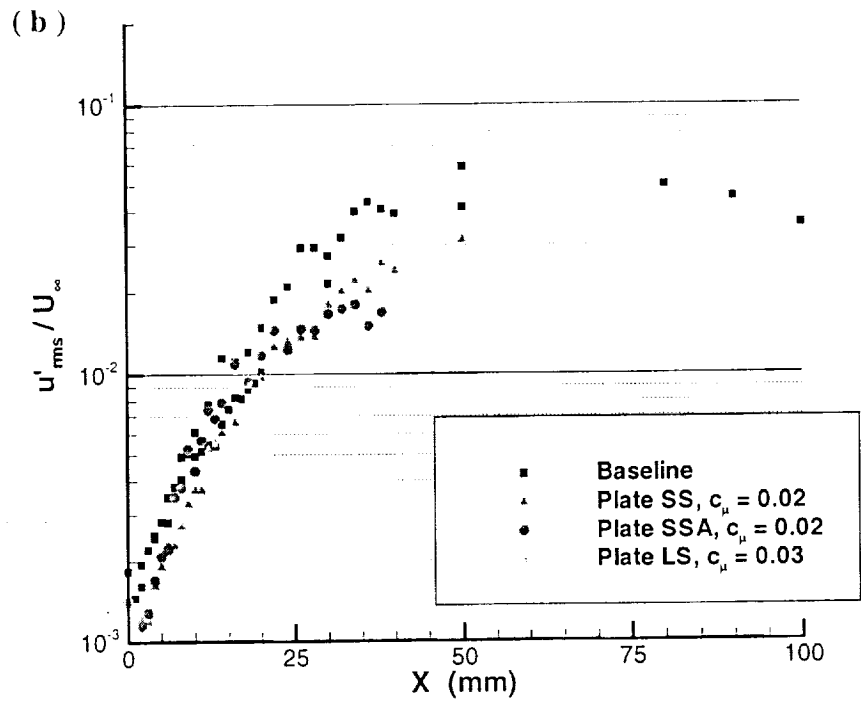


Figure 3.66: Streamwise evolution of velocity fluctuations using steady blowing control. a) rms b) second cavity mode, c) third cavity mode.

3.7.3 Near-Zero Net Mass Oscillatory Blowing

3.7.3.1 Effect of forcing frequency and blowing amplitude

The effects of the forcing frequency and blowing amplitude on the mean and rms velocity are shown in Figure 3.67 and Figure 3.68, respectively. Three cases from the SSA configuration $f_f = 580\text{Hz}$ and $\langle c_\mu \rangle = 2 \times 10^{-4}$, $f_f = 580\text{Hz}$ and $\langle c_\mu \rangle = 7 \times 10^{-4}$, and $f_f = 300\text{Hz}$ and $\langle c_\mu \rangle = 2 \times 10^{-4}$ are examined. At $X = 0\text{mm}$, the mean and rms velocity profiles are almost indistinguishable. At $X = 20\text{mm}$, the $f_f = 300\text{Hz}$ case shows little effect while the $f_f = 580\text{Hz}$ cases produce fuller velocity profiles and larger peak rms velocities. At $X = 50\text{mm}$, the two $f_f = 580\text{Hz}$ cases show fuller velocity profiles and significantly broader rms velocity profiles. These results indicate that oscillatory blowing is effective in enhancing the mixing of the shear layer.

The streamwise evolution of the spectra is shown in Figure 3.69 to Figure 3.71. Figure 3.69 and Figure 3.70 show spectra for $f_f = 580\text{Hz}$ $\langle c_\mu \rangle = 2 \times 10^{-4}$ and $f_f = 580\text{Hz}$ $\langle c_\mu \rangle = 7 \times 10^{-4}$, respectively. The forcing frequency is the dominant feature of the spectra, and its amplitude is larger at the higher momentum coefficient. In Figure 3.71, the spectra of the $f_f = 300\text{Hz}$, $\langle c_\mu \rangle = 2 \times 10^{-4}$ case are shown. The amplitudes over all the frequencies are comparable to the baseline case with the exception of that at the forcing frequency. Previous results show that for similar blowing amplitudes, forcing at $f_f = 300\text{Hz}$ is not as effective as higher forcing frequencies above 500Hz .

The effect of the forcing frequency and blowing amplitude on the streamwise evolution of the rms velocities is shown in Figure 3.72. The broadband rms velocities are

compared in Figure 3.72a. Over the range of linear growth, the amplitude growth are unchanged with the oscillatory blowing. In the region of nonlinear growth, the $f_f = 300Hz$ case is very similar to the baseline case. On the other hand for the $f_f = 580Hz$ cases, the amplitude growth occurs at larger magnitudes. The streamwise evolution of the rms velocities centered on the second and third cavity modes are shown in Figure 3.72b and Figure 3.72c. The growth for the $f_f = 580Hz$ cases are smaller over the range of measurement; on the other hand for the $300Hz$ case the growth is similar to the baseline. The rms velocities centered on the forcing frequencies, $300Hz$ and $580Hz$, are shown in Figure 3.72d and Figure 3.72e, respectively. It is evident that the forcing is more effective at $580Hz$. In Figure 3.72d, the $f_f = 300Hz$ case shows relatively small changes compared to the baseline and $f_f = 580Hz$. On the other hand in Figure 3.72e, the $580Hz$ cases show dramatically increased growth rates and saturates at a more upstream station, compared to the baseline and $f_f = 300Hz$ case.

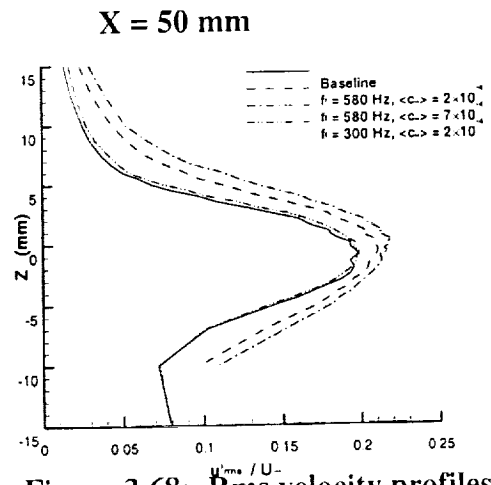
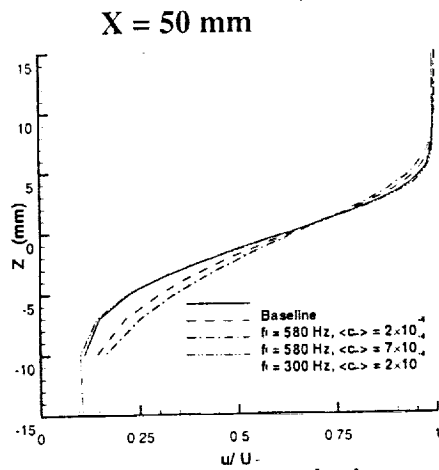
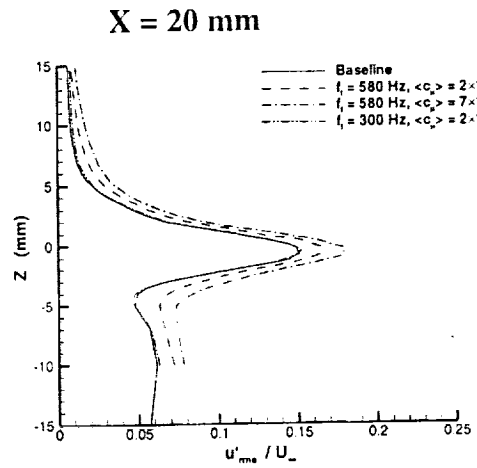
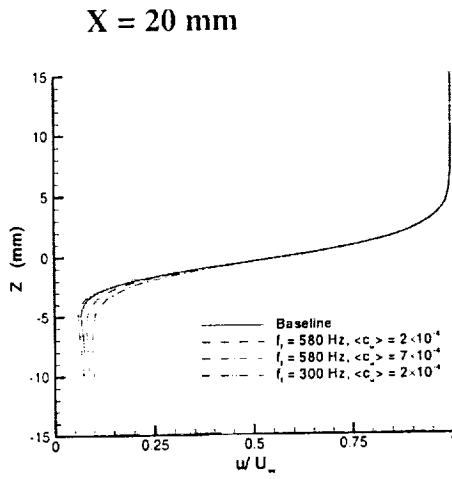
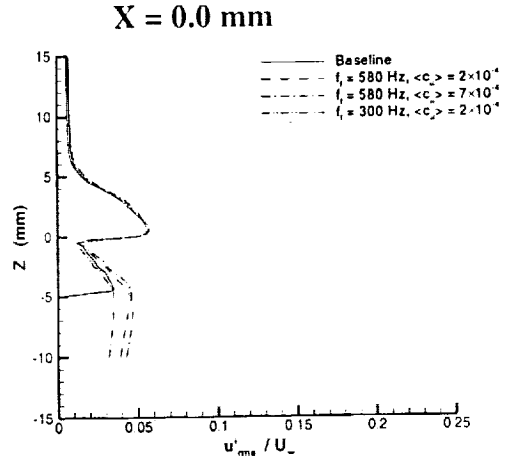
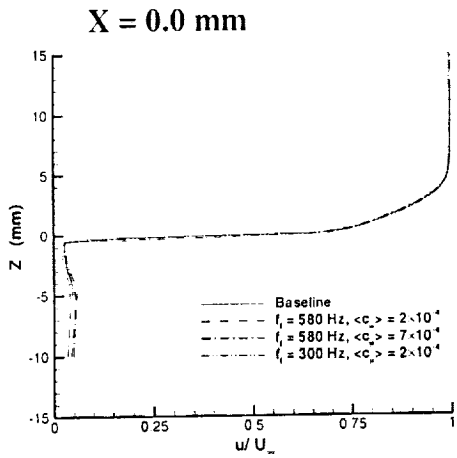


Figure 3.67: Mean velocity profiles with oscillatory blowing control, configuration SS.

Figure 3.68: Rms velocity profiles with oscillatory blowing control, configuration SS.

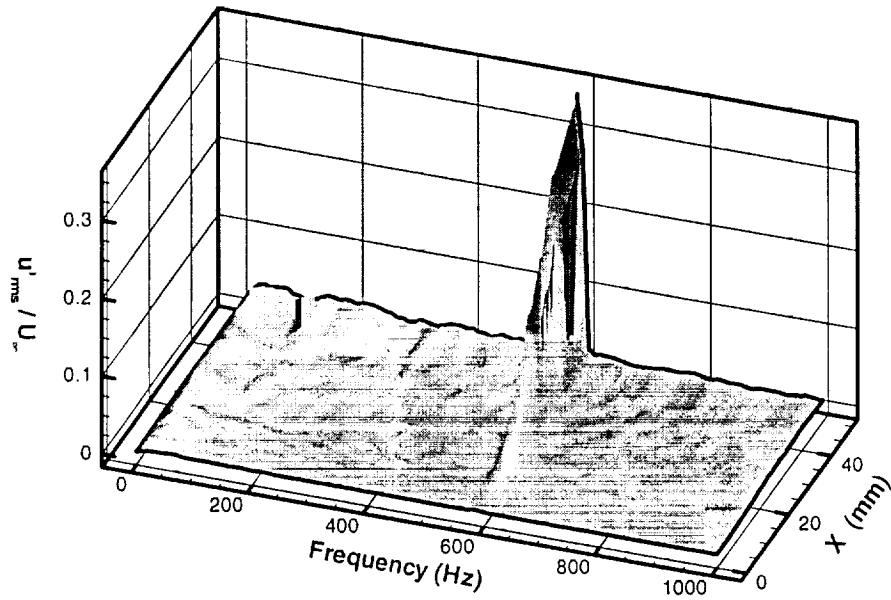


Figure 3.69: Streamwise evolution of spectra with oscillatory blowing control; configuration SS, $f_t = 580 \text{ Hz}$, $\langle c_\mu \rangle = 2 \times 10^{-4}$.

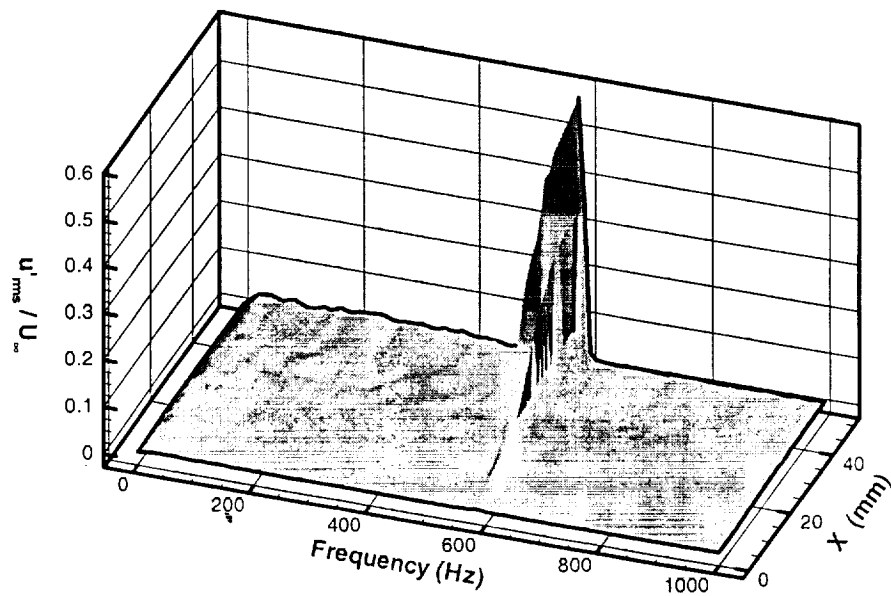


Figure 3.70: Streamwise evolution of spectra with oscillatory blowing control; configuration SS, $f_t = 580 \text{ Hz}$, $\langle c_\mu \rangle = 7 \times 10^{-4}$.

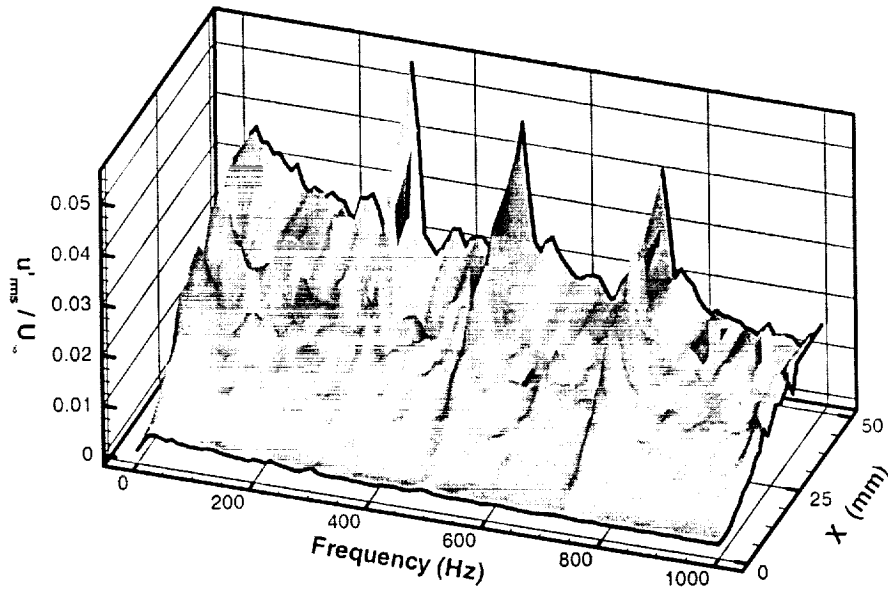
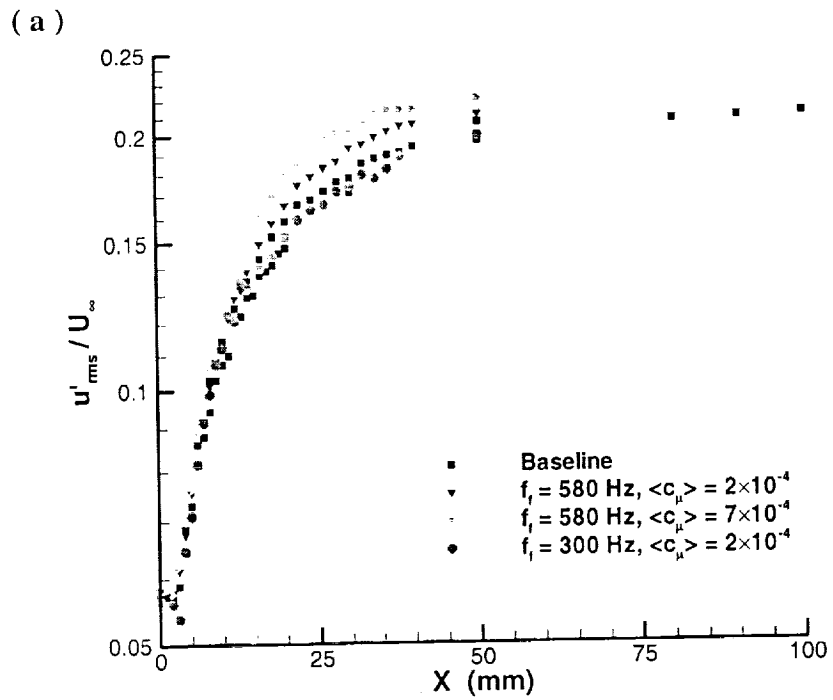
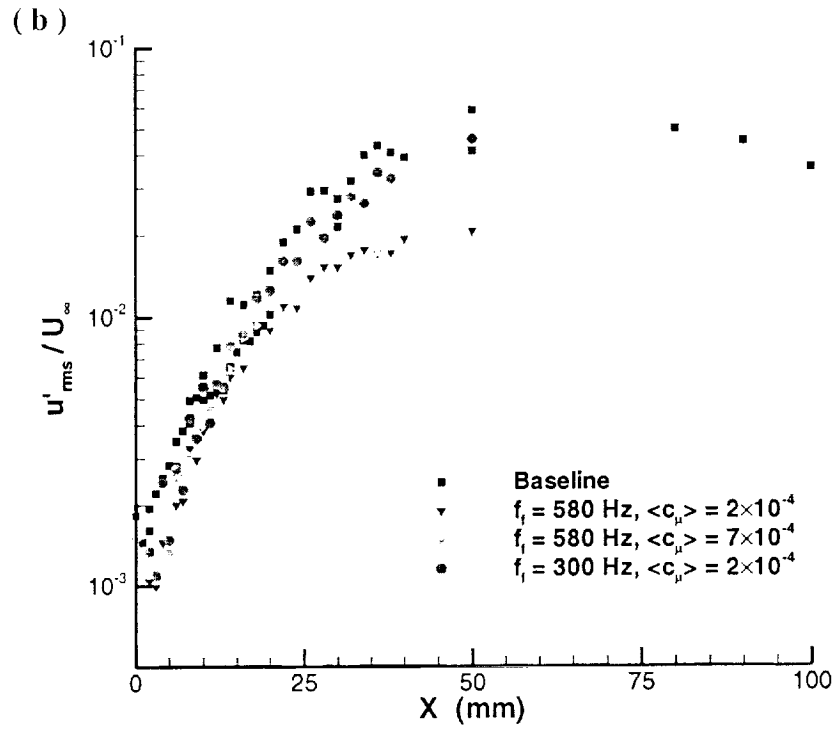
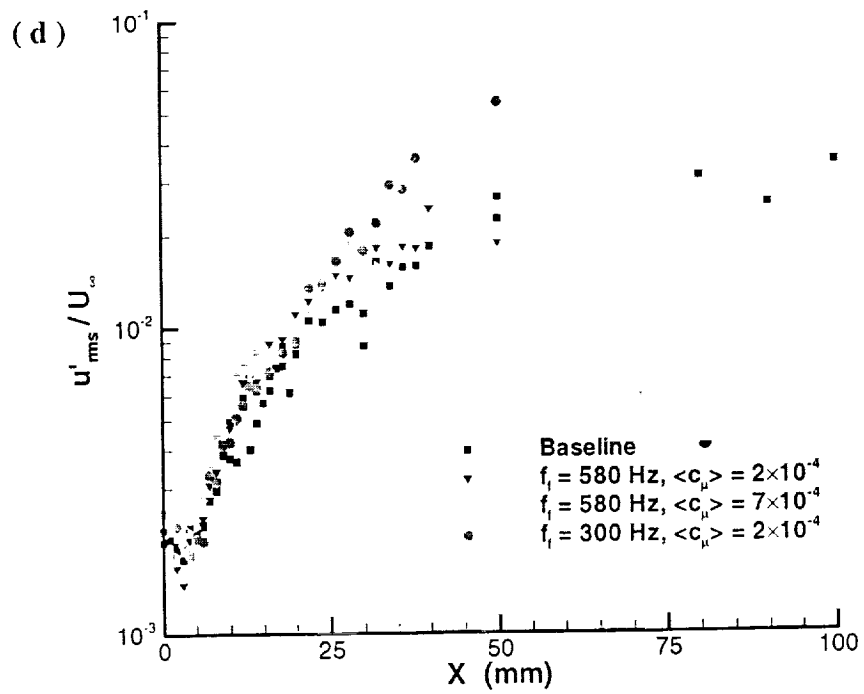
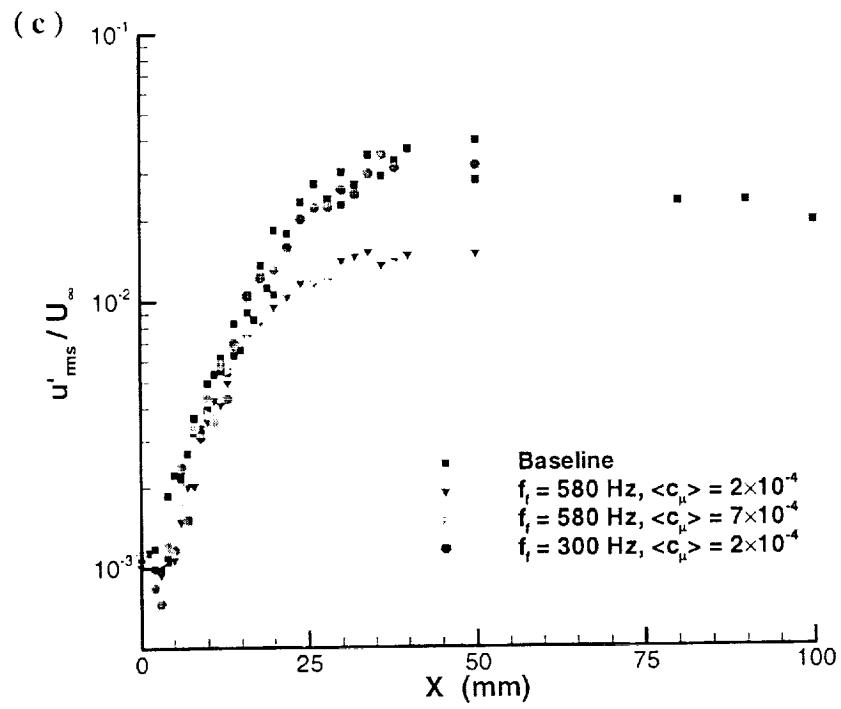


Figure 3.71: Streamwise evolution of spectra with oscillatory blowing control; configuration SS, $f_f = 300 \text{ Hz}$, $\langle c_{\mu} \rangle = 2 \times 10^{-4}$.







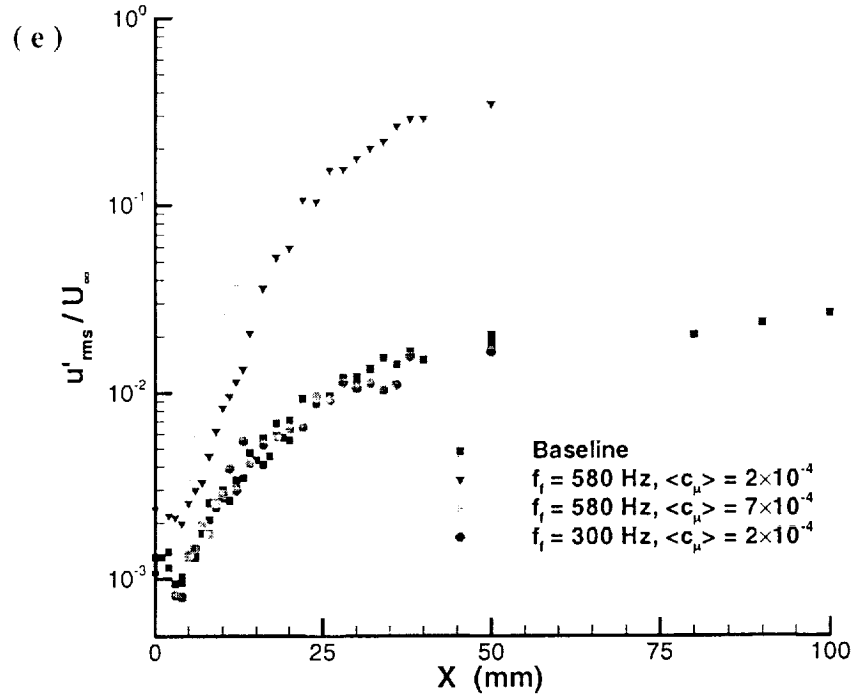


Figure 3.72: Streamwise evolution of velocity fluctuations using oscillatory blowing control for Plate SS: a) rms b) second cavity mode, c) third cavity mode, d) 300Hz, e) 580Hz.

3.7.3.2 Effect of blowing angle

The effect of blowing angle on the mean and rms velocity profiles is shown in Figure 3.73 and Figure 3.74, respectively. Two hole configurations and blowing conditions are examined: configuration SS with $\langle c_{\mu} \rangle = 7 \times 10^{-4}$ and configuration SSA with $\langle c_{\mu} \rangle = 6 \times 10^{-4}$. The forcing frequency is 580Hz. At the cavity lip ($X=0mm$), the profiles are similar to the baseline. At $X=20mm$, the mean velocity profiles for the SS and SSA configurations are more full than the baseline case and the rms velocity profiles are broader. The profiles for the SSA configuration show the largest changes. Further downstream at $X=50mm$, the mean velocity profiles are fuller for both of the SS and SSA

configurations. Over the range of measurement, the fuller mean velocity profiles and broader rms velocity profiles are obtained with the SSA configuration. These results indicate that the blowing at an angle is more effective in enhancing the mixing within the shear layer.

Figure 3.75 shows streamwise evolution of the spectra with the SSA configuration. The forcing frequency of 580Hz is the dominant feature of the spectra.

The effect of blowing angle on the streamwise evolution of the rms velocities is examined in Figure 3.76. The broadband rms velocities, and the rms velocity fluctuations centered on the second and third cavity modes, and the forcing frequency of 580Hz are shown. In Figure 3.76a, b, c, and d, the rms velocities for the SSA configuration are similar to the rms velocities in the SS configuration over the range of measurements.

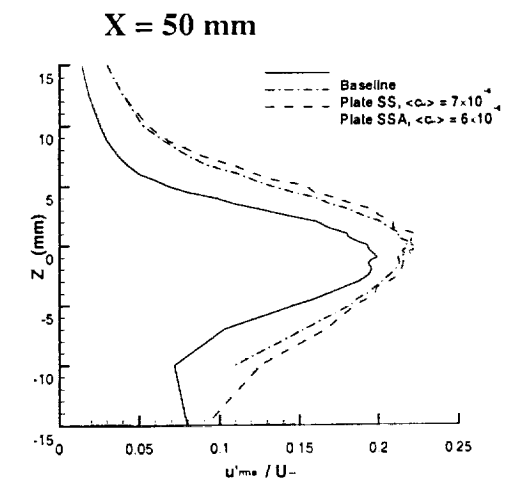
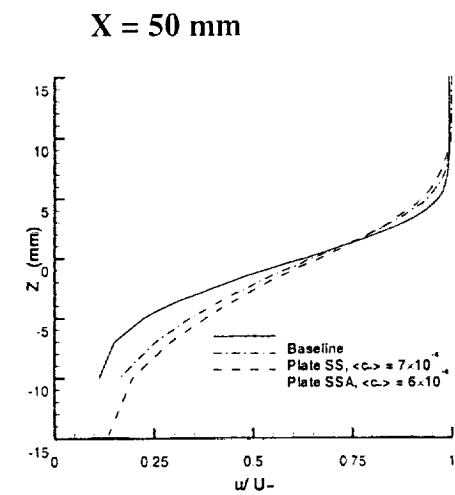
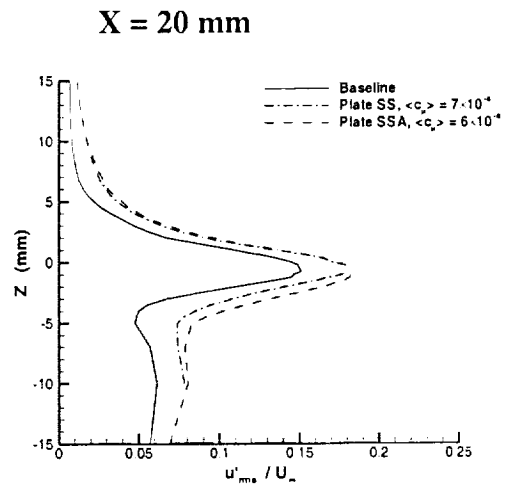
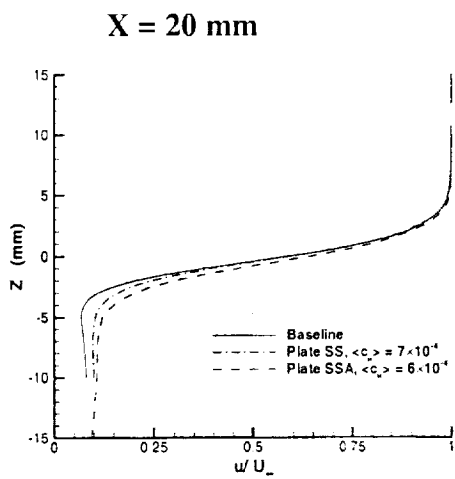
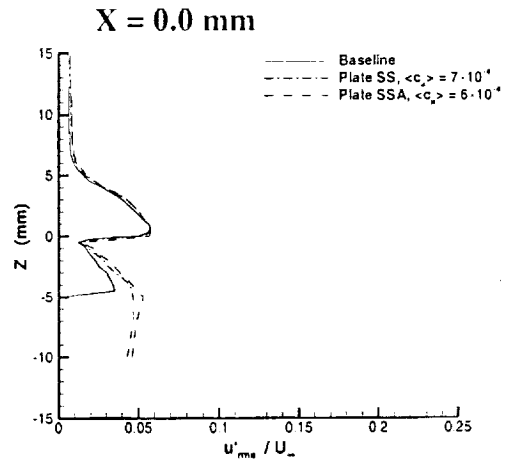
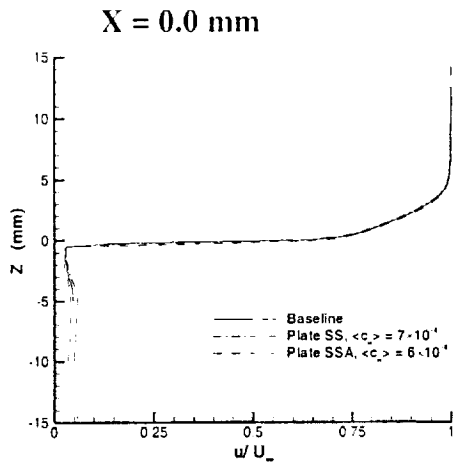


Figure 3.73: Mean velocity profiles with oscillatory blowing control.

Figure 3.74: Rms velocity profiles with oscillatory blowing control.

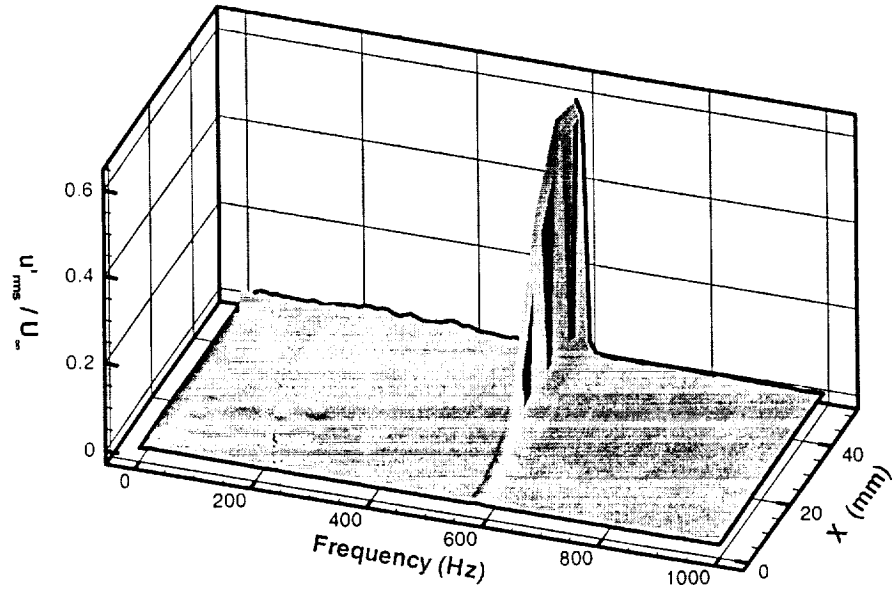
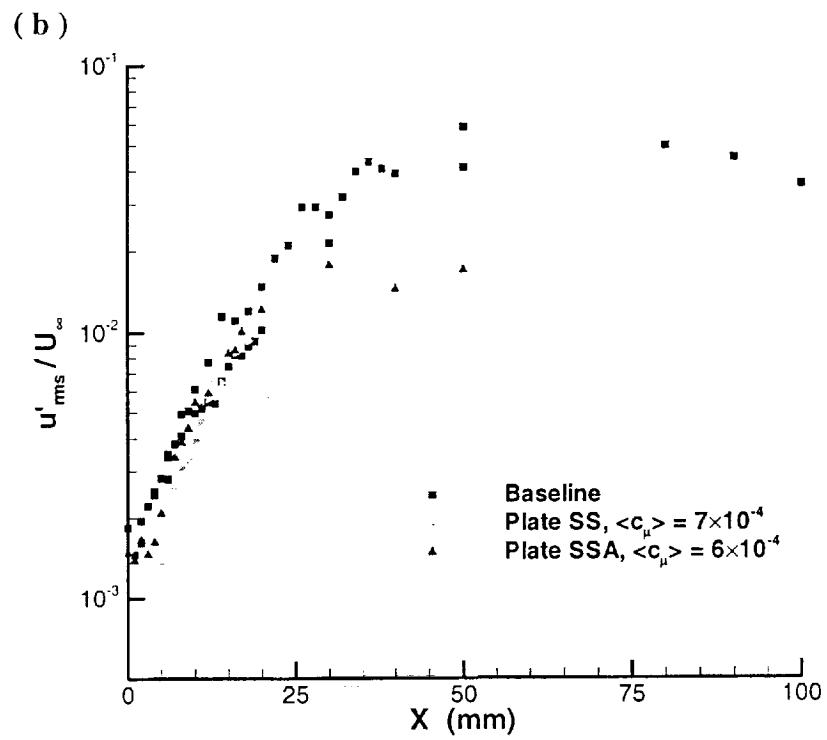
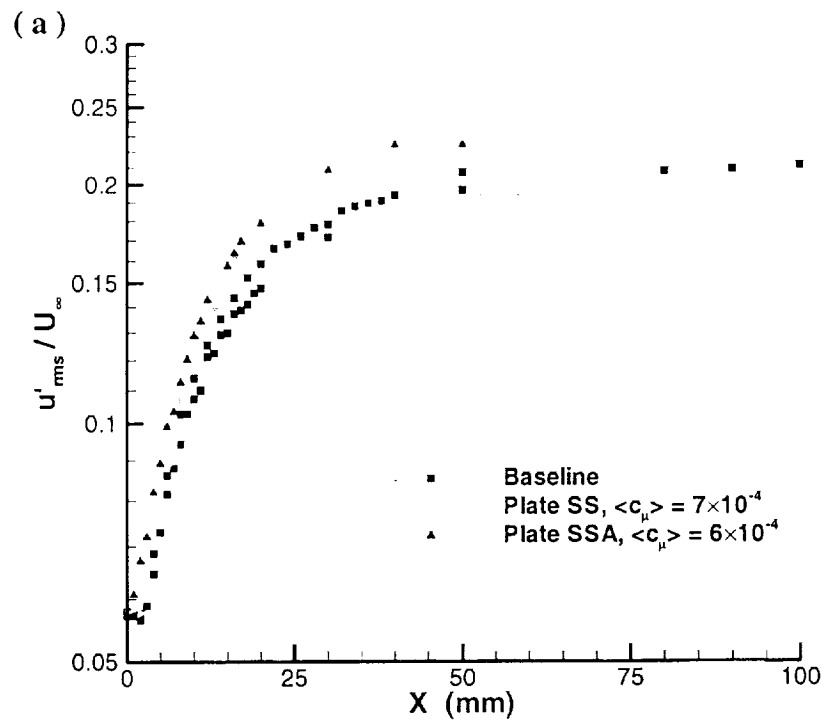


Figure 3.75: Streamwise evolution of spectra with oscillatory blowing control; configuration SSA, $f_f = 580 \text{ Hz}$, $\langle c_\mu \rangle = 6 \times 10^{-4}$.



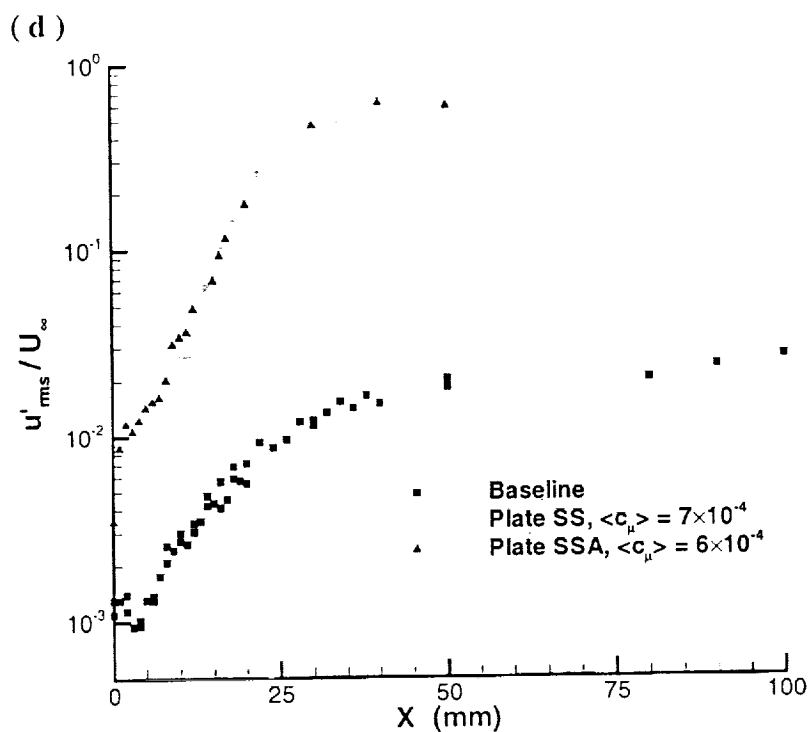
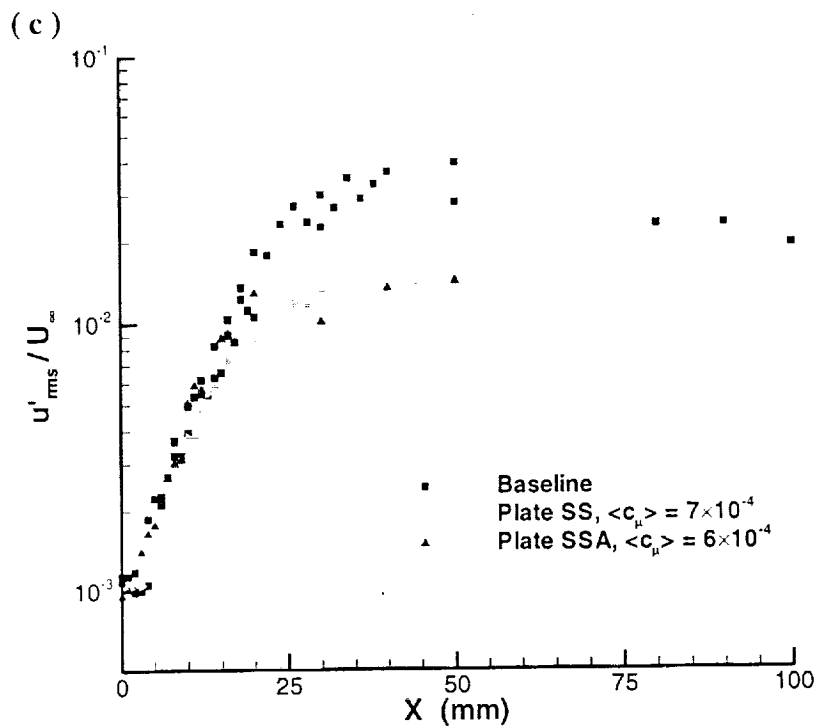


Figure 3.76: Streamwise evolution of velocity fluctuations using oscillatory blowing control at $f_i = 580\text{Hz}$: a) rms, b) second cavity mode, c) third cavity mode. d) 580Hz.

4 Concluding Remarks

An experimental study of the control of cavity resonance using near-zero net mass oscillatory blowing has been conducted. The freestream Mach number is 0.2 and the cavity has a length-to-depth ratio of four. The blowing was applied just upstream of the cavity front wall through interchangeable plate configurations. These configurations enabled the effects of hole size, hole shape, and blowing angle to be examined. An actuator to provide either steady or near-zero net mass oscillatory blowing was designed and fabricated. This actuator provided a range of blowing amplitudes and forcing frequencies. The blowing amplitude is characterized in terms of a momentum coefficient. The detailed measurements obtained in the experiment include fluctuating pressure data at the rear cavity wall and front floor of the cavity, and hot-wire measurements of the cavity shear layer. Spectral and wavelet analysis techniques are applied to understand the dynamics and mechanisms of the cavity flow with control.

4.1 Summary of Results

4.1.1 Steady blowing

The following observations of the cavity flow with steady blowing control are made.

- Effect of blowing amplitude: A range of momentum coefficients 1×10^{-3} to 0.4 were examined. Steady blowing at the larger amplitudes is more effective in reducing the SPL of the resonant cavity modes.

- Effect of hole size: Three round hole sizes were examined. The larger diameter holes are more effective in the control of cavity resonance.
- Effect of hole shape: Three hole/slot shapes were examined: round holes, and streamwise slots and spanwise (long) slots. The streamwise slot configuration is not as effective for control compared to a round hole of equal area. The spanwise (long) slot is not as effective as the other configurations.
- Effect of blowing angle: Two blowing angles, 45° and 90° , using the round hole and streamwise slot configurations were examined. For a given momentum coefficient, the steady blowing at 45° is more effective than blowing at 90° . Furthermore, the 45° configuration yields the largest overall reduction in the SPL.

4.1.2 Near-zero Net mass oscillatory blowing

The following observations of the cavity flow with near-zero net mass oscillatory blowing control are made.

- Effect of blowing amplitude: A range of unsteady momentum coefficients 5×10^{-7} to 8×10^{-2} was examined. The large (1×10^{-5}) unsteady momentum coefficients are the most effective in suppressing the cavity resonance.
- Effect of forcing frequency: A range of forcing frequencies from 100Hz to 650Hz was examined. The oscillatory blowing at forcing frequencies greater than 500Hz (Strouhal number based on the cavity length greater than 1.0) are the most effective. The oscillatory blowing at forcing frequencies below 350Hz (Strouhal number less than 0.76) are the least effective.

- Effect of hole size: The larger diameter holes are more effective in the control of cavity resonance.
- Effect of hole shape: The three hole/slot shapes yield similar reductions in the amplitude of the resonant cavity modes. The spanwise (long) slot is the most effective in reducing the SPL of the second mode; however the SPL amplitudes are increased at the lower frequencies.
- Effect of blowing angle: For a given momentum coefficient, the oscillatory blowing at 45° is more effective than blowing at 90° . For the streamwise slots, the effectiveness of the two blowing configurations is comparable.
- The control of cavity resonance using near zero net mass oscillatory blowing and steady blowing are compared. Near-zero net mass oscillatory blowing is much more effective as momentum coefficients up two orders of magnitude smaller than those required for steady blowing are needed.

4.2 Dynamics and mechanisms of control

- For oscillatory blowing, the effectiveness of control is found to strongly depend on the blowing amplitude, forcing frequency, and hole size. The hole shape and blowing angle are found to be less significant parameters.
- The autocorrelation analysis shows that there is no clear effect on the size of the large-scale structures when oscillatory blowing is employed.
- The cross-correlation analysis shows that oscillatory blowing is effective in modifying the feedback loop associated with the cavity resonance.

- The wavelet analysis reveals that the mode switching behavior in the cavity flow is not suppressed. However the amplitude modulation is reduced and the frequency of modulation occurs at higher frequencies.
- The bispectral analysis suggests that with oscillatory blowing, the nonlinear interactions amongst the resonant modes are reduced, and the dominant nonlinear interactions are associated with the forcing frequency.
- The hot-wire measurements in the shear layer reveal that oscillatory blowing enhances the mixing in the shear layer. This effect is enhanced by blowing at 45°.

4.3 Recommendations

The following are recommendations for future work:

1. In order to apply the oscillatory blowing to full-scale applications, the relevant scaling parameters must be determined. Parameter studies that include the ratios of hole size to the boundary layer (or momentum thickness); hole spacing to cavity width; jet velocity to freestream velocity, and non-dimensional forcing frequency should be conducted.
2. A full-scale application of current interest is the weapons bay. For this application it is of interest to assess the effectiveness of near zero net mass oscillatory blowing at higher Mach numbers.

5 References

- ¹ Davy, R., "Airframe Noise Characteristics of a 1/11 Scale Airbus Model," *AIAA Paper* 98-2335, June 1998.
- ² Fethney, P., and Jelly, A. H., "Airframe Self-Noise Studies on the Lockheed L1011 Tri-Star Aircraft," *AIAA Paper* 80-1061, June 1980.
- ³ Rockwell, D. and Naudascher, E., "Review—Self-Sustaining Oscillations of Flow Past Cavities," *Journal of Fluids Engineering*, Vol. 100, June 1978, pp. 152-165.
- ⁴ Rossiter, J. E., "Wind-Tunnel Experiments on the Flow Over Rectangular Cavities at Subsonic and Transonic Speeds," *ARC R&M* No. 3438, October 1964.
- ⁵ Heller, H. H., and Bliss, D. B., "The Physical Mechanism of Flow-Induced Pressure Fluctuations in Cavities and Concepts for Their Suppression," *AIAA Paper* 75-491, March 1975.
- ⁶ Tam, C., and Block, P., "On the Tones and Pressure Oscillations Induced by Flow Over Rectangular Cavities," *Journal of Fluid Mechanics*, Vol. 89 part 2, 1978, pp. 373-399.
- ⁷ Chokani, N., "Flow Induced Oscillations in Cavities – A Critical Survey." *DGLR/AIAA Paper* 92-02-159, May 1992.
- ⁸ Hankey, W. L. and Shang, J. S., "Analyses of Pressure Oscillations in an Open Cavity," *AIAA Journal*, Vol. 18, August 1980, pp. 892-898.
- ⁹ Zhang, X. and Edwards, J. A., "Computational Analysis of Unsteady Supersonic Cavity Flows Driven by Thick Shear Layers," *Aeronautical Journal*, November 1988, pp. 365-374.
- ¹⁰ Baysal, O., Yen, G., and Fouladi, K., "Navier-Stokes Computations of Cavity Aeroacoustics with Suppression Devices," *Journal of Vibrations and Acoustics*, Vol. 116, January 1994, pp. 105-112.
- ¹¹ Morgenstern Jr., A., and Chokani, N., "Hypersonic Flow Past Open Cavities," *AIAA Journal*, Vol. 32, December 1994, pp. 2387-2393.

- ¹² Sinha, N., Dash, S. M., Chidambaram, N., and Findlay, D., "A Perspective on the Simulation of Cavity Aeroacoustics," *AIAA Paper 98-0286*, January 1998.
- ¹³ Plentovich, E. B., "Three-Dimensional Cavity Flow Fields at Subsonic and Transonic Speeds," *NASA TM-4209*, 1990.
- ¹⁴ Stallings Jr., R. L., and Wilcox Jr., F. J., "Experimental Cavity Pressure Distributions at Supersonic Speeds," *NASA TP-2683*, 1987.
- ¹⁵ Tracy, M. B., and Plentovich, E. B., "Cavity Unsteady-Pressure Measurements at Subsonic and Transonic Speeds," *NASA TP-3669*, 1997.
- ¹⁶ Rona, A., Chen, X. X., Zhang, X., and Edwards, J. A., "Control of Cavity Flow Oscillations through Leading Edge Flow Modification," *AIAA Paper 98-0672*, January 1998.
- ¹⁷ Perng, S. W., and Dolling, D. S., "Passive Control of Pressure Oscillations in Hypersonic Cavity Flow," *AIAA Paper 96-0444*, January 1996.
- ¹⁸ Kim, I., and Chokani, N., "Navier-Stokes Study of a Supersonic Cavity Flowfield with Passive Control," *Journal of Aircraft*, Vol. 29, March-April 1992, pp. 217-223.
- ¹⁹ Vakili, A. D., Wolfe, R., Nagel, T., and Lambert, E., "Active Control of Cavity Aeroacoustics in High Speed Flows," *AIAA Paper 95-0678*, January 1995.
- ²⁰ Cattafesta III, L. N., Garg, S., Choudhari, M. and Li, F., "Active Control of Flow-Induced Cavity Resonance," *AIAA Paper 97-1804*, July 1997.
- ²¹ Shaw, L. "Active Control for Cavity Acoustics," *AIAA Paper 98-2347*, June 1998.
- ²² Sarno, R. L., and Franke, M. E., "Suppression of Flow-Induced Pressure Oscillations in Cavities," *J. of Aircraft*, Vol. 31, January-February. 1994, pp. 90-96.
- ²³ Lamp, A. M. and Chokani, N., "Computation of Cavity Flows with Suppression Using Jet Blowing," *J. of Aircraft*, Vol. 34, July-August. 1997, pp. 545-551. (Also *AIAA Paper 96-0446*).
- ²⁴ Seifert, A., Bachar, T. and Wagnaski, I., "Delay of Airfoil Stall by Periodic Excitation," *J. of Aircraft*, Vol. 33, July-August. 1996, pp. 691-698.
- ²⁵ Seifert, A. and Pack, L. G., "Oscillatory Control of Separation at High Reynolds Numbers," *AIAA Paper 98-0214*, January 1998.

- ²⁶ Seifert, A. and Pack, L. G., "Oscillatory Excitation of Unsteady Compressible Flows over Airfoils at Flight Reynolds Numbers," *AIAA Paper 99-0925*, January 1999.
- ²⁷ Seifert, A. and Pack, L. G., "Active Control of Separated Flows on Generic Configurations at High Reynolds Numbers," *AIAA Paper 99-3403*, July 1999.
- ²⁸ Lin, J., "Control of Low-Speed Turbulent Separated Flow Over a Backward-Facing Ramp," *NASA TM 109740*, 1991.
- ²⁹ McManus, K., Ducharme, A., Goldey, C., and Magill, J., "Pulsed Jet Actuators for Suppressing Flow Separation," *AIAA Paper 96-0442*, January 1996.
- ³⁰ Magill, J., and McManus, K., "Control of Dynamic Stall using Pulsed Vortex Generator Jets," *AIAA Paper 98-0675*, January 1998.
- ³¹ McManus, K., and Magill, J., "Separation Control in Incompressible and Compressible Flows using Pulsed Jets," *AIAA Paper 96-1948*, June 1996.
- ³² Kegerise, M.A., "An Experimental Investigation of Flow-Induced Cavity Oscillations," Ph.D. Thesis, Syracuse University, Syracuse, New York, August 1999.
- ³³ Bendat, J., and Piersol, A., "*Random Data: Analysis and Measurement Procedures.*" 2nd Edition, John Wiley & Sons, New York, 1986.
- ³⁴ Kim, Y. C., and Powers, E. J., "Digital Bispectral Analysis and Its Applications to Nonlinear Wave Interactions," *IEEE Transactions on Plasma Science*, Vol. PS-7, No. 2, June 1979, pp. 120-131.
- ³⁵ Hajj, M. R., Miksad, R. W., and Powers, E. J., "Perspective: Measurements and Analyses of Nonlinear Wave Interactions With Higher-Order Spectral Moments," *J. of Fluids Engineering*, Vol.119, March 1997, pp. 3-13.
- ³⁶ Farge, M., "Wavelet Transforms and Their Application to Turbulence," *Annu. Rev. Fluid Mech.*, Vol. 24, 1992, pp. 395-457.
- ³⁷ Walker, S. H., Gordeyev, S. V., and Thomas, F. O., "A Wavelet Transform Analysis Applied to Unsteady Aspects of Supersonic Jet Screech Resonance," *Experiments in Fluids*, Vol. 22, 1997, pp. 229-238.
- ³⁸ Jordan, D., Miksad, R. W., and Powers, E. J., "Implementation of the Continuous Wavelet Transform for the Digital Time Series Analysis," *Rev. Sci. Instrum*, Vol. 68, No. 3, March 1997, pp. 1484-1494.

- ³⁹ Kegerise, M. A., Spina, E. F., and Cattafesta III, L. N., "An Experimental Investigation of Flow-Induced Cavity Oscillations," *AIAA Paper 99-3705*, June 1999.
- ⁴⁰ McManus, K. and Magill, J., "Airfoil Performance Enhancement Using Pulsed Jet Separation Control," *AIAA Paper 97-1971*, June 1997.
- ⁴¹ Margason, R. J., "Fifty Years of Jet in Cross Flow Research," *AGARD-CP-534*, April 1993.
- ⁴² Miksad, R. W., Jones, F. L., Ritz C. P., and Powers, E. J., "The Role of Nonlinear Wave Interactions in Laminar-Turbulent Transition," *Arch. Mech.*, Vol. 39, No. 3, 1987, pp. 177-205.
- ⁴³ Cattafesta III, L. N., Garg, S., Kegerise, M. S., and Jones, G. S., "Experiments on Compressible Flow-Induced Cavity Oscillations," *AIAA Paper 98-2912*, June, 1998.

A Appendices

A.1 Actuator Design

The actuator was designed to produce both steady and oscillatory blowing control. Three constraints drove the design of the actuator. First, the actuator was required to operate over a range of forcing frequencies including the third cavity mode. Secondly to minimize losses due to viscous effects, the actuator had to be installed within the tunnel plenum and as close as possible to the lip of the cavity front wall. Finally, it was necessary that the actuator be compatible with the existing cavity model in order to minimize the tunnel set-up time.

The different actuator components are shown in Figure A.1 through Figure A.9 and are described in Table A.1. The assembly drawing of the actuator is shown in Figure A.10, and an exploded view is shown in Figure A.11. The rotor, bearings, rotor axle, and rotor cap are assembled into one unit that is contained within the housing. The motor bolts onto the exterior of the motor mount and is connected to the rotor axle via a coupling; this coupling is located within the motor mount. The high-pressure air supply is connected to the housing end plate, while the delivery to the vacuum is connected to the hole on top of the delivery chamber. In the wind tunnel, the housing assembly sits astride the model sidewalls with the rotor axis perpendicular to the sidewalls. The mid section of the lower side of the assembly forms the ceiling of the model. The delivery

chamber is bolted in between the model sidewalls and forms the model ceiling and the front cavity wall.

Table A.1: Description of the actuator components.

Component Name	Description	Material	Quantity
Delivery Chamber	See Figure A.1	6061-T6 Aluminum	1
Delivery Chamber Side Wall	See Figure A.2	6061-T6 Aluminum	1
Hole Insert Plate	See Figure A.3	6061-T6 Aluminum	1
Housing	See Figure A.4	6061-T6 Aluminum	1
Motor Mount	See Figure A.5	6061-T6 Aluminum	1
Rotor	See Figure A.6	Teflon	1
Rotor Axle	See Figure A.7	6061-T6 Aluminum	1
Rotor Cap	See Figure A.8	6061-T6 Aluminum	1
Housing End Plate	See Figure A.9	6061-T6 Aluminum	1
Flexible Coupling	Rocom AT0062	N/A	1
Ball Bearing	77R10	N/A	2

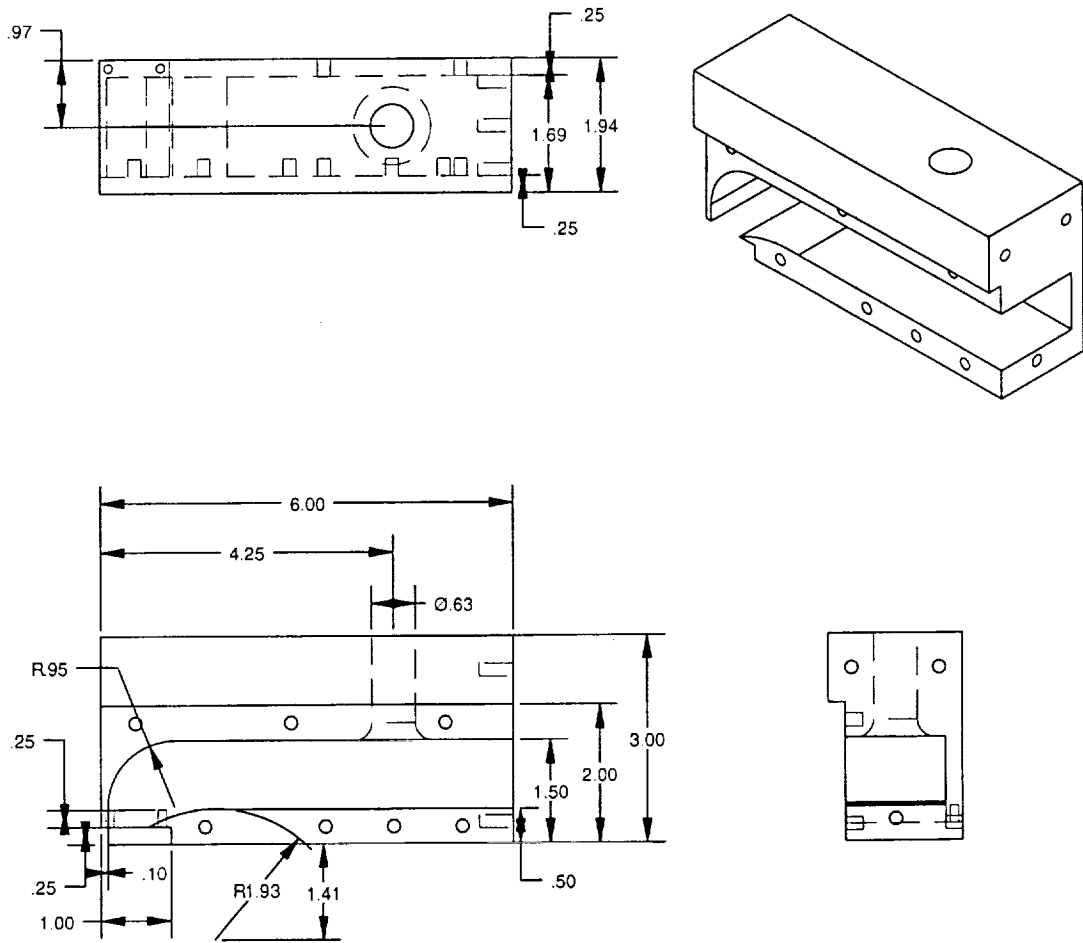


Figure A.1: Actuator delivery chamber.

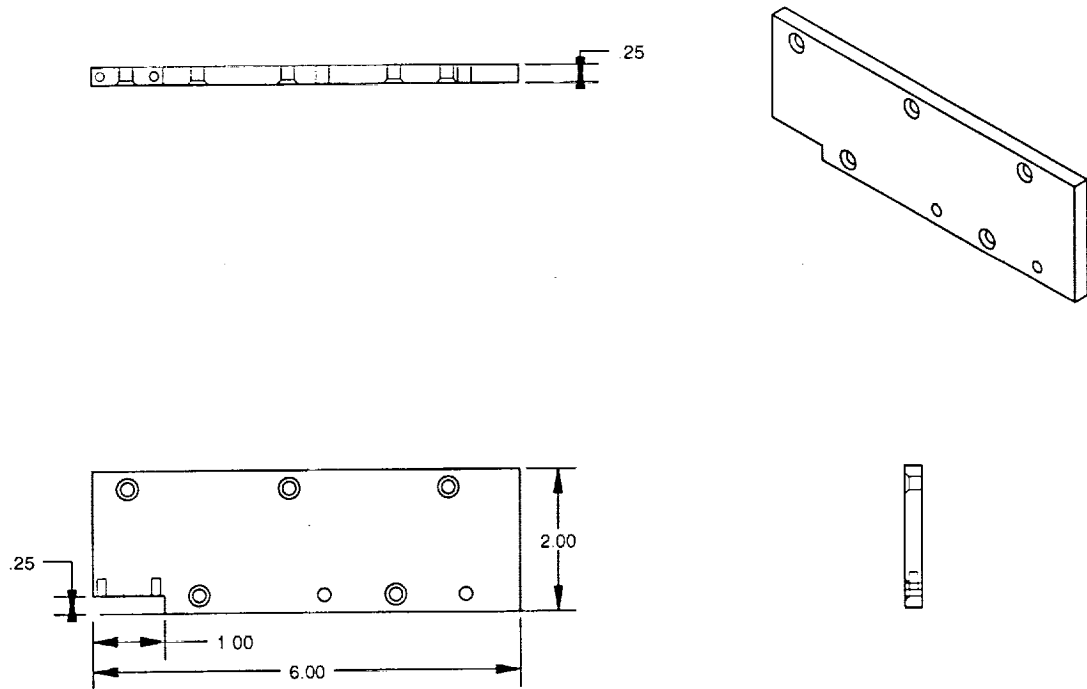


Figure A.2: Side wall of the delivery chamber.

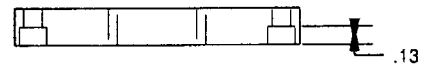
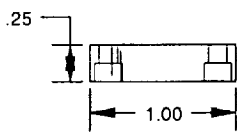
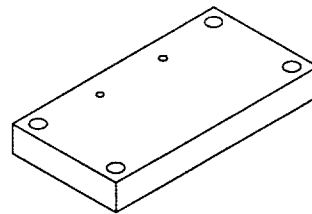
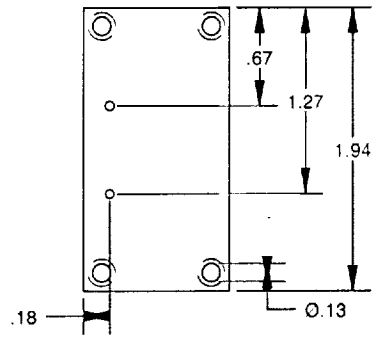


Figure A.3: Hole insert plate.

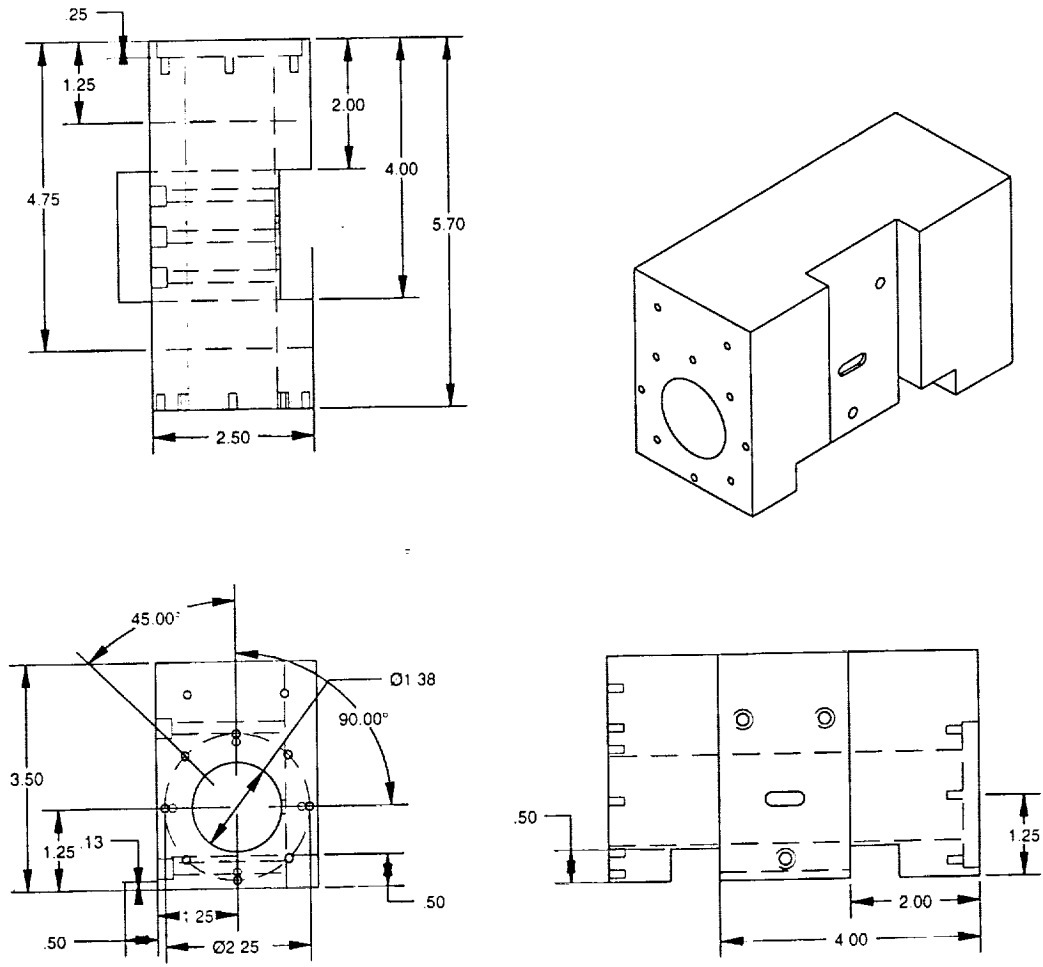


Figure A.4: Actuator housing which contains the rotor assembly.

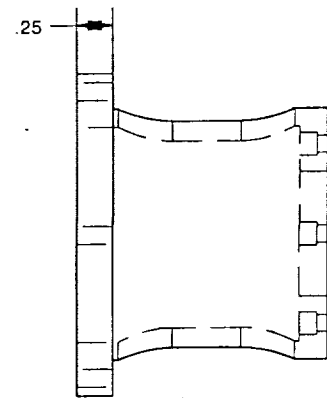
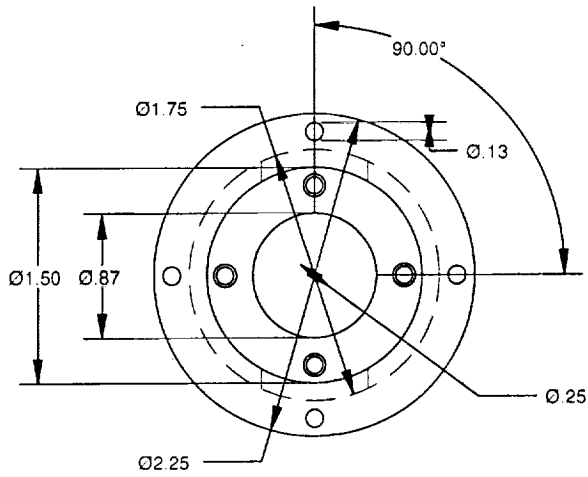
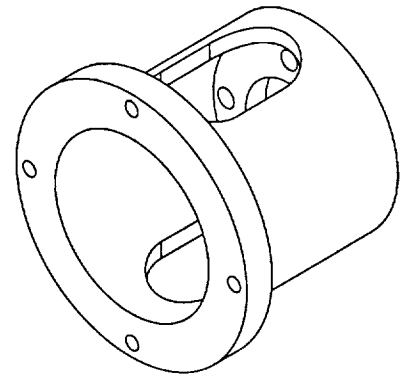
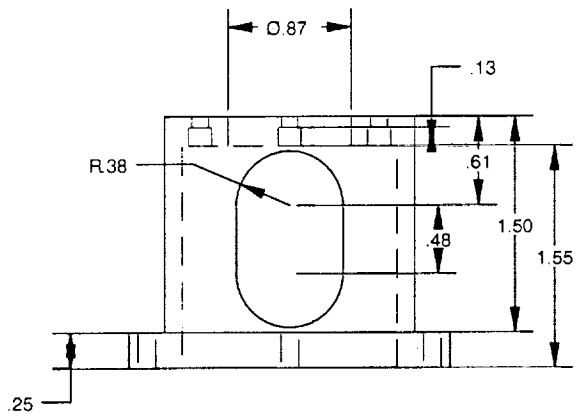


Figure A.5: Motor mount, which attaches the motor to the housing assembly.

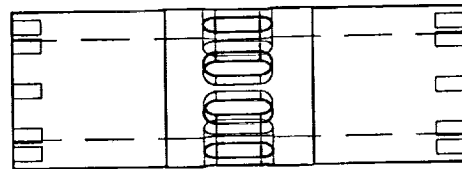
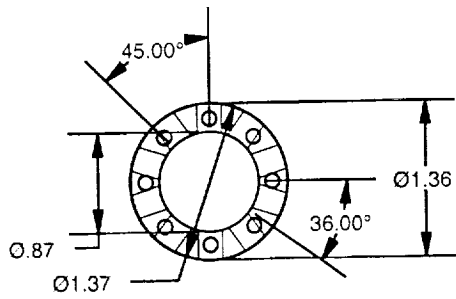
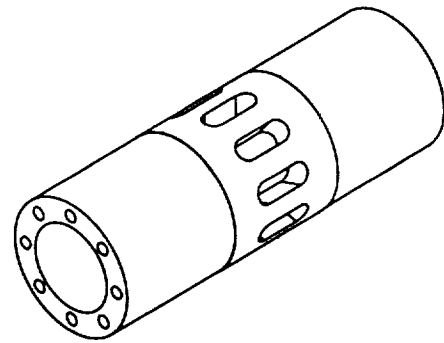
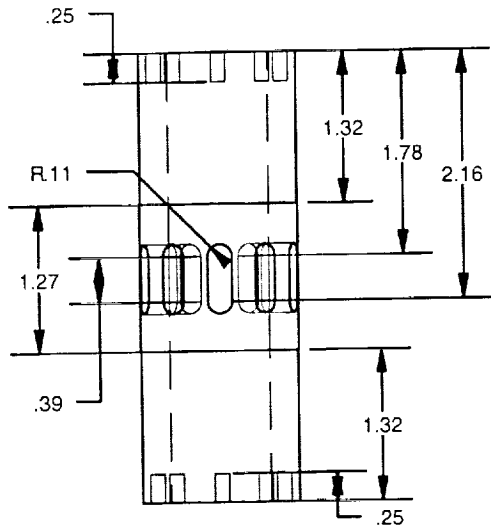


Figure A.6: Rotor.

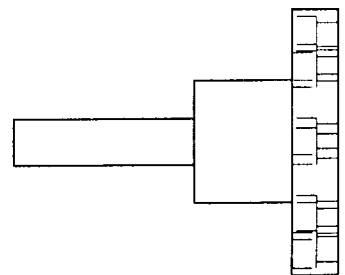
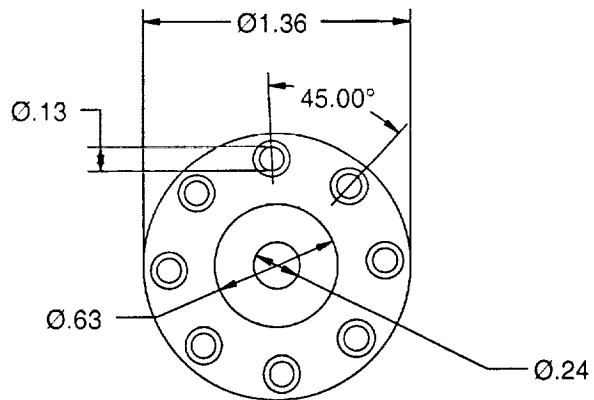
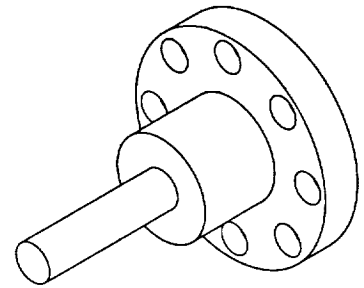
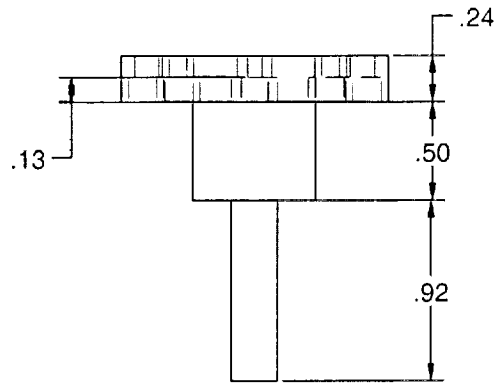


Figure A.7: Rotor axle. Links the motor to the rotor via a coupling.

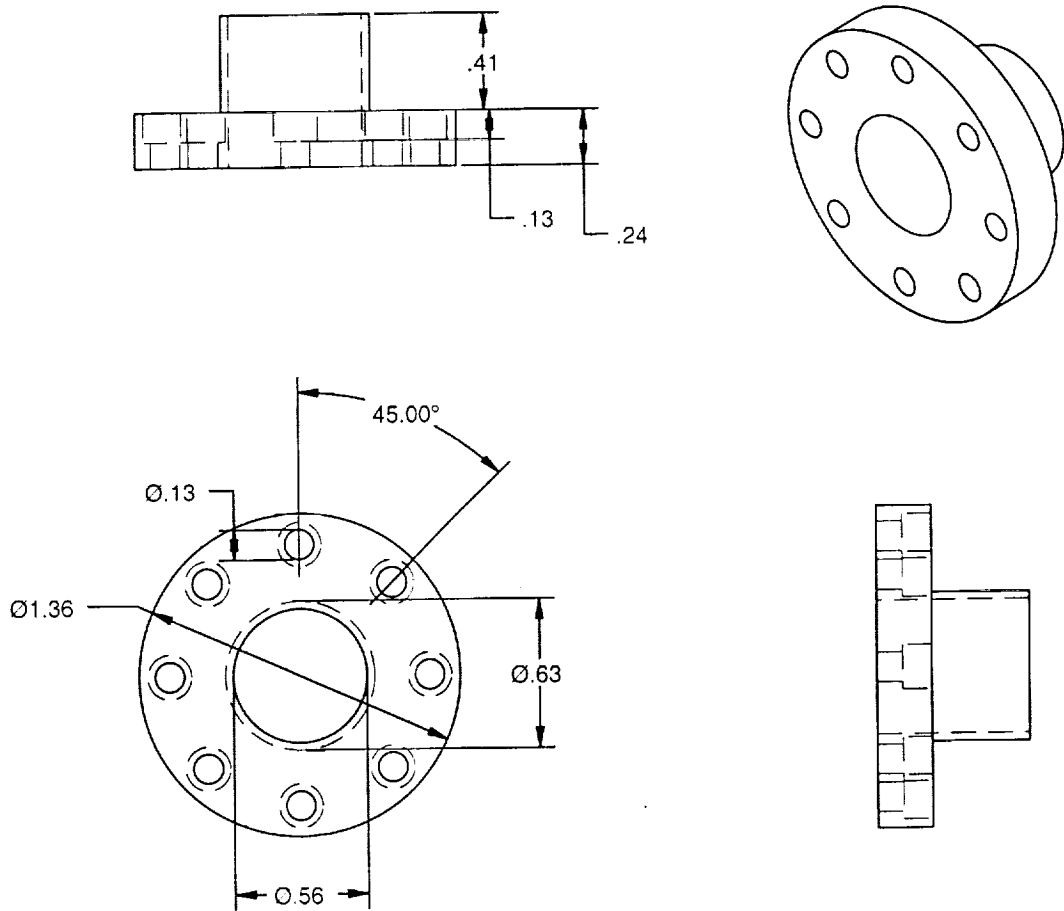


Figure A.8: Rotor cap.

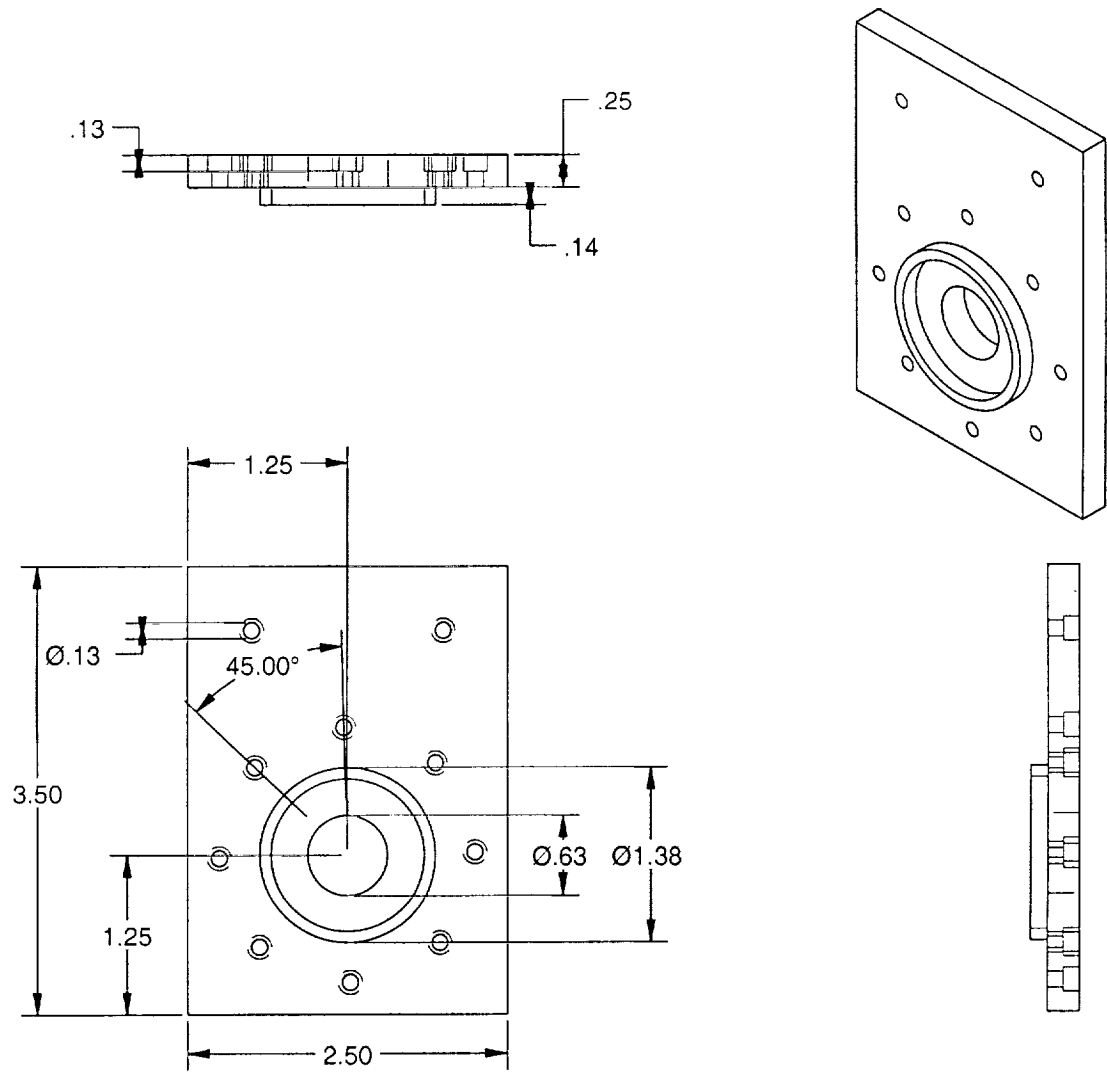


Figure A.9: Housing end plate.

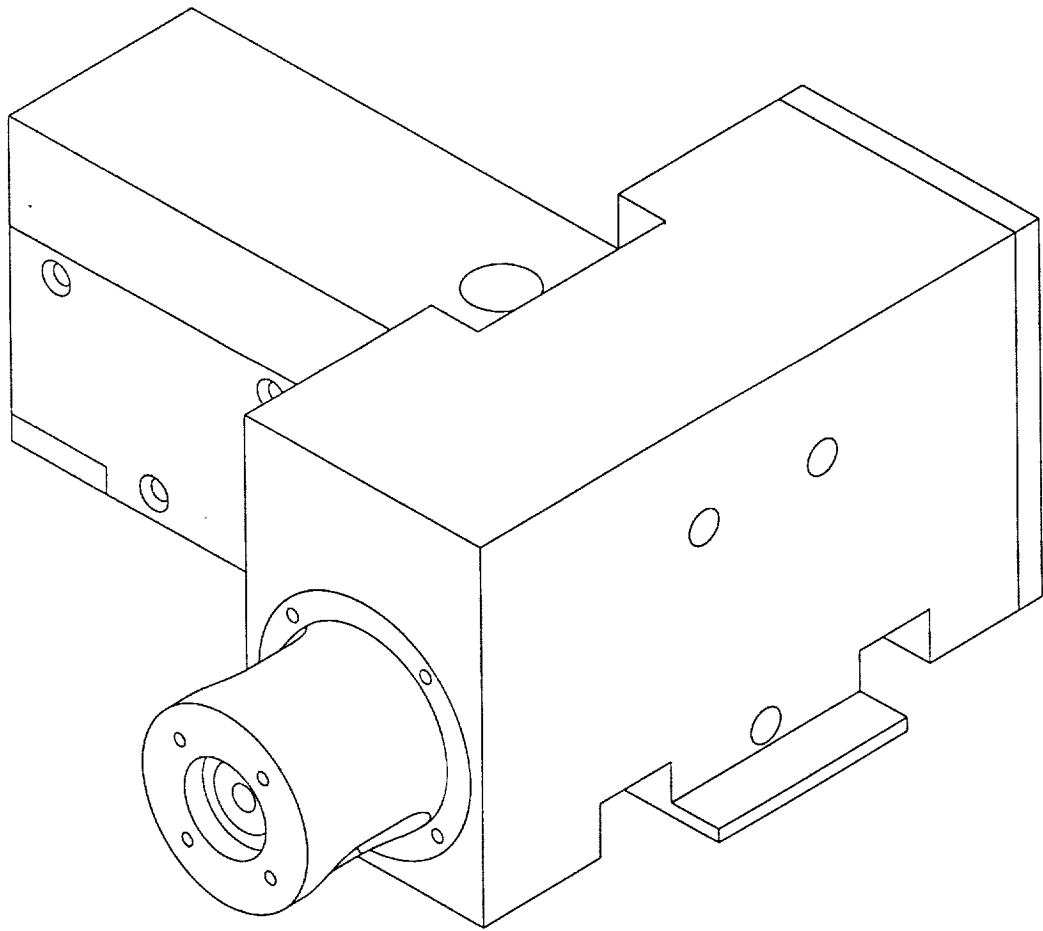


Figure A.10: Assembly drawing of the actuator.

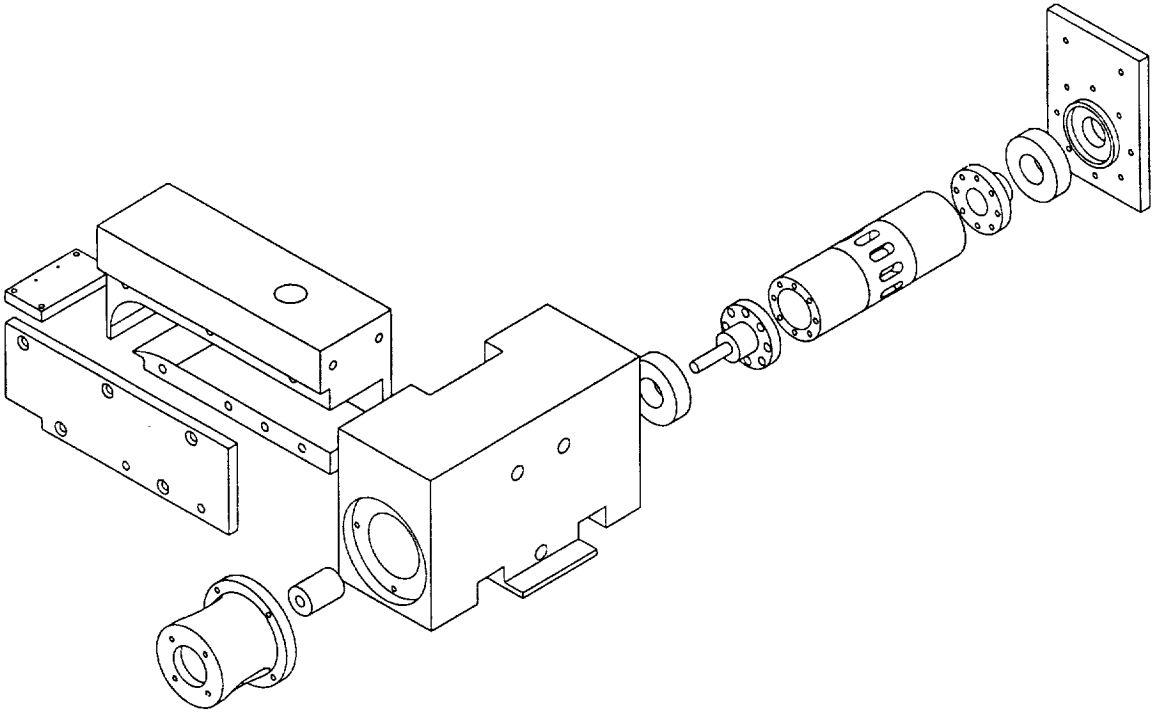


Figure A.11: Exploded assembly view of the actuator with coupling and bearings.

A.2 Experimental Uncertainty

Table A.2: Uncertainty of tunnel properties and calculated values.

Expression	Accuracy
M_∞	0.8 %
P_{t_∞}	0.05 %
T_{t_∞}	0.01 %
c_μ	6 %
$\langle c_\mu \rangle$	35 %

Table A.3: Repeatability of tunnel properties between runs.

Value	Repeatability
P_t	$\pm 1\%$
M_∞	$\pm 1\%$
T_t	$\pm 2\%$

Abstract

The near-zero net mass oscillatory blowing control of a subsonic cavity flow has been experimentally investigated. An actuator was designed and fabricated to provide both steady and oscillatory blowing over a range of blowing amplitudes and forcing frequencies. The blowing was applied just upstream of the cavity front wall through interchangeable plate configurations. These configurations enabled the effects of hole size, hole shape, and blowing angle to be examined. A significant finding is that in terms of the blowing amplitude, the near zero net mass oscillatory blowing is much more effective than steady blowing; momentum coefficients up two orders of magnitude smaller than those required for steady blowing are sufficient to accomplish the same control of cavity resonance.

The detailed measurements obtained in the experiment include fluctuating pressure data within the cavity wall, and hot-wire measurements of the cavity shear layer. Spectral and wavelet analysis techniques are applied to understand the dynamics and mechanisms of the cavity flow with control. The oscillatory blowing is effective in enhancing the mixing in the cavity shear layer and thus modifying the feedback loop associated with the cavity resonance. The nonlinear interactions in the cavity flow are no longer driven by the resonant cavity modes but by the forcing associated with the oscillatory blowing. The oscillatory blowing does not suppress the mode switching behavior of the cavity flow, but the amplitude modulation is reduced.

Acknowledgements

The work presented here was the basis of the first authors Ph.D. dissertation. The authors would also like to acknowledge the other members of the graduate committee from North Carolina State University: Dr. DeJarnette, Dr. Hassan, and Dr. Trussell.

The authors are grateful for the assistance LaTunia Paek provided with the instrumentation used for the bench top experiments. This work could not have been completed without the help from technicians Rick Clark, Ron Harvey, and Jerome Harris of the Probe Calibration Tunnel. They operated the tunnel and installed the test set-up. Also Andy Harrison from Wyle Laboratories provided assistance for the electronics. Their work is greatly appreciated.

Skip Richardson and Mike Breedlove at the Mechanical and Aerospace Engineering Department at North Carolina State University fabricated the actuator used in this research. Skip also provided much needed technical support and rework of the actuator at a moments notice. Their work is deeply appreciated.

This research was supported by the Cooperative Agreement NCC-1-335 between the Flow Physics and Control Branch at NASA Langley Research Center and North Carolina State University.